Design of high-speed robots with drastically reduced energy consumption

Rafael Balderas Hill

To cite this version:

Rafael Balderas Hill. Design of high-speed robots with drastically reduced energy consumption. Automatic. École centrale de Nantes, 2019. English. NNT : 2019ECDN0028 . tel-02932456

HAL Id: tel-02932456
https://theses.hal.science/tel-02932456

Submitted on 7 Sep 2020

HAL is a multi-disciplinary open access archive for the deposit and dissemination of scientific research documents, whether they are published or not. The documents may come from teaching and research institutions in France or abroad, or from public or private research centers.

L'archive ouverte pluridisciplinaire **HAL**, est destinée au dépôt et à la diffusion de documents scientifiques de niveau recherche, publiés ou non, émanant des établissements d'enseignement et de recherche français ou étrangers, des laboratoires publics ou privés.

UNIVERSITE BRETAGNE LOIRE / MATHSTIC

CENTRALE NANTES

THESE DE DOCTORAT DE

L'ÉCOLE CENTRALE DE NANTES
COMUE UNIVERSITE BRETAGNE LOIRE

ECOLE DOCTORALE N° 601
Mathématiques et Sciences et Technologies
de l'Information et de la Communication
Spécialité : *Automatique, productique et robotique*

Par
Rafael BALDERAS HILL

Conception des robots rapides à consommation énergétique drastiquement réduite

Thèse présentée et soutenue à Nantes, le 25 Septembre 2019
Unité de recherche : Laboratoire des Sciences du Numérique de Nantes (LS2N)

Rapporteurs avant soutenance :

Nicolas Andreff	Professeur des universités, Université de Franche-Comté – FEMTO-ST
Belhassen Chedli Bouzgarrou	Maître de conférences, HDR, Sigma-Clermont – Institut Pascal

Composition du Jury :

Président :	Nicolas Mansard	Directeur de recherche, LAAS – CNRS
Examinateurs :	Christine Chevallereau	Directrice de recherche, LS2N – CNRS
	Viviane Pasqui	Maître de conférences, HDR, ISIR – GEMA
Directeur de thèse :	Sébastien Briot	Chargé de recherche, HDR, LS2N – CNRS
Co-encadrants de thèse :	Abdelhamid Chriette	Maître de conférences, LS2N – ECN
	Philippe Martinet	Directeur de recherche, CHORALE – INRIA

Abstract

It is well-known that one of the most representative future challenges in industrial robotics, is to increase the energy efficiency of robot manipulators. In industrial applications, such as high-speed pick-and-place operations, the accuracy is typically the most important criteria to measure the robot performance. Nevertheless, the design trends to operate at high speeds are shifting to the design of robots, which are not only accurate, but also they can perform in an energy-efficient way. When performing high-speed motions in pick-and-place robots, a significant amount of energy is required to move and stop the robot in the desired positions. This mainly occurs when achieving a desired high speed since a large amount of energy must be brought to make the robot move, and then this energy is dissipated to stop the robot in the braking phase. This is not efficient at all. It would be smarter to store the energy.

This thesis proposes an actuation principle for reducing the energy consumption of high-speed robots by placing variable stiffness springs (VSS) in parallel to the motors that actuate the links of a high-speed robot. The main idea is to smartly tune online the force/displacement relation of the VSS, associated to the VSS stiffness, so that the robot is put in near a resonance mode, thus considerably decreasing the energy consumption during fast pseudo-periodic pick-and-place motions. By adding a spring with controllable stiffness in parallel to the robot actuated links, two performances are achieved: *i*) direct power connection between the motor and the robot links, thus ensuring accuracy at high-speeds; *ii*) control of the stored potential energy to be released per cycle of the pick-and-place motion, thus exploiting the robot natural dynamics at high-speeds, and therefore reducing the energy consumption.

The experimental results of the suggested approach on an industrial-sized prototype show the drastic reduction of energy consumption for fast quasi-periodic pick-and-place-like motions.

Finally, we extend the concept of exploiting the natural dynamics for robots in other applications in which they are not necessarily required to perform high-speed tasks, but in which a continuous exchange from potential to kinetic energy may be smartly exploited.

Keywords: high-speed pick-and-place robots, variable stiffness springs, exploiting the natural dynamics, exchange from potential to kinetic energy, reduction of the energy consumption.

Résumé

Il est bien connu qu'un des plus importants défis de la robotique industrielle est d'augmenter l'efficacité énergétique des robots manipulateurs. Dans les applications industrielles, telles que les opérations de prise et dépose à grande vitesse, la précision est généralement le critère le plus important pour mesurer les performances du robot. Cependant, les méthodes de conception des robots rapides ont évolué vers la conception des robots, pas seulement précis, mais également performants sur le plan énergétique. Lorsque des robots de prise et dépose effectuent des mouvements à grande vitesse, une quantité importante d'énergie est nécessaire pour déplacer et arrêter le robot dans les positions souhaitées. Cela se produit principalement lorsque la vitesse élevée souhaitée est atteinte, car une grande quantité d'énergie doit être apportée pour faire bouger le robot, puis cette énergie est dissipée pour arrêter le robot en phase de freinage. Ce n'est pas efficace du tout. Il serait plus pertinent d'avoir un stockage d'énergie.

Cette thèse propose un principe d'actionnement pour réduire la consommation d'énergie des robots à grande vitesse en plaçant des ressorts à raideur variable en parallèle des actionneurs d'un robot rapide. L'idée est de régler la raideur de ces ressorts à l'aide d'autres actionneurs afin de mettre le robot à proximité de modes de résonance lors de son déplacement (les trajectoires de prise et dépose étant pseudo-oscillantes). En ajoutant un ressort à raideur variable en parallèle des liaisons actionnées par le robot, deux performances sont obtenues: *i*) la connexion directe entre les liaisons du moteur et du robot, garantissant ainsi la précision à grande vitesse, et *ii*) le contrôle de l'énergie potentielle stockée à libérer par cycle du mouvement de prise et dépose, exploitant ainsi la dynamique naturelle du robot à haute vitesse et réduisant la consommation d'énergie.

Les résultats expérimentaux de l'approche suggérée sur un prototype de taille industrielle montrent la réduction drastique de la consommation d'énergie pour des mouvements rapides pseudo-oscillants.

Finalement, nous étendons le concept d'exploitation de la dynamique naturelle des robots dans d'autres applications dans lesquelles ils n'exécutent pas forcement des tâches à grandes vitesses, mais dans lesquelles un échange continu d'énergie potentielle à énergie cinétique peut être exploité intelligemment.

Mots-clés: robots rapides de prise et dépose, ressort à raideur variable, exploiter la dynamique naturelle, échange entre énergie potentielle et énergie cinétique, réduction de la consommation d'énergie.

Acknowledgements

Before beginning this manuscript, I would like to express some words to the people who have guided me, shared time with me, and supported me during the past three years.

Firstly, I would like to express my great appreciation to my thesis director, Sébastien Briot for his valuable and constructive guidance during the planning and development of this thesis. With his useful critiques and comprehensive experience on dynamics, he has been a great mentor throughout this journey. I am extremely grateful for the balance he has put between guiding me and encouraging me to be autonomous during this research.

I would like to thank my co-supervisors, Abdhelhamid Chriette and Philippe Martinet, for the time they have shared with me, their patience and their wise advises provided for the development of this work and during the editing of the research articles.

I would like to express my gratitude also to Stéphane Jolivet, David Llevat and Philippe Lemoine for their patience to help me to build and to implement the prototype for the experimental validations. Their combined advises helped me to improve the different parts of the prototype, including the mechanics and electronics.

I also would like to express my gratitude to my thesis defense committee and especially to Profs. Nicolas Andreff and Chedli Bouzgarrou. Their detailed and valuable comments have contributed to the quality of this manuscript.

My PhD life would not have been the same without my friends. I address a particular acknowledgement to my friend Saman Lessanibahri who is finishing his PhD thesis as well. We have spent very good moments together since the Master. I would like to also address special thanks to my friends and colleagues David, Marlène, Sébastien, Johan, Victor, Emmanuel, Susana, Tahir, Zhongmou, Julian, Franco, Guillaume, Minglei, Cathe, Antoine, Elias, Erick, Elaheh, Jing, for having interesting discussions and sharing beautiful moments with me.

I would like to express a special thank to the Mexican Council of Science and Technology (CONACYT) for sponsoring my PhD studies, their support was very important during these three years of PhD studies.

I would like to express all my gratitude and love to my parents Arturo and Mercedes, and to my brothers Arturo and Juan, who have always encouraged me to accomplish my objectives and most importantly to wisely advise me during all my life. I am eternally grateful to them for their love, education and never ending support.

And finally, last but by no means least, I would like to express my tremendous gratitude and my love to my girlfriend Stephanie. I am not sure that this thesis would have concluded successfully without her comprehension, patience and love.

To my parents, Arturo and Mercedes
To the woman I love, Stephanie
To the memory of my grandparents, Josefina and Armando.

Table of Contents

Abstract **i**

Résumé **iii**

Acknowledgements **v**

Table of Contents **ix**

List of Figures **xv**

List of Tables **xxv**

Nomenclature **xxix**

Introduction **1**

1 State of the art **5**

1.1 Historical evolution of high-speed robots 6

1.1.1 Origins 6

1.1.2 Towards achieving more speed for robots in industrial applications . 11

1.2 Towards designing energy-efficient high-speed robots 18

1.2.1 Conventional techniques for energy minimization 19

1.2.1.1 Beginnings with static balancing techniques 19

1.2.1.2 Design of lightweight robot architectures 21

1.2.1.3 Motion planning techniques 24

1.2.1.4 Redesign of electric cabinets 27

1.2.1.5 Use of elastic passive compliance: SEAs and VSAs 29

1.2.2 Increasing the energy efficiency of pick-and-place robots: use of springs 35

1.3 Existing strategies for increasing the energy efficiency of high-speed robots 41

1.4 Summary 42

2 Dynamic and power consumption modeling of an energy-efficient high-speed robot 45

2.1 Actuation concept based on parallel variable stiffness springs 46

2.1.1 Architecture description of variable stiffness springs 47

2.1.2 Resonance aspects of springs in parallel to motors: Case study with 1-DOF robot 50

2.2 Dynamic analysis of the parallel configuration of variable stiffness springs with the actuated links of parallel robots 54

2.2.1 Dynamic modeling of parallel robots 54

2.2.1.1 Dynamic model of tree-loop robots 54

2.2.1.2 Dynamic model of parallel robots 56

2.2.2 Dynamic modeling of variable stiffness springs 57

2.3 Energy consumption modeling 59

2.3.1 Working principle of motor drive system 59

2.3.2 Modeling of the motor drive system 60

2.3.3 Operation modes 64

2.3.4 Model of energetic losses 66

2.4 Simulation of physical models and identification of preponderant energetic losses 69

2.5 Summary 74

3 Exploiting robot natural motions in order to reduce the energy consumption 77

3.1 Performing energy-efficient pick-and-place motions in the case of known dynamic parameters 78

3.1.1 Matching pick-and-place boundary conditions with the robot free-response 78

3.1.1.1 Solution of boundary value problems by using the shooting method 81

3.1.1.2 BVP applied on energy-efficient high-speed robots 83

3.1.2 Application of the energy-efficient motion generator to a five-bar mechanism with VSS: for constant and variable payload 89

3.1.2.1 First set of boundary pick-and-place constraints: for constant and variable payload 90
3.1.2.2 Second set of boundary pick-and-place constraints: for constant and variable payload 96
3.1.3 Application of the energy-efficient motion generator to a Delta robot with VSS: for constant and variable payload 99
3.1.3.1 First set of boundary pick-and-place constraints: for constant and variable payload 100
3.1.3.2 Second set of boundary pick-and-place constraints: for constant and variable payload 105
3.2 Performing energy-efficient pick-and-place motions in the case of unperfectly known dynamic parameters 110
3.2.1 Online solution of boundary value problem 111
3.2.2 Adaptive feedback linearization 113
3.2.3 Application of the online motion generator to a five-bar mechanism with VSS 117
3.2.3.1 Case without adaptive law and unperfectly known parameters 117
3.2.3.2 Case with adaptive law 118
3.3 Summary 122

4 Prototype and experimental validations 125
4.1 Description of the prototype 126
4.1.1 CAD modeling and prototyping of robot and variable stiffness system 126
4.1.2 Technical description of robot revolute joints and variable stiffness joints 131
4.1.3 Instrumentation and communication 133
4.2 Identification of dynamic parameters 136
4.2.1 Identification procedure based on Least Squares method 136
4.2.2 Identified dynamic parameters of the robot and the variable stiffness system 139
4.3 Experimental results for reducing energy consumption 145
4.3.1 Controller design 145
4.3.2 Synthonization of controller gains 148

4.3.3 Results 149
4.3.3.1 First set of boundary pick-and-place constraints 149
4.3.3.2 Second set of boundary pick-and-place constraints 155
4.4 Summary 161

5 Exploiting natural dynamics: other application cases 165

5.1 Definition of application cases 166
5.2 Reducing the energy consumption of an omnidirectional spherical rolling robot 167
5.2.1 Description of spherical rolling robot with mobile masses 168
5.2.2 Modeling of spherical rolling robot with mobile masses 169
5.2.2.1 Geometric Model 170
5.2.2.2 First Order Kinematic Model 171
5.2.2.3 Second Order Kinematic Model 171
5.2.2.4 Dynamic Model 172
5.2.3 Modeling of variable stiffness springs in parallel configuration with the mobile masses 173
5.2.3.1 Rolling Robot with VSS in Parallel 173
5.2.4 Energy-efficient motion generation and control 174
5.2.4.1 Motion generation for spherical rolling robot 175
5.2.4.2 Variable stiffness joint trajectories from VSS placed in parallel 177
5.2.4.3 Optimization problem formulation: cost function and decision variables 179
5.2.5 Simulation results 180
5.2.5.1 SolidWorks model 180
5.2.5.2 ADAMS Model 181
5.2.5.3 Model Properties and Parameters 181
5.2.5.4 Simulations 182
5.3 Increasing the feasible static-wrench workspace of robots 186
5.3.1 Exploiting natural oscillations for enlarging feasible static-wrench workspace 188
5.3.1.1 Shooting method applied on robot manipulators with heavy payloads 188

5.3.1.2 Initial oscillations for achieving optimal aspect-connecting velocity 189
5.3.2 Case study: 2-DOF serial robot 190
5.4 Summary 197

Conclusion **199**

A Dynamic model of the five-bar mechanism **207**

B Dynamic model of the 3-DOF Delta robot **209**

C Equations and joints specifications of the variable stiffness system **211**

D Dynamic model of the 2R serial robot with payload **215**

E List of publications of presented works **217**

References **219**

List of Figures

1.1 Unimate robot (first industrial robot) [Malone 2011]. 6
1.2 Unimate robot in production lines of General motors [Malone 2011]. 7
1.3 Expansion of industrial robots from 1950 to 1970. 8
1.4 Expansion of industrial robots from 1970 to 1980. 9
1.5 Two main inventions towards the designing of faster robots. On the left a SCARA robot is shown, and on the right the first direct-driven robot is presented. 11
1.6 AdeptOne SCARA robot [Adept]. 11
1.7 Schematic of patent of Delta robot by Reymond Clavel [Clavel 1990]. . . . 12
1.8 Applications of Delta robots. 13
1.9 Examples of high-speed robots. 16
1.10 Examples of high-speed robots (continued). 17
1.11 Examples of static balanced mechanisms. 20
1.12 Delta robot with the balancing mechanism [Baradat 2008]. 21
1.13 Anthropomorphic lightweight robot for high-speed safe interaction [Kim 2017]. 22
1.14 High-speed CDPR FALCON-7 [Kawamura 2000]. 24
1.15 Power consumption with method proposed in [Riazi 2016]. 25
1.16 Block diagram proposed for the time scaling strategy to minimize the energy consumption (TET stands for Task Execution Time). [Pellicciari 2013]. 26
1.17 DC-based power architecture [Pellicciari 2015]. 28
1.18 Classical AC power system [Pellicciari 2015]. 28
1.19 Schematic of SEA 30
1.20 Examples of SEAs applied on applications related to absorbing impacts and increase peak power (walking robots) and for human-interaction for increasing safety. 31
1.21 Schematic of variable stiffness actuator. 32
1.22 Examples of designs by following the port-based modeling approach presented in [Visser 2010]. 33

1.23 Actuator with Adjustable Stiffness (AwAS) developed by IIT from the VIACTORS project. 34
1.24 Schematic of constant stiffness spring in parallel to the motor. 36
1.25 Examples of robots with constant stiffness springs in parallel [Barreto 2016]. 37
1.26 Slow serial manipulator with VSS in parallel [Goya 2012]. 39

2.1 On the left, a 2R serial robot with variable stiffness linear springs in parallel arrangement with the links is shown. On the right the same 2R serial robot with variable stiffness torsional springs is presented (the grey circles denote the actuated joints). 47
2.2 On the left, a five-bar mechanism with variable stiffness linear springs in parallel arrangement with the actuated links is shown. On the right the same parallel robot with variable stiffness torsional springs is presented (the grey circles denote the actuated joints). 47
2.3 A general serial robot with variable stiffness linear springs in parallel configuration with the links. 48
2.4 A general serial robot with variable stiffness torsional springs in parallel configuration with the links. 48
2.5 A general parallel robot with variable stiffness linear springs in parallel configuration with the actuated links. 49
2.6 A general parallel robot with variable stiffness torsional springs in parallel configuration with the actuated links. 49
2.7 one-degree-of-freedom robot with torsional spring of constant k in parallel. 51
2.8 one-degree-of-freedom robot with VSS in parallel. 53
2.9 Virtual tree structure 55
2.10 Power transmission system of variable stiffness springs in parallel to the motors. q_{a_i} and q_{s_j} represent the parallel robot joints and variable stiffness joints coordinates, respectively, and $i = 1, ..., n$, $j = 1, ..., n_s$. 58
2.11 Schematic of three-phase brushless motor drive system 61
2.12 Electric circuit of the brushless motor with three phases 61
2.13 Electromotive forces [Chapman 1991] 62
2.14 Motor scheme with load attached to the rotor. 64
2.15 Motoring mode 65
2.16 Freewheeling motoring mode 66
2.17 Generating mode 66

2.18 Freewheeling generating mode 67
2.19 Five-bar mechanism parameterization with two actuated joints q_{11} and q_{21} located at A_{11} and A_{21}, respectively, and three passive joints q_{12}, q_{22} and q_{13} located at A_{12}, A_{22} and A_{13}, respectively. 70
2.20 Multiple-point pick-and-place sequence in the five-bar mechanism workspace: $A \rightarrow B$ (travel time: 0.27 s), $B \rightarrow C$ (travel time: 0.23 s), $C \rightarrow D$ (travel time: 0.21 s), $D \rightarrow E$ (travel time: 0.3 s), $E \rightarrow F$ (travel time: 0.29 s), $F \rightarrow B$ (travel time: 0.25 s), $B \rightarrow A$ (travel time: 0.18 s). 72
2.21 Input torque for the first joint of the parallel robot for nominal actuation. . 73
2.22 Input torque for the second joint of the parallel robot for nominal actuation. 73
2.23 Energetic losses for the nominal actuation, i.e. the losses from the two motors in the active joints q_{11} and q_{21} of the five-bar mechanism. 74
2.24 Energy losses decoupled from the energetic model in order to show how preponderant is each loss when performing a nominal high-speed pick-and-place operation. 74

3.1 Decomposition of a video taken from real a pick-and-place application in the bread industry. The desired pick-and-place positions are represented by P_A, P_B, P_C, P_D, P_E and P_F. The time connecting these desired positions are defined according to the following sequence: $P_A \rightarrow P_B$ (travel time: $\approx$ 0.3 s), $P_B \rightarrow P_C$ (travel time: $\approx$ 0.1 s), $P_C \rightarrow P_D$ (travel time: $\approx$ 0.27 s), $P_D \rightarrow P_E$ (travel time: $\approx$ 0.23 s), $P_E \rightarrow P_F$ (travel time: $\approx$ 0.3 s). The red dot represents the end-effector position [Kawasaki robotics]. 79
3.2 Graphical interpretation of classic solution of shooting method for a BVP. 82
3.3 Graphical interpretation of shooting method for solving the BVP for the robot-plus-VSS system. 85
3.4 Five-bar mechanism parameterization with two actuated joints q_{11} and q_{21}, and three passive joints q_{12}, q_{22} and q_{13}. The variable stiffness torsional springs are located in parallel to the two actuated joints defined by q_{s1} and q_{s2}. 91
3.5 Multiple-point pick-and-place sequence in the five-bar mechanism workspace: $A \rightarrow B$ (travel time: 0.2 s), $B \rightarrow C$ (travel time: 0.4 s), $C \rightarrow D$ (travel time: 0.4 s), $D \rightarrow E$ (travel time: 0.2 s), $E \rightarrow F$ (travel time: 0.4 s). The pick-and-place points are connected through the trajectories generated from the shooting method. 93

3.6 Input torques for the first joint of the parallel robot for the two cases: Nominal fifth-degree polynomial and variable stiffness with trajectories from BVP with constant payload. 93

3.7 Input torques for the second joint of the parallel robot for the two cases: Nominal fifth-degree polynomial and variable stiffness with trajectories from BVP with constant payload. 94

3.8 Input torques from the joints that actuate the variable stiffness joints from the VSS for the task with constant payload. 94

3.9 Energetic losses for the two cases compared: Nominal fifth-degree polynomial and variable stiffness with trajectories from BVP with constant payload. 94

3.10 Input torques for the first joint of the parallel robot for the two cases: Nominal fifth-degree polynomial and variable stiffness with trajectories from BVP with variable payload. 95

3.11 Input torques for the second joint of the parallel robot for the two cases: Nominal fifth-degree polynomial and variable stiffness with trajectories from BVP with variable payload. 95

3.12 Input torques from the joints that actuate the variable stiffness joints from the VSS for the task with variable payload. 96

3.13 Energetic losses for the two cases compared: Nominal fifth-degree polynomial and variable stiffness with trajectories from BVP with variable payload. 96

3.14 Multiple-point pick-and-place sequence in the five-bar mechanism workspace: $A \rightarrow B$ (travel time: 0.2 s), $B \rightarrow C$ (travel time: 0.4 s), $C \rightarrow D$ (travel time: 0.2 s), $D \rightarrow E$ (travel time: 0.4 s), $E \rightarrow F$ (travel time: 0.2 s). The pick-and-place points are connected through the trajectories generated from the shooting method. 97

3.15 Energetic losses for the two cases compared: Nominal fifth-degree polynomial and variable stiffness with trajectories from BVP with constant payload. 98

3.16 Energetic losses for the two cases compared: Nominal fifth-degree polynomial and variable stiffness with trajectories from BVP with variable payload. 99

3.17 Delta robot parameterization with three actuated joints q_1, q_2 and q_3. The variable stiffness torsional springs are located in parallel to the three actuated joints defined by q_{s1}, q_{s2} and q_{s3}. 100

3.18 Pick-and-place sequence in the workspace of the Delta robot: $G \rightarrow H$ (travel time: 0.12 s), $H \rightarrow I$ (travel time: 0.06 s), $I \rightarrow J$ (travel time: 0.14 s), $J \rightarrow K$ (travel time: 0.08 s), $K \rightarrow L$ (travel time: 0.11 s). The pick-and-place points are connected through the trajectories generated from the shooting method. 101

3.19 Pick-and-place sequence for the Delta robot in the three planes: $G \rightarrow H$ (travel time: 0.12 s), $H \rightarrow I$ (travel time: 0.06 s), $I \rightarrow J$ (travel time: 0.14 s), $J \rightarrow K$ (travel time: 0.08 s), $K \rightarrow L$ (travel time: 0.11 s). The pick-and-place points are connected through the trajectories generated from the shooting method. 102

3.20 Input torques for the first joint of the Delta robot for the two cases: Nominal fifth-degree polynomial and variable stiffness with trajectories from BVP for the first set of pick-and-place conditions and for a constant payload. 103

3.21 Input torques for the second joint of the Delta robot for the two cases: Nominal fifth-degree polynomial and variable stiffness with trajectories from BVP for the first set of pick-and-place conditions and for a constant payload. 103

3.22 Input torques for the third joint of the Delta robot for the two cases: Nominal fifth-degree polynomial and variable stiffness with trajectories from BVP for the first set of pick-and-place conditions and for a constant payload. 104

3.23 Energetic losses for the two cases compared: Nominal fifth-degree polynomial and variable stiffness with trajectories from BVP on the Delta robot for the first set of pick-and-place conditions and for a constant payload. . . 104

3.24 Energetic losses for the two cases compared: Nominal fifth-degree polynomial and variable stiffness with trajectories from BVP on the Delta robot for the first set of pick-and-place conditions and for a variable payload. . . 105

3.25 Pick-and-place sequence for the Delta robot: $G \rightarrow H$ (travel time: 0.12 s), $H \rightarrow I$ (travel time: 0.06 s), $I \rightarrow J$ (travel time: 0.1 s), $J \rightarrow K$ (travel time: 0.06 s), $K \rightarrow L$ (travel time: 0.1 s), $L \rightarrow M$ (travel time: 0.08 s). The pick-and-place points are connected through the trajectories generated from the shooting method. 106

3.26 Pick-and-place sequence for the Delta robot in the three planes: $G \rightarrow H$ (travel time: 0.12 s), $H \rightarrow I$ (travel time: 0.06 s), $I \rightarrow J$ (travel time: 0.1 s), $J \rightarrow K$ (travel time: 0.06 s), $K \rightarrow L$ (travel time: 0.1 s), $L \rightarrow M$ (travel time: 0.08 s). The pick-and-place points are connected through the trajectories generated from the shooting method. 107
3.27 Input torques for the first joint of the Delta robot for the two cases: Nominal fifth-degree polynomial and variable stiffness with trajectories from BVP for the second set of pick-and-place conditions and for a constant payload. 107
3.28 Input torques for the second joint of the Delta robot for the two cases: Nominal fifth-degree polynomial and variable stiffness with trajectories from BVP for the second set of pick-and-place conditions and for a constant payload. 108
3.29 Input torques for the third joint of the Delta robot for the two cases: Nominal fifth-degree polynomial and variable stiffness with trajectories from BVP for the second set of pick-and-place conditions and for a constant payload. 108
3.30 Energetic losses for the two cases compared: Nominal fifth-degree polynomial and variable stiffness with trajectories from BVP on the Delta robot for the second set of pick-and-place conditions and for a constant payload. 108
3.31 Energetic losses for the two cases compared: Nominal fifth-degree polynomial and variable stiffness with trajectories from BVP on the Delta robot for the second set of pick-and-place conditions and for a variable payload. . 109
3.32 Block diagram of online solution of the BVB combined with adaptation law for dealing with dynamics uncertainties. 110
3.33 BVP solved online for generating the desired optimal trajectories within the control system. 113
3.34 Online motion generator, adaptation law and feedback linearization integrated in the complete control scheme. 116
3.35 Multiple-point pick-and-place sequence in the five-bar mechanism workspace: $A \rightarrow B$ (travel time: 0.3 s), $B \rightarrow C$ (travel time: 0.4 s), $C \rightarrow D$ (travel time: 0.3 s), $D \rightarrow E$ (travel time: 0.4 s), $E \rightarrow F$ (travel time: 0.25 s). . . . 118
3.36 Energetic losses for the two cases compared: Nominal and by using VSS. . 119
3.37 Adaptation of inertial parameter zz_{11R}. 120

3.38 Adaptation of inertial parameter zz_{21R}. 121
3.39 Energetic losses for the two cases compared: Nominal and by using VSS. . 121

4.1 CAD of five-bar mechanism. 127
4.2 CAD of variable stiffness system. 128
4.3 Spring schematic 128
4.4 CAD of five-bar mechanism with VSS in parallel. 130
4.5 Real prototype in isometric view. 130
4.6 Real prototype in front view. 131
4.7 Detailed description of robot active joint and variable stiffness joint. 132
4.8 Detailed description of passive joints. 132
4.9 Motor drive system [Siemens]. 133
4.10 Motor drive system connection diagram [Siemens]. 134
4.11 Comparison between measured and calculated input torques from robot actuated joint 1. 143
4.12 Comparison between measured and calculated input torques from robot actuated joint 2. 143
4.13 Comparison between measured and calculated input torques from variable stiffness system associated to the VSS in parallel to the first actuated link. 144
4.14 Comparison between measured and calculated input torques from variable stiffness system associated to the VSS in parallel to the second actuated link. 144
4.15 Real-time control system for experimental validation with dSPACE controller card. Once the task finished, the data from velocities and input torques are saved from ControlDesk in order to feed the energy consumption model from Eq. (2.43). 147
4.16 Multiple-point pick-and-place sequence in the five-bar mechanism workspace: $A \to B$ (travel time: 0.32 s), $B \to C$ (travel time: 0.31 s), $C \to D$ (travel time: 0.30 s), $D \to E$ (travel time: 0.31 s), $E \to B$ (travel time: 0.34 s), $B \to A$ (travel time: 0.31 s). 151
4.17 Input torques grouping the first actuation chain considering a nominal case and the case when using VSS for the first set of boundary pick-and-place constraints. 152
4.18 Input torques grouping the second actuation chain considering a nominal case and the case when using VSS for the first set of boundary pick-and-place constraints. 153

4.19 Comparison of energetic losses for two types of actuation: nominal and case when using VSS and considering the friction effects due to the VSS for the first set of boundary pick-and-place constraints. 154
4.20 Comparison of energetic losses for two types of actuation: nominal and case when using VSS and without considering the friction effects due to the VSS for the first set of boundary pick-and-place constraints. 155
4.21 Tracking errors along the trajectory generated for the first set of boundary pick-and-place conditions in order to show that thanks to the direct power connection between the motors and the proximal links of the five-bar robot we can ensure accuracy at high-speeds. 155
4.22 Multiple-point pick-and-place sequence in the five-bar mechanism workspace: $A \rightarrow B$ (travel time: 0.33 s), $B \rightarrow C$ (travel time: 0.32 s), $C \rightarrow D$ (travel time: 0.32 s), $D \rightarrow E$ (travel time: 0.31 s), $E \rightarrow B$ (travel time: 0.33 s), $B \rightarrow A$ (travel time: 0.31 s). 157
4.23 Input torques grouping the first actuation chain considering a nominal case and the case when using VSS for the second set of boundary pick-and-place constraints. 158
4.24 Input torques grouping the second actuation chain considering a nominal case and the case when using VSS for the second set of boundary pick-and-place constraints. 158
4.25 Comparison of energetic losses for two types of actuation: nominal and case when using VSS and considering the friction effects due to the VSS for the second set of boundary pick-and-place constraints. 159
4.26 Comparison of energetic losses for two types of actuation: nominal and case when using VSS and without considering the friction effects due to the VSS for the second set of boundary pick-and-place constraints. 160
4.27 Tracking errors along the trajectory generated for the second set of boundary pick-and-place conditions in order to show that thanks to the direct power connection between the motors and the proximal links of the five-bar robot we can ensure accuracy at high-speeds. 161

5.1 Reciprocating mass driven rolling robots 169
5.2 Schematic of the rolling robot without elastic elements 169
5.3 Schematic of the rolling robot with VSS 174
5.4 Joint control scheme 177

5.5 CAD models of the rolling robots 181
5.6 `ADAMS` models of the rolling robots 182
5.7 Trajectories from the four reciprocating masses in order to move the center of mass of the sphere. 184
5.8 Trajectories computed from the optimal motion planner for the spring bases of the VSS. 184
5.9 Forces computed along the masses trajectories without springs. 184
5.10 On the left the forces computed along the masses trajectories are shown when VSS are place in parallel. On the right the forces from adjusting the VSS springs bases are shown. 185
5.11 Energy consumed from the two types of actuation. 185
5.12 On the left, the graphical interpretation of the disconnection between aspects due to actuation limits on a 2R serial robot workspace. *A* and *B* represent the boundary conditions which seek to be joined thanks to the BVP. On the right, the kinematic structure of the 2-DOF robot with payload is shown. 191
5.13 Torques computed from the exciting-plus-BVP trajectory for the case 1. . . 193
5.14 Optimal trajectory for connecting two points by solving the BVP from boundaries of case 1. *A* and *B* represent the boundary conditions of case 1 and they are joined thanks to the solution of the BVP. 193
5.15 Torques computed from the exciting-plus-BVP trajectory for the case 2. . . 194
5.16 Optimal trajectory for connecting two points by solving the BVP from boundaries of case 2. *A* and *B* represent the boundary conditions of case 2 and they are joined thanks to the solution of the BVP. 194
5.17 Torques computed from the exciting-plus-BVP trajectory for the case 3. . . 195
5.18 Optimal trajectory for connecting two points by solving the BVP from boundaries of case 3. *A* and *B* represent the boundary conditions of case 3 and they are joined thanks to the solution of the BVP. 195
5.19 Torques computed from the exciting-plus-BVP trajectory for the case 4. . . 196
5.20 Optimal trajectory for connecting two points by solving the BVP from boundaries of case 4. *A* and *B* represent the boundary conditions of case 4 and they are joined thanks to the solution of the BVP. 196

List of Tables

3.1 RMS values of input torques for nominal case and for case when using VSS in parallel (constant payload). 92

3.2 RMS values of input torques for nominal case and for case when using VSS in parallel (variable payload). 93

3.3 RMS values of input torques for nominal case and for case when using VSS in parallel (constant payload). 98

3.4 RMS values of input torques for nominal case and for case when using VSS in parallel (variable payload). 98

3.5 RMS values of input torques for nominal case and for case when using VSS in parallel for the Delta robot for the first set of pick-and-place conditions and for constant payload. 102

3.6 RMS values of input torques for nominal case and for case when using VSS in parallel for the Delta robot for the first set of pick-and-place conditions and for a variable payload. 102

3.7 RMS values of input torques for nominal case and for case when using VSS in parallel for the Delta robot for the second set of pick-and-place conditions and for a constant payload. 106

3.8 RMS values of input torques for nominal case and for case when using VSS in parallel for the Delta robot for the second set of pick-and-place conditions and for a variable payload. 109

3.9 RMS values of input torques for nominal case and for case when using VSS in parallel without using the adaptation law. 119

3.10 RMS values of input torques for nominal case and for case when using VSS in parallel by considering adaptation of the inertial parameters. 120

4.1 Spring specifications 129

4.2 Inertial dynamic parameters from CAD model. 137

4.3 RMS values of input torques for nominal case and for case when using VSS in parallel for the first set of boundary pick-and-place conditions considering the friction effects. 153

4.4 RMS values of input torques for nominal case and for case when using VSS in parallel for the first set of boundary pick-and-place conditions without considering the friction effects. 153

4.5 RMS values of input torques for nominal case and for case when using VSS in parallel for the first set of boundary pick-and-place conditions considering the friction effects and by analyzing the distribution of torques for the actuation with VSS. 154

4.6 RMS values of input torques for nominal case and for case when using VSS in parallel for the first set of boundary pick-and-place conditions without considering the friction effects and by analyzing the distribution of torques for the actuation with VSS. 154

4.7 RMS values of input torques for nominal case and for case when using VSS in parallel for the second set of boundary pick-and-place conditions considering the friction effects. 159

4.8 RMS values of input torques for nominal case and for case when using VSS in parallel for the second set of boundary pick-and-place conditions without considering the friction effects. 159

4.9 RMS values of input torques for nominal case and for case when using VSS in parallel for the second set of boundary pick-and-place conditions considering the friction effects and by analyzing the distribution of torques for the actuation with VSS. 160

4.10 RMS values of input torques for nominal case and for case when using VSS in parallel for the second set of boundary pick-and-place conditions without considering the friction effects and by analyzing the distribution of torques for the actuation with VSS. 160

5.1 Mass properties: `ADAMS` model 182

5.2 Relevant parameters: `ADAMS` model 183

5.3 `ADAMS` Contact Model Parameters 183

5.4 Maximum values of input torques and optimal values for $\dot{\mathbf{q}}_A$ from the solution of the BVP. 192

C.1 Components of the joints from the variable stiffness system and the five-bar active joints. 213

Nomenclature

In this nomenclature, the main variables and abbreviations used in this manuscript are presented. Additionally, it should be noted that the following conventions were used:

- vectors and matrices in bold style;
- scalar variables and names of points in italic styles;
- abbreviations of terms in regular style

Symbols

$\mathcal{F}_0(\boldsymbol{O}, \mathbf{x}_0, \mathbf{y}_0, \mathbf{z}_0)$	global frame
$\mathcal{F}_p(\boldsymbol{P}, \mathbf{x}_p, \mathbf{y}_p, \mathbf{z}_p)$	platform frame
P	represents moving platform
M_i	motors that actuate n robot actuated joints
M_{s_j}	motors that actuate n_s variable stiffness joints
l_{OA}	distance from point O to point A
$\mathbf{q}_a$	vector of robot active joints
$\mathbf{q}_s$	vector of variable stiffness joints associated to the VSS
t	time
$\mathbf{x}$	vector of platform pose
β	amplitude of periodic trajectory
ω	angular velocity
f	frequency
zz	moment of inertia
m	mass of a rigid body
$\mathbf{g}$	gravity vector
$\mathbf{A}$	parallel kinematic Jacobian matrix
$\mathbf{B}$	serial kinematic Jacobian matrix
L_t	Lagrangian of the virtual tree structure
L_p	Lagrangian of the platform

$\boldsymbol{\tau}_{ta}$	vector of virtual input efforts
$\mathbf{w}_p$	wrench of the platform
$\boldsymbol{\tau}$	vector of robot input efforts
$\boldsymbol{\lambda}$	vector of Lagrange multipliers
$\mathbf{M}$	matrix of inertia
$\mathbf{c}$	vector of Coriolis, centrifugal and gravitational effects
$\mathbf{f}_a$	vector grouping the active joint friction terms
$\boldsymbol{\tau}_s$	vector of force/displacement relation associated to the VSS coupled to the robot in parallel
$\mathbf{K}$	stiffness matrix grouping the stiffness constants of the springs k
$\mathbf{M}_s$	matrix of inertia associated to the VSS dynamics
$\mathbf{h}_s$	vector of Coriolis, centrifugal and gravitational effects
$\mathbf{f}_s$	vector grouping the variable stiffness joint friction terms
P_{motor}	resistive losses due to resistances in the motor phases
P_{brake}	resistive losses due to braking resistance
P_{damp}	damping losses
P_{cond}	conduction losses
P_{switch}	switching losses
$P_{rectifier}$	rectification losses
P_{losses}	model of power losses
α	slope of a differential equation
$\dot{\boldsymbol{\tau}}$	time differentiation of $\boldsymbol{\tau}$ to obtain the robot jerk equations
$\dot{\boldsymbol{\tau}}_{vss}$	time differentiation of $\boldsymbol{\tau}_{vss}$ to obtain VSS jerk equations
h	differential equation
$\mathbf{E}$	vector of boundary constraints from BVP
$\mathbf{s}$	decision variable vector for BVP
zz_R	regrouped inertial effects in the active joint axes
J_1, J_2	regrouped inertial effects on the two axes of the VSS joints
f_s	static friction effects associated to the robot active joints
f_{vss}	static friction effects associated to the variable stiffness system from the VSS
$\boldsymbol{\chi}$	vector of dynamic parameters related to the robot
$\boldsymbol{\chi}_s$	vector of dynamic parameters related to the VSS
$\mathbf{W}$	matrix of robot configuration variables for identification

$\mathbf{W}_s$	matrix of VSS configuration variables for identification
$\mathbf{K}_p$, $\mathbf{K}_i$, $\mathbf{K}_d$	symmetric positive definite matrices
$\boldsymbol{\nu}_a$, $\boldsymbol{\nu}_s$	auxiliary control inputs
A	coordinate system
${}^B\mathbf{R}_C$	rotation matrix
$\hat{\mathbf{p}}_i; \quad i = 1, \ldots, 4$	unit vector
J	cost function
F	input force
$\mathbf{x_{DecVar}}$	decision variable

Abbreviations

VSS	variable stiffness springs
VSA	variable stiffness actuator
DOF	degrees-of-freedom
PUMA	Programmable Universal Machine for Assembly
SCARA	Selective Compliance Assembly Robot Arm
RMS	root means square
SEA	series elastic actuator
BVP	boundary value problem
CTC	Computed Torques Control
LM	Levenberg-Marquardt
PID	Proportional Integral Derivative

Introduction

Context of the thesis

During the last decades, robotics research communities and companies have kept special attention on addressing the problem of increasing the energy efficiency of high-speed industrial robots. Typically, the most common tasks for high-speed robots in industrial applications are to pick and place objects in different positions of the robot workspace. For such types of high-speed operations, a significant amount of energy is required to move and stop the robot in the desired positions. This mainly occurs when achieving a desired high speed since a large amount of energy must be brought to make the robot move, and then this energy is dissipated to stop the robot in the braking phase. This is not efficient at all.

The literature review shows that, in order to solve this problem, the conventional techniques developed over the last few years are mainly three (see Chapter 1):

- designing lightweight robot architectures, thus permitting the use of less powerful motors;
- for slow motions, gravity-balancing techniques have been proposed in order to reduce the input efforts;
- classical motion planning techniques for optimizing the robot trajectory and operation.

Even if the aforementioned techniques have shown their effectiveness to increase the energy efficiency, firstly, designing a lightweight robot structure leads to worsen the robot stiffness, affecting the accuracy of the robot. Although gravity-balancing techniques can compensate the input efforts to move slow pick-and-place robots, these techniques cannot be applied for high-speed robots for which the inertial effects are preponderant. Finally, even if classical motion planning techniques have been used to optimize the robot trajectory to keep the input torques constrained, these methods do not fully exploit the robot dynamics, leading to lower percentages of energy reduction.

More recently, variable stiffness actuators (VSAs) have been introduced for decreasing the energy consumption of pick-and-place robots by smartly storing energy in their springs. Nevertheless, the serial arrangement of springs and motors of the VSAs decreases the accuracy of the robot end-effector due to uncontrolled deflections at high-speeds.

In order to solve this problem and to increase the energy efficiency while ensuring accuracy at high-speeds, this thesis proposes the use of parallel arrangement of variable stiffness springs (VSS) and motors. The idea is to smartly tune online the stiffness of the VSS so that the robot is put in near a resonance mode, thus considerably decreasing the energy consumption during fast quasi-periodic pick-and-place motions. Furthermore, the parallel configuration of VSS and motors ensures the load balancing at high-speed without losing the accuracy of the robot.

Contributions of the thesis

This manuscript presents several major contributions which are listed as follows:

- **The design of an energy-efficient actuation chain for performing high-speed pick-and-place motions:** It appears in Chapter 1 that, in order to reduce the energy consumption of robots, three approaches are developed in most of the cases: *i*) conventional techniques based on designing lightweight robot architectures, thus allowing the use less powerful motors; *ii*) generation of classical motion planning techniques that do not fully exploit the robot natural dynamics; *iii*) the use of variable stiffness springs (VSS), in series and in parallel to the motors, in order to have an energy storage to carry out the reduction of the energy consumption, being this latter the most attractive for seeking to exploit the robot natural dynamics. Despite rather encouraging results, the works done for reducing the energy consumption by using springs have drawbacks, such as lack of accuracy when placing VSS in series, lack of energetic analysis due to the fact that the energy consumed by the motors that adjust the VSS are not taken into account, and the fact that they have been only applied for slow robots. For this reason in Chapter 2, we present the actuation concept based on VSS in parallel configuration to the motors, for high-speed robots. This actuation chain is constituted of a variable stiffness spring which is placed in parallel to the actuated joints of a high-speed robot manipulator, which can be either serial or parallel. This means that there is a motor to actuate the robot joint, and there is an additional motor which modifies the equilibrium position, and thus the stiffness of the VSS placed in parallel. This additional motor controlling the stiffness of the VSS, and thus the exchange from potential to kinetic energy, will allow to exploit the natural dynamics of the robot for fast quasi-periodic motions. Additionally, in Chapter 2, we propose an energy consumption model in order to estimate the energetic losses of the full actuation, i.e. *robot-plus-VSS*, when performing high-speed tasks, thus considering the energy consumed by the motors that actuate the VSS.

- **The proposition of a motion generator that exploits the natural dynamics of pick-and-place robots:** In Chapter 3, we propose an energy-efficient motion generator that exploits the robot natural motions. This is done by matching the desired pick-and-place motions with the robot free-response. The main idea is to exploit the combined motion of the parallel robot active joints and the variable stiffness joints from the VSS placed in parallel. This is done in order to exploit the force/displacement relation of the VSS associated to the VSS optimal stiffness, so that we minimize the robot and VSS input torques simultaneously, and thus the full actuation chain energy consumption for fast quasi-periodic motions. In addition to that, thanks to the developed energy consumption model, we compare our actuation principle, i.e. *robot-plus-VSS*, with a nominal type of actuation in which there is no elastic element, and the trajectories are typically defined by polynomial laws. Simulations of the suggested approach on a five-bar mechanism and on a Delta robot are performed and show the drastic reduction of energy consumption.

- **Experimental proof of the new actuation concept:** In addition to the numerical simulations, an experimental prototype was designed and commissioned to perform fast quasi-periodic motions in order to validate the theoretical formulations. These experimental results are shown in Chapter 4, and demonstrate the successful validation of the new actuation concept to perform fast energy-efficient pseudo-periodic motions, and thus to exploit the natural dynamics of the robot. The experimental results show a considerable increase on the energy efficiency of the robot while performing pick-and-place-like motions.

- **Extending the concept of exploiting natural dynamics to robots in other applications:** One of the advantages of the concept of exploiting the natural dynamics is that it can be applied for any robot in which an exchange from potential to kinetic energy may appears. That is why in Chapter 5, we present an extension of this concept of exploiting the natural motions of robots, for robotic systems in other applications: *i*) for reducing the energy consumption of a mobile robot by using VSS in parallel, and *ii*) for increasing the feasible static-wrench workspace of robots carrying a payload for which the reachable workspace is usually limited due to the maximal value of the torque that each actuator of the robot joints can deliver.

Let us now start with a bibliographical overview of high-speed robots and a review of existing solutions for energy consumption reduction.

CHAPTER 1

State of the art

1.1. *Historical evolution of high-speed robots* p. 6
1.2. *Towards designing energy-efficient high-speed robots* p. 18
1.3. *Existing strategies for increasing the energy efficiency of high-speed robots* p. 41
1.3. *Summary* p. 42

This Chapter is dedicated to present a review on the historical evolution of industrial robots, emphasizing their use for high-speed industrial operations, such as pick-and-place tasks. First of all, a bibliographical review on the well-known architectures for performing high-speed tasks in industrial applications, is presented.

On the second part of this Chapter, a review on some already available solutions, such as lightweight robots or classical motion planning techniques, for increasing the energy efficiency of robot manipulators will be presented. The efficiency of such robots is shown and their advantages and drawbacks are discussed. Additionally, we will recall some preceding works on passive compliant actuation, which is a recently introduced type of actuation for reducing the energy consumption of pick-and-place robots, and from which this thesis is motivated. We will thus firstly introduce the so-called variable stiffness actuators (VSAs), which is a type of compliant actuation based on serial arrangement of springs and motors, and finally on a second stage we will present a bibliographical review of the actuation concept based on parallel elastic actuation.

Finally, it is proposed to use a new actuation concept for high-speed robots based on variable stiffness springs (VSS) in parallel to the motors, for increasing the energy efficiency at high-speeds. The VSS are used as energy storage for carrying ot the reduction of the energy consumption and their parallel configuration with the motors ensure the load balancing at high speed without losing the accuracy of the robot.

1.1 Historical evolution of high-speed robots

In this Section, we propose to make a brief review of the evolution of industrial robots, emphasizing their importance for high-speed applications. The most significant milestones of the history of industrial high-speed robots are mentioned, combined with a description of the most representative robots designed in the last decades. It is worth noticing that we do not make an exhaustive list of all existing high-speed robots, but rather to give key points in the development of these robotic systems.

1.1.1 Origins

In order to talk about high-speed robots, it is firstly necessary to make a brief overview of the beginnings of industrial robots. The idea of designing and prototyping robots for industrial applications dates back to the 1950's with the beginning of *Industrial Robotics* [Gasparetto 2019]. Nevertheless, some inventions in automation took place before, e.g. a programmable paint-sprayer device in 1938 [Koetsier 2019], or a teleoperated manipulator invented by Goertz in 1949. There are several works dealing with the true origins of industrial robotics, such as [Ceccarelli 2001][Ceccarelli 2004][Siciliano 2008][Gasparetto 2016]. However, the history of industrial robots is typically set in the 1950's with the inventor George Devol, who designed in 1954 a *Programmable Article Transfer* [Devol 1954]. Such device was the basis for designing and prototyping the Unimate robot (Fig. 1.1), which is considered the first true industrial robot in history [Malone 2011]. The Unimate robot, which was hydraulically actuated, was used for first time in a production line of General Motors for transporting die castings from an assembly line (Fig.1.2).

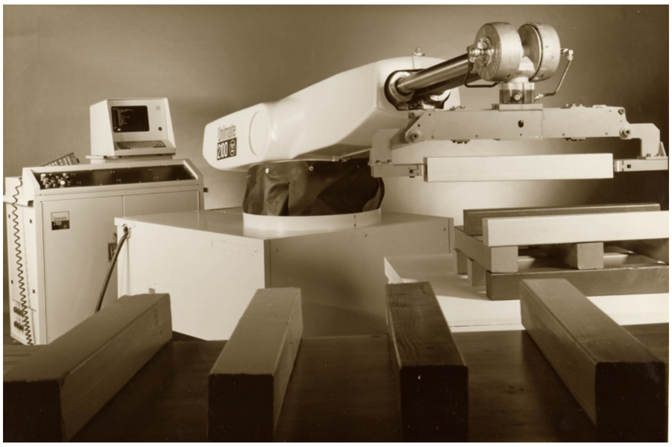

Figure 1.1: Unimate robot (first industrial robot) [Malone 2011].

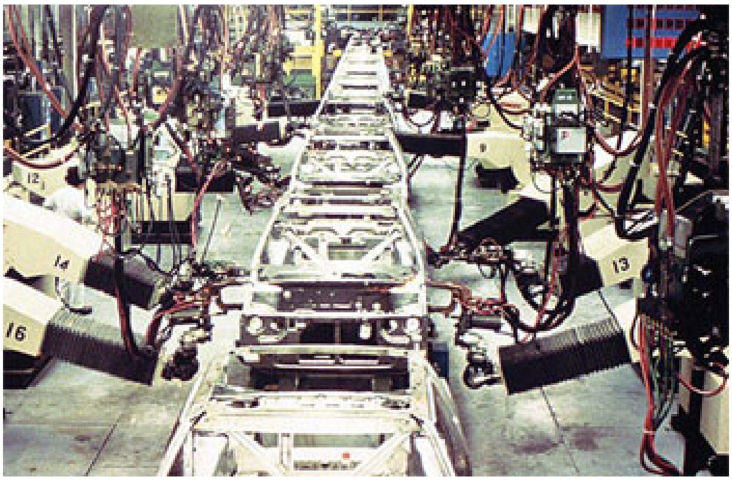

Figure 1.2: Unimate robot in production lines of General motors [Malone 2011].

After this breakthrough towards the development of industrial robots, several robot manufacturing companies appeared with the objective of building such types of machines. One of the first companies that emerged for getting involved on the designing of industrial robots was AMF Corporation. For instance, in 1962 the first cylindrical robot called Versatran was designed and manufactured by this company [Birnie 1974]. The robot Versatran was used in the production lines of Ford in Ohio USA and in some production companies of Japan (See Fig. 1.3a).

The expansion of industrial robots in Europe took place in the 1960's with the company Svenska Metallverken in Sweden, which implemented Unimate robots for very first tasks involving pick-and-place tasks [Westerlund 2000]. Years later, in Norway, the first painting robot was manufactured by the Trallfa Company [IFR] (Fig. 1.3b). It is worth mentioning that the appearance of robots allowed to automatize other important production tasks such as welding. Unimation was the first company to manufacture welding robots, while General Motors was the first company to install this kind of systems in their automotive plants, in 1969. Years after, FIAT installed the first welding robot in Europe at their plants in Turin (Italy) [IFR] (See Fig. 1.3d). For a non-exhaustive list of the existing industrial robots from 1950 to 1970, the reader can refer to the list of figures stacked in Fig. 1.3.

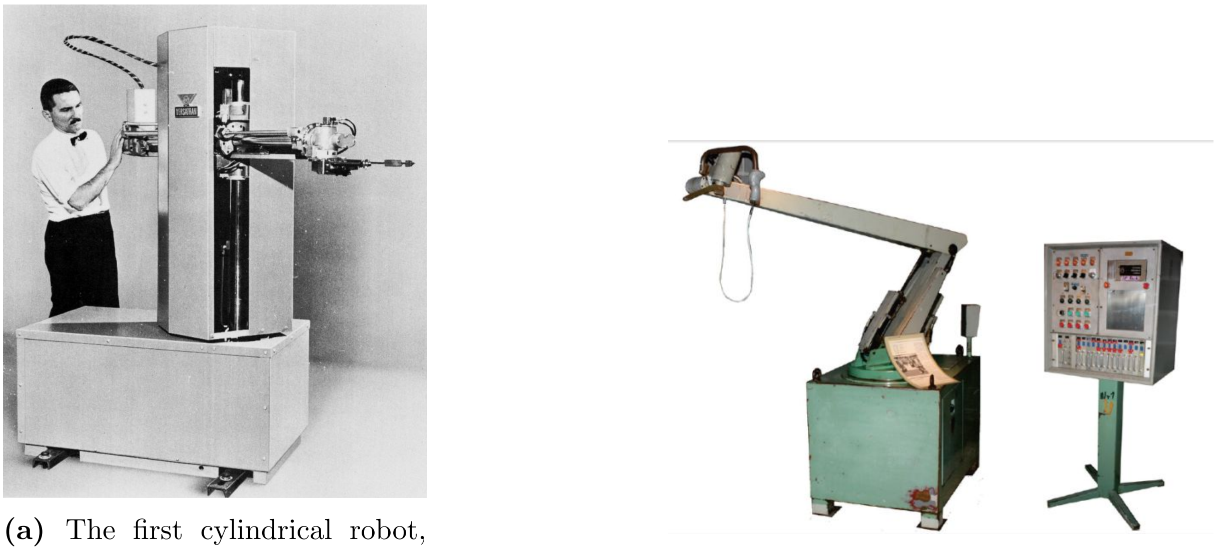

(a) The first cylindrical robot, the Versatran from AMF Corporation in 1962 [Birnie 1974].

(b) First commercial painting robot in 1969 [IFR].

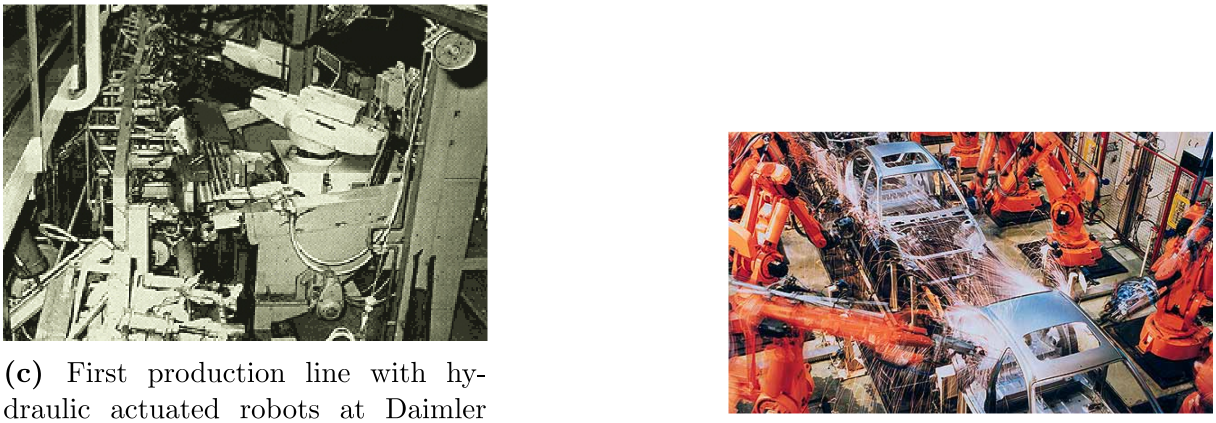

(c) First production line with hydraulic actuated robots at Daimler Benz, Sindelfingen by KUKA in 1971 [IFR].

(d) First production line of welding robots in Europe in 1972 [IFR].

Figure 1.3: Expansion of industrial robots from 1950 to 1970.

As it can be seen from the aforementioned generation of industrial robots, between 1954 and 1970, most of the prototypes of industrial robots were mainly actuated by means of hydraulic actuators. The shifting from hydraulic to electric actuators took place in 1970 with the developments of electronic components and microprocessors. This change to electric motors allowed to implement control systems able to deal with more complex and computationally expensive tasks, thus approaching to an era of industrial robots which could react fast enough to perform faster industrial operations.

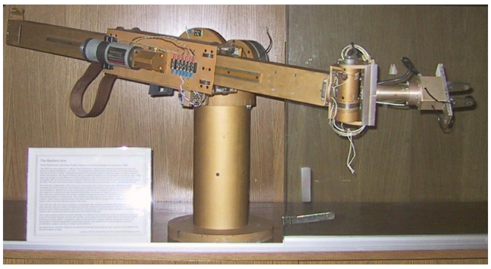

(a) Vicarm/Stanford arm at Vicarm Inc, USA in 1973 [Scheinman 1973].

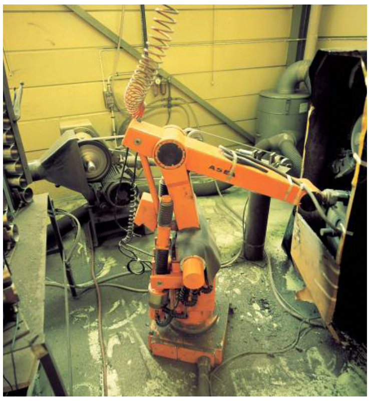

(b) The first fully electric robot, IRB 6 from ASEA in 1974 [IFR].

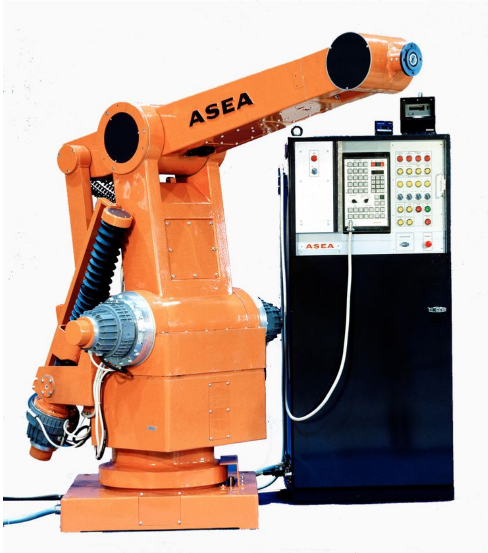

(c) ABB developed an industrial robot with a payload up to 60 kg in 1975 [IFR].

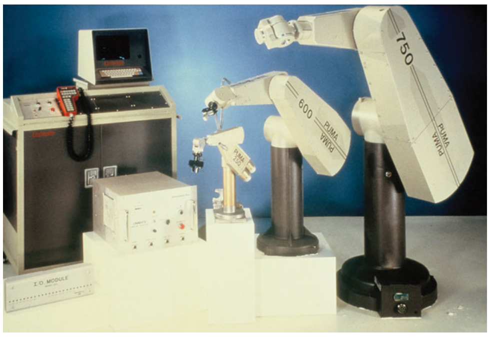

(d) PUMA was developed by Unimation/Vicarm; USA, with support from General Motors in 1978 [Gasparetto 2019].

Figure 1.4: Expansion of industrial robots from 1970 to 1980.

Continuing with the evolution of industrial robots and with the shifting from hydraulic to electric actuation, in 1973 Prof. Scheinman developed the famous Stanford Arm (Fig. 1.4a) [Scheinman 1973]. This prototype was the first six-degree-of-freedom robot actuated by six electric motors and controlled by six microprocessors. It had five revolute joints and one prismatic joint designed by a combination of harmonic drives and gearbox composed of spur gears.

One year later, in 1974, what is considered the first true fully-electric industrial robot was designed by ASEA (now ABB) [IFR]. This industrial robot was called IRB6 and it had an anthropomorphic design as it can be seen in Fig. 1.4b. The arm of this robot mimicked the arm of a human, and it had a payload of 6 kg, with five DOF. It was used in industrial applications to polish stainless steel tubes [IFR]. A year after, in order to meet with the demands of the automotive industry of having more payload, ABB developed an industrial robot with a payload up to 60 kg called IRB60 (Fig. 1.4c). It was first used by the company Saab in Sweden for welding car assemblies [IFR]. Continuing with the evolution of robots actuated by electric motors, in 1978 Unimation/Vicarm with support of General Motors, developed the well-known Programmable Universal Machine for Assembly (PUMA) weighted less than five pounds and able to perform tasks involving handling small parts in production lines (Fig. 1.4d) [Gasparetto 2019].

Towards the designing of faster robots, in 1978 the Japanese scientist Hiroshi Makino developed the SCARA-robot (Selective Compliance Assembly Robot Arm), which was made of three revolute joints with parallel axis and a prismatic joint placed at the end of the kinematic chain (Fig. 1.5a) [Makino 1980]. Its structure lightness allowed to implement faster controllers allowing to speed-up tasks such as the assembly of small objects. Another relevant invention towards the designing of faster robots was the appearance of direct drive actuated robots. The first prototype implementing direct drive actuators was the CMU Direct Drive Arm [Asada 1983]. It is shown in Fig. 1.5b and it was developed by Kanade and Asaka at Carnegie Mellon University. This robot could perform tasks with high accuracy and faster operational speeds due to the fact that there was no need of intermediate gears or chain systems for the transmission system.

Finally, in 1984, what is considered the first commercially industrial high-speed robot was developed by AdeptOne (See Fig. 1.6), combining the SCARA-based design and the use of direct drive actuators [Gasparetto 2019]. From this time in history of industrial robotics, the career towards the design of high-speed robots started by creating new kinematic structures, implementing faster controllers, designing new transmission systems, etc.

These scientific and technical inventions allowed to use robots in other applications different from the automotive industry, such as in the electronics, food and pharmaceutical sectors. Additionally, it is worth mentioning that SCARA robots were included in the assembly lines in the Japanese industries. This impulses Japan to become in the 1980's, not only the leader on robot manufacturing, but also in the production of electronic components [Adept].

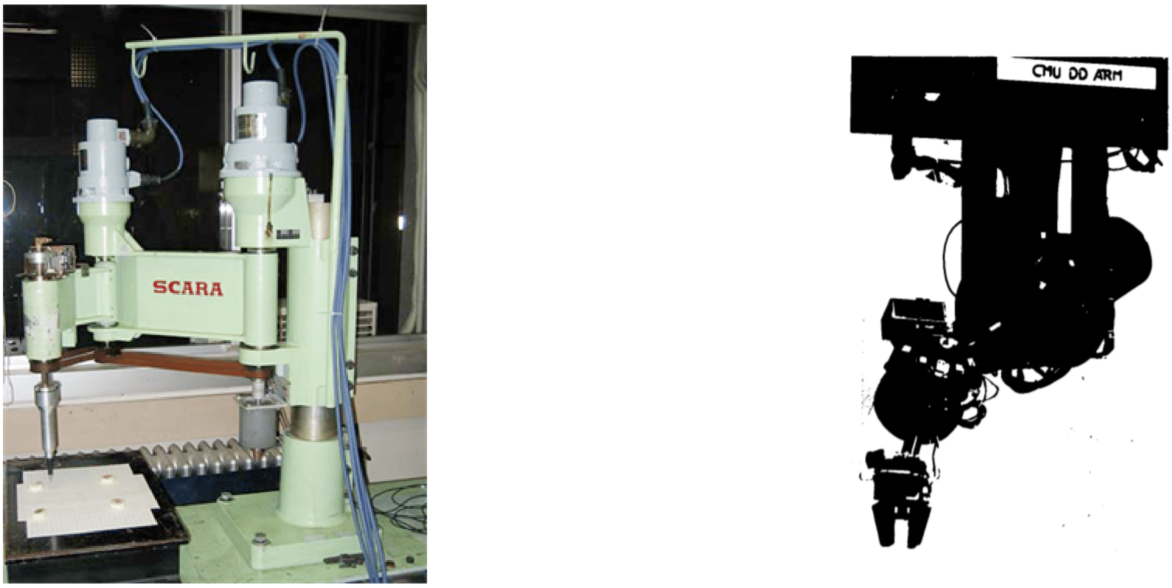

(a) First prototype of SCARA robot [Makino 1980].

(b) The first prototype of direct-driven robot [Asada 1983].

Figure 1.5: Two main inventions towards the designing of faster robots. On the left a SCARA robot is shown, and on the right the first direct-driven robot is presented.

Figure 1.6: AdeptOne SCARA robot [Adept].

1.1.2 Towards achieving more speed for robots in industrial applications

The great advances on electric-driven robots due to the development of faster processors, servo controllers and direct-drive motors, allowed to take industrial robots from the 1990's to nowadays to another level of operational speeds.

The need of robots that could perform high-speeds attract the attention of several industrial sectors due to the possibility of increasing their productivity, and thus their

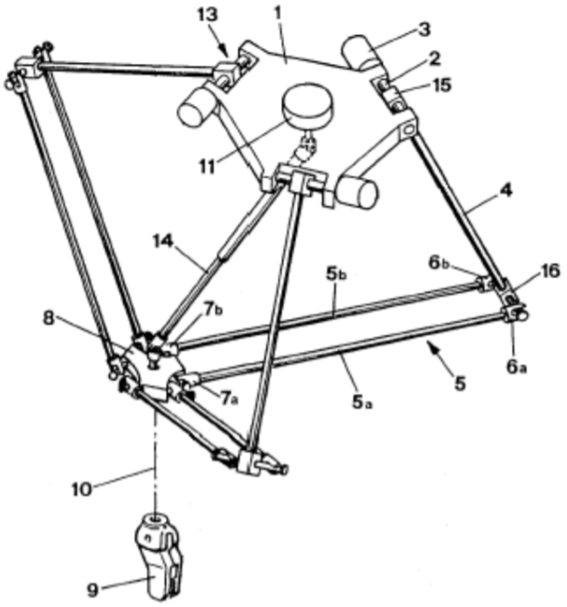

Figure 1.7: Schematic of patent of Delta robot by Reymond Clavel [Clavel 1990].

economical incomes. That is why between the end of the 1980's and the beginnings of the 1990's, the scientific research communities were pushed to design innovative kinematic structures capable of performing high-speed industrial operations. It was then that the idea of implementing parallel kinematic chains instead of the classical serial chain took relevance within the research communities. This is due to the fact that a parallel kinematic chain could lead to a type of lightweight robot capable of performing high speeds. Additionally, in terms of accuracy, the parallel robots divide the load among their several legs of the system, allowing to create more rigid mechanisms.

Thus, by following this boom on the developing of kinematic architectures that could perform faster operational speeds, in 1986 the Swiss scientist Reymond Clavel conceived the so-called Delta robot [Clavel 1990]. This parallel mechanism had three translational DOFs and one rotational DOF (See. Fig. 1.7). This parallel robot was a breakthrough towards the design of several high-speed parallel manipulators, devoted mainly for pick-and-place operations.

In Fig. 1.7, the schematic of the patent of the Delta robot from Prof. Clavel is shown. The main idea of its conception is the use of parallelograms, from which three articulated arms are connected. The three parallelograms restrict completely the orientation of the platform which remains with only three translational DOFs. The actuators are mounted

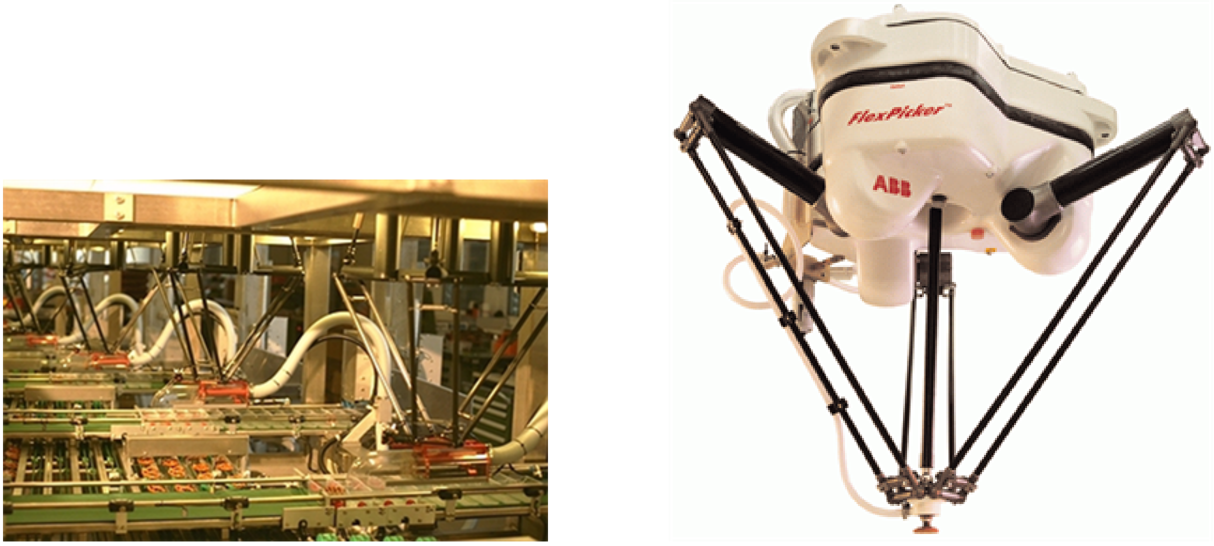

(a) Delta robots packaging pretzels [Bonev 2001].

(b) The Flex-Picker robot from ABB [Pierrot 1999].

Figure 1.8: Applications of Delta robots.

on the base and the links are made from a low-weighted material allowing for the mobile platform to achieve accelerations up to 50 G in experimental environments and 12 G in industrial applications [Clavel 1990]. This makes the Delta robot an ideal mechanism for performing pick-and-place operations.

The first application of a Delta-like robot in a commercial-industrial sector was in 1992 by the company Demaurex, which had six Delta robots operating in a robotized work-cell for loading pretzels into trays [Bonev 2001] (See Fig. 1.8a). Later in 1998, ABB developed the Flex-Picker robot (Fig. 1.8b), which is based on a Delta kinematic structure and it was considered the fastest pick-and-place robot in the world [Pierrot 1999]. It is an industrial version of the Delta robot with 4-DOF, and can produce accelerations and velocities above 10 G and 10 m/s, respectively. The cycle period can be below to 0.4 s.

The appealing characteristics in terms of operational speeds that parallel manipulators had brought to industrial applications, such as pick-and-place tasks, attracted the attention of several researchers and companies. That is why from the 1998 to nowadays, they started to design and build new mechanisms based on parallel structures in order to operate at high speeds. Among several examples of high-speed pick-and-place robots, we can list non-exhaustively:

- the *H4 prototypes (symmetrical and asymmetrical)* (Fig. 1.9a–Fig. 1.9b): The H4 prototypes were presented within the development of a new family of 4-DOF high-speed parallel manipulators at LIRMM [Pierrot 1999][Pierrot 2009][Pierrot 2001]. The first prototype for validating this family of high-speed robots was equipped with rotatory drives, and it achieved accelerations higher than 5 G.

- the *double SCARA robot* (Fig. 1.9c): It is one of the most popular 4-DOF mechanism, together with the Flex-Picker robot. It can perform pick-and-place tasks with a precision of 0.005 mm in a workspace of 150 mm x 105 mm. It can perform tasks with pick-and-place cycles below to 0.5 s;

- the *Par4 (future Quattro)* (Fig. 1.9d): It is based on an architecture of a Delta robot, but it has four legs instead of three. It is a 4-DOF dedicated to pick-and-place operations. It can reach accelerations up to 13 G with pick-and-place cycle times below to 0.25 s;

- the *Heli4* (Fig. 1.9e): It is a 4-DOF parallel robot, inspired from a Delta architecture, but overcoming its limitations by using an articulated traveling plate. It has a symmetrical design with accelerations above 100 m/s^2 and velocity of 10 m/s. The moving parts are made from carbon fiber materials.

- the *X4 robot* (Fig. 1.9f): It is a 4-DOF high-speed robot developed in the University of Tsinghua. It can achieve accelerations of the order of 120 m/s^2 and velocities of 8 m/s. The repeatability of this robot is of 0.2 mm, and can carry payload up to 4 kg in cycle times of 0.8 s.

- the *Veloce robot* (Fig. 1.10a): It is 4-DOF high-speed parallel robot developed at LIRMM. It is mainly designed for high-speed pick-and-place operations. It consists of four kinematic chains and 4-DOF, from which 3 are independent translation degrees in the three dimensions, and 1 rotational degree around the vertical axis. It is able to reach 10 m/s of maximum velocity and accelerations of 200 m/s^2, with a payload up to 10 kg.

- the *Ragnar* (Fig. 1.10b): It is 4-DOF high-speed robot producing three translational and one rotational motion. The payload of this robot is 3 kg, with maximum accelerations of 10 G with pick-and-place cycles of 0.5 s. This robot is an industrial robot typically dedicated for food handling industry [Bai 2016].

- the *Schoenflies Motion Generator* (SMG Fig. 1.10c): It was designed at the McGill University by the Prof. Angeles [Angeles 2006]. It has three translation degrees of freedom and one rotational motion. It can perform pick-and-place operations of 0.5 s of cycle period;

- the *IRSBot-2* prototype (Fig. 1.10d): It is a 2-DOF translational robot able to reach 20 G of acceleration with repeatability lower than 30 microns in its operational workspace. In addition to that the parallelogram configuration of its proximal links increases the intrinsic stiffness of the architecture. As compared to the Par2 robot, the only spatial architecture robot with 2-translational DOF found in the literature, the IRSBot-2 is simpler, and therefore less subject to uncontrolled parasitic effects, and has a larger workspace, since it has only two legs.

- the *Par2* (Fig. 1.10e): It is a 2-DOF robot for high-speed pick-and-place operations. It is based on the Quattro robot and it has the following characteristics. All the elements of the distal parts of the legs are only subject to traction/compression effects. This leads to a lighter structure with better acceleration capacities. The authors successfully built a prototype that can reach 53 G. However, even if its acceleration capacities are impressive, its accuracy is poor.

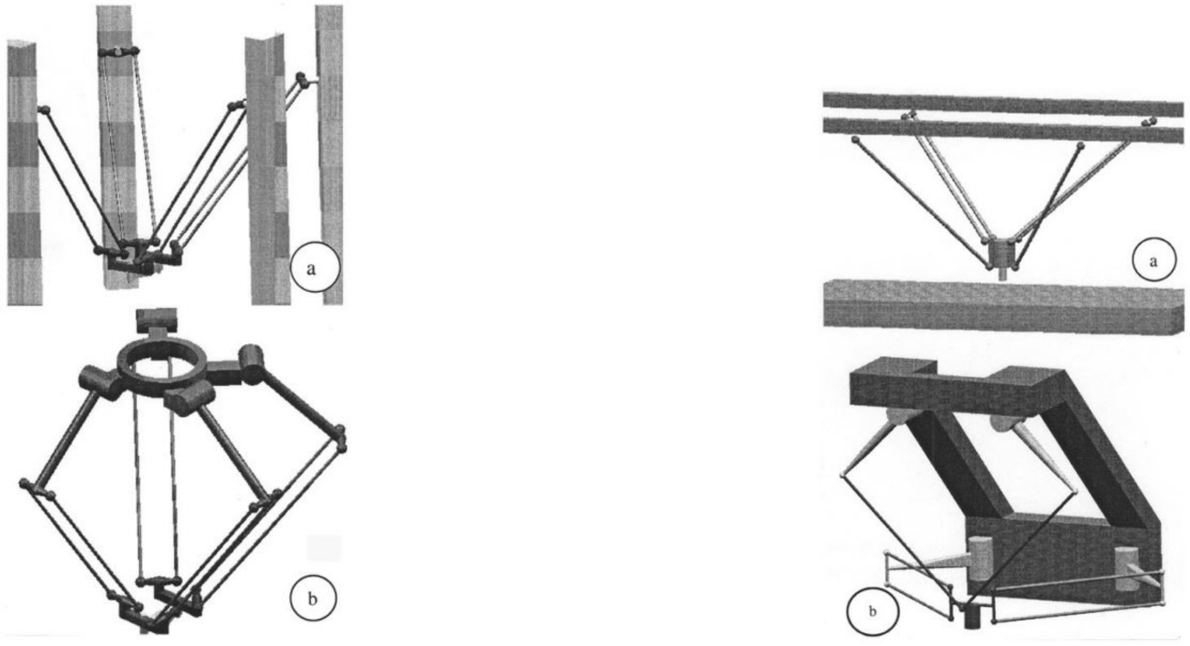

(a) H4 robot with symmetrical design [Pierrot 2001].

(b) H4 robot with asymmetrical design [Pierrot 2001].

MITSUBISHI

(c) SCARA robot from Mitsubishi [Mitsubishi].

(d) the Quattro from Adept [Nabat 2005].

Revolute actuator
Forearm
"Spatial parallelogram"
Traveling plate
Helical joint
Revolute joint
Ending part
Part #2
Part #1

(e) Heli4 prototype [Nabat 2007].

(f) X4 prototype [Mo 2017].

Figure 1.9: Examples of high-speed robots.

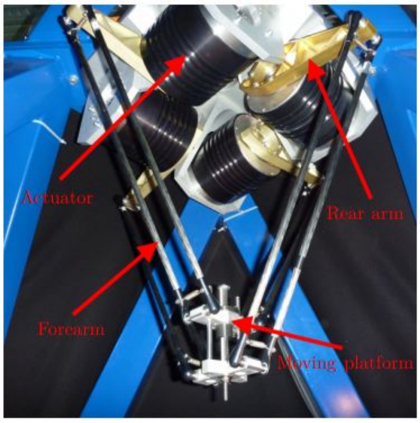
Actuator
Rear arm
Forearm
Moving platform

(a) Veloce prototype [Penta Robotics 2004].

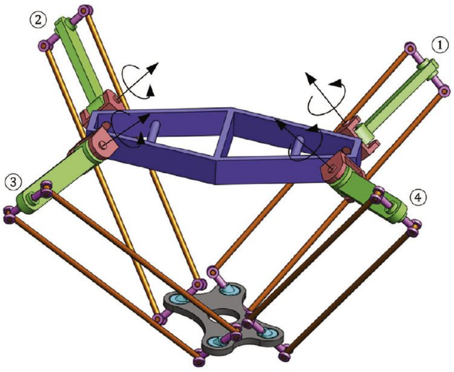

(b) Ragnar robot [Bai 2016].

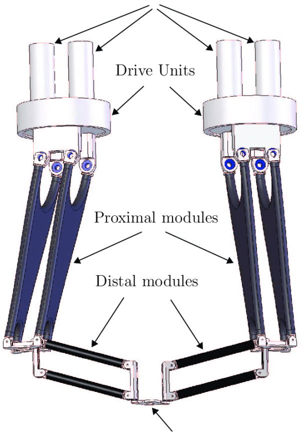
Drive Units
Proximal modules
Distal modules

(c) the SMG from McGill University [Angeles 2006].

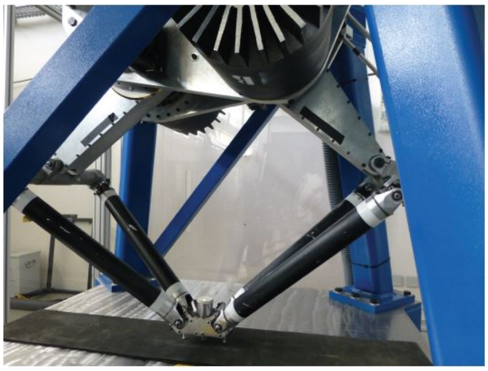

(d) IRSbot-2 from IRCCYN (LS2N) [Germain 2013].

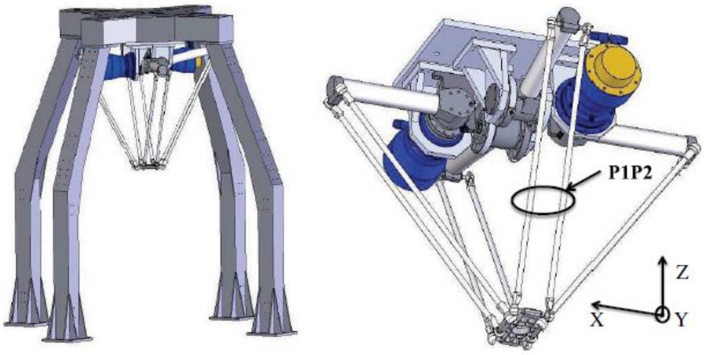

(e) Par2 robot [Company 2011].

Figure 1.10: Examples of high-speed robots (continued).

To summarize this Section, it can be seen that most of the developments of robots for performing industrial applications, such as pick-and-place operations, since the 1990's, have been with the objectives of designing not only accurate robots, but also robots that can operate at high speeds.

In the recent decades, nonetheless, the design trends to operate at high-speeds have shifted to the design of robots that in addition to be fast, they could perform as energy-efficient as possible [Brossog 2015]. The motivations to do that rely on the environmental impacts of processing a robot, which includes the motors and the drivers with their respective energetic losses, the materials for manufacturing the robot links, chassis and joints, electrical cabinet, etc.

The literature review shows that there are two main directions from which the environmental impacts of an industrial robot may be reduced [Carabin 2017]:

- Decrease of the electrical consumption:
    - By re-designing the robot architecture, the electrical cabinet, etc;
    - Motion planning;
    - New types of actuators;
- Decrease of the use of impacting materials
    - Lightweight robots;
    - Design by using materials with low environmental impacts.

In this thesis, we will concentrate on decreasing the environmental impact by following the direction of reducing the electrical consumption of high-speed robots. In what follows, in Section 1.2, we will thus perform a short review on the conventional techniques for minimizing the energy consumption of robots. The most significant achievements in terms of percentages of energy reduction will be mentioned, combined with a brief description of the most representative techniques for energy minimization.

1.2 Towards designing energy-efficient high-speed robots

In order to improve the energy efficiency of high-speed robots, researchers from different disciplines have come up with several strategies which can involve control-based approaches, optimization-based approaches or design-based approaches, etc. Additionally, it is worth mentioning that minimizing the energy consumption of robots in general, is a problem involved in different disciplines of robotics, e.g. humanoid robots, mobile robots, robot manipulators operating at slow speeds, etc.

For all the previously mentioned, in this Section, we will thus present a review on the available techniques for energy minimization of high-speed robots. Additionally, it should be noted that we will not only focus on strategies for the energy reduction of robots operating at high speeds, but also a review on techniques developed in other research fields, which may be suitable for high-speed robots. Finally, the main objectives of this thesis will be stated, and the proposed concept for reducing the energy consumption of high-speed robots will be explained. Let us make a bibliographical review of these approaches.

1.2.1 Conventional techniques for energy minimization

1.2.1.1 Beginnings with static balancing techniques

One of the first strategies developed by the research communities for reducing the energy consumption of robot manipulators, for slow speeds, were based on static balancing techniques. Some of the most relevant state-of-the-art works can be found in [Arakelian 2000][Herder 2001][Lessard 2007][Baradat 2008][Arakelian 2015]. It should be noted that balancing techniques is a well-known problem in the field of mechanical engineering covered with more than 500 state-of-the-art literature references. Nonetheless, in the review presented on this work, we will non-exhaustively list some of the most relevant works on the state of the art.

The main idea of such balancing systems is to compensate the efforts due to gravitational forces by means of static equilibrium, thus reducing the input torques by the motors, and therefore leading to decrease the energy consumption. Additionally, since the actuator efforts are reduced, less powerful motors can be used to actuate the joints of the robot manipulator.

As it can be seen, the objective of having a static balanced system, from an energetic point of view, is thus to minimize the input torques. Static balancing, complete or partial, is typically achieved by adding counterweights or a spring to the links of the robot [Baradat 2008]. This is done with the aim of enforcing the potential energy of the system to remain constant for all configurations of the robots. This means that the robot will

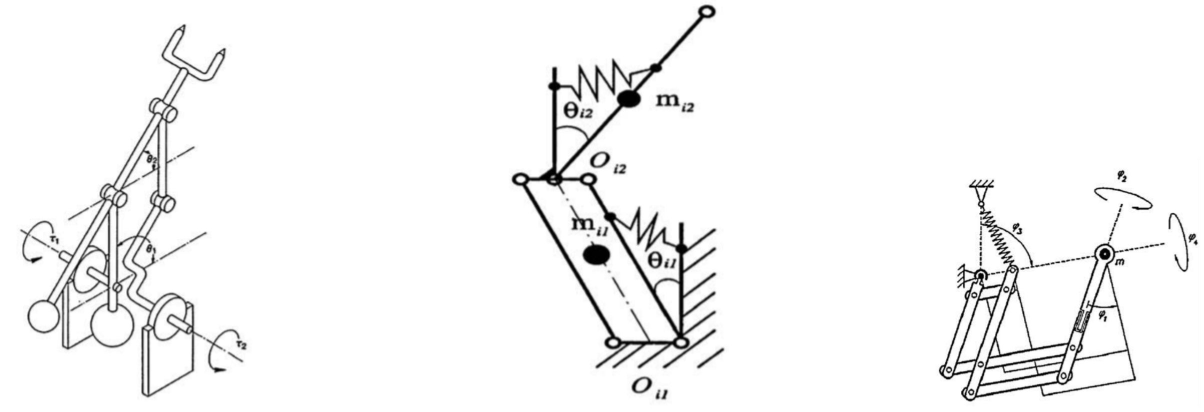

(a) Balancing by using counterweights [Newman 1986].

(b) Balancing by using springs [Ebert-Uphoff 2000].

(c) Balancing by using auxiliary mechanisms [Herder 2002].

Figure 1.11: Examples of static balanced mechanisms.

remain statically stable for any configuration, thus requiring zero actuator torques for static loads. Among several examples of mechanisms statically balanced, we can define a non-exhaustive list below:

- Balancing by using counterweights [Newman 1986][Agrawal 2004][Arakelian 2015] (An example is shown in Fig. 1.11a).
- Balancing by using springs [Ebert-Uphoff 2000][Herder 2001][Arakelian 2015] (An example is shown in Fig. 1.11b).
- Balancing with auxiliary mechanisms [Leblond 1998][Herder 2002][Arakelian 2015] (An example is shown in Fig. 1.11c).

Among some of the most representative results in terms of input torque minimization by using gravity-balancing techniques, the reader can refer to the works in [Lessard 2007] [Baradat 2008][Briot 2015a]. For instance, the authors in [Lessard 2007] make a comparison study of between implementing springs or counterweights for statically balancing a parallel robot for medical 3D-ultrasound images. They show that by using springs for statically balance the system, it is possible to reduce the RMS of the input torques of the full actuation chain, i.e. considering all the active joints of the robot, up to 72 % with respect to a case in which there is no spring attached to the parallel robot. For the case of using counterweights, the reduction of the RMS of the input torques can reach up to 73 %

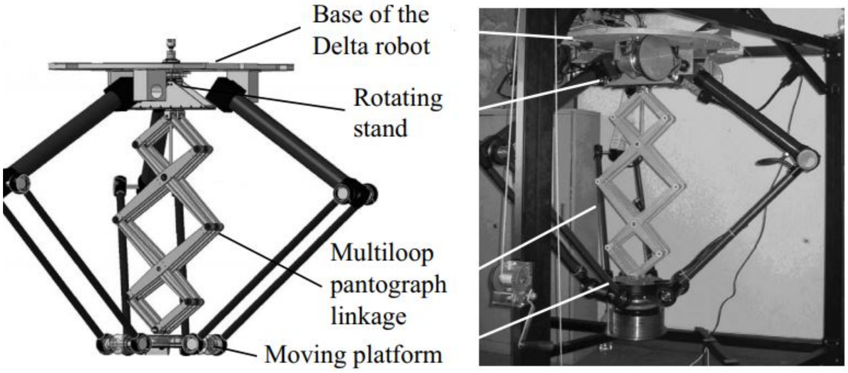

Figure 1.12: Delta robot with the balancing mechanism [Baradat 2008].

with respect to the nominal case. Other representative work is presented in [Briot 2015a], in which the authors propose a new gravity-compensation system for cancellation of the static loads of variable payloads.

Other representative work, in which the gains on input torques reduction are impressive, is the one in [Baradat 2008]. The authors of [Baradat 2008] propose the use of an auxiliary system based on a pantograph mechanism mounted on a rotating stand connected with the base as shown in Fig. 1.12. It should be noted that, different to other works on gravity-balancing, in [Baradat 2008], the authors study not only the static mode, but also the gains on dynamic mode, i.e. faster motions. Based on the results presented in [Baradat 2008], the improvements on input torques show that in static mode the gains are of the order of 77 % of reduction, while in dynamic mode the gains on input torque reduction are of the order of 40 % considering the full actuation chain, i.e. all the actuators from the active joints.

From all the aforementioned works, even if at slow speeds, gravity-balancing techniques have shown their effectiveness to compensate the input torques required to move the links of slow robots (and thus to reduce the energy consumption), these techniques cannot be applied for high-speed robots. This is due to the fact that at high speed, the inertial effects are preponderant. Additionally, some other drawbacks of these techniques is that its design complexity may be of low practicability, and the robustness to load variations is not ensured.

1.2.1.2 Design of lightweight robot architectures

Designing lightweight robot architectures have become a research topic of great interest for robotics communities in the recent years. This is due to the fact that lightweight robots

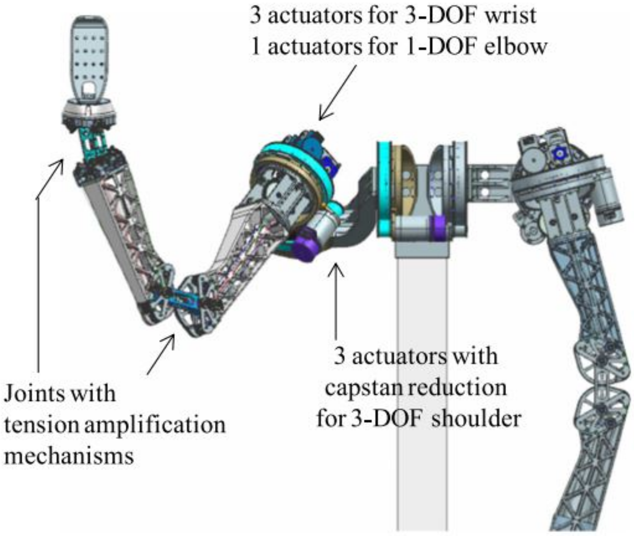

Figure 1.13: Anthropomorphic lightweight robot for high-speed safe interaction [Kim 2017].

implies achieving higher operational speeds, less weight, less powerful actuators and thus lower energy consumption. For this reason, one of the most conventional approaches to reduce the energy consumption of high-speed robots is by designing lightweight robot architectures, e.g. by using carbon fiber to lowering the moving elements mass, thus permitting the use of less powerful motors. The main drawback of this design approach is that in manipulators with lightweight architectures operating at high speeds undesirable vibrations may appear. This is due to the fact that the lightweight architecture affects the robot stiffness, worsening the accuracy of the robot at high speeds.

In order to overcome with the aforementioned accuracy issues some interesting works in structural optimization have been developed [Wang 1993][Briot 2018]. The main idea of such strategies is to increase the fundamental frequency of vibration by optimally distributing the mass and the stiffness of the manipulator. Thus, if high fundamental frequency is achieved, then the bandwidth for the lightweight manipulator increases, allowing to perform fast motions with stable end-effector control, thus increasing the accuracy. Despite encouraging results in structural optimization for improving the accuracy of lightweight robots, these approaches have been mainly limited to single-link manipulators.

Other interesting work for designing high-speed lightweight robots was proposed by Prof. Kim in 2017 [Kim 2017]. The robot is shown in Fig. 1.13, and it is designed for performing high-speed human-robot interaction. It is a 7-DOF manipulator with low inertia and high stiffness. All seven motors are mounted at the shoulder and the motion transmission to the elbow and the wrist is done by means of steel wires, similar to a cable-driven manipulator. The novelty in its design is a lightweight tension-amplification mechanism used to increase the stiffness without increasing the mass and inertia. The accuracy of the robot is comparable to that one of an industrial robot with a repeatability of 0.425 mm for speed cycles of 5.35 m/s. It is worth noticing that even if this result is impressive, the standard ISO for repeatability of an industrial robot is set to 0.1 mm.

Other interesting results on the reduction of energy consumption through the designing of lightweight architectures are those from the project FP7 DEMAT [DEMAT 2010]. The main objective of this project was to improve the energetic efficiency of machining processes by replacing the masses of the machining systems with recyclable skeletal structures. Even if the results on energy minimization are impressive with percentages of 30 % of energy reduction, it requires of complex design phase for the controllers in the system integration and well-skilled users with knowledge on designing of composites.

Other promising types of parallel robots, towards designing lightweight architectures for using less energy in industrial applications, are the so-called cable-driven parallel robots (CDPRs). CDPRs are a class of parallel robots in which the moving platform is connected to a fixed frame by means of cables. Furthermore, pulleys serve as transmission system to guide the cables from the winches to the cable exit points, and the moving platform is controlled by modifying the cable lengths. As it is known, CDPRS compared with the classical parallel robots constituted of rigid links, have several advantages such as low mass of the moving elements, and larger workspace. As a consequence, they can be used in several applications such as handling operations [Albus 1992], large-scale assembly [Pott 2010], fast pick-and-place operations [Kawamura 2000], etc. Since most of the energy that the actuators most delivered is to compensate the gravitational wrench due to the payload, and considering that the links are based on cables, relatively small actuator can be used, and therefore less energy consumption is required. The fastest cable-driven pick-and-place robot is the FALCON-7 shown in Fig. 1.14 [Kawamura 2000]. This CDPR can perform a motion of 0.325 m in a cycle time of 0.08 s, attaining maximum speeds of about 13 m/s, and maximum accelerations of 43 G. Even if the capabilities in terms of speed are impressive, undesired vibrations due to the elasticity on the cables lead to worsen the accuracy of the end-effector.

From all the aforementioned works, even if the lightweight architectures permit to use less powerful actuators, and thus to minimize the energy consumption due to smaller

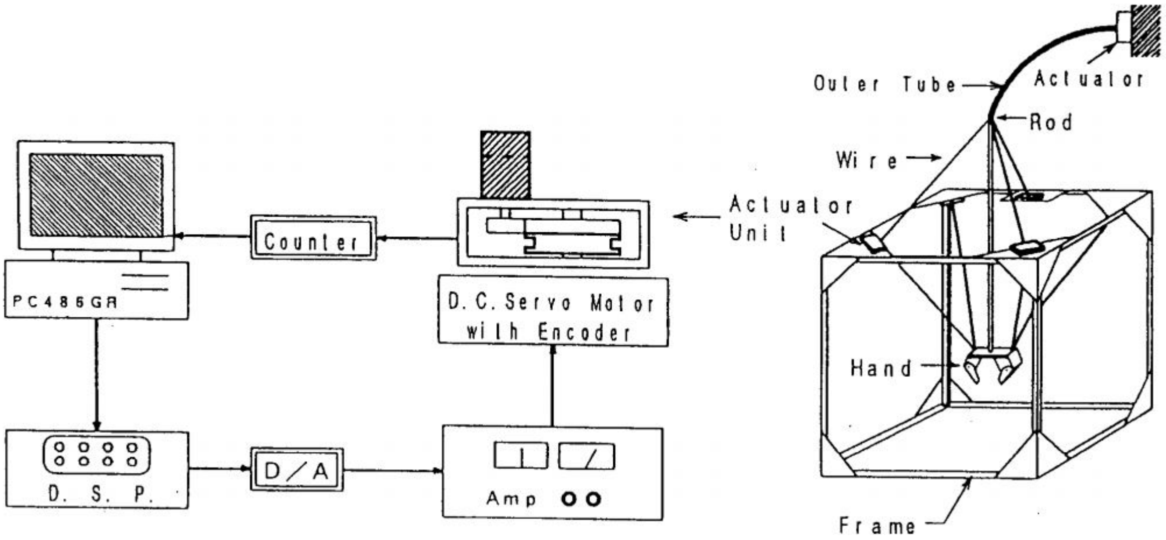

Figure 1.14: High-speed CDPR FALCON-7 [Kawamura 2000].

actuator size, the design phase may be of high complexity, and specific to a type of kinematic structure. In addition to that, the stiffness may be compromised while designing a lightweight architecture, thus losing the accuracy of the high-speed mechanism.

1.2.1.3 Motion planning techniques

On the attempt to reduce the energy consumption of industrial robots, other interesting solutions apart from designing lightweight structures have been proposed in the literature review. In this Subsection, we will focus on presenting the available techniques based on motion planning strategies in order to minimize the energy consumption.

One of the most recent works related to reduce the energy consumption through the generation of optimal trajectories took place in 2013 with the cooperative project FP7 AREUS (Automation and Robotics for European Sustainable manufacturing). This project had the objective of optimizing the energy consumption of robot manipulators in robotized work-cells [AREUS 2013]. Some of the most representative works resulted from this cooperative project for the reduction of the energy consumption can be found in [AREUS 2013][Pellicciari 2013][Riazi 2016][Gleesona 2016]. The two main approaches followed in order to reduce the energy consumption within this project were based on optimization algorithms in order to minimize the acceleration and deceleration phases of the robot trajectories, and by implementing regenerative cycles with complex electric arrangements based on DC grids. In this Subsection, we concentrate on describing the

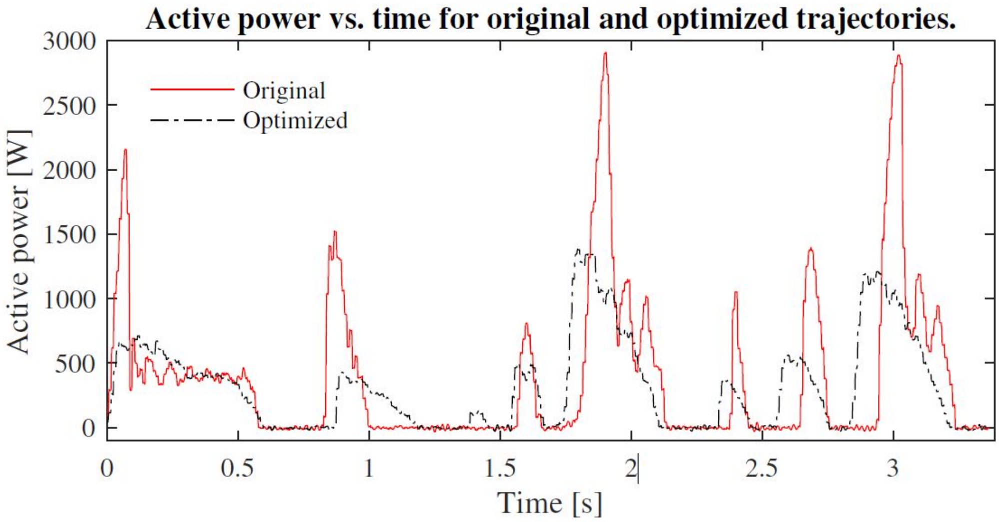

Figure 1.15: Power consumption with method proposed in [Riazi 2016].

strategies based on optimal trajectories. One of the works for reducing the energy consumption through the generation optimal trajectories is the one in [Riazi 2016]. In that work, the authors formulated different candidate objective functions based on acceleration and energetic criteria, and through a time-optimal motion planner they performed the energy reduction for a typical non-high-speed industrial task. The resulted fastest cycle from the time-optimal motion generator was of 2.2 s with an energy saving of 33 %, and a reduction of the peak-power of 69 %. For a visualization of these reductions on the power consumption, in Fig. 1.15, some results from [Riazi 2016] are shown. Even if these results are impressive, they did not impose constraints on the final time, since the time-optimal planner takes care of calculating the most optimal one for reducing the energy consumption, which in a typical pick-and-place operation is not the case.

Other relevant work for the generation of optimal trajectories for industrial robots was proposed in [Pellicciari 2013], also from the FP7 AREUS project. In [Pellicciari 2013], the generation for the trajectories follow from a different planning concept in which energy-efficient optimal trajectories are calculated by means of constant time scaling, starting from pre-scheduled pick-and-place motions which respect the actuator limits [Pellicciari 2013]. The main idea of this method, which is described in the block diagram of Fig. 1.16, is to start with a pre-scheduled joint trajectory compatible with the actuator constraints. Then, the overall power consumption is estimated with the input torques calculated from the pre-scheduled trajectory, and then if the actuator torque and energetic constraints are not respected, a time scaling strategy is used to update the

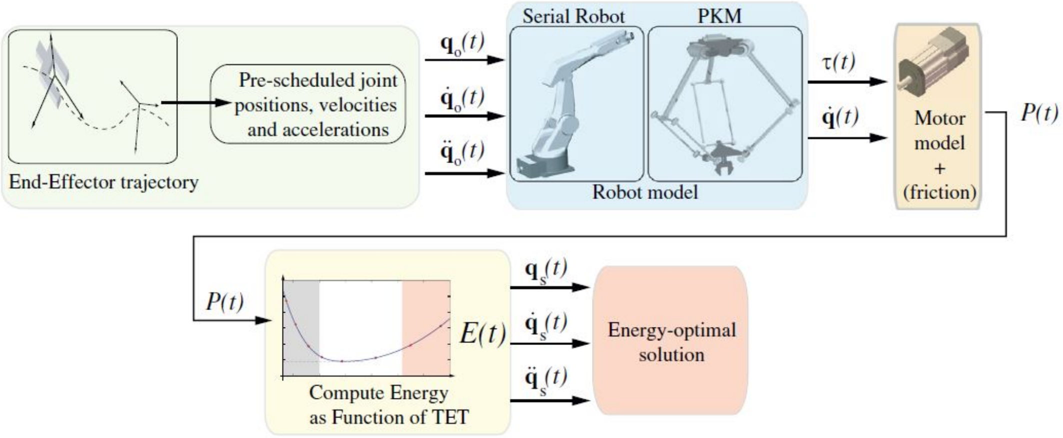
End-Effector trajectory
Pre-scheduled joint positions, velocities and accelerations
$\mathbf{q}_o(t)$
$\dot{\mathbf{q}}_o(t)$
$\ddot{\mathbf{q}}_o(t)$
Serial Robot
PKM
Robot model
$\tau(t)$
$\dot{\mathbf{q}}(t)$
Motor model + (friction)
$P(t)$
$P(t)$
$E(t)$
Compute Energy as Function of TET
$\mathbf{q}_s(t)$
$\dot{\mathbf{q}}_s(t)$
$\ddot{\mathbf{q}}_s(t)$
Energy-optimal solution

Figure 1.16: Block diagram proposed for the time scaling strategy to minimize the energy consumption (TET stands for Task Execution Time). [Pellicciari 2013].

trajectory. Time scaling strategies are well-known in cooperative manipulation for modifying trajectories of multiple robots. The main idea is to scale the trajectory speed so that all joint torques remain within the admissible torque boundaries. The fastest pick-and-place trajectory executed for the simulation results from the time-scaling method of [Pellicciari 2013], was of 6 s. The energy gains obtained by following the time-scaling approach vary between 30 to 40 %. Even if the percentages of reduced energy consumption are very impressive, the pick-and-place trajectory is performed at slow speeds, thus having less preponderant inertial effects.

It is worth noticing that from the aforementioned methods based on trajectory planning techniques, the final execution time is used as decision variable to minimize the energy consumption. The concept behind this is to generate trajectories with smoother acceleration and deceleration phases, leading to have lower peak torques and therefore less energetic losses in the braking phase of the motors. Even if the aforementioned approaches show impressive results in terms on energy reduction, we can summarize some drawbacks towards the designing of energy-efficient high-speed robots.

- The final execution time must be adjusted to scale the trajectory so that smoother accelerations are generated. Typically for a high-speed pick-and-place operation the final time is imposed;

- Even if the results for generating energy-efficient trajectories lead to energy reduction up to 60 % in experimentation, the cycle times are slower compared to the ones on a typical high-speed industrial task.

1.2.1.4 Redesign of electric cabinets

As it was previously mentioned another approach to reduce the energy consumption of robots in robotized work-cells consists on redesigning the electric drive system used to actuate and control the robot manipulators. The main motivation of this approach comes from the new advances in power electronics that nowadays researchers working on electronic technologies have come up with. It should be noted that in the literature review, to the best of our knowledge, the percentages on energy gained by using this electric approach are not well specified. Nonetheless, since we seek to present a global overview on the available strategies for energy consumption minimization of industrial robots, a brief review on these technologies will be done in this Subsection.

Some of the most important works on redesigning the electric cabinets for robotic industrial applications in order to reduce the energy consumption are presented in the works from [Meike 2011][Pellicciari 2015]. There are two main strategies to take care of the reduction of the energy consumption of robots based on electric technologies: *i*) Use of capacitors in order to enforce regenerative phases in the motor drive systems, and *ii*) the use of DC-grid electrical power supply. This permits to have less conversion stages, compared to classic AC-driven systems, thus reducing the conduction losses. Let us first discuss about the first strategy.

It is well-known that capacitors, as their mechanical counterparts springs, can store some form of energy. A capacitor is a passive electronic component that stores electrical energy in an electrical field. This feature is very attractive for electrics communities due to the possibility to enforce what is called regenerative phases in electrical systems, such as a motor drive system actuating an industrial robot. Thus, the idea of reducing the energy consumption by using capacitors is that since industrial robots are typically actuated by electrical motors, a regenerative braking can be used in the electrical motor's generator/motor transitions [Meike 2011]. This technology implemented in [Meike 2011] for industrial robotic applications shows that energy savings between 5 % to 20 % can be achieved. Even if this technology may be attractive for the electrics communities to reduce the energy consumption of industrial robots, the storage capacity is limited, and it is not free of energetic losses due to the addition of extra electric components which dissipate energy. Additionally, even if at high-speeds, in which the accelerations are high, super-capacitors may be used, the economic expenses of implementing super-capacitors are very high [Meike 2011].

As previously mentioned, a second technology for redesigning more energy-efficient

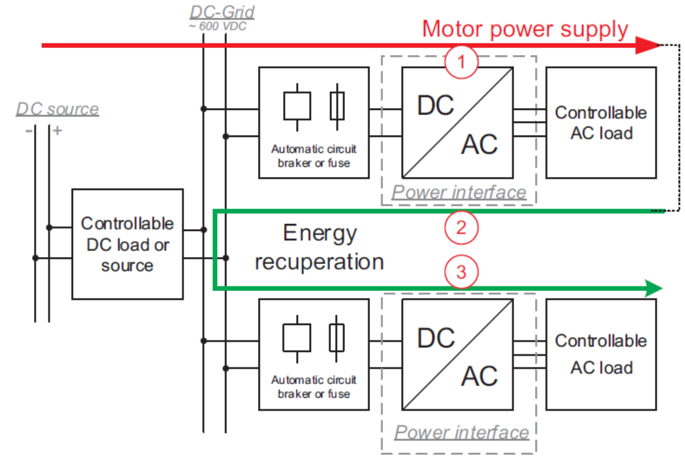
DC-Grid
~ 600 VDC
Motor power supply
DC source
- +
Controllable DC load or source
Automatic circuit braker or fuse
DC
AC
Controllable AC load
Power interface
Energy recuperation
1
2
3

Figure 1.17: DC-based power architecture [Pellicciari 2015].

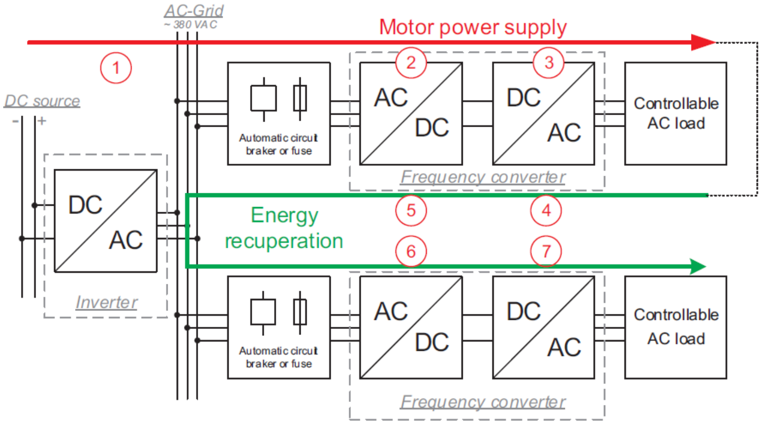
AC-Grid
~ 380 VAC
Motor power supply
DC source
- +
DC
AC
Inverter
Automatic circuit braker or fuse
AC
DC
Frequency converter
Controllable AC load
Energy recuperation
1
2
3
4
5
6
7

Figure 1.18: Classical AC power system [Pellicciari 2015].

electric cabinets of industrial robots, is by designing electric power supplies based in DC-grids [Pellicciari 2015]. Typically in an industrial motor drive architecture for actuating the robots, AC-driven motors are used. This is due to their capabilities to perform faster direction changes and quick starts and stops. Additionally, they can provide of higher voltages for carrying for instance higher payloads. Within the FP7 AREUS project [AREUS 2013], however, the authors proposed to design DC-grid power supplies rather than AC-driven grids with fewer conversion stages, and therefore less conduction losses and also higher voltage power delivery. The DC-based power architecture proposed in [Pellicciari 2015] is shown in Fig. 1.17. This novel DC-based architecture supply the power to the first load in a single conversion, whereas energy exchange between the two loads is performed in two conversions (i.e. 2-3). A classical AC-driven grid used in a state-of-the art power system required of at least 7 conversion stages to control the output loads (See. 1.18). As it can thus be seen, the work in [Pellicciari 2015] reduced the power stages from 7 to 3 conversion phases, thus reducing the loses due to conduction. The results on the energy reduction reported in [Pellicciari 2015] are of 30 % with respect to a classical AC power system.

1.2.1.5 Use of elastic passive compliance: SEAs and VSAs

From the aforementioned strategies towards designing high-speed robots, it is worth noticing that all those approaches, from the actuation aspects, consider classical motor-load connection for transmitting the motion to the robot joints. Moreover, it seems that the methods for reducing the energy consumption with a classical type of actuation have come to a limit on the reduction which can be achieved. Probably it is necessary to define new actuation principles?. That is why in the last decades researchers investigating methods for decreasing the energy consumption of robots, not necessarily for industrial applications, have come up with the idea of using elastic elements combined with the electric motors so that a mechanical energy storage can be realized. Let us thus make a review on these actuation concepts.

The idea of using elastic elements combined with the motors dates back to 1995 with the invention of the so-called Series Elastic Actuator (SEA) by Gill Pratt and Matt Williamson [Pratt 1995a]. SEAs are compliant actuators that decouple the motor and the output load by means of a spring in series that may serve to absorb impact loads, to provide mechanical energy storage or to increase the peak power output (See the schematic of Fig. 1.19). The stiffness of this type of actuator is set by the spring constant. According to [Gomes 2016], the first applications in which this type of actuator were used encompasses human-robot interaction for increasing the safety, e.g. the arms of the humanoid robot Cog back in 1999 [Brooks 1999], and to absorb impacts of walking robots, e.g. a biped walking robot at MIT back in 1995 [Pratt 1995b].

This important development towards the use of mechanical energy storage to improve the dynamic performance of robots, motivates several researchers from 1995 to nowadays to come up with different prototype realizations following the series-elastic-based actuation concept. Among several application examples, we can non-exhaustively list:

- Spring Flamingo Robot (Fig. 1.20a): It is a planar bipedal walking robot with 6-DOF in total consider both legs, with their respective hip, knee and ankle joints.

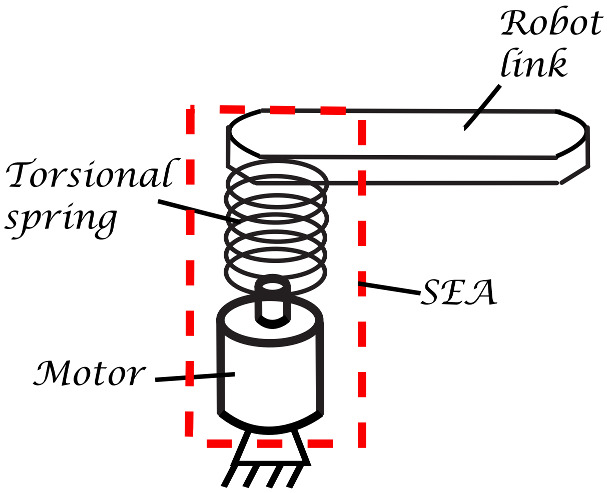

Figure 1.19: Schematic of SEA

SEAs drive these 6-DOF, and it was developed by Gill Pratt in 1999. It can walk on flat terrain at 1.25 m/s and can walk over uphill and downhill terrains.

- Bipedal walking robot M2 (Fig. 1.20b): It is an extension of the work developed from the Flamingo robot. It has 12-DOF, 6 on each leg distributed as follows. 3-DOF on the hip, 2-DOF on the ankle and 1-DOF on the knee. SEAs are used for actuating the joints. It was developed in 1999 by David Robinson.

- Cog robot (Fig. 1.20c): It was the first robot in which SEAs were applied on a robot manipulator. The arm of this robot have 6-DOF from which all of them are actuated by means of SEAs. Moreover, it can perform hammering tasks efficiently thanks to the elastic springs in series of the motors, which serve to absorb and increase the peak torque output to perform the repetitive hammering task. It was designed in 1999 by Rodney Brooks.

- Lower limb robot Corndog (Fig. 1.20d): This is another lower limb robot in which electromechanical SEAs are used to absorb the impact shocks while walking. It was developed by David Robinson in 2000.

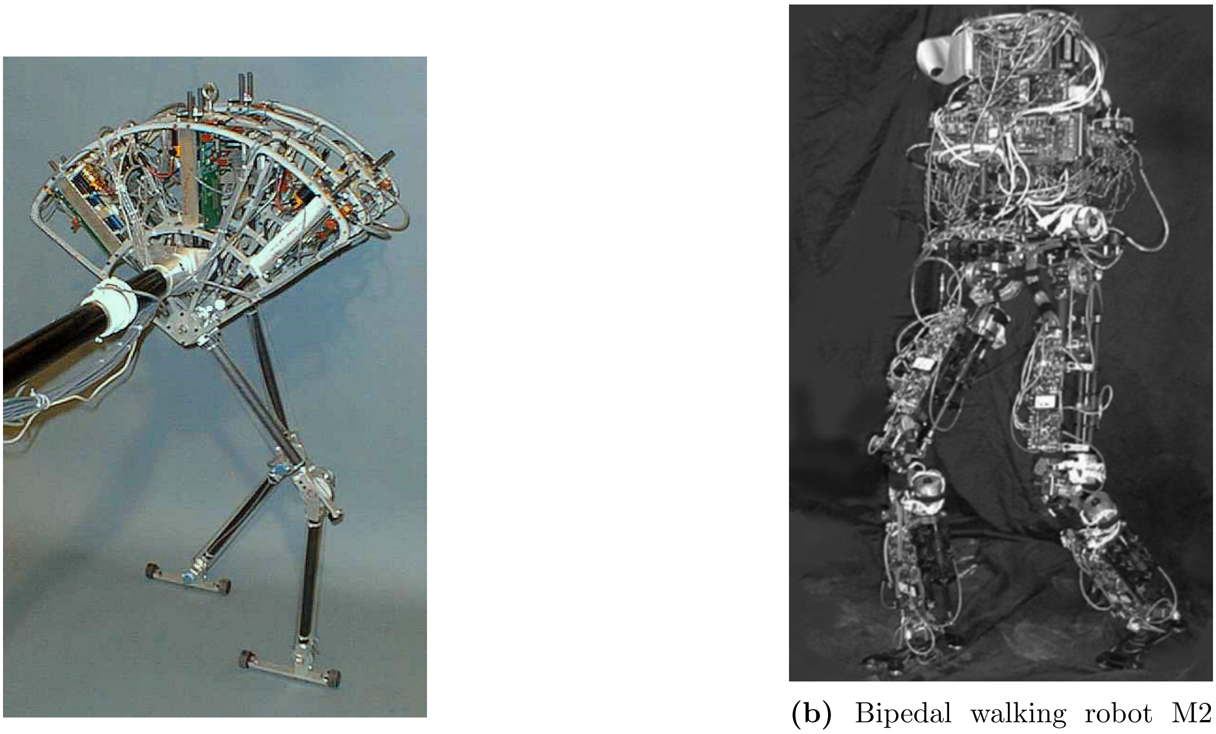

(a) Flamingo robot [Pratt 1998].

(b) Bipedal walking robot M2 [Robinson 1999].

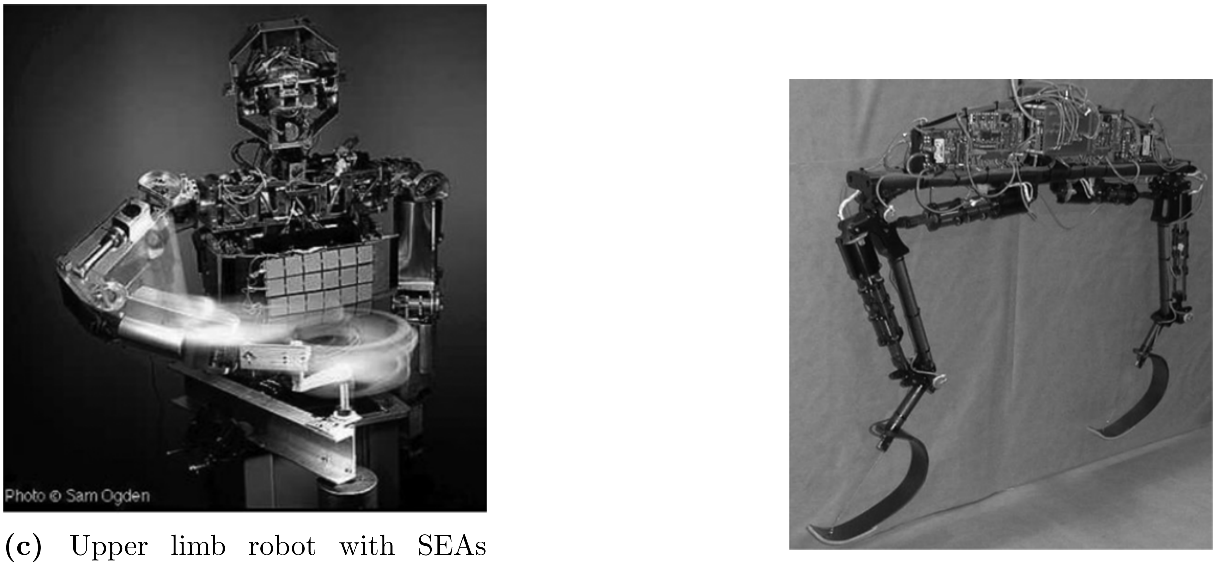

(c) Upper limb robot with SEAs [Brooks 1999].

(d) Corndog robot [Krupp 2000].

Figure 1.20: Examples of SEAs applied on applications related to absorbing impacts and increase peak power (walking robots) and for human-interaction for increasing safety.

It is worth noticing that the aforementioned list is not exhaustive, nonetheless, from 2000 to nowadays more and more implementations of SEAs were developed. Additionally,

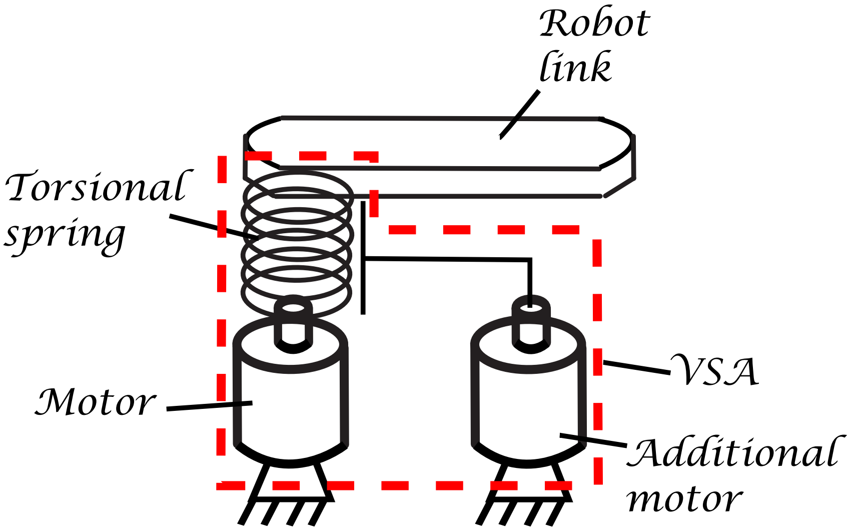

Figure 1.21: Schematic of variable stiffness actuator.

it should be mentioned that nowadays SEAs are also used in applications such as assistive exoskeletons or for prosthetic devices (See. [Pratt 2002][Kong 2010][Lagoda 2010]).

Continuing with the developments on the used of elastic elements for inducing mechanical energy storage, and thus improvements on the dynamic performances of robots, the so-called Variable Stiffness Actuators (VSAs) were introduced in the 2000's [Fasse 1994] [Vanderborght 2008][Tonietti 2005][Schiavi 2008]. VSAs are actuators designed in order to overcome the limitations of the SEAs in terms of stiffness adaptability. As it was previously mentioned since the stiffness of the SEAs is fixed by the spring constant, the level of compliance to adapt for different tasks is limited. On the contrary, VSAs overcome this problem. VSAs are actuators consisting of a motor which is connected to the output link by a spring in series (like the SEAs), and whose stiffness is variable and can be controlled (See Fig. 1.21). As shown in Fig. 1.21, the adaptation of the VSA stiffness is performed thanks to an additional actuator which serves to control for instance the spring equilibrium position (anchor point) so that the VSA stiffness can vary.

One of the most representative works in which VSAs were used for improving the dynamic performances of robots were the results presented within the cooperative project VIACTORS in 2009 [VIACTORS 2009]. This project had as main objective to develop variable stiffness actuators (based on springs in series) able to efficiently store and release mechanical energy, react softly when interacting with the environment, and provide natural characteristics based on biological systems such as human muscles. It should be noted that since in the context of this thesis, we are interested in the energetic aspects, here

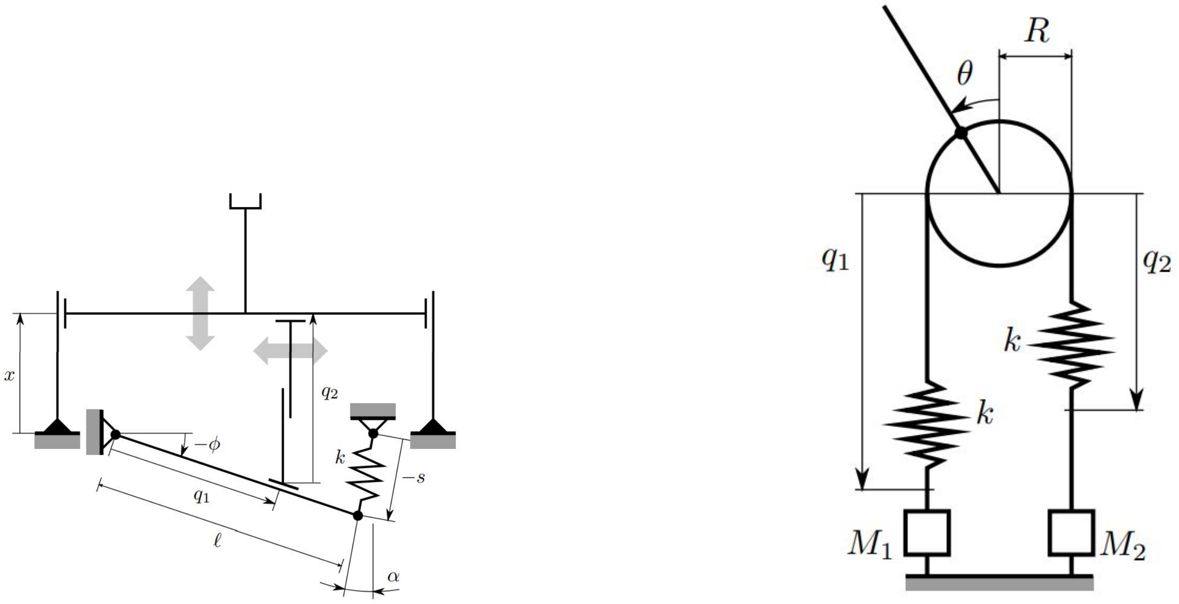

(a) Design of lever arm with VSA [Visser 2010].

(b) Antagonistic setup of VSAs and output link [Visser 2010].

Figure 1.22: Examples of designs by following the port-based modeling approach presented in [Visser 2010].

we will present an overview on the results from [VIACTORS 2009] related on efficiently storing and releasing mechanical energy, even if they are not specifically oriented towards industrial robots. The two main approaches followed in [VIACTORS 2009], in order to efficiently store and release the mechanical energy from the VSAs are based on an optimal design approach, and secondly, by exploiting the natural dynamics for minimizing the energy consumption. Let us thus, based on [VIACTORS 2009], present some of the most representative results in terms of increasing energy efficiency by using VSAs.

To start with the design approach, the works in [Carloni 2012][Visser 2011][Visser 2010] present a port-based modeling framework in which guidelines for designing energy-efficient VSAs are given. The main idea of this approach based on a port-based formulation, is to study the energy performance of several VSAs designs based on a bond graph, which represents the energy flow through the different mechanical components of the VSAs designs. This allows to establish an energetic metric from which optimal VSAs designs can be synthesized. Based on this metric, the authors in [Visser 2010] present two energy-efficient VSA designs coupled in series to a 1-DOF robot (See Fig. 1.22a–Fig. 1.22b). They show that by following the energy-based design guideline, it is possible to change

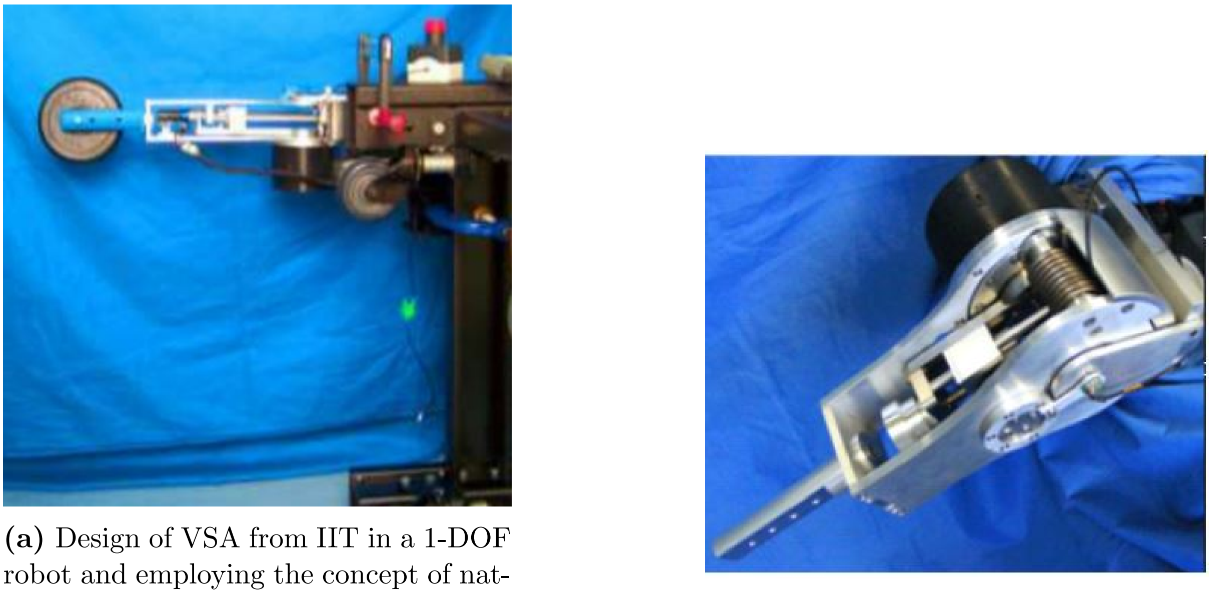

(a) Design of VSA from IIT in a 1-DOF robot and employing the concept of natural dynamics [Jafari 2011].

(b) Joint design from VSA [Jafari 2011].

Figure 1.23: Actuator with Adjustable Stiffness (AwAS) developed by IIT from the VIACTORS project.

the stiffness of the VSA without using energy. Even if this result is very impressive, the main issue is that they neglect the friction effects, and additionally, only one state at a time can operate, either the robot position or the VSA, limiting the system to operate energy efficiently simultaneously for any robot configuration.

The second approach for efficiently operate the VSAs is presented in the works from [Haddadin 2011][Jafari 2011]. It should be noted that for the purposes of this thesis, the strategy presented in [Haddadin 2011][Jafari 2011] is more appealing than the aforementioned design approach. The authors of [Jafari 2011], thanks to the continuous exchange from spring potential energy of the VSA to kinetic energy, propose to exploit the natural dynamics for minimizing the energy consumption. The main idea is to match the natural frequency of the robot (resonance frequency), with the desired motion frequency of the given task. This concept was validated on a single-degree-of-freedom robot by using the so-called VSA AwAS from IIT (See Figs. 1.23) [Jafari 2011]. The results show that for a periodic task oscillating at 3 Hz during 10 seconds, by exploiting the natural dynamics, i.e. approaching to the natural frequency through the adjustment of the VSA, the energy consumption can be reduced up to 25 %. Even if this percentage of reduction is impressive, the energy required to adjust the stiffness of the VSA is not considered, thus not analyzing the energy consumed by the full actuation chain. Additionally, due to the serial arrangement of springs and motors in the VSAs, the accuracy of the output link may be compromised due to the fact that uncontrolled robot deflections may appear at higher speeds.

It is worth mentioning that to the best of our knowledge, the first time the concept of natural dynamics was introduced to a robot manipulator was in the PhD dissertation of Matthew Williamson in 1999, for a single-DOF link [Williamson 1999]. Nonetheless, the concept of natural dynamics in robotics was introduced before in 1990 for a passive dynamic walker by Tad McGeer [McGeer 1990].

As it can be seen from all the aforementioned, VSAs have shown a great potential to decrease the energy consumption of several robots, mainly oriented to human-robot interaction applications for increasing safety, to walking machines to perform more energy efficient gait cycles, to design mechatronic systems which behave more human-like, such as muscles, and few works oriented to robot manipulators. Additionally, other appealing characteristic of such actuators is their possibility to adapt the stiffness for different operational situations. Thanks to all these developments on compliant actuation, recently, VSAs have been introduced to robot manipulators involved in more industrial-like applications, such as pick-and-place operations. That is why in what follows we devote a complete Subsection for reviewing the most representative techniques for reducing the energy consumption of pick-and-place robots by using springs, and from which this thesis is motivated.

1.2.2 Increasing the energy efficiency of pick-and-place robots: use of springs

From the aforementioned review of techniques for energy minimization, it can be seen that towards the designing of high-speed pick-and-place robots, the most promising techniques in the bibliographical survey are the use of variable stiffness, combined with a strategy for exploiting the natural dynamics. This is due to the fact that VSA springs, allowing tunable stiffness, would permit to put the robot in near a resonance mode, thus considerably decreasing the energy consumption during fast quasi-periodic pick-and-place motions. Nevertheless, as previously mentioned, the serial arrangement of springs and motors in the VSA leads to uncontrolled robot deflections at high-speeds and, thus, to a poor positioning accuracy of its end-effector.

In order to solve the aforementioned issue in terms of accuracy from the VSAs, which

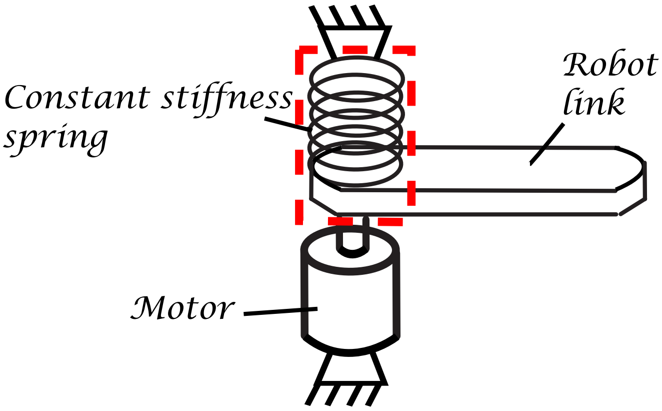

Figure 1.24: Schematic of constant stiffness spring in parallel to the motor.

limit their use in pick-and-place robots due to poor accuracy, a novel type of actuation based on *constant* stiffness springs in parallel to the motors, for slow pick-and-place robots in [Schiehlen 2005][Barreto 2016][Uemura 2009], and for a humanoid robot in [Haq 2011][Haq 2012], have been proposed. The main idea is to place the constant stiffness springs in parallel so that the required torque to move the output load is distributed between the motor and the parallel spring (See Fig. 1.24). This is possible since the constant stiffness spring in parallel supplies part of the required input effort to move the output load, thus reducing the energy consumption. Let us give more insights of the works in [Schiehlen 2005][Barreto 2016][Uemura 2009][Haq 2011][Haq 2012], implementing this actuation principle.

The work in [Schiehlen 2005], presented in 2005, proposes to exploit the dynamic characteristics of placing springs in parallel for a slow serial manipulator performing periodic trajectories. The main idea of the work in [Schiehlen 2005], is to propose a prescribed limit cycle as reference motion for the robot manipulator. Then, by using a gradient-descent based approach [Schiehlen 2005], the optimal values for the spring constants and the pretension parameters of the springs placed in parallel to the links are calculated so that the free-response of the robot converge to the referenced limit cycle, thus minimizing the input torques, and therefore the energy consumed. For a given slow periodic trajectory (limit cycle) on a 2-DOF manipulator with springs in parallel (See Fig. 1.25a), the results in terms of energy reduction in [Schiehlen 2005], show that they can have energy savings between 50 to 60 % of consumption. Even if these results are impressive, they only validated the concept in simulation. Additionally, they neglect the friction effects, and do not consider the effort required to pretense the spring for the desired referenced

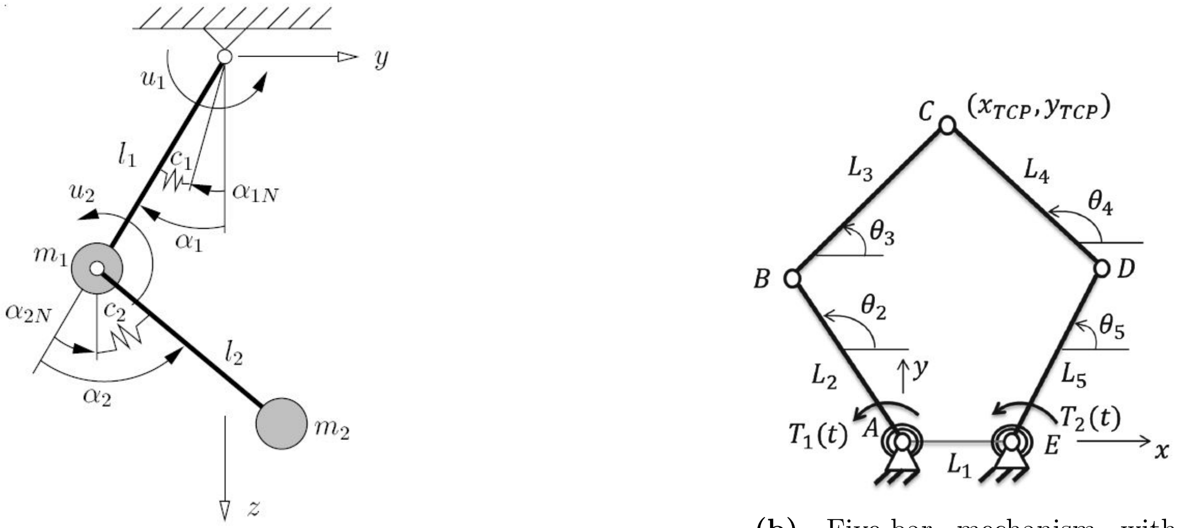

(a) Serial robot with springs in parallel [Barreto 2016].

(b) Five-bar mechanism with constant stiffness springs in parallel [Barreto 2016].

Figure 1.25: Examples of robots with constant stiffness springs in parallel [Barreto 2016].

limit cycle. In addition to that, the prescribed periodic trajectories are not pick-and-place-like motions, since the amplitude and frequency of oscillation remain constant, and they do not impose constraints on the initial and final velocities and accelerations. Nevertheless, this is a breakthrough towards reducing the energy consumption by exploiting the dynamic characteristics that placing a spring in parallel brings.

Continuing with the actuation concept of using springs in parallel for reducing the energy consumption, Prof. Corves in [Barreto 2016], proposes through an optimization problem formulation, to obtain the required constants for two springs placed in parallel to the actuated links of a five-bar mechanism (See Fig. 1.25b), so that the input torques are minimized. The main idea is that for a given desired final *place position* and *place time*, through a search algorithm, an optimal trajectory connecting the pick and place points through cosines and obtaining the optimal spring constants, the input torques are minimized. The simulation results of the work in [Barreto 2016] show that for a desired pick-and-place trajectory of one single segment of 0.5 s, and neglecting the friction effects, they can save 68 % of energy consumption. These results are very impressive, nonetheless, they do not consider the friction effects, and they have a lack of adaptability for quasi-periodic tasks. Additionally, it is not very clear how they ensure the constraints on velocities and accelerations, typical from a pick-and-place operation.

Other representative work on the use parallel springs for energy minimization, is the work from Prof. Uemura in 2009 [Uemura 2009]. The authors in [Uemura 2009] propose a resonance-based motion control method, which optimizes the stiffness of the springs placed in parallel to the links of a serial robot manipulator in order to exploit as best as possible the resonance modes of the robot. The main idea of this controller is that for a given desired periodic trajectory for the joints of the robot, thanks to a stiffness adaptation method and an iterative control law, the optimal stiffness constants of the springs are calculated so that the actuator efforts are minimized. The details of this control approach are not give here, nevertheless, the reader can refer to [Uemura 2009]. Simulation results of this approach on a 2-DOF serial robot with constant stiffness springs in parallel show that for a given periodic motion of period equal to 0.5 s oscillating during a total time of 10 s, the input torques can be reduced by 90 %. It is worth noticing that during the 10 s, the iterative control law must converge to the optimal stiffness, thus not constraining the final time as it is done in a pick-and-place operation. Even if the results are impressive, the level of compliance to adapt to more pick-and-place-like tasks, in which the periods of oscillations may vary, is restricted due to a lack of adaptability due to the constant stiffness springs. Additionally, the friction effects are neglected in their simulations and the energy consumption for the given oscillating trajectory is not analyzed.

As it was previously mentioned, in this Chapter we seek to give an overview of the available techniques for minimizing the energy consumption of robots, even if they are not exclusively dedicated for pick-and-place operations. That is why, another interesting work is developed at IRCCyN (LS2N) in 2011 and in 2012, in which springs in parallel were implemented by the authors in [Haq 2011][Haq 2012] for a bipedal robot. In these works the authors performed an exhaustive energetic comparison of two different types of actuation: *i*) the use of constant stiffness springs in parallel, and *ii*) a nominal type of actuation in which no springs were attached in parallel to the bipedal robot joints. In order to exploit the natural dynamics of this bipedal robot thanks to the addition of the springs, a torque criteria was minimized thanks to a non-linear optimizer, in which the spring constants were set as decision variables over a desired cyclic gait. The results of this approach in [Haq 2011][Haq 2012] showed that by adding torsional springs in the support joints it is possible to reduce the energy consumption by 85 % with respect to the nominal type of actuation for a gait cycle of 0.85 m/s. Even if this result is impressive for a bipedal robot, they considered all joints frictionless and additionally, the use of constant

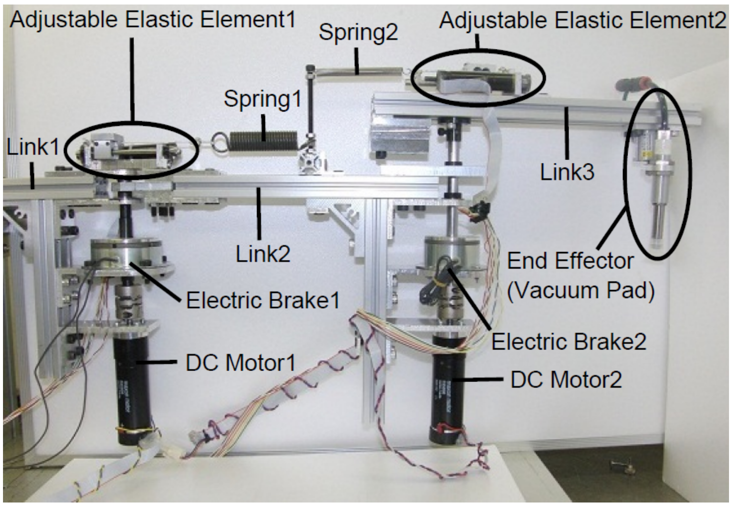

Figure 1.26: Slow serial manipulator with VSS in parallel [Goya 2012].

stiffness springs may restrict the adaptability to different gait velocities. Nevertheless, for the research on bipedal robots was a breakthrough towards the designing of more energy-efficient walking robots due to the fact that before, the use of springs in this type robots were mainly used for absorbing impact shocks and not for improving the energy efficiency of the actuation itself.

In order to overcome the limitations in terms of adaptability of the constant stiffness springs placed in parallel, the authors in [Goya 2012] for a slow robot manipulator, proposed similar as in the VSAs, to use an additional motor to vary the stiffness of the springs placed in parallel to the motors that actuate the joints. These springs are called variable stiffness springs (VSS) [Goya 2012]. To best of our knowledge, the authors in [Goya 2012], were the first on introducing the concept of using variable stiffness springs (VSS) in parallel to the motors for improving the adaptability to quasi-periodic tasks for a slow pick-and-place robot. The approach that the authors in [Goya 2012] propose to minimize the energy consumption for slow quasi-periodic tasks is to adapt the stiffness of the VSS by means of what they call, elasticity adaptation control law which requires a nonlinear force/displacement relation for the springs, so that the output stiffness of the VSS can be controllable. The results for a two-segment pick-and-place trajectory of cycles equal to 5 s and 3 s, respectively for each segment, show that they can reduce the energy consumption by 72 % in experiments. Even if these results are impressive for a first implementation of VSS for improving the adaptability in a pick-and-place tasks, among several issues, we can list:

- The friction is neglected in the results they present, which makes difficult to conclude exactly which is the real gain on energy consumption. This is due to the fact that as it can be seen in Fig. 1.26, several intermediate transmission components are used to actuate the VSS, and thus for slow pick-and-place cycles as the ones used for their experiments, the friction effects may have an important effect, since the tasks are slow. Additionally, it is not specify whether the motors have gearbox or not, which would add more energetic losses in the actuation chain;

- The energy required to adjust the stiffness of the VSS is not considered when analyzing the percentages of energy gains. This may lead to an inaccurate percentage of energy saving due to the fact that the energy consumed by the motors that vary the VSS stiffness is underestimated, thus having a lack of energetic analysis of the full actuation chain. Additionally, their energetic index to calculate the energy reduction is based on the voltage and the current only, thus underestimating all the energetic losses, such as resistance losses, conduction losses, rectification losses, etc.;

- The cycle times used for the experiments are very slow, far from a typical high-speed cycle time. Furthermore, it is not clear how the authors in [Goya 2012], enforce physically with the prototype, a nonlinear force/displacement relation for the VSS, and how they measure the stiffness of the VSS in order to control it through the elasticity control system.

- They use linear springs for a serial manipulator, which is composed of only revolute joints. This may lead to reduce the operational workspace of the robot due to the fact that the linear springs, being deformed by translational motions, do not move naturally with the revolute joints of the robot, thus restricting the rotation of the robot links to the maximal tension/compression spring limits. Additionally, since they place linear springs in parallel to the actuated joints, the only way to approximate the force/displacement relation when the linear spring is deformed, is by an approximation from the arc longitude that the linear spring generates when the revolute joints of the robot rotate. This may lead to have an inaccurate force/displacement relation for the dynamic model.

From all the aforementioned drawbacks, it is difficult to conclude of the interest of the approach proposed in [Goya 2012]. Nevertheless, it sets a conceptual starting point towards performing energy-efficient pick-and-place motions.

1.3 Existing strategies for increasing the energy efficiency of high-speed robots

Despite the aforementioned rather encouraging results when using VSAs for reducing the energy consumption of pick-and-place robots, the available solutions have drawbacks in terms of accuracy, lack of energetic analysis, and they have been only applied for slow robots. The lack of accuracy is due to the fact that the serial configuration of springs and motors leads to uncontrolled robot deflections at high speeds and the lack of energetic analysis is due to the fact that previous works underestimate the energy required to adjust the springs of the VSAs, thus not considering the losses of the full actuation chain.

The use of springs in parallel to the motors seems to be a promising solution for increasing the energy efficiency while ensuring the accuracy of the robot. Nevertheless, as it was shown the main issue is that the use of a constant stiffness spring limit the capabilities of adaptation for quasi-periodic tasks. That is why in [Goya 2012], a novel actuation concept based on variable stiffness springs in parallel was introduced for a slow robot manipulator. The results in [Goya 2012] are impressive, nonetheless, the control-based strategy they propose to minimize the energy consumption at slow speeds do not fully exploit the natural dynamics of the robot. This is due to the fact that instead of exploiting the dynamic equations, the authors in [Goya 2012] seek to find an optimal evolution of the stiffness of the VSS, which can only be computed by enforcing a non-linear force displacement relation of the VSS, which complexifies the control system, being more prone to converge towards a local minima of energy reduction. Additionally, the concept of using VSS in parallel was only validated at slow speeds and without considering the energy required to adjust the VSS.

Furthermore, it is worth to emphasize that up to now on the aforementioned works seeking to exploit the robot natural dynamics, accuracy along the full robot trajectory is imposed in the motion strategies. Nevertheless, in a pick-and-place operation typically involving to undergo from a point A of *pick* to a point B of *place*, it is required only to ensure high accuracy in the boundary positions (A and B). This means that there is not accuracy restriction on the motion planner connecting these boundary points, except collisions or external environment, as long as it is the most energy-efficient.

Therefore, the aim of this thesis is to reduce the energy consumption for *high-speed pick-and-place robots* by studying the actuation principle based on VSS *in parallel* to the motors, contrary to [Jafari 2011] in which they were mounted in series, as said previously.

By placing the VSS in parallel, as it was done in [Goya 2012] for slow speeds, we will ensure direct power connection between the motor and links of the robot (and thus to have accuracy in the boundaries at *high-speeds*), and also to have tunable energy storage through the VSS. Additionally, contrary to what was done in [Jafari 2011][Goya 2012], we will deal with the minimization of the energetic losses from *the full actuation chain*, i.e., both the parallel robot joints motors and the variable stiffness springs motors. Moreover, different to what it has been done in [Goya 2012], in which the authors proposed to find motion profiles for the stiffness rather than the variable stiffness joints, we will directly generate the joint trajectories for the motors that actuate the VSS from the dynamic model, so that we can exploit as best as possible the natural dynamics of the robot performing high-speed pick-and-place tasks. It is worth mentioning that in what follows along this manuscript, we will refer to the term *variable stiffness* in the sense of having a variable force/displacement spring for the VSS. This means that the spring stiffness constant will remain unmodified, and the VSS force/displacement relation will be controlled thanks to the variation of the spring equilibrium positions.

This thesis is thus divided as follows: Chapter 2 presents the modeling of the actuation chain used for high-speed robots based on variable stiffness springs in parallel to the motors that actuate the links of the pick-and-place robots. In addition to that, a model of energetic losses is formulated considering the overall motor drive system. This to have a way to estimate the energy consumed by the motors in their different operation modes considering all the energetic losses of the full actuation chain. In Chapter 3, we will propose an algorithm based on a boundary value problem (BVP) which will seek to exploit the natural dynamics of the robot-plus-VSS, so that the input torques and therefore the energy consumption of the full actuation chain can be drastically reduced. Chapter 4 presents the prototype and the experimental results of our new energy-efficient actuation concept for fast quasi-periodic pick-and-place-like motions. In Chapter 5, an extension of the concept of exploiting the natural dynamics of robots is applied to robotic systems in other applications. Finally, the conclusions and the perspectives of the thesis work will be discussed.

1.4 Summary

In the first Section of this Chapter, we have presented a short historical review of the evolution of industrial robots, going from the very first robot manipulators performing not so highly dynamic tasks in the industry, to industrial robots performing high-speed operations, such as pick-and-place tasks. We have seen that the latter being a highly dynamic operation, an enormous amount of energy is required to move and stop the robot. This mainly occurs when achieving a desired high speed since a large amount of energy must be brought to make the robot move, and then this energy is dissipated to stop the robot in the braking phase. This is not efficient at all.

In Section 1.2, it was shown that the conventional technique to reduce the energy consumption at high-speeds consists in designing lightweight robot architectures, thus allowing the use of less powerful actuators. However, designing a lightweight robot structure may lead to worsen the robot stiffness, affecting the accuracy of the robot. Additionally, it was shown that on the attempt of reducing the energy consumption of pick-and-place robots, some researchers have developing classical motion planners that do not full exploit the natural dynamics of the robots, and therefore the reduction of energy consumption is limited up to a certain percentage.

It was additionally shown that recently a promising solution for reducing the energy consumption of pick-and-place robots based on the use of compliant actuation has been introduced. It was shown that the use of VSAs allows to tune the stored potential energy in springs arranged in series to the motors in order to adapt to different tasks. They were first used in applications, such as human-robot interaction or walking robots, nevertheless, they have been recently introduced to pick-and-place robots. Finally, in order to overcome the issue of having serial configuration of springs and motors, the parallel compliant actuation have been recently used. This type of actuation consists of a constant stiffness springs in parallel to the actuators. Even if this solve the problem of accuracy of the VSAs, the level of compliance to adapt to quasi-periodic tasks is limited by the spring constant.

Finally in Section 1.3, we have presented our proposition, which will be developed along this manuscript, to increase the energy efficiency of high-speed robots. This will be done basically by using the actuation concept based on VSS in parallel to the motors, combined with a strategy to exploit the natural dynamics at high-speeds. Let us thus, in the following Chapter, present the actuation concept based on VSS in parallel to the motors. This actuation principle seeks to ensure tunable energy storage so that it is possible to put the system near to a resonance mode for fast quasi-periodic motions and to assure load balancing at high-speeds, thus not losing the accuracy of high-speed robots.

CHAPTER 2

Dynamic and power consumption modeling of an energy-efficient high-speed robot

2.1. *Actuation concept based on parallel variable stiffness springs* p. 46
2.2. *Dynamic analysis of the parallel configuration of variable stiffness springs with the actuated links of parallel robots* p. 54
2.3. *Energy consumption modeling* p. 59
2.4. *Simulation of physical models and identification of preponderant energetic losses* p. 69
2.5. *Summary* p. 74

This Chapter is dedicated to present the new actuation concept of using variable stiffness springs in parallel to the robot actuated links in order to increase energy efficiency for fast quasi-periodic motions. Firstly, the actuation concept is presented and the expected advantages in terms of energy efficiency are given. In addition to that, the architecture description of this new variable stiffness actuation chain will be defined, both for the cases of linear springs and for torsional springs.

A basic example on a one-degree-of-freedom robot with a spring in parallel is presented in order to analytically demonstrate the resonance aspects of using parallel elastic actuation. This to show the potential of using springs in parallel for exploiting the natural dynamics, and thus for increasing the energy efficiency.

The second part of this Chapter is devoted to present the computations for the dynamic modeling of parallel robots with variable stiffness springs in parallel. In addition to that, in order to estimate the energy consumed on a robot when performing high-speed motions, an energy consumption model is proposed and simulations are performed. It is worth mentioning that these simulations will allow to identify in which operation modes of the robot motors most of the energy is lost.

2.1 Actuation concept based on parallel variable stiffness springs

In order to increase the energy efficiency while ensuring the accuracy when performing high-speed pick-and-place operations, the purpose of this thesis is to dynamically exploit a new actuation concept based on the use of parallel arrangement of variable stiffness springs (VSS) and motors for high-speed robots (See Fig. 2.1 and Fig. 2.2). The VSS are used as energy storage for carrying out the reduction of the energy consumption and their parallel configuration with the motors ensures the load balancing at high-speed without losing the accuracy of the robot.

The use of parallel configuration of springs and motors, thus, allows to obtain interesting properties for improving energy efficiency at high-speeds, they can be summarized below:

- By placing the VSS in parallel to the actuated links of the parallel robot, we will ensure direct power connection between the motors and the links of the robot, and thus to have accuracy at high-speeds. Furthermore, contrary to the work in [Jafari 2011], in which the stiffness cannot be controlled simultaneously with the link positions because the VSS are placed in series with the motors, here, thanks to the addition of VSS in parallel, we ensure simultaneous accuracy and tunable stiffness. This decoupling property allows to vary the VSS stiffness while the robot moves. It should be noted that since we use motors to control the force/displacement relation of the VSS, we induce a force oscillator in order to exploit the natural dynamics. Additionally, contrary to works in [Jafari 2011][Goya 2012], we consider the energy consumed by the motors that adjust the VSS, considering in this way, the energetic losses in the full actuation chain;

- By adding the spring in parallel with tunable stiffness, it is possible to have control of the stored spring potential energy to be released per cycle of a given quasi-periodic pick-and-place motion. We expect that this will allow to exploit the natural dynamics of high-speed robots, thus drastically reducing the energy consumption;

- With the VSS in parallel, the required efforts to move the links of the high-speed manipulator are distributed between the motor that actuates the link and the parallel spring, thanks to its stored potential energy.

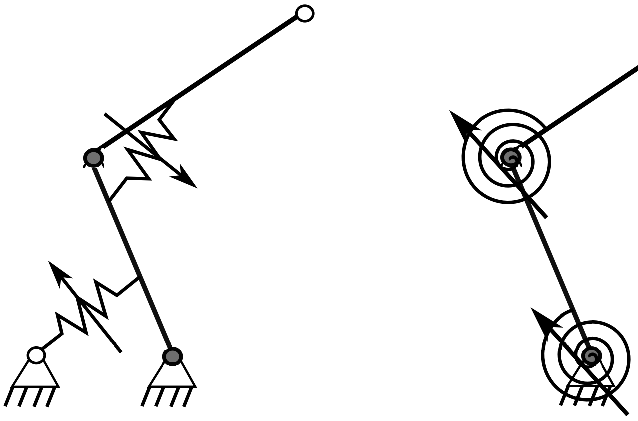

Figure 2.1: On the left, a 2R serial robot with variable stiffness linear springs in parallel arrangement with the links is shown. On the right the same 2R serial robot with variable stiffness torsional springs is presented (the grey circles denote the actuated joints).

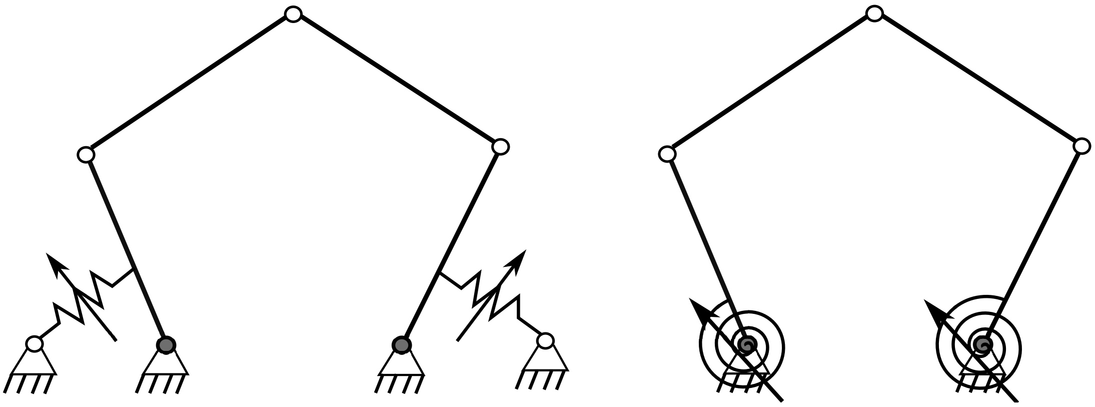

Figure 2.2: On the left, a five-bar mechanism with variable stiffness linear springs in parallel arrangement with the actuated links is shown. On the right the same parallel robot with variable stiffness torsional springs is presented (the grey circles denote the actuated joints).

2.1.1 Architecture description of variable stiffness springs

In this Subsection, the architecture description of the new actuation concept based on variable stiffness springs in parallel will be explained. According to Fig. 2.3 and Fig. 2.4, and to Fig. 2.5 and Fig. 2.6, we will consider a general serial manipulator and a parallel manipulator, respectively. Both types of architectures are composed of a rigid fixed base, which is attached to the global frame $\mathcal{F}_0(\boldsymbol{O}, \mathbf{x}_0, \mathbf{y}_0, \mathbf{z}_0)$, a rigid moving platform, attached to $\mathcal{F}_p(\boldsymbol{P}, \mathbf{x}_p, \mathbf{y}_p, \mathbf{z}_p)$, and n active joint variables (n corresponding as well to the number

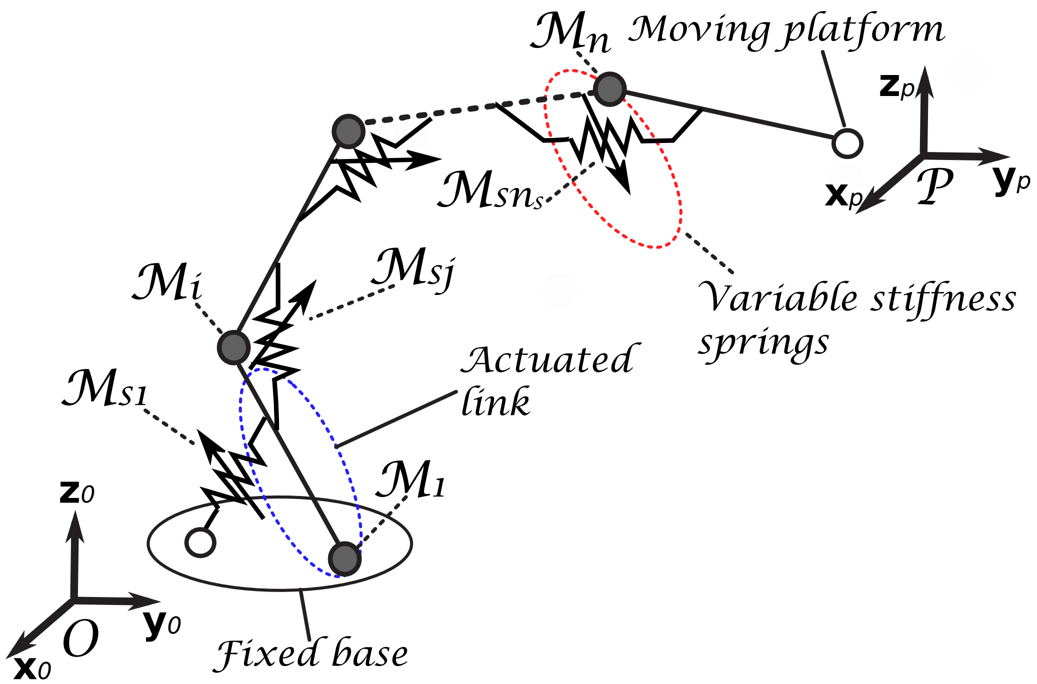

$\mathcal{M}_n$
Moving platform
$\mathbf{z}_p$
$\mathbf{x}_p$
$\mathcal{P}$
$\mathbf{y}_p$
$\mathcal{M}_{sn_s}$
$\mathcal{M}_i$
$\mathcal{M}_{sj}$
Variable stiffness springs
Actuated link
$\mathcal{M}_{s1}$
$\mathcal{M}_1$
$\mathbf{z}_0$
$\mathbf{y}_0$
O
$\mathbf{x}_0$
Fixed base

Figure 2.3: A general serial robot with variable stiffness linear springs in parallel configuration with the links.

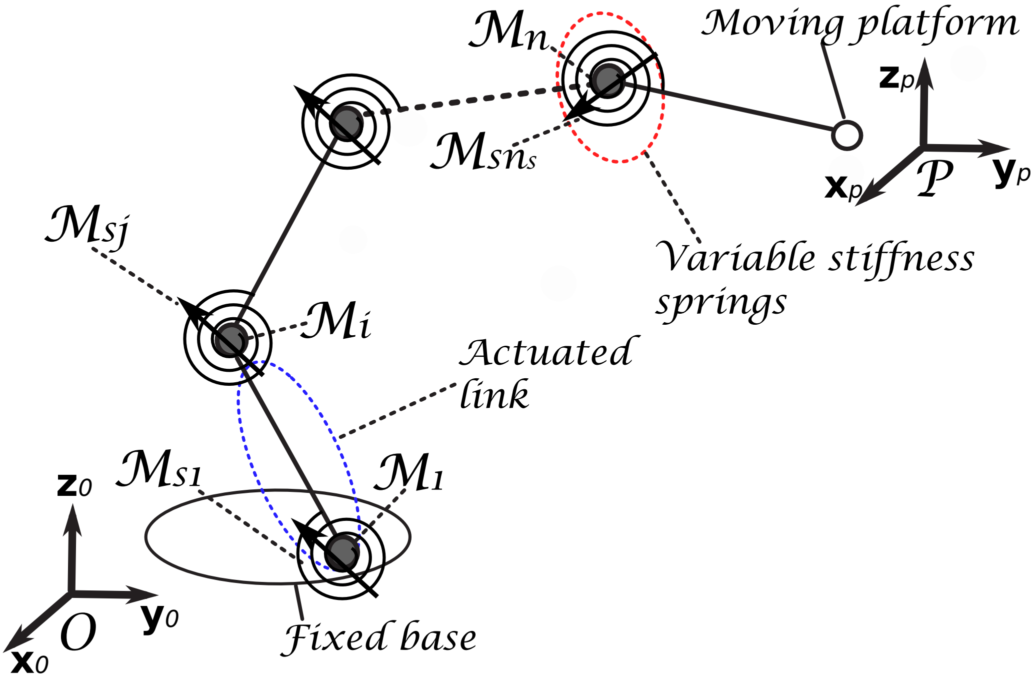

$\mathcal{M}_n$
Moving platform
$\mathbf{z}_p$
$\mathcal{M}_{sn_s}$
$\mathbf{x}_p$
$\mathcal{P}$
$\mathbf{y}_p$
$\mathcal{M}_{sj}$
Variable stiffness springs
$\mathcal{M}_i$
Actuated link
$\mathbf{z}_0$
$\mathcal{M}_{s1}$
$\mathcal{M}_1$
$\mathbf{y}_0$
O
$\mathbf{x}_0$
Fixed base

Figure 2.4: A general serial robot with variable stiffness torsional springs in parallel configuration with the links.

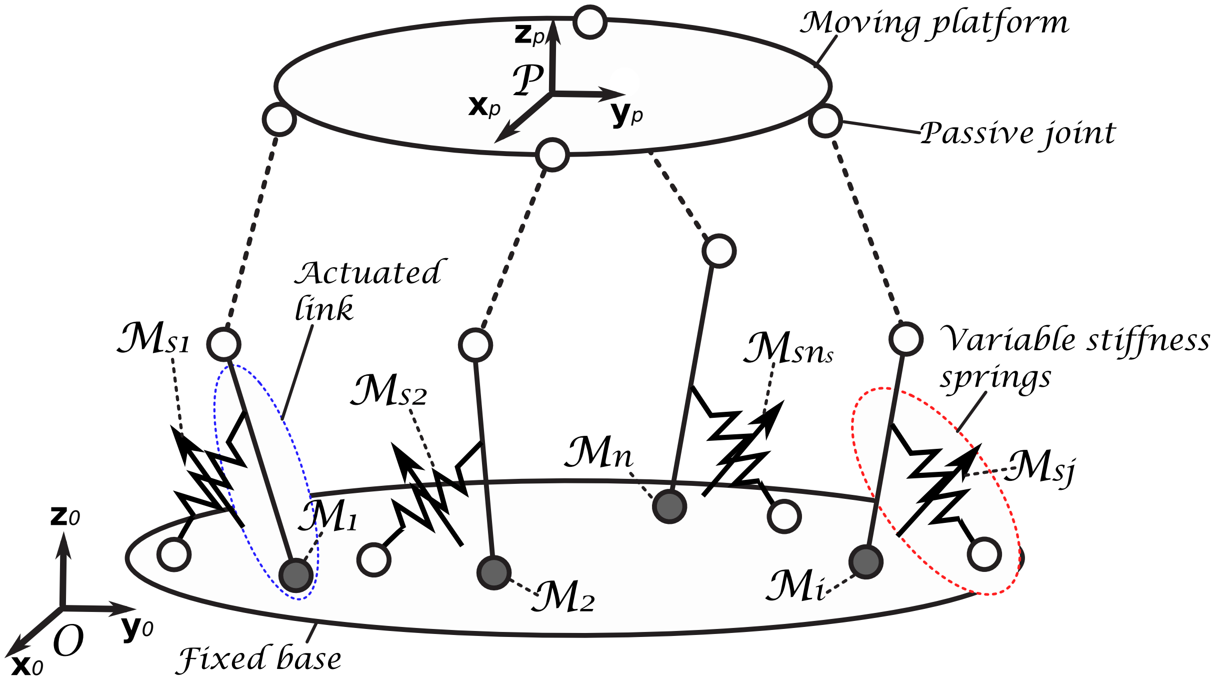
Moving platform
$\mathbf{z}_p$
$\mathcal{P}$
$\mathbf{x}_p$
$\mathbf{y}_p$
Passive joint
Actuated link
$\mathcal{M}_{s1}$
$\mathcal{M}_{s2}$
$\mathcal{M}_{sn_s}$
Variable stiffness springs
$\mathcal{M}_{sj}$
$\mathcal{M}_n$
$\mathcal{M}_1$
$\mathcal{M}_2$
$\mathcal{M}_i$
$\mathbf{z}_0$
O
$\mathbf{y}_0$
$\mathbf{x}_0$
Fixed base

Figure 2.5: A general parallel robot with variable stiffness linear springs in parallel configuration with the actuated links.

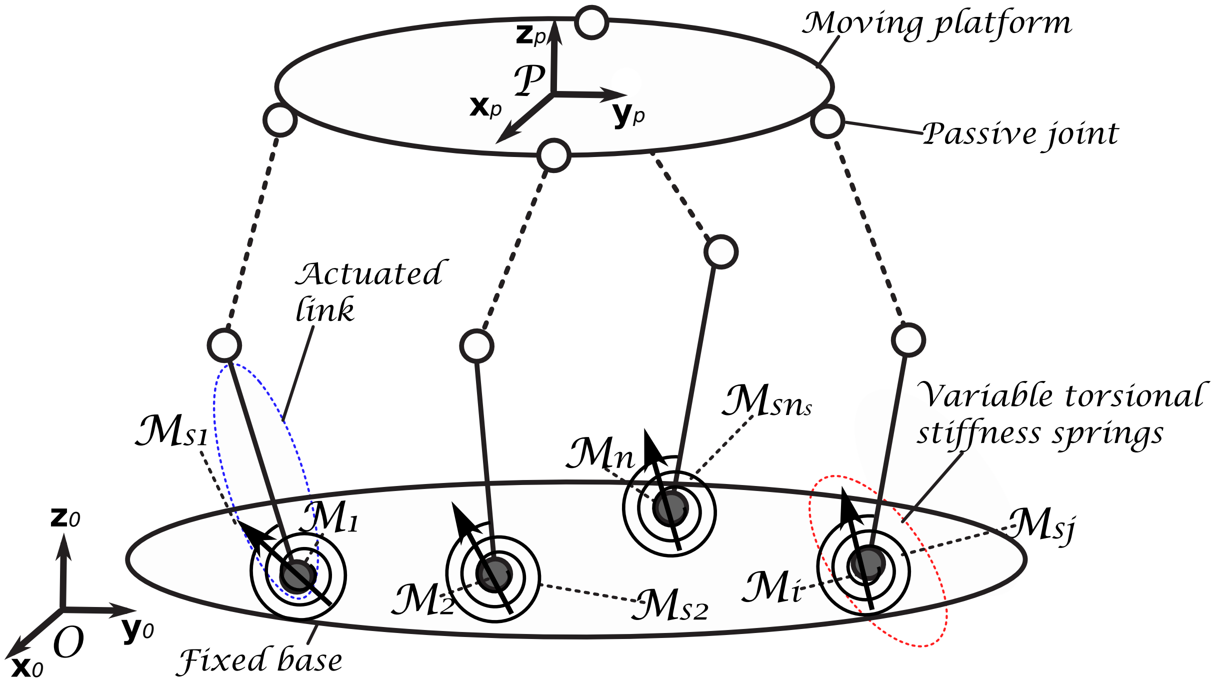
Moving platform
$\mathbf{z}_p$
$\mathcal{P}$
$\mathbf{x}_p$
$\mathbf{y}_p$
Passive joint
Actuated link
$\mathcal{M}_{s1}$
$\mathcal{M}_{sn_s}$
Variable torsional stiffness springs
$\mathcal{M}_n$
$\mathcal{M}_1$
$\mathcal{M}_{sj}$
$\mathcal{M}_2$
$\mathcal{M}_{s2}$
$\mathcal{M}_i$
$\mathbf{z}_0$
O
$\mathbf{y}_0$
$\mathbf{x}_0$
Fixed base

Figure 2.6: A general parallel robot with variable stiffness torsional springs in parallel configuration with the actuated links.

of legs). For the variable stiffness system, we will consider n_s variable stiffness joints in parallel to the actuated links of the serial and parallel manipulators, with linear springs in Fig. 2.3 and Fig. 2.5, and with torsional springs in Fig. 2.4 and Fig. 2.6, respectively. It is worth noticing that as depicted from Fig. 2.3 to Fig. 2.6, the variable stiffness springs are placed in parallel to the robot actuated links, thus ensuring direct power connection between motors and links of the robot.

The parameterization of the different bodies of the kinematic architectures from Fig. 2.3 to Fig. 2.6 is defined as follows:

- P represents the moving platform;
- M_i represents the motors that actuate the n parallel robot actuated links, and $i = 1, ..., n$;
- M_{s_j} represents the motors that actuate the n_s variable stiffness joints, and $j = 1, ..., n_s$.

It is important to mention that the actuation concept based on VSS is applicable to both, serial robots and parallel robots. Nevertheless, since most of the fast pick-and-place operations in industrial applications are performed by using parallel mechanisms (due to greater rigidity, higher speed and higher accuracy), in what follows in Chapters 3 and 4, the algorithm developments will be focused on parallel robots with VSS.

2.1.2 Resonance aspects of springs in parallel to motors: Case study with 1-DOF robot

As mentioned in Chapter 1, typically, when performing high-speed pick-and-place operations, repeatability and minimum-time pick-and-place execution cycles are the two main goals to be achieved by a robot manipulator. That is why, the use of a conventional stiff actuator, i.e. classical motor-load connection, combined with a dedicated joint/task controller bring the possibility to achieve an accurate trajectory tracking in those repetitive tasks. A well-established control principle is the use of dynamic-model-based control, such as the classical Computed Torque Control [Spong 1989][Pagis 2015a][Khalil 2004] in which the high nonlinearities typical for parallel robots are compensated by control action. Even if the combination of conventional stiff actuation and torque control schemes have shown its efficiency to minimize the deviation of the joint motion with respect to the

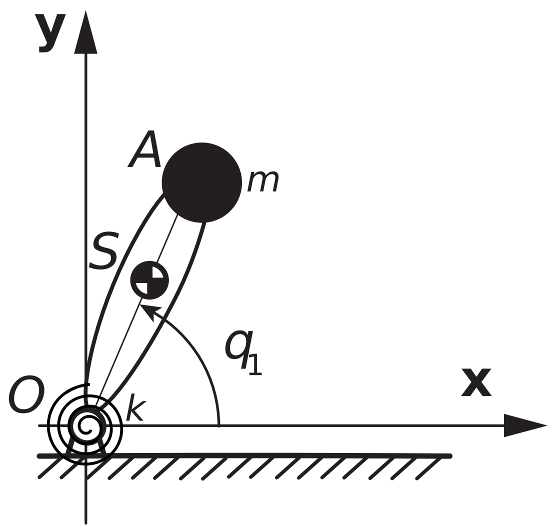

Figure 2.7: one-degree-of-freedom robot with torsional spring of constant k in parallel.

desired one, thus having a good tracking, an enormous amount of energy is required to make the robot move at high-speeds. This mainly occurs when achieving a desired high speed since a large amount of energy must be brought to make the robot move, and then this energy is dissipated to stop the robot [Brossog 2015]. This is not efficient at all, it would be smarter to store the energy through the use of a passive elastic element.

For actively controlled systems that are required to oscillate at a constant amplitude and frequency, it is possible to find a unique set of spring constants, placed in parallel to the motors, such that the actively controlled system remains conservative, i.e. with a periodic exchange of kinetic and spring potential energy. For instance, let us consider the actively controlled planar one-degree-of-freedom (1-DOF) robot with torsional spring in parallel from Fig. 2.7. Here, the robot is moving into the ($\mathbf{x}O\mathbf{y}$) plane, orthogonal to the gravity field. The actuation of the robot is provided by q_1. It has a link length l_{OA}, a length to the center of mass l_{OS}, a payload mass m, a link mass m_1, a link inertia zz_1 in O and a spring constant k. The equation of motion for this system reads simply:

$$\tau = (zz_1 + m_1 l_{OS}^2 + ml^2)\ddot{q}_1 + kq_1 \tag{2.1}$$

For a prescribed oscillatory motion evolving on time t with constant amplitude β and angular velocity ω described by the following expressions:

$$q_1(t) = \beta \mathrm{sin}(\omega t) \tag{2.2}$$

$$\dot{q}_1(t) = \omega\beta\text{cos}(\omega t) \tag{2.3}$$

$$\ddot{q}_1(t) = -\omega^2\beta\text{sin}(\omega t) \tag{2.4}$$

The actuator effort in (2.1) follows from the principle of inverse dynamics by:

$$\tau(t) = (-(zz_1 + m_1 l_{OS}^2 + ml^2)\omega^2 + k)\beta\text{sin}(\omega t) \tag{2.5}$$

Thus, for a value of spring constant $k = (zz_1 + m_1 l_{OS}^2 + ml^2)\omega^2$, and neglecting the friction, the actively controlled one-degree-of-freedom robot will remain conservative, thus vanishing the input torques τ. For pick-and-place robots, however, it is not the same case due to the fact that the tasks are defined by pseudo-periodic oscillatory motions, where the amplitudes and frequencies of oscillation may vary. This would mean that for each pseudo-frequency $f = \omega/2\pi$ of the pick-and-place cycles, a different set of spring constants k would be required. Physically, this would mean to change the springs at each variation of cycle time of the pick-and-place motion, which would result of low practicability. That is why, by using variable stiffness springs we try to maximize the spectrum of achievable amplitudes and frequencies of pick-and-place motions, which enforce the system to remain conservative, thus exploiting the aforementioned resonance principle for fast quasi-periodic tasks. In order to show this concept, let us now consider a planar 1-DOF robot with torsional VSS in parallel evolving into the $(\mathbf{x}O\mathbf{y})$ plane, orthogonal to the gravity field (See Fig. 2.8). The additional actuation from the motor that varies the equilibrium position of the VSS, so that the stiffness changes, is parameterized by q_s. In addition to that, we will consider an inertia term J_s associated to the dynamics of the variable stiffness system. It should be noted that the dynamics associated to J_s has been always neglected in the literature review (See [Haddadin 2011][Jafari 2011][Goya 2012]), nonetheless, it might be of great importance when analyzing the energy consumption in the full actuation chain. By considering the additional variable stiffness joint variable q_s from the VSS in parallel to the 1-DOF robot, the motion equation in (2.1) becomes:

$$\tau = (zz_1 + m_1 l_{OS}^2 + ml^2)\ddot{q}_1 + k(q_1 - q_s) \tag{2.6}$$

and the dynamics of the VSS system is expressed by:

$$\tau_{vss} = J_s\ddot{q}_s - k(q_1 - q_s) \tag{2.7}$$

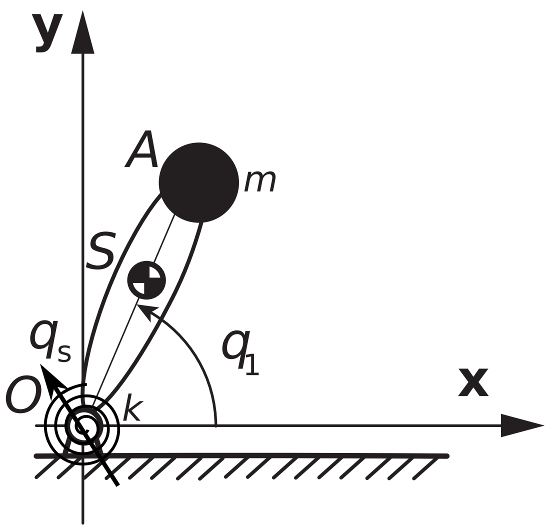

Figure 2.8: one-degree-of-freedom robot with VSS in parallel.

Considering the prescribed oscillatory motion for the 1-DOF joint variable (2.2)-(2.4), one could think of simply, in the same vein as for k, to compute q_s for $\tau = 0$ from (2.6):

$$q_s = \frac{(zz_1 + m_1 l_{OS}^2 + ml^2)\ddot{q}_1 + kq_1}{k} \tag{2.8}$$

$$q_s = \frac{(-(zz_1 + m_1 l_{OS}^2 + ml^2)\omega^2 + k)}{k} \beta \sin(\omega t) \tag{2.9}$$

Even if expression (2.9) ensures that for any pseudo-frequency of the pick-and-place cycles, the 1-DOF robot will remain conservative, i.e. with $\tau = 0$, the input efforts to modify the VSS grouped in τ_{vss} are not ensured to be minimum, unless J_s is time-variant, which is not the case here. This means that, if we seek to exploit the resonance principle for the full actuation chain, i.e. the robot and the VSS, it is thus necessary to find a combined motion of q_1 and q_s, such that τ and τ_{vss} are simultaneously minimized, i.e. to optimally distribute the efforts τ and τ_{vss} in the actuation chain, while respecting the desired amplitude β and angular velocity ω of the robot task. This should be possible since the force/displacement relation $k(q_1 - q_s)$, associated to the VSS optimal stiffness, is dependent on q_1 and q_s, which are controllable variables (since we propose a forced oscillator). That is why in order to exploit the force/displacement relation, so that we can minimize the input efforts of the full actuation chain, i.e. robot-plus-VSS, and therefore reducing the energy consumption, in Chapter 3, a method for exploiting the natural dynamics in the full actuation chain will be formalized. This will permit to exploit the aforementioned resonance principle for any pseudo-frequency of a given pick-and-place task, while keeping bounded the input efforts required to adjust the VSS, which in the literature review have been always neglected.

2.2 Dynamic analysis of the parallel configuration of variable stiffness springs with the actuated links of parallel robots

2.2.1 Dynamic modeling of parallel robots

In order to compute the dynamic model of parallel robots with VSS in parallel, we will firstly compute the dynamic model of parallel robots and then the dynamic model of the VSS. The methodology presented in [Khalil 2004][Briot 2015b] will be used to compute the dynamic model of parallel robots. The main idea is to calculate the dynamic model in two steps:

1. The first step consists in virtually opening the parallel robot closed-loops so that the platform is virtually disassembled from the rest of the structure (See Fig. 2.9). In this way, two systems will be obtained: *i*) a tree structure in which each leg joint is virtually actuated, and *ii*) a free body: the platform. Then, the dynamic model of each system is computed.

2. The second step consists on closing the loops by using loop-closure equations and Lagrange multipliers, which represent the joint constraints applied to the platform that are required to close the loops of the real robot.

2.2.1.1 Dynamic model of tree-loop robots

In order to develop the dynamic equations of a parallel manipulator based on the aforementioned steps, we will assume a parallel robot composed of n degrees of freedom driven by n active joints (with M_i motors from the parameterization). The position and velocity of the parallel robot can be described as:

- $\mathbf{q}_a$ and $\dot{\mathbf{q}}_a$ representing the n-dimensional vectors of active joint variables and of active joint velocities, respectively, and whose position and velocity elements go from q_{a_i} to q_{a_n}, and from $\dot{q}_{a_i}$ to $\dot{q}_{a_n}$, respectively;

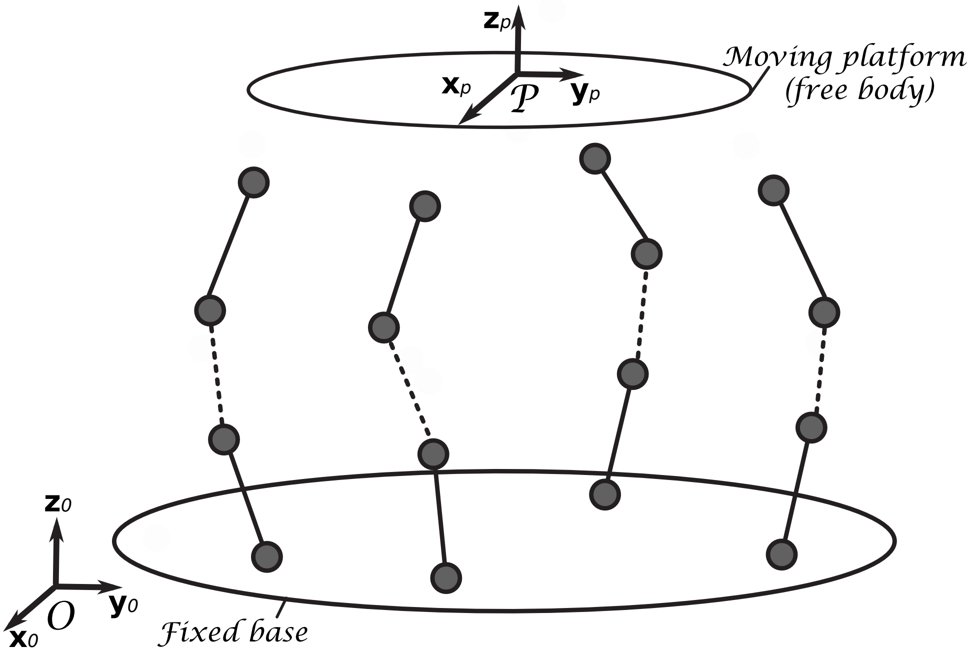

Figure 2.9: Virtual tree structure

- $\mathbf{x}$ and $\dot{\mathbf{x}}$ representing the n-dimensional vectors of platform pose and of its time derivatives, respectively.

All these variables are linked through the loop-closure equations of the real robot [Merlet 2006], which directly relate the displacements $\mathbf{q}_a$ of the active joints to the moving platform coordinates $\mathbf{x}$ by the following constraint equation:

$$\mathbf{h}(\mathbf{x}, \mathbf{q}_a) = \mathbf{0} \tag{2.10}$$

Once the values of $\mathbf{x}$ are found as functions of $\mathbf{q}_a$, it is possible to solve the inverse geometric problem [Merlet 2006]. Furthermore, by differentiating expression (2.10), one can compute the input-output kinematic constraint that relates $\dot{\mathbf{x}}$ with the active joint velocities $\dot{\mathbf{q}}_a$, and which will later serve to reassemble the virtual structure:

$$\mathbf{A}\dot{\mathbf{x}} + \mathbf{B}\dot{\mathbf{q}}_a = \mathbf{0} \tag{2.11}$$

where $\mathbf{A}$ and $\mathbf{B}$ are the $(n \times n)$ parallel and serial kinematic Jacobian matrices, respectively [Merlet 2006].

By using the Lagrange formalism, the dynamics related to the virtual efforts of the open-loop tree structure can be written as follows:

$$\boldsymbol{\tau}_{ta} = \frac{\mathrm{d}}{\mathrm{d}t}\left(\frac{\partial L_t}{\partial \dot{\mathbf{q}}_a}\right)^T - \left(\frac{\partial L_t}{\partial \mathbf{q}_a}\right)^T \tag{2.12}$$

where:

- L_t represents the Lagrangian of the virtual tree structure and its value depends on the active joints ($\mathbf{q}_a$, $\dot{\mathbf{q}}_a$);
- $\boldsymbol{\tau}_{ta}$ is the $(n \times 1)$ vector, which corresponds to the virtual input efforts in the actuated joints of the parallel robot related to the Lagrange L_t of the virtual tree structure.

Then, thanks to the Lagrangian formalism, the dynamics of the moving platform can be computed as follows:

$$\mathbf{w}_p = \frac{\mathrm{d}}{\mathrm{d}t}\left(\frac{\partial L_p}{\partial \dot{\mathbf{x}}}\right)^T - \left(\frac{\partial L_p}{\partial \mathbf{x}}\right)^T \tag{2.13}$$

where:

- L_p represents the Lagrangian of the platform and its value depends on the platform pose and of its time derivatives ($\mathbf{x}$, $\dot{\mathbf{x}}$);
- $\mathbf{w}_p$ is the $(n \times 1)$ vector, which corresponds to the wrench of the platform expressed in the base frame and related with the Lagrange L_p of the free moving platform.

2.2.1.2 Dynamic model of parallel robots

Since the dynamic model of the virtual tree structure and of the free moving platform do not take into account the closed-loop characteristics of the parallel robot, for reassembling the tree structure and the free moving platform in order to compute the dynamic model of the real parallel robot, it is thus necessary to take into account the loop-closure constraints. In order to do so, Lagrange multipliers $\boldsymbol{\lambda}$ are used to compute the input torques of the closed-loop structure [Briot 2015b]. The torques can thus be computed in relation of the Lagrange multipliers $\boldsymbol{\lambda}$ by:

$$\boldsymbol{\tau} = \boldsymbol{\tau}_{ta} - \mathbf{B}^T\boldsymbol{\lambda} \tag{2.14}$$

$$\mathbf{w}_p = \mathbf{A}^T\boldsymbol{\lambda} \tag{2.15}$$

where

- $\boldsymbol{\tau}$ is the n-dimensional vector of the robot input efforts;
- $\boldsymbol{\lambda}$ is the n-dimensional vector of Lagrange multipliers, and it groups the wrenches applied by the virtual tree structure on the platform so that the virtual structure can have the same motion as the parallel robot.

Then, considering matrix $\mathbf{A}$ to be full rank (in this work it will be always the case), i.e. out of Type 2 singularities [Gosselin 1990], the general solution of the dynamic model can be computed by obtaining $\boldsymbol{\lambda}$ from expression (2.15), and then substituting it into equation (2.14):

$$\boldsymbol{\tau} = \boldsymbol{\tau}_{ta} - \mathbf{B}^T \mathbf{A}^{-T} \mathbf{w}_p \tag{2.16}$$

which, according to [Briot 2015b], can also be written under the form:

$$\boldsymbol{\tau} = \mathbf{M}\ddot{\mathbf{q}}_a + \mathbf{c}(\mathbf{q}_a, \dot{\mathbf{q}}_a) + \mathbf{f}_a \tag{2.17}$$

where $\mathbf{M}$ is an $(n \times n)$ definite positive matrix of inertia depending on the active joints coordinates $\mathbf{q}_a$ and platform coordinates $\mathbf{x}$. $\mathbf{c}$ is an n-dimensional vector of Coriolis, centrifugal and gravitational effects and its value depends on the active joint coordinates $\mathbf{q}_a$, and their time derivatives $\dot{\mathbf{q}}_a$. $\mathbf{f}_a$ is an n-dimensional vector grouping the active joint friction terms.

2.2.2 Dynamic modeling of variable stiffness springs

Before developing the dynamic modeling of the VSS, it is worth mentioning that in the scope of this thesis, it has been chosen to use torsional springs for the VSS. This is done due the fact that, as it will be shown in Chapter 4, the experimental benchmark is composed of only revolute joints. Thus, since pure torsional springs are deformed with only the application of torques (same for actuating revolute joints), the VSS actuation would be more motion-natural by using torsional springs in the full actuation chain (See Fig. 2.10).

In what follows, for the dynamic model of the VSS, we will refer to $\mathbf{q}_s$ and $\dot{\mathbf{q}}_s$ as the n_s-dimensional vectors of variable stiffness joint variables and of variable stiffness joint velocities, respectively, and whose position and velocity elements go from q_{s_j} to $q_{s_{ns}}$, and from $\dot{q}_{s_j}$ to $\dot{q}_{s_{ns}}$, respectively. n_s represents the additional VSS active joints, which based on the kinematic architecture of Fig. 2.6, are driven by M_{s_j} motors.

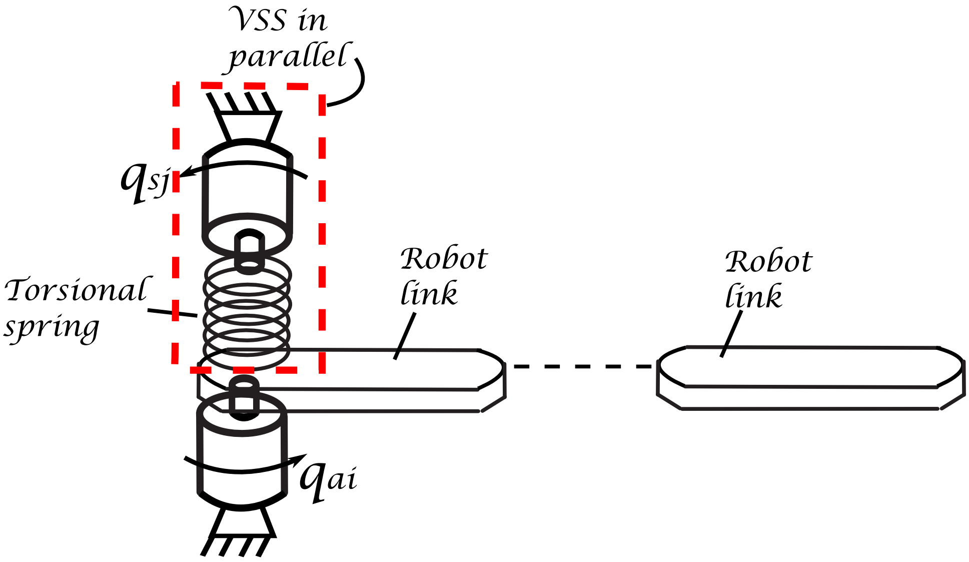

Figure 2.10: Power transmission system of variable stiffness springs in parallel to the motors. q_{a_i} and q_{s_j} represent the parallel robot joints and variable stiffness joints coordinates, respectively, and $i = 1, ..., n$, $j = 1, ..., n_s$.

For the dynamic modeling, let us consider a parallel robot with variable stiffness torsional springs in parallel to the actuated links (see Fig. 2.6). According to Fig. 2.10, the deformation of the torsional spring, and therefore the VSS stiffness, can be adjusted by means of q_{a_i}, due to the parallel coupling of spring and link, and by the additional actuated joint q_{s_j}.

By considering the effects of the elastic deformation of the springs (due to q_{a_i} and q_{s_j}) with their force-displacement relations, the dynamics in (2.17), become:

$$\boldsymbol{\tau} = \mathbf{M}\ddot{\mathbf{q}}_a + \mathbf{c}(\mathbf{q}_a, \dot{\mathbf{q}}_a) + \mathbf{f}_a + \boldsymbol{\tau}_s \tag{2.18}$$

where $\boldsymbol{\tau}_s$ is the n_s-dimensional vector of elastic torques associated to the VSS coupled to the robot in parallel, and whose analytic expression follows from the Lagrange formalism:

$$\boldsymbol{\tau}_s = \mathbf{K}(\mathbf{q}_a - \mathbf{q}_s) \tag{2.19}$$

where $\mathbf{K}$ is the $(n_s \times n_s)$ stiffness matrix, and the dynamics of the VSS is expressed by:

$$\boldsymbol{\tau}_{vss} = \mathbf{M}_s\ddot{\mathbf{q}}_s + \mathbf{h}_s(\mathbf{q}_s, \dot{\mathbf{q}}_s) + \mathbf{f}_s - \boldsymbol{\tau}_s \tag{2.20}$$

where $\mathbf{M}_s$ is an $(n_s \times n_s)$ definite positive matrix of inertia depending on the variable stiffness joints coordinates $\mathbf{q}_s$, and $\mathbf{h}_s$ is an n_s-dimensional vector of Coriolis, centrifugal and gravitational effects and its value depends on the variable stiffness joints coordinates $\mathbf{q}_s$ and their time derivatives $\dot{\mathbf{q}}_s$. $\mathbf{f}_s$ is an n_s-dimensional vector grouping the variable stiffness joint friction terms.

It is worth mentioning that later in Chapter 3, it will be shown that it is an advantageous property to have the acceleration terms from dynamic equations (2.18) and (2.20), decoupled from the matrices of inertia $\mathbf{M}$ and $\mathbf{M}_s$, respectively. This is due to the fact that the algorithm for exploiting the natural dynamics in Chapter 3 requires to express the dynamic equations in its decoupling form.

2.3 Energy consumption modeling

In order to study the energetic performance of the robot manipulators while performing high-speed motions, several consumption models have been formulated, such as in [Goya 2012]. Even if those models have been used to estimate the energy consumed for different tasks of robot manipulators, they are simplified models that take into account only the dissipated energy from resistive losses, thus underestimating the losses coming from the driver of the motor. That is why in this Section, a detailed power consumption model, which takes into account the motor-plus-driver losses, is formulated. In addition to that, we consider the power losses of the full actuation chain, i.e. the losses from the M_i motors that actuate the active joints of the robot, plus the M_{s_j} motors that actuate the VSS (see the parameterization of Section 2.1.1). For this work we consider direct-drive three-phase brushless motors to actuate the joints of the parallel robot and the variable stiffness joints (M_i, M_{s_j}, respectively), therefore avoiding energetic losses due to gearboxes.

2.3.1 Working principle of motor drive system

There are two main parts to be modeled in the three-phase brushless motor drive system: the driver and the motor. The electromechanical schematics of such motor drive systems vary from manufacturer to manufacturer depending on the type of driver for energizing each phase of the brushless motor. However, a general schematic, found in [Pillay 1989], can be synthesized according to Fig. 2.11, in which five sections can be identified in their electromechanical system:

- Three-phase rectifier: Converts the three-phase AC voltage from the input line supply to a DC voltage at the output, i.e. the DC bus voltage at the node connecting the capacitor and the braking resistance;

- Braking: It is composed of a capacitor C_s in parallel to a resistance R_{brake}. The capacitor store voltage to a specified limit when the current circulates in the opposite direction (braking), and the rest of the current is dissipated through the braking resistance when the switch in its line is closed;

- Voltage source inverter: It consists of a configuration of six-transistor-commutable bridge ($S_1, ...S_6$) that controls the energization of each phase of the brushless motor. Moreover, a freewheeling diode ($D_1, ...D_6$) is placed in parallel to each transistor in order to provide a path to release energy stored in the inductors L of each phase of the motor when they are being commuted;

- Three-phase brushless motor: The phases are placed in a Wye (Y-shaped) configuration that connects all the windings to a central point. Each phase has a resistance R and an inductor L in series as in any typical one-phase electric motor;

- External resistance: It can be placed optionally in the driver configuration in case higher loads must be handled by the driver system contributing to the dissipation of the energy (R_{ext}).

2.3.2 Modeling of the motor drive system

For the modeling of the complete motor drive system, the methodology presented in [Pillay 1989][Millman 1986] will be used. Firstly, the state space equations of the electric part of the motor (Fig. 2.12) are computed by considering the Ohm's and Kirchhoff's circuit laws [Chapman 1991] as follows:

$$\begin{bmatrix} V_A \\ V_B \\ V_C \end{bmatrix} = \begin{bmatrix} R & 0 & 0 \\ 0 & R & 0 \\ 0 & 0 & R \end{bmatrix} \begin{bmatrix} I_A \\ I_B \\ I_C \end{bmatrix} + \begin{bmatrix} L & 0 & 0 \\ 0 & L & 0 \\ 0 & 0 & L \end{bmatrix} \frac{d}{dt} \begin{bmatrix} I_A \\ I_B \\ I_C \end{bmatrix} + \begin{bmatrix} e_a \\ e_b \\ e_c \end{bmatrix} \tag{2.21}$$

where V_A, V_B, V_C are the phase voltages, I_A, I_B, I_C represent the stator phase currents and e_a, e_b, e_c are the back-electromotive forces (voltages) that opposes the change in current

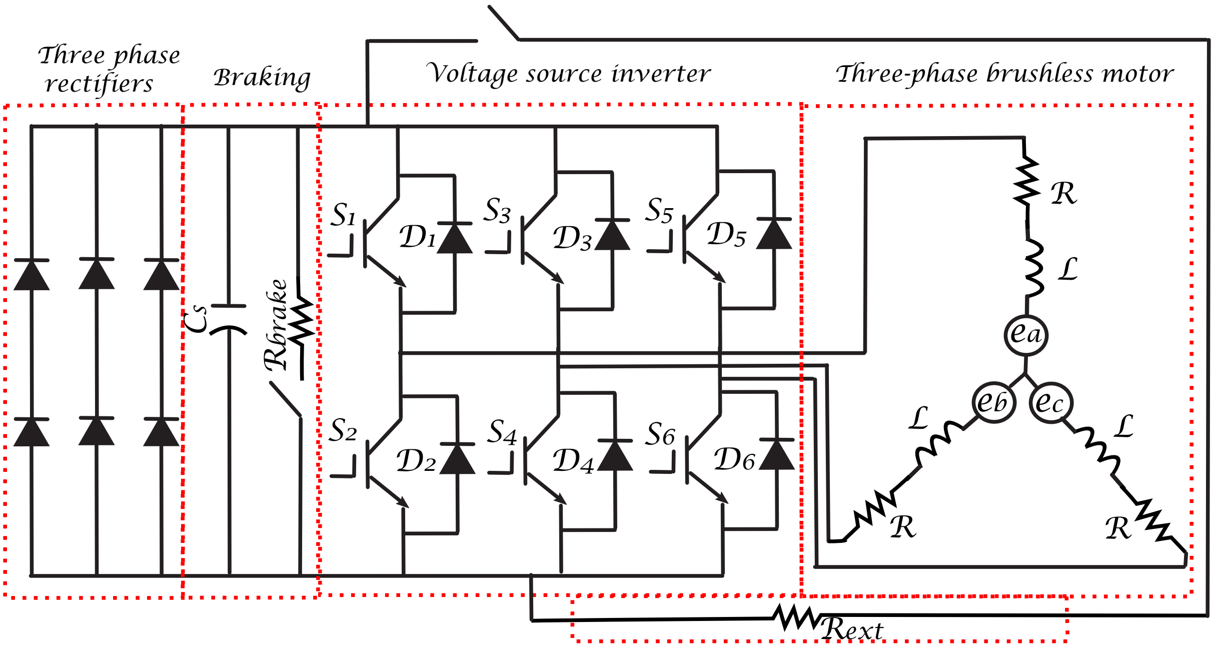
Three phase rectifiers
Braking
Voltage source inverter
Three-phase brushless motor
Cs
Rbrake
S1
D1
S3
D3
S5
D5
S2
D2
S4
D4
S6
D6
R
L
ea
eb
ec
L
R
L
R
Rext

Figure 2.11: Schematic of three-phase brushless motor drive system

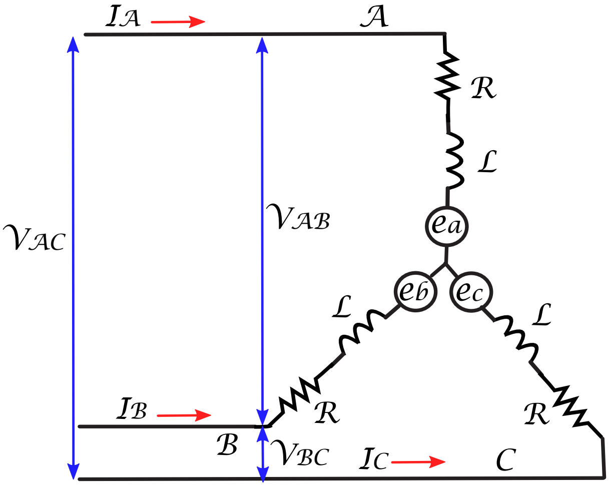
IA
A
R
L
VAC
VAB
ea
eb
ec
L
L
IB
R
R
B
VBC
IC
C

Figure 2.12: Electric circuit of the brushless motor with three phases

which induced it, they are displaced 120 degrees from phase to phase, and they can be modeled according to Fig. 2.13 as follows:

$$e_a = K_e f(\theta_e)\omega_m \tag{2.22}$$

$$e_b = K_e f(\theta_e - 2\pi/3)\omega_m \tag{2.23}$$

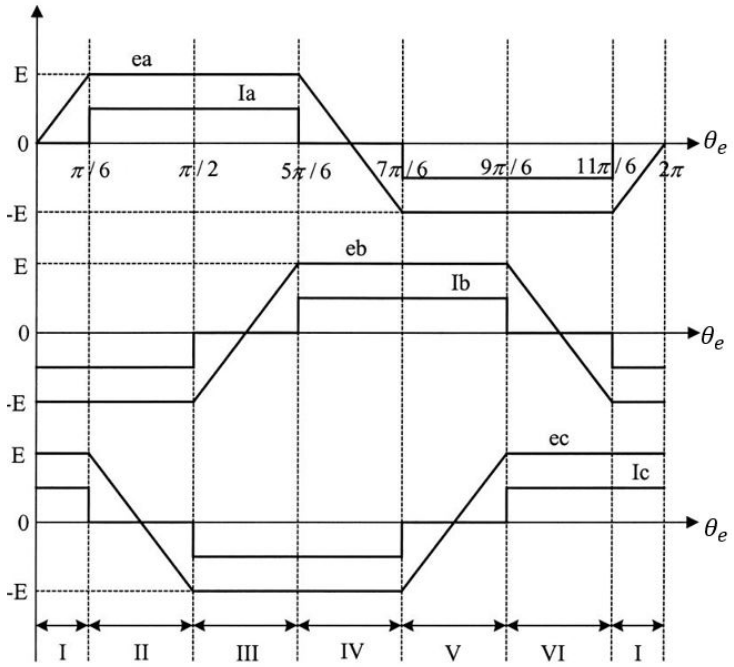

Figure 2.13: Electromotive forces [Chapman 1991]

$$e_c = K_e f(\theta_e + 2\pi/3)\omega_m \tag{2.24}$$

$$e_a = \begin{cases} (6E/\pi)\theta_e & (0 < \theta_e < \pi/6) \\ E & (\pi/6 < \theta_e < 5\pi/6) \\ -(6E/\pi)\theta_e + 6E & (5\pi/6 < \theta_e < 7\pi/6) \\ -E & (7\pi/6 < \theta_e < 11\pi/6) \\ (6E/\pi)\theta_e - 12E & (11\pi/6 < \theta_e < 2\pi) \end{cases} \tag{2.25}$$

$$e_b = \begin{cases} -E & (0 < \theta_e < \pi/2) \\ (6E/\pi)\theta_e - 4E & (\pi/2 < \theta_e < 5\pi/6) \\ E & (5\pi/6 < \theta_e < 9\pi/6) \\ -(6E/\pi)\theta_e + 10E & (9\pi/6 < \theta_e < 11\pi/6) \\ E & (11\pi/6 < \theta_e < 2\pi) \end{cases} \tag{2.26}$$

$$e_c = \begin{cases} E & (0 < \theta_e < \pi/6) \\ -(6E/\pi)\theta_e + 2E & (\pi/6 < \theta_e < \pi/2) \\ -E & (\pi/2 < \theta_e < 7\pi/6) \\ (6E/\pi)\theta_e - 8E & (7\pi/6 < \theta_e < 9\pi/6) \\ E & (9\pi/6 < \theta_e < 2\pi) \end{cases} \tag{2.27}$$

where K_e is the back electromotive force constant, $f(\theta_e)$ is a trapezoidal function, θ_e is the angle of phase commutation in the electrical cycle and ω_m is the rotor speed from the motor. It is worth mentioning that the trapezoidal commutation is common in high-speed applications or when high torques are required, which is the case for high-speed pick-and-place operations.

Once the back electromotive forces of the three phases have been fully parameterized, the line-to-line voltages can be computed as follows:

$$V_{AB} = V_A - V_B = R(I_A - I_B) + L\left(\frac{dI_A}{dt} - \frac{dI_B}{dt}\right) + (e_a - e_b) \tag{2.28}$$

$$V_{BC} = V_B - V_C = R(I_B - I_C) + L\left(\frac{dI_B}{dt} - \frac{dI_C}{dt}\right) + (e_b - e_c) \tag{2.29}$$

By Kirchoffs Current Law:

$$I_A + I_B + I_C = 0 \tag{2.30}$$

Substituting I_C into V_{BC}:

$$V_{BC} = R(I_A + 2I_B) + L\left(\frac{dI_A}{dt} + \frac{dI_B}{dt}\right) + (e_b - e_c) \tag{2.31}$$

Finally, based on [Pillay 1989], the electromagnetic torque induced in the brushless motor can be thus expressed as function of the three phases by:

$$\tau_e = \frac{e_a I_A + e_b I_B + e_c I_C}{\omega_m} \tag{2.32}$$

For modeling of the mechanical part of the motor drive system, let us consider one phase from the brushless motor with a load attached to it as shown in Fig. 2.14. From the principle of torque balance, the electromagnetic torque τ_e from expression (2.32) can be also expressed as function of the mechanical parameters in presence of external load

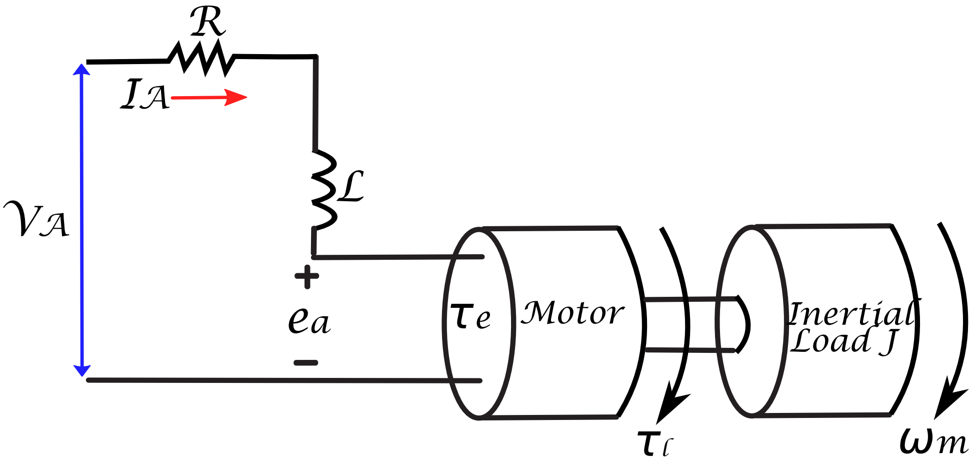

Figure 2.14: Motor scheme with load attached to the rotor.

J:

$$\tau_e = \tau_L + J\dot{\omega}_m + B\omega_m \tag{2.33}$$

where τ_L is the load torque, J is the inertial load, B is the damping factor.

Finally, from the aforementioned computations, the dynamics of the electromechanical system can be grouped by the following expression:

$$\begin{bmatrix} \dot{I}_A \\ \dot{I}_B \\ \dot{\omega}_m \end{bmatrix} = \begin{bmatrix} \frac{-R}{L} & 0 & 0 \\ 0 & \frac{-R}{L} & 0 \\ 0 & 0 & \frac{-B}{J} \end{bmatrix} \begin{bmatrix} I_A \\ I_B \\ \omega_m \end{bmatrix} + \begin{bmatrix} \frac{2}{3L} & \frac{1}{3L} & 0 \\ -\frac{1}{3L} & \frac{1}{3L} & 0 \\ 0 & 0 & \frac{1}{J} \end{bmatrix} \begin{bmatrix} V_{AB} - e_{ab} \\ V_{BC} - e_{bc} \\ \tau_e - \tau_L \end{bmatrix} \tag{2.34}$$

2.3.3 Operation modes

Based on the behavior that the load, connected to the electric motor, performs, it is possible to classify the motor motions into four different operation modes. These operation modes mainly differ one from each other depending on how the current circulates through the overall electric circuit of the motor drive system. These four operation modes are classified as follows:

- **Motoring mode:** Let us assume that in the one-phase motor subsystem of Fig. 2.14, initially running at no-load steady-state conditions, is attached an external inertial load. Since the rotor was initially at steady state, the application of a load will result in a net torque $\tau_{net} = \tau_L - \tau_e$. The effect of this load torque will be to

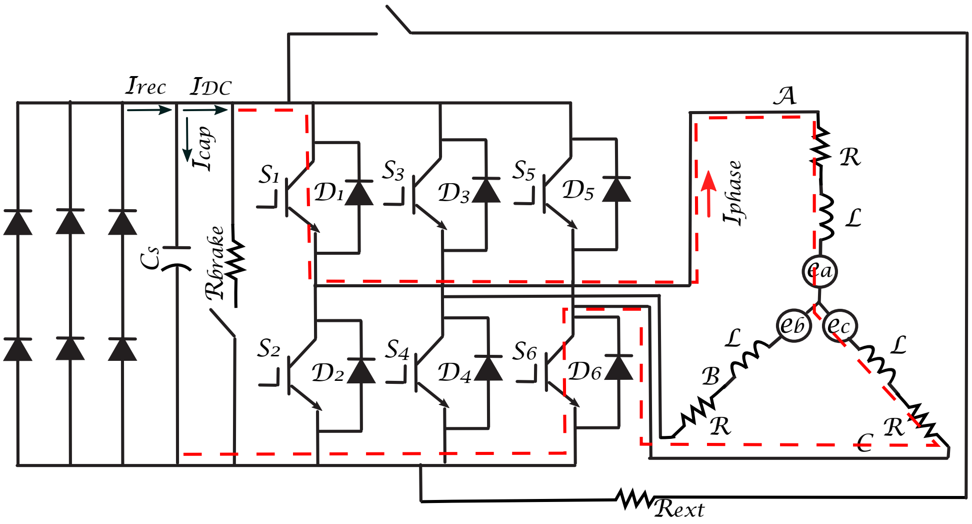

Figure 2.15: Motoring mode

drop the induced voltage e_a, thus increasing the current flow I_A:

$$I_A \uparrow = \frac{V_A - e_a \downarrow}{R} \tag{2.35}$$

The result of this physical phenomena is that the induced electromagnetic torque τ_e will be in the direction of motion of the rotor, and power will be converted from electrical form to mechanical form, thus working as a motor (See Fig. 2.15).

- **Generating mode:** In the generating mode, the induced back electromagnetive force e_a will increase and be larger than the voltage V_A, which will result in reversing the current I_A as shown in Fig. 2.17, and it will recharge the capacitor until its storage capacity limit and then it will dissipate in the braking resistance R_{brake}.

- **Freewheeling motoring and generating modes:** This mode occurs mainly in the transition of changing the phases to be energized from the brushless motor. It is called freewheeling to the configuration of the diodes in parallel to the transistors of the voltage source inverter and it is used for suppressing sudden voltage peaks due to sudden switching on the six-transistor-commutable bridge (See Fig. 2.16 and Fig. 2.18).

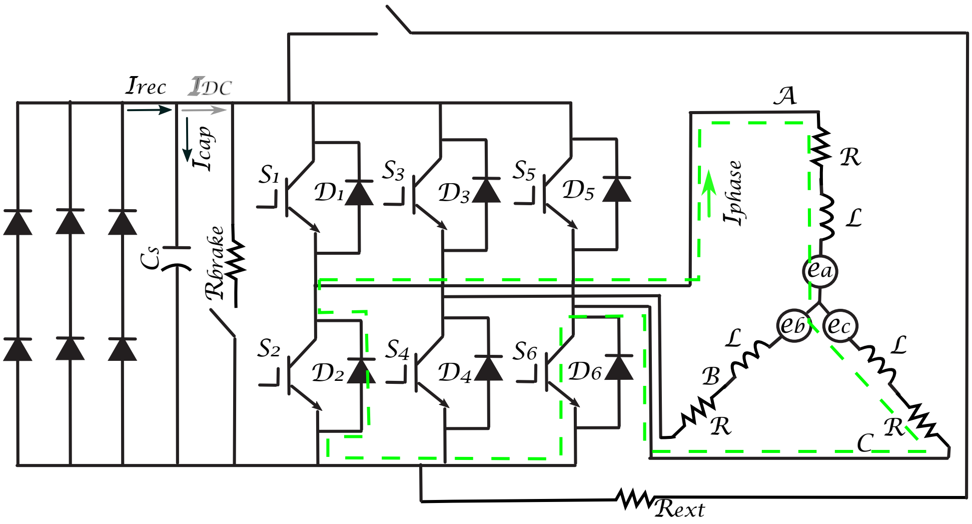
Irec
IDC
Icap
Cs
Rbrake
S1
D1
S3
D3
S5
D5
S2
D2
S4
D4
S6
D6
Iphase
A
R
L
ea
eb
ec
L
B
R
L
R
C
Rext

Figure 2.16: Freewheeling motoring mode

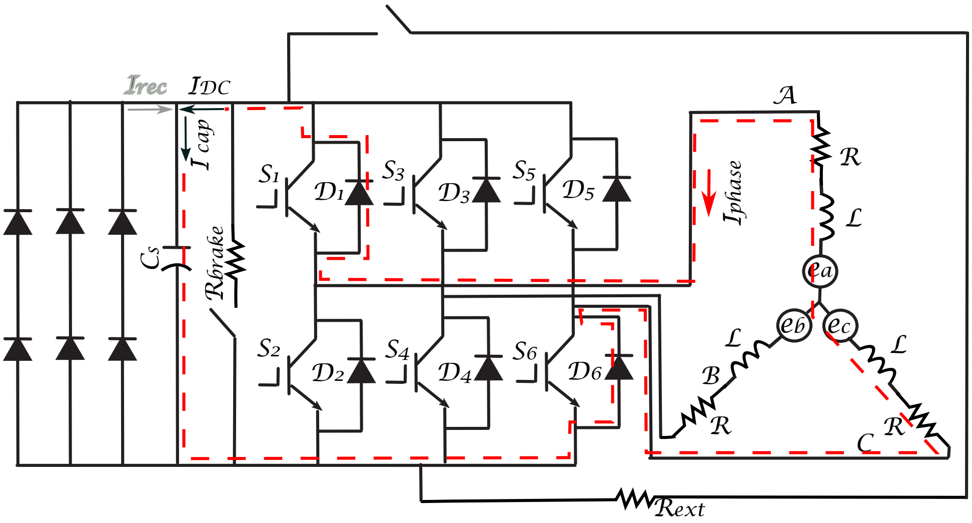
Irec
IDC
Icap
Cs
Rbrake
S1
D1
S3
D3
S5
D5
S2
D2
S4
D4
S6
D6
Iphase
A
R
L
ea
eb
ec
L
B
R
L
R
C
Rext

Figure 2.17: Generating mode

2.3.4 Model of energetic losses

Based on the aforementioned electromechanical models and motor operation modes, five types of power losses can be identified:

- **Resistive losses**: These are heat losses that occur when current flows through the resistances of each phase of the brushless motors and the braking resistances. The mathematical expression is given by:

$$P_{motor} = R_{phase} I^2 \tag{2.36}$$

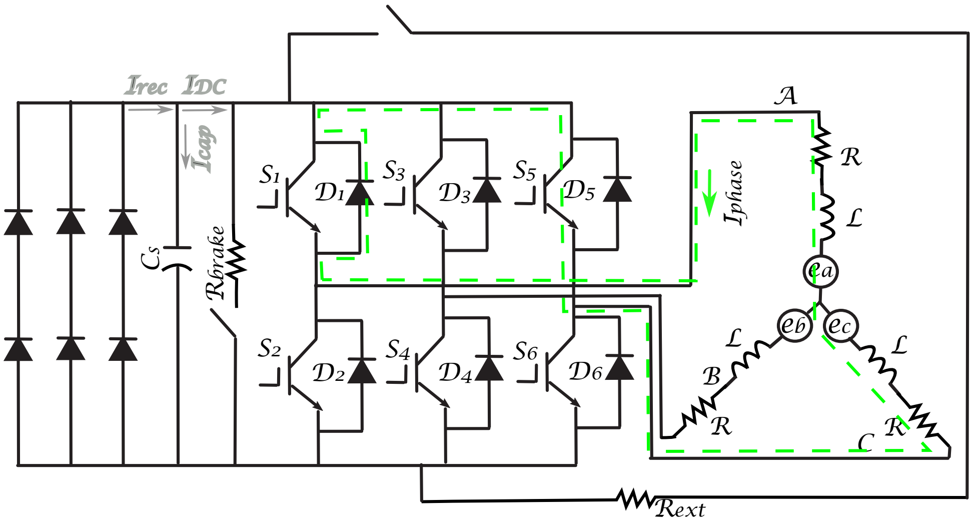

Figure 2.18: Freewheeling generating mode

$$P_{brake} = R_{brake} I^2 \tag{2.37}$$

where I encompasses the currents for each motor phase depending on which phase is energized, and R_{phase} and R_{brake} are the electrical resistances from the braking and motor sections, respectively. This loss is identified in the generating mode when the capacitor reach its full capacity and the current dissipates through the braking resistance (See Fig. 2.17). For high-speeds these losses are preponderant due to the fact that in the acceleration-deceleration cycles an enormous amount of energy is required to move and stop the payload, leading to an increase in the current, which in absence of capacitor, dissipates in the braking resistance.

- **Damping losses**: These are mechanical losses due to the mechanical coupling between the motor and drive shaft modeled by:

$$P_{damp} = B \dot{q}_k^2 \tag{2.38}$$

where B is the damping coefficient and $\dot{q}_k$ is the velocity of the kth motor axis, where $k = 1, ..., (n + n_s)$. Since there is always load connected to the rotor of the motor, this mechanical loss is present in the four operation modes.

- **Conduction losses**: The conduction losses are electrical losses due to the current flow through the transistors and diodes occurring in the three phase rectification and the six-transistor-commutable bridge. They are modeled as follows:

$$P_{cond} = \underbrace{u_{ce}I_{c_{av}} + r_c I^2_{c_{rms}}}_{transistors} + \underbrace{u_D I_{D_{av}} + r_D I^2_{D_{rms}}}_{diodes} \tag{2.39}$$

where u_{ce} is the collector-to-emitter voltage and $I_{c_{av}}$ is the collector current, r_c is the on-state resistance and $I_{c_{rms}}$ is the RMS value of the collector current. u_D is the diode forward voltage and $I_{D_{av}}$ is the diode current, r_D is the on-state resistance and $I_{D_{rms}}$ is the RMS value of the diode current. This power loss is encountered in the in the motoring, freewheeling motoring and freewheeling generating modes.

- **Switching losses**: These losses occur due to the continuous switching in the six-transistor-commutable bridge of the motor driver when energizing each phase of the motor. The relationship is given by:

$$P_{switch} = \underbrace{u_{ce}I_{c_{av}}f_{sw}}_{transistors} + \underbrace{u_D I_{D_{av}}f_{sw}}_{diodes} \tag{2.40}$$

  where f_{sw} is the switching frequency from the six-transistor-commutable bridge. Since the commutable bridge needs to be working during the full operation of the brushless motor in order to change phase energizations, this power loss is encountered in the four operation modes.

- **Rectification losses**: These are electrical losses generated from the power supply of three phase rectification modeled as follows:

$$P_{rectifier} = u_{DR}I_{DR_{av}} + r_{DR}I^2_{DR_{rms}} \tag{2.41}$$

  where u_{DR} is the diode rectifier forward voltage and $I_{DR_{av}}$ is the diode rectifier current, r_{DR} is an on-state resistance and $I_{DR_{rms}}$ is the RMS value of the diode rectifier current. Same as the commutable bridge, the rectification takes place during the full operation cycle of the brushless motor, thus this power loss is found in the four operation modes.

It should be mentioned that the currents $I_{c_{av}}$, $I_{c_{rms}}$, $I_{D_{av}}$, $I_{D_{rms}}$, $I_{DR_{av}}$ and $I_{DR_{rms}}$, associated to the conduction, switching and rectification losses due to the diodes and transistors, are functions of the phase currents I_A, I_B and I_C of the motor and thus, by using the model of the brushless motor in expressions (2.32) and (2.33), and functions of the motor electromagnetic torque $\boldsymbol{\tau}_e$, and input torques $\boldsymbol{\tau}$.

Finally, by grouping the aforementioned power losses, the following model of losses results:

$$\begin{aligned} P_{losses} &= P_{motor} + P_{brake} + P_{damp} \\ &P_{cond} + P_{switch} + P_{rectifier} \end{aligned} \tag{2.42}$$

which integrated over an interval of operational time $t \in [t_0, t_f]$, results in the following energetic model:

$$\begin{aligned} \int_0^{t_f} P_{losses} dt = \int_0^{t_f} &(P_{motor} + P_{brake} + P_{damp} \\ &P_{cond} + P_{switch} + P_{rectifier}) dt \end{aligned} \tag{2.43}$$

2.4 Simulation of physical models and identification of preponderant energetic losses

By investigating the aforementioned mathematical formulations (modeling of the dynamics of parallel robots and the energetic losses of their motor drive systems) it is not obvious how to exploit the resonance principle for fast quasi-periodic motions in order to minimize the energy consumption. For this reason in this Section, thanks to a simulation analysis of the dynamic and energetic model for a parallel robot, we seek to identify which power loss from (2.42) is the most preponderant in the full actuation chain when performing high-speed motions. This will allow to determine the preponderant terms from the energetic model. In order to perform the simulations, we will analyze the models by considering a case of nominal actuation in which the parallel robot is assembled without springs, and whose high-speed pick-and-place motions are parameterized thanks to classical fifth-order polynomials.

The case study chosen for this analysis is a planar five-bar mechanism whose schematic is shown in Fig. 2.19. This robot (Fig. 2.19) is a 2-DOF parallel robot able to perform two translations in the plane (O, $\mathbf{x}_0$, $\mathbf{y}_0$), and which is composed of two legs:

- A first leg composed of 3-R joints whose axes are parallel, directed along $\mathbf{z}_0$ and located at points A_{11}, A_{12} and A_{13}, the joint located at point A_{11} being actuated, and

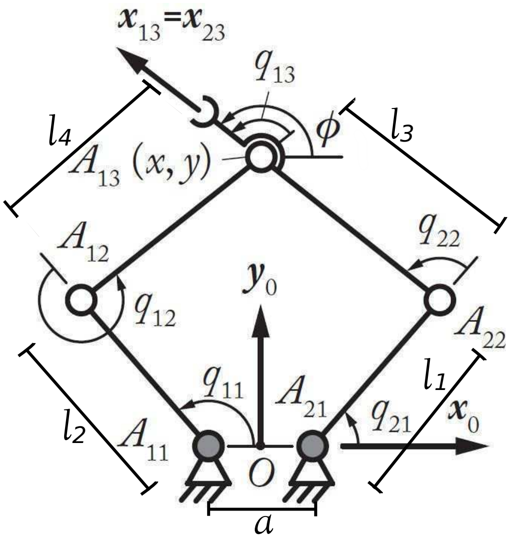

Figure 2.19: Five-bar mechanism parameterization with two actuated joints q_{11} and q_{21} located at A_{11} and A_{21}, respectively, and three passive joints q_{12}, q_{22} and q_{13} located at A_{12}, A_{22} and A_{13}, respectively.

- A second leg composed of 2-R joints whose axes are parallel, directed along $\mathbf{z}_0$ and located at points A_{21} and A_{22}, the joint located at point A_{21} being actuated.

All other joints are passive (A_{12}, A_{22}, A_{13}). Thus, the actuation of the parallel robot is provided by $\mathbf{q}_a = [q_{11}, q_{21}]^T$. The vector of moving platform pose is given by $\mathbf{x} = [x, y]^T$. a is the distance between the actuated joints. Finally, ℓ_1 and ℓ_2 represent the length of the proximal links of the robot, and ℓ_3 and ℓ_4 represent the length of the distal links of the robot.

The numerical values of the geometric and dynamic parameters for the five-bar mechanism were defined according to a real parallel robot called RobEcolo which can be found in [RobEcolo 2015][Kaci 2018], and have the following values:

- regrouped moment of inertia on the axis of the two proximal links $zz_{11R} = 0.133$ kg.m^2 and $zz_{21R} = 0.122$ kg.m^2;
- Coulomb friction terms of the actuated joints $f_{s1} = 0.659$ Nm and $f_{s2} = 0.225$ Nm;
- end-effector mass $m_R = 1.84$ kg;
- link lengths of the two proximal links $\ell_1 = \ell_2 = 0.28$ m;
- link lengths of the two distal links $\ell_3 = \ell_4 = 0.4$ m;

- distance between the axes of the actuated links $a = 0.250$ m.

The motor parameters used to examine the energetic performance, using the energetic model (2.43) were defined according to the motor specifications found in [Siemens] by the following values:

- electrical resistances $R_{phase} = 0.2\ \Omega$, $R_{brake} = 18\ \Omega$;
- damping coefficient $B = 0.005$ Nm/s;
- on-state resistances $r_c = r_D = r_{DR} = 0.003\ \Omega$;
- forward and collector-to-emitter voltages $u_D = u_{DR} = u_{ce} = 0.8$ V;
- switching frequency $f_{sw} = 20$ KHz.

The simulations were performed by using the dynamic model of the real parallel robot called RobEcolo [RobEcolo 2015][Kaci 2018], which is a wooden five-bar mechanism whose dynamic model, following the methodology presented in Section 2.2, is given by the following equations:

$$\boldsymbol{\tau} = \mathbf{ZZ}\ddot{\mathbf{q}} + \mathbf{B}^T\boldsymbol{\lambda} + \begin{bmatrix} f_{s_1}\mathrm{sign}(\dot{q}_{11}) \\ f_{s_2}\mathrm{sign}(\dot{q}_{21}) \end{bmatrix} \tag{2.44}$$

$$\mathbf{w}_p = \mathbf{A}^T\boldsymbol{\lambda} = m_R\ddot{\mathbf{x}} \tag{2.45}$$

where $\mathbf{A}$ and $\mathbf{B}$ are computed from the input-output kinematic constraint relation (2.11), and $\mathbf{ZZ} = \mathrm{diag}(zz_{11R},\ zz_{21R})$, with zz_{11R} and zz_{21R} representing moments of inertia regrouped on the two axis of the two proximal links. The dynamic model of the five-bar mechanism can be found in Appendix A.

In order to analyze the dynamics of the five-bar robot and the energy consumed by the actuators with which it is driven, multiple pick-and-place desired points are defined in the workspace of the five-bar mechanism as shown in Fig. 2.20. In order to define these points, it was considered that the standard cycles for a high-speed pick-and-place operation can reach an amplitude up to 30 cm long. In addition to that, variable cycle times (quasi-periodic motions) were defined between consecutive pick-and-place points. The aim, thus, is to go multiple times to these points by means of fifth-degree order polynomials defined in the robot joint space, and then to analyze the energetic model (2.43) in order identify the most preponderant power loss. These pick-and-place points

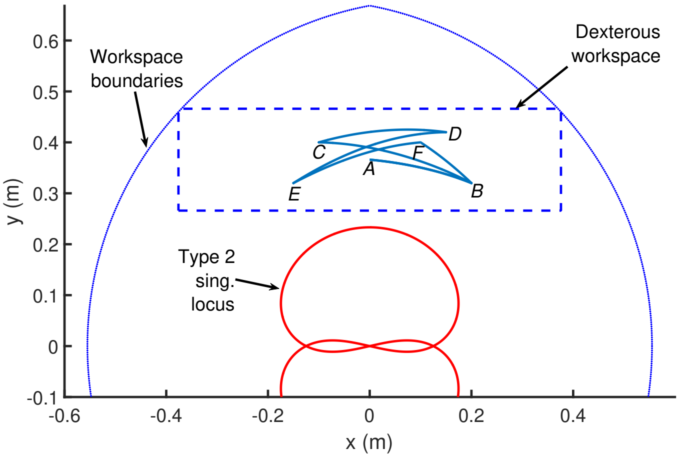

Figure 2.20: Multiple-point pick-and-place sequence in the five-bar mechanism workspace: $A \rightarrow B$ (travel time: 0.27 s), $B \rightarrow C$ (travel time: 0.23 s), $C \rightarrow D$ (travel time: 0.21 s), $D \rightarrow E$ (travel time: 0.3 s), $E \rightarrow F$ (travel time: 0.29 s), $F \rightarrow B$ (travel time: 0.25 s), $B \rightarrow A$ (travel time: 0.18 s).

are defined according to Fig. 2.20 and their values are $A = [0, 0.366]$, $B = [0.2, 0.32]$, $C = [-0.1, 0.4]$, $D = [0.15, 0.42]$, $E = [-0.15, 0.32]$ and $F = [0.1, 0.4]$ (m).

The simulation setup, in order to analyze the interaction between the models associated to the dynamics of the five-bar robot and the electrical behavior of the motors actuating their two active joints, was defined as follows:

1. To compute the robot torques along the desired pick-and-place trajectory from Fig. 2.20 and according to the dynamic model (2.44)-(2.45).

2. To input the calculated torques into the model of energetic losses (2.43), respectively for each motor, which takes into account as well the full motor drive system considering the generated back electromagnetic voltages and torques.

Once the simulation setup has been defined, firstly, Figures 2.21 and 2.22 show the input torques computed along the nominal trajectory from the quasi-periodic sequence in Fig 2.20. Then, Figures 2.23 and 2.24 show the energetic losses computed from inputting the robot torques into the consumption model (2.43) when performing a nominal trajectory. It is worth noticing that based on the losses decoupled in Fig 2.24, most of the energetic losses occurring in the motor-drive system are due to resistive and conduction losses with a 53 % and 37 % of contribution, respectively. Mathematically speaking, this means that the squared of the electric currents from the resistive losses in (2.36)-

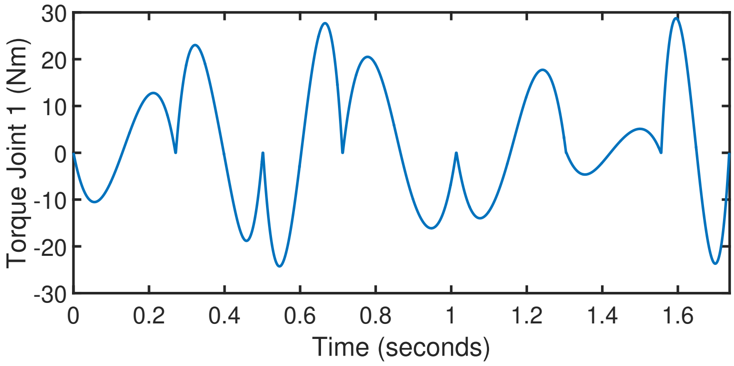

Figure 2.21: Input torque for the first joint of the parallel robot for nominal actuation.

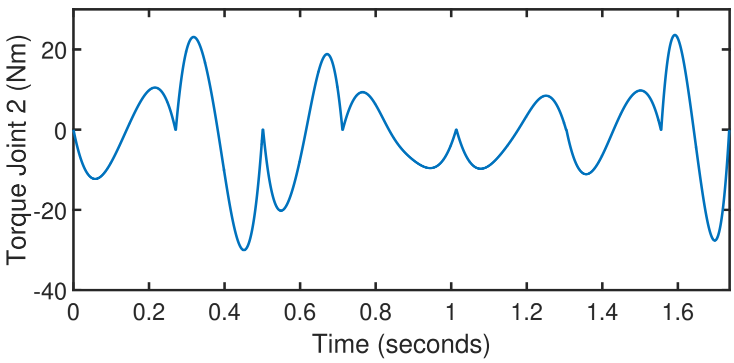

Figure 2.22: Input torque for the second joint of the parallel robot for nominal actuation.

(2.37), and the RMS of the electric currents from the conduction losses in (2.39), which are functions of the electromagnetic torques, and thus of the input robot torque amplitude and RMS, respectively, are the most preponderant terms in the energy consumption model. Moreover, it is worth to mention that different to the proposed energetic model in [Haddadin 2011][Jafari 2011][Goya 2012], here we do not neglect the conduction losses, which based on the aforementioned analysis have an important electric loss contribution of 37 % in the actuation chain.

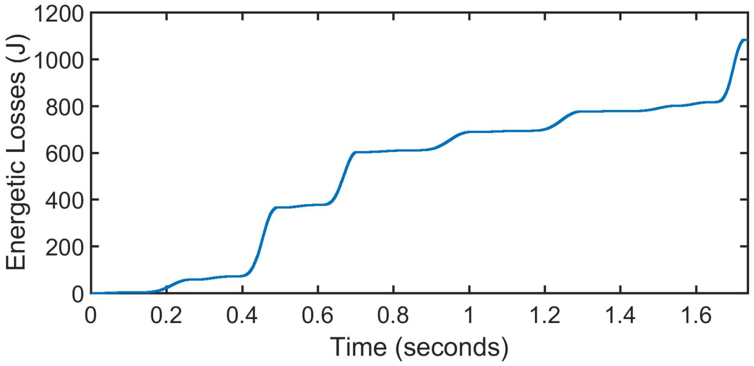

Figure 2.23: Energetic losses for the nominal actuation, i.e. the losses from the two motors in the active joints q_{11} and q_{21} of the five-bar mechanism.

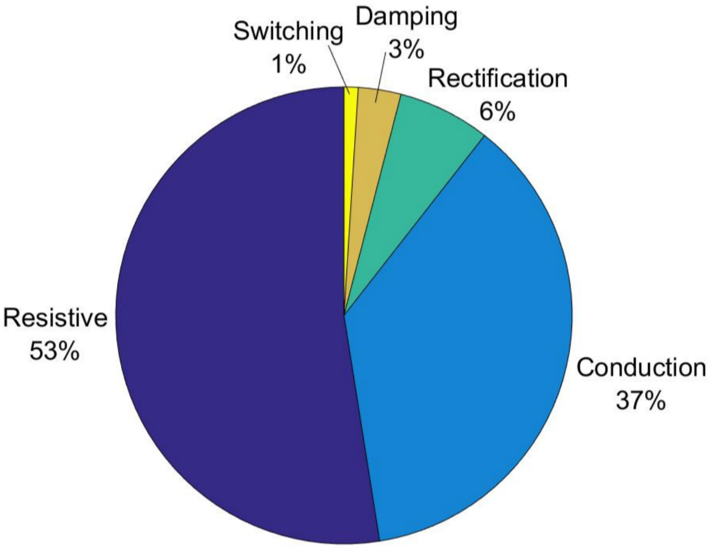

Figure 2.24: Energy losses decoupled from the energetic model in order to show how preponderant is each loss when performing a nominal high-speed pick-and-place operation.

2.5 Summary

In this Chapter, a novel promising concept based on parallel variable stiffness springs have been introduced. This type of actuation chain in parallel to the actuated links, allows to not only have tunable energy storage, but also have a direct power connection of the motors and the links of the parallel robot, thus ensuring accuracy at high-speeds.

In addition to that, in Section 2.1.1 it was shown the potential of using the resonance principle for exploiting the natural dynamics, and thus to reduce the input efforts.

This was presented on a one-degree-of-freedom robot with constant stiffness, and variable stiffness spring placed in parallel in which the conditions of resonance along one motion frequency can be analytically solved. The main issue of using constant stiffness springs is that, for a pick-and-place robot moving quasi-periodically, a constant stiffness spring would not be adequate due to the fact that the resonance modes would not have the possibility to be set along all possible range of motion frequencies. That is why, by using variable stiffness springs, we intend to exploit the dynamics of robots for all set motion pseudo-frequencies. In order to do so, Section 2.2 of this Chapter presented a general dynamic model for parallel robot with variable stiffness springs, which we seek to exploit in the following Chapters, in order to increase the energy efficiency. Furthermore, since we pursue to analyze the energetic losses in the full actuation chain, i.e. robot-plus-variable stiffness springs, a model of power losses has been developed.

Based on the computations in Section 2.4, an analysis of the influence of the different energetic losses was done in order to identify which are the preponderant terms of the consumption model. It was shown that, the resistive and conduction losses provide most of the losses in the actuation chain, being these two functions of the electric currents, and thus of the input torques. Additionally, it was shown that for a typical high-speed pick-and-place operation, in the deceleration phases, corresponding to the motor operating as a generator, most of the energy is dissipated due to the electric currents circulating towards the braking resistance of the motor driver. That is why in the next Chapter, we seek to develop a strategy to exploit the natural motions of the parallel robot thanks to the use of VSS in order to minimize the input torques RMS in the full actuation chain, and thus the energy consumption (mostly resistive and conduction losses in the braking phases), for high-speed quasi-periodic tasks. It should be mentioned that we decided to analyze the input torques RMS due to the fact that since the amplitude of the electric current is related to the peak of its waveform, and thus associated to the limited duty region of the motor (overheating region), it results more adequate to measure the RMS torque value, which corresponds to the effective region where the motor can operate continuously without overheat. The strategy for exploiting the robot natural motions will be done thanks to the formulation of a boundary value problem in which both, the parallel robot and the variable stiffness dynamics (2.18) and (2.20), respectively, are coupled and solved for the desired boundary quasi-periodic pick-and-place conditions, by formulating a shooting algorithm, which will be implemented thanks to the Levenberg-Marquardt solver from Matlab.

CHAPTER 3

Exploiting robot natural motions in order to reduce the energy consumption

3.1. *Performing energy-efficient pick-and-place motions in the case of known dynamic parameters* p. 78
3.2 *Performing energy-efficient pick-and-place motions in the case of unperfectly known dynamic parameters* p. 110
3.3. *Summary* p. 122

This Chapter presents a strategy for exploiting the natural dynamics of high-speed robots by using the actuation principle based on VSS in parallel with the robot actuated links. Since a pick-and-place operation is described by quasi-periodic oscillatory motions, through the addition of the VSS it should be possible to exploit such quasi-oscillations in order to match the free-response of the system with the desired pick-and-place conditions. Hence, Section 3.1 presents a strategy to exploit the robot natural motions by adjusting the VSS stiffness in parallel so that the robot pseudo-periodic pick-and-place oscillations match the free-response of the system. This is done thanks to the formulation of a boundary value problem (BVP) in which both the parallel robot and VSS dynamic equations are solved for the desired boundary pick-and-place conditions, by using the so-called "shooting method". Simulations of the suggested approach for different desired high-speed pick-and-place sequences and for constant and variable payload on a five-bar mechanism and on a Delta robot are performed. The simulations results show a drastic reduction of the input torques and therefore of the energy consumption. Finally, in Section 3.2, an online motion generator combined with an adaptation law is developed for exploiting the natural dynamics even if the dynamic parameters are unperfectly known.

3.1 Performing energy-efficient pick-and-place motions in the case of known dynamic parameters

In this Section, a strategy for performing energy-efficient natural pick-and-place motions will be presented. This strategy seeks to exploit the natural motions of the robot by formulating a boundary value problem (BVP). The main idea is that in order to optimize the input effort distribution in the full actuation chain, i.e. the efforts required to move the robot joints and the efforts to adjust the VSS, we will seek to exploit the combined motion of the parallel robot active joints and the VSS joints. This will be done with the aim of exploiting the force/displacement relation (related to the VSS optimal stiffness) that couples the robot and the VSS dynamic equations, so that we minimize the robot and the VSS input torques, and therefore the energy consumption simultaneously for the full actuation chain. Let us start with the formulation.

3.1.1 Matching pick-and-place boundary conditions with the robot free-response

Previously in Section 2.1, it was shown that for a 1-DOF robot that oscillates at a constant amplitude and frequency, it is possible to find a unique constant stiffness spring with constant k, such that the free-response of the system converge to the desired periodic trajectory, thus vanishing the input torque τ. Nevertheless, as well in Section 2.1, it was shown that for pseudo-periodic oscillatory motions, which is the case when performing pick-and-place operations, is not the same case since those tasks may have variable amplitudes and frequencies of oscillations (for instance see Fig. 3.1). This is mainly due to the fact that for each pseudo-frequency, there exists a different set of spring constants for enforcing the free-response to converge to the desired pseudo-periodic trajectory. This is the reason why we showed as well that by placing a VSS in parallel to the 1-DOF robot, it is possible to vanish the robot input torque τ by adjusting the equilibrium position of the spring so that we match the desired motion with the robot free-response even if the motion is quasi-periodic. Nevertheless, as previously mentioned in Section 2.1, the total effort in the full actuation chain would not be reduced since the VSS efforts are not constrained. This is due to the fact that we impose the desired motion to the robot active joint for the full desired cycle, which strongly constrains the force/displacement relation of the VSS since not only depends on the VSS coordinate, but also on the robot active joints (see

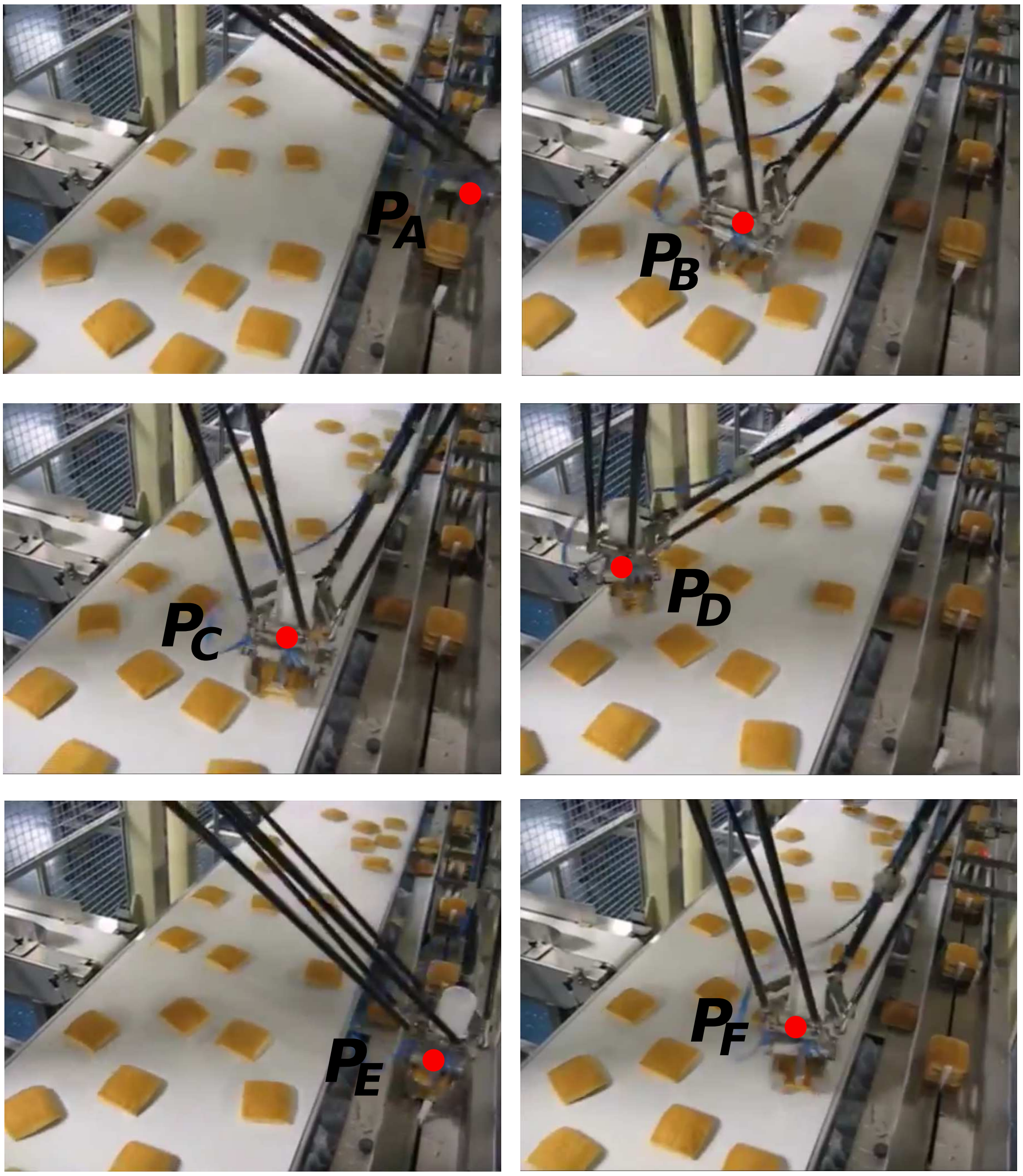

Figure 3.1: Decomposition of a video taken from real a pick-and-place application in the bread industry. The desired pick-and-place positions are represented by P_A, P_B, P_C, P_D, P_E and P_F. The time connecting these desired positions are defined according to the following sequence: $P_A \rightarrow P_B$ (travel time: ≈ 0.3 s), $P_B \rightarrow P_C$ (travel time: ≈ 0.1 s), $P_C \rightarrow P_D$ (travel time: ≈ 0.27 s), $P_D \rightarrow P_E$ (travel time: ≈ 0.23 s), $P_E \rightarrow P_F$ (travel time: ≈ 0.3 s). The red dot represents the end-effector position [Kawasaki robotics].

Subsection 2.2.2). This means that in order to fully exploit the force/displacement relation, which couples the robot and the VSS dynamics, we need to find a combined motion of the robot joint coordinate and the evolution of the equilibrium position of the spring from the VSS, while ensuring accuracy in the boundaries of the task (*pick* and *place*). This is due to the fact that, as previously mentioned, for a high-speed pick-and-place operation, we are only interested in ensuring accuracy in the boundaries, allowing to let the robot joint free in between the boundaries, thus allowing to fully exploit the VSS force/displacement relation. That is why, in this Section we propose a strategy to exploit the robot natural dynamics for pseudo-oscillatory motions, while reducing the input efforts in the full actuation, i.e. minimizing the input torques from the robot active joints and the efforts required to adjust the VSS for fast quasi-periodic tasks, thus exploiting the resonance principle for the full actuation chain. Additionally, contrary to the 1-DOF case, here we will deal with more complex kinematic architectures, in which the inertia matrix may be joint-dependent. Let us start with the formulation.

During an energy-efficient pick-and-place operation, there are two main performances expected to be achieved from the high-speed robot: *i*) to accurately meet the desired boundary conditions (*pick* or *place* positions), and *ii*) to perform the task with minimum energy-demand from the actuators, both expected performances to be completed in a given motion duration. This means that there is no restriction for the robot on how to go from the initial to the final positions, except eventual collisions within the robot links, external environment or singularity loci, as long as it is the most energy-efficient. Additionally, it is worth noticing that since we seek to minimize the energetic losses, we need to ensure that during the deceleration phase, in which most of the energy is dissipated in the braking resistance as heat, the robot arrives to the *place* state with minimum torque, thus decreasing the electric currents, and therefore, the resistive losses (and the associated conduction losses), which represent 53 % of loss for the actuation chain.

That is why, based on this previous hypothesis, in this Subsection we propose an algorithm based on a BVP, which can solve a set of dynamic equations (for instance (2.18) and (2.20), for $\boldsymbol{\tau} = 0$ and $\boldsymbol{\tau}_{vss} = 0$, related to the input torques and therefore to the energetic losses (2.43)) subjected to boundary constraints (*pick* or *place* positions), and the solution of those dynamic equations, if it exists, ensures the convergence to unforced differential equations, i.e. $\boldsymbol{\tau} = 0$ and $\boldsymbol{\tau}_{vss} = 0$, thus exploiting the system free-response.

In order to solve boundary value problems, several numerical methods exist. For instance the reader can refer to [Ascher 1987] for an overview of those methods. However, one of the most powerful is the so-called *shooting method* [Roberts 1972][Schiehlen 2005]. The *shooting method* is a numerical algorithm seeking to adjust the solution of a differential equation to match its solution boundaries with desired boundary conditions of the BVP. The adjustment of the solution of the differential equations, to match the desired boundary conditions, is done by *shooting out* different values for a decision variable, defined from the set of variables governing the differential equations, until the solution of the differential equations respects the set of desired boundary conditions. The decision variable may be updated optimally by using a gradient-descent approach [Neuberger 2009]. Additionally, it is worth emphasizing that *shooting methods* have proven optimal convergence effectiveness in case of squared optimization problems, i.e. same number of boundary constraints as number of decision variables [Roberts 1972].

Therefore, by following the aforementioned functioning principle for solving BVPs through *shooting methods*, here, we will formulate a *shooting* algorithm seeking to find the optimal stiffness of the VSS, associated to the force/displacement relation in (2.20), and controlled with $\mathbf{q}_a$ and $\mathbf{q}_s$, such that the robot free-response matches as best as possible the desired boundary conditions during the deceleration phase, even if the task is quasi-periodic, i.e. with variable cycle times. This allows to have a fixed set of spring constants for any pseudo-frequency, and by tuning $\mathbf{q}_a$ and $\mathbf{q}_s$, while respecting the boundary constraints, we ensure the convergence of (2.18) and (2.20) as two unforced second order differential system, thus decreasing the input torques and the energetic losses of the full actuation chain, i.e. robot-plus-VSS.

3.1.1.1 Solution of boundary value problems by using the shooting method

In the field of numerical analysis, a boundary value problem (BVP) is defined by a differential equation subjected to a set of additional constraints, called boundary constraints.

Mathematically speaking, a BVP is defined when, for solving a differential equation, two conditions are given at different values of the independent variable (time in our case) of the differential equation [Roberts 1972], i.e.:

$$\ddot{h} = f(t, h, \dot{h}), \qquad a < t < b \tag{3.1}$$

with the boundary conditions defined by:

$$h(a) = P_A, \qquad h(b) = P_B \tag{3.2}$$

where (3.1) is a second order differential equation, t is the independent variable, which in this case is the time, P_A and P_B are the desired boundary conditions defined at $t = a$

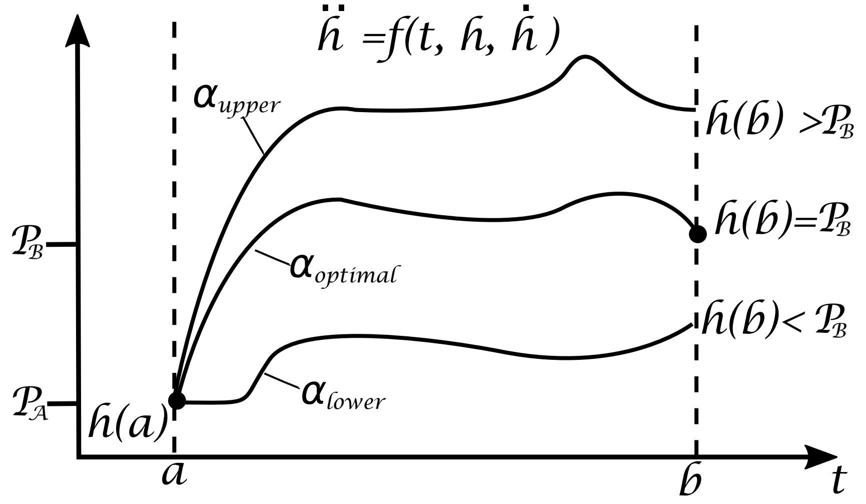

Figure 3.2: Graphical interpretation of classic solution of shooting method for a BVP.

and $t = b$ of the BVP, respectively.

The classical way to solve the BVP (3.1)-(3.2), is by using the so-called *shooting method* [Roberts 1972], which treats the BVP as an initial value problem (IVP) [Roberts 1972], with the initial conditions given by:

$$h(a) = P_A, \qquad \dot{h}(a) = \alpha \tag{3.3}$$

where α represents the first derivative of $h(t)$ at $t = a$, or in other words, the slope of the solution at $t = a$, and the objective is to choose α, so that the solution of (3.1) satisfies the remaining boundary condition $h(b) = P_B$ from (3.2).

Practically speaking, the main idea of the *shooting method* is to numerically integrate (3.1), for different values of the slope α, and then to take the solution of the differential equation that satisfies the boundary condition $h(b) = P_B$ (see Fig. 3.2 for a graphical interpretation).

A more detailed algorithm flow can be synthesized as follows:

1. Solve the differential equation (3.1) with the initial conditions $h(a) = P_A$ and $h(b) = P_B$;
2. Evaluate the solution $h(b)$ at $t = b$ and compare this value to the target value of $h(b) = P_B$;
3. Adjust the value of α (either increasingly or decreasingly) until a desired function tolerance and accuracy of the constraints are achieved;

4. Once the specified function tolerances and accuracy are satisfied, numerically integrates $\ddot{h} = f(t, h, \dot{h})$ in order to obtain the velocity $\dot{h}$, and the position h.

Thus, in a similar vein, this work proposes to use a BVP formulation to exploit the natural motions of the pseudo-periodic pick-and-place oscillations of the parallel robot. This is done by modifying the stiffness (controlled with $\mathbf{q}_s$ and $\mathbf{q}_a$ according to (2.19)), instead of the slope α, to adjust the solution of the differential equations (2.18) and (2.20), for $\boldsymbol{\tau} = 0$ and $\boldsymbol{\tau}_{vss} = 0$, to match the desired boundary pick-and-place conditions of the parallel robot. If a solution for such BVP is found, i.e. the function tolerances and constraint accuracies are satisfied, this will ensure the convergence of expressions (2.18) and (2.20) as two unforced differential systems, decreasing the input efforts in the full actuation chain when performing high-speed pick-and-place motions. In addition to that, thanks to the solution of both robot and VSS dynamic equations, (2.18) and (2.20) respectively, the VSS will vary simultaneously with the motions of the robot.

3.1.1.2 BVP applied on energy-efficient high-speed robots

Based on the aforementioned physical analysis of the motor operating modes in Chapter 2, we have seen that most of the losses in the full actuation chain, during a high-speed task, are due to the braking resistances in the motor generating modes, i.e. when the robot is decelerating (braking). Additionally, according to the physical expression (2.19), which represents the force/displacement relation coupling the robot and the VSS dynamic equations, the natural motion can be fully exploited thanks to a combined motion of the spring and the parallel robot coordinates represented by $\mathbf{q}_s$ and $\mathbf{q}_a$, respectively. That is why, here we propose the formulation of a BVP in which by integrating the dynamic equations ($\boldsymbol{\tau}$, $\boldsymbol{\tau}_{vss}$) we find an optimal combined motion of $\mathbf{q}_s$ and $\mathbf{q}_a$, such that the efforts in the full actuation chain ($\boldsymbol{\tau}$, $\boldsymbol{\tau}_{vss}$) decrease while respecting the desired boundary conditions. Additionally, it is worth emphasizing that we will not constrain the robot active joint $\mathbf{q}_a$ for the full pick-and-place cycle, but only for the boundaries, allowing to fully exploit the force/displacement relation (2.19) that couples the robot-plus-VSS dynamics.

Similarly, as for the definition of α in (3.3), for defining the decision variable allowing to fully exploit (2.19), so that $\boldsymbol{\tau}$, $\boldsymbol{\tau}_{vss}$ tends to zero, let us express the force/displacement relation $\boldsymbol{\tau}_s$ from (2.18) and (2.20), respectively as follows:

$$\begin{aligned} \boldsymbol{\tau}_s = \mathbf{K}(\mathbf{q}_a - \mathbf{q}_s) = -(\mathbf{M}\ddot{\mathbf{q}}_a + \mathbf{c}(\mathbf{q}_a, \dot{\mathbf{q}}_a) + \mathbf{f}_a) \\ \boldsymbol{\tau}_s = \mathbf{K}(\mathbf{q}_a - \mathbf{q}_s) = \mathbf{M}_s\ddot{\mathbf{q}}_s + \mathbf{h}_s(\mathbf{q}_s, \dot{\mathbf{q}}_s) + \mathbf{f}_s \end{aligned} \tag{3.4}$$

Based on expressions in (3.4), it should be observed that in order to fully exploit the natural dynamics of the robot-plus-VSS system, the optimal VSS equilibrium positions related to $\boldsymbol{\tau}_s$, are dependent not only on the VSS and robot configuration $\mathbf{q}_s$ and $\mathbf{q}_a$, respectively, but also on their first time derivatives $\dot{\mathbf{q}}_s$ and $\dot{\mathbf{q}}_a$ (related to Coriolis and centrifugal effects), and their second time derivatives $\ddot{\mathbf{q}}_s$ and $\ddot{\mathbf{q}}_a$ (related to the inertia effects). That is why, in order to optimally exploit the natural motions of the robot through the VSS stiffness, the decision variable to adjust the solution of (2.18) and (2.20), must be defined as function of the robot and the VSS positions, velocities and accelerations.

Normally, during a typical high-speed pick-and-place task, the robot is required to arrive to the desired boundary position, represented either by the *pick* or the *place* of the cycle, with null velocities and accelerations. Additionally, by considering the aforementioned analysis in which it is noted that the acceleration terms $\ddot{\mathbf{q}}_s$ and $\ddot{\mathbf{q}}_a$ contribute to (3.4) for exploiting the natural dynamics, to apply the BVP formulation during the multiple pick-and-place segments, it is required to have higher-order dynamic equations. This is due to the fact that since the shooting algorithm is based on an integration method in which differential equations are numerically integrated for a given set of boundary constraints, the order of the systems (2.18) and (2.20) would allow to integrate up to velocity constraints of the pick-and-place task, thus not constraining the accelerations.

Therefore, with the purpose of being able to specify acceleration constraints in the integration step of the BVP formulation, we will thus time differentiate the dynamic expressions (2.18) and (2.20) in order to obtain the jerk equations, which allows to perform numerical integration for acceleration boundary constraints:

$$\dot{\boldsymbol{\tau}} = \mathbf{M}\dddot{\mathbf{q}}_a + \dot{\mathbf{M}}\ddot{\mathbf{q}}_a + \dot{\mathbf{c}} + \mathbf{K}(\dot{\mathbf{q}}_a - \dot{\mathbf{q}}_s) + \dot{\mathbf{f}}_a \tag{3.5}$$

$$\dot{\boldsymbol{\tau}}_{vss} = \mathbf{J}_s\dddot{\mathbf{q}}_s - \mathbf{K}(\dot{\mathbf{q}}_a - \dot{\mathbf{q}}_s) + \dot{\mathbf{f}}_s \tag{3.6}$$

where the sign functions from the active joint friction terms in $\mathbf{f}_a$ and $\mathbf{f}_s$, in order to obtain $\dot{\mathbf{f}}_a$ and $\dot{\mathbf{f}}_s$, respectively, are approximated to tanh functions, which are time differentiable.

Since the *shooting method* is an algorithm which adjust the initial differential parameters such that the differential equations converge towards the boundary conditions at t_f, the main idea is that, in order to let the initial robot states free, i.e. initial robot velocities

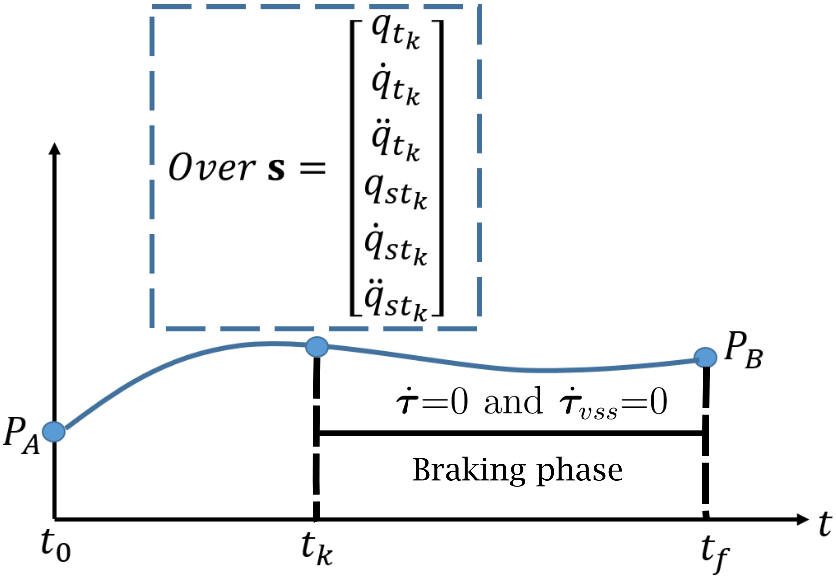

$\text{Over } \mathbf{s} = \begin{bmatrix} q_{t_k} \\ \dot{q}_{t_k} \\ \ddot{q}_{t_k} \\ q_{st_k} \\ \dot{q}_{st_k} \\ \ddot{q}_{st_k} \end{bmatrix}$
P_A
P_B
$\dot{\boldsymbol{\tau}}$=0 and $\dot{\boldsymbol{\tau}}_{vss}$=0
Braking phase
t_0
t_k
t_f
t

Figure 3.3: Graphical interpretation of shooting method for solving the BVP for the robot-plus-VSS system.

and accelerations, we will reformulate a shooting algorithm for finding an energy-efficient optimal motion during the braking phase. This is due to the fact that as it was previously mentioned, more than 50 % of the energetic losses, in the high-speed pick-and-place cycle, occur during the generating mode of the motor, i.e. decelerating phase.

According to Fig. 3.3, in a given *pick* (P_A) and *place* (P_B) cycle with given duration t_f, most of the energetic losses are accumulated during the braking phase of the high-speed motion. That is why, we can consider the full cycle as two motion segments, i.e. a motion segment from t_0 to t_k, and a braking segment from t_k to t_f, in which t_k represents the time at which the braking phase starts. Following this motion definition, since we are interested on minimizing the energetic losses, mainly at the braking phase, we will formulate the BVP, which computes the trajectory from the numerical integration of the dynamic equations, to start at t_k, leading to let the intermediate positions, velocities and accelerations manipulable to adjust the solutions of (3.5) and (3.6) for solving $\dot{\boldsymbol{\tau}}$=0 and $\dot{\boldsymbol{\tau}}_{vss}$=0, while respecting the boundary constraints at t_f. For the motion segment defined from t_0 to t_k, in which the energetic losses remain without drastic increases, and less preponderant with respect to the braking phase, we will use a classical polynomial law motion, permitting to reach the optimal intermediate robot and VSS positions, velocities and accelerations computed from the BVP, and thus to minimize the energetic losses.

Firstly, since the objective is to find the solutions for $\dot{\boldsymbol{\tau}}$=0 and $\dot{\boldsymbol{\tau}}_{vss}$=0, we compute $\dddot{\mathbf{q}}$ and $\dddot{\mathbf{q}}_s$ from (3.5) and (3.6) by:

$$\dddot{\mathbf{q}}_a = -\mathbf{M}^{-1}(\dot{\mathbf{M}}\ddot{\mathbf{q}}_a + \dot{\mathbf{c}} + \mathbf{K}(\dot{\mathbf{q}}_a - \dot{\mathbf{q}}_s) + \dot{\mathbf{f}}_a) \tag{3.7}$$

$$\dddot{\mathbf{q}}_s = \mathbf{J}_s^{-1}(\mathbf{K}(\dot{\mathbf{q}}_a - \dot{\mathbf{q}}_s) - \dot{\mathbf{f}}_s) \tag{3.8}$$

Since during the specification of the desired pick-and-place task, it is required to define constraints in the boundaries, we impose the desired initial and final desired pick and place positions, velocities and accelerations, and the desired initial and final VSS positions, velocities and accelerations denoted by:

$$\begin{cases} \mathbf{q}_a(0) = \mathbf{q}^*_{a0} \text{ and } \mathbf{q}_a(t_f) = \mathbf{q}^*_{at_f} \\ \dot{\mathbf{q}}_a(0) = \dot{\mathbf{q}}^*_{a0} \text{ and } \dot{\mathbf{q}}_a(t_f) = \dot{\mathbf{q}}^*_{at_f} \\ \ddot{\mathbf{q}}_a(0) = \ddot{\mathbf{q}}^*_{a0} \text{ and } \ddot{\mathbf{q}}_a(t_f) = \ddot{\mathbf{q}}^*_{at_f} \end{cases} \qquad \begin{cases} \mathbf{q}_s(0) = \mathbf{q}^*_{s0} \text{ and } \mathbf{q}_s(t_f) = \mathbf{q}^*_{st_f} \\ \dot{\mathbf{q}}_s(0) = \dot{\mathbf{q}}^*_{s0} \text{ and } \dot{\mathbf{q}}_s(t_f) = \dot{\mathbf{q}}^*_{st_f} \\ \ddot{\mathbf{q}}_s(0) = \ddot{\mathbf{q}}^*_{s0} \text{ and } \ddot{\mathbf{q}}_s(t_f) = \ddot{\mathbf{q}}^*_{st_f} \end{cases} \tag{3.9}$$

In order to minimize the robot-plus-VSS input torques while ensuring to reach the desired *place* position, velocity and acceleration, to start the next pick-and-place cycle, the following errors vectors are minimized in the BVP formulation:

$$\mathbf{E} = \begin{cases} \mathbf{E}_{q_a}(\mathbf{s}) = \mathbf{q}_a(t_f, \mathbf{s}) - \mathbf{q}^*_{at_f} \\ \mathbf{E}_{\dot{q}_a}(\mathbf{s}) = \dot{\mathbf{q}}_a(t_f, \mathbf{s}) - \dot{\mathbf{q}}^*_{at_f} \\ \mathbf{E}_{\ddot{q}_a}(\mathbf{s}) = \ddot{\mathbf{q}}_a(t_f, \mathbf{s}) - \ddot{\mathbf{q}}^*_{at_f} \\ \mathbf{E}_{q_s}(\mathbf{s}) = \mathbf{q}_s(t_f, \mathbf{s}) - \mathbf{q}^*_{st_f} \\ \mathbf{E}_{\dot{q}_s}(\mathbf{s}) = \dot{\mathbf{q}}_s(t_f, \mathbf{s}) - \dot{\mathbf{q}}^*_{st_f} \\ \mathbf{E}_{\ddot{q}_s}(\mathbf{s}) = \ddot{\mathbf{q}}_s(t_f, \mathbf{s}) - \ddot{\mathbf{q}}^*_{st_f} \end{cases} \tag{3.10}$$

where the parameterization for the trajectories of the robot and VSS joints positions, velocities and accelerations during braking $\ddot{\mathbf{q}}_a(t)$, $\dot{\mathbf{q}}_a(t)$, $\mathbf{q}_a(t)$ and $\ddot{\mathbf{q}}_s(t)$, $\dot{\mathbf{q}}_s(t)$, $\mathbf{q}_s(t)$ is defined from the numerical integration of $\dddot{\mathbf{q}}_a(t)$ and $\dddot{\mathbf{q}}_s(t)$, respectively once the boundary error vectors in (3.10) are satisfied.

The parameter vector $\mathbf{s}$, used as decision variable vector to enforce the convergence of (3.10), is parameterized as follows. Since the expression that couples the robot and the VSS dynamics (2.18) and (2.20), respectively, is associated to $\boldsymbol{\tau}_s$ in (2.19), which states

Algorithm 1 : BVP applied on robot and VSS jerk equations.

```
Input: $i \leftarrow 0, max_i \leftarrow 100$, $t_{int} \leftarrow [t_k, ..., t_f]$, $h > 0$ (integration step), $\mathbf{s}_{k_0} \leftarrow [1, 1, ..., 1]^T$, $t_k > 0$, $t_f > 0$

while $|\mathbf{E}_{q_a}| > \boldsymbol{\epsilon}_1$, $|\mathbf{E}_{\dot{q}_a}| > \boldsymbol{\epsilon}_2$, $|\mathbf{E}_{\ddot{q}_a}| > \boldsymbol{\epsilon}_3$, $|\mathbf{E}_{q_s}| > \boldsymbol{\epsilon}_4$, $|\mathbf{E}_{\dot{q}_s}| > \boldsymbol{\epsilon}_5$, $|\mathbf{E}_{\ddot{q}_s}| > \boldsymbol{\epsilon}_6$, $i \leq max_i$ do

    $[\mathbf{q}_a, \dot{\mathbf{q}}_a, \ddot{\mathbf{q}}_a, \mathbf{q}_s, \dot{\mathbf{q}}_s, \ddot{\mathbf{q}}_s]_i = \mathbf{RK4}(t_{int}, \mathbf{s}_k, h, (\dddot{\mathbf{q}}_a, \dddot{\mathbf{q}}_s))$ ▷ Numerical integration with Runge-Kutta 4-th order of eqs. (3.7)-(3.8)

    $[\mathbf{E}(t_f, \mathbf{s}_k)]_i = \begin{cases} \mathbf{E}_{q_a}(\mathbf{s}_k) = \mathbf{q}_a(t_f, \mathbf{s}_k) - \mathbf{q}^*_{at_f} \\ \mathbf{E}_{\dot{q}_a}(\mathbf{s}_k) = \dot{\mathbf{q}}_a(t_f, \mathbf{s}_k) - \dot{\mathbf{q}}^*_{t_f} \\ \mathbf{E}_{\ddot{q}_a}(\mathbf{s}_k) = \ddot{\mathbf{q}}_a(t_f, \mathbf{s}_k) - \ddot{\mathbf{q}}^*_{at_f} \\ \mathbf{E}_{q_s}(\mathbf{s}_k) = \mathbf{q}_s(t_f, \mathbf{s}_k) - \mathbf{q}^*_{st_f} \\ \mathbf{E}_{\dot{q}_s}(\mathbf{s}_k) = \dot{\mathbf{q}}_s(t_f, \mathbf{s}_k) - \dot{\mathbf{q}}^*_{st_f} \\ \mathbf{E}_{\ddot{q}_s}(\mathbf{s}_k) = \ddot{\mathbf{q}}_s(t_f, \mathbf{s}_k) - \ddot{\mathbf{q}}^*_{st_f} \end{cases}$ ▷ BVP errors (* means desired value)

    $[\mathbf{J}]_i = \frac{\partial \mathbf{E}(t_f, \mathbf{s}_k)}{\partial \mathbf{s}_k}$ ▷ Gradients

    $[\Delta \mathbf{s}_k]_i = \mathbf{LMUpdate}(\mathbf{s}_k, \mathbf{J})$ ▷ Levenberg-Marquardt update based on [Moré 1978]

    $[\mathbf{s}_k]_{i+1} = [\mathbf{s}_k]_i + [\Delta \mathbf{s}_k]_i$ ▷ Update of parameter vector $\mathbf{s}_k = [\mathbf{q}_a(t_k), \dot{\mathbf{q}}_a(t_k), \ddot{\mathbf{q}}_a(t_k), \mathbf{q}_s(t_k), \dot{\mathbf{q}}_s(t_k), \ddot{\mathbf{q}}_s(t_k)]^T$

end while

Output: $\mathbf{s}_k$, $\mathbf{q}_a(t_{int}, \mathbf{s}_k), \dot{\mathbf{q}}_a(t_{int}, \mathbf{s}_k), \ddot{\mathbf{q}}_a(t_{int}, \mathbf{s}_k), \mathbf{q}_s(t_{int}, \mathbf{s}_k), \dot{\mathbf{q}}_s(t_{int}, \mathbf{s}_k), \ddot{\mathbf{q}}_s(t_{int}, \mathbf{s}_k)$
```

that the optimal stiffness can be computed thanks to a combined motion $\mathbf{q}_s$ and $\mathbf{q}_a$, and their first and second time derivatives (see (2.19)), the decision variable vector $\mathbf{s}$ for the BVP formulation, was chosen to be $\mathbf{s} = [\mathbf{q}_a(t_k), \dot{\mathbf{q}}_a(t_k), \ddot{\mathbf{q}}_a(t_k), \mathbf{q}_s(t_k), \dot{\mathbf{q}}_s(t_k), \ddot{\mathbf{q}}_s(t_k)]^T$ as shown in Fig. 3.3. $t_k \in [t_0, t_f]$, represents the time at which the robot starts the deceleration phase (generating mode) towards the ending of the motion segment (only one t_k is defined since we have a squared BVP problem). It is worth noticing that the decision variable vector $\mathbf{s}$ takes into account the robot and the VSS positions, velocities and accelerations from (3.4), thus considering all the dynamic effects.

Thus, the shooting method is applied to iteratively find the parameter vector $\mathbf{s}$, such that expressions in (3.10) converge to zero by formulating the nonlinear BVP defined in Algorithm 1. It should be noted that from the aforementioned algorithm, to compute the BVP error vectors grouped in $\mathbf{E}(t_f, \mathbf{s}_k)$, it is necessary for $\mathbf{M}$ to be numerically invertible, i.e. out of Type 2 singularity [Gosselin 1990]. Thus, in the integration step, an inversion-checking condition representing the proximity to singularity is added to verify the invertibility of the decoupling matrix $\mathbf{M}$.

The different elements of the pseudo-code provided in Algorithm 1 are defined as follows: max_i is the maximum number of iterations i, $\boldsymbol{\epsilon}_{1 \ldots 6}$ represent the BVP errors thresholds, $\ddot{\mathbf{q}}_a$, $\dot{\mathbf{q}}_a$, $\mathbf{q}_a$ and $\ddot{\mathbf{q}}_s$, $\dot{\mathbf{q}}_s$, $\mathbf{q}_s$ are obtained from numerical integration of $\dddot{\mathbf{q}}_a$ and $\dddot{\mathbf{q}}_s$, respectively, and $\mathbf{E}(t_f, \mathbf{s}_k)$ groups the BVP error vectors to be minimized. The parameter vector $\mathbf{s}_k$, used as decision variable vector to enforce the convergence of the BVP error vectors (See Algorithm 1), is defined as a vector of robot positions, velocities and accelerations, and of VSS positions, velocities and accelerations, at the time instant t_k representing the time when the robot braking phase starts, and occurring between t_0 and t_f of the BVP: $\mathbf{s}_k = [\mathbf{q}_a(t_k), \dot{\mathbf{q}}_a(t_k), \ddot{\mathbf{q}}_a(t_k), \mathbf{q}_s(t_k), \dot{\mathbf{q}}_s(t_k), \ddot{\mathbf{q}}_s(t_k)]^T$ as shown in Fig. 3.3, $t_k \in [t_0, t_f]$ (only one t_k is defined since we have a squared BVP problem). In order to define the braking instant t_k, we evaluate the dynamic equations grouped in (2.18) and (2.20), respectively for the robot and the VSS, for different values of t_k on the motion segment valued from t_0 to t_k. This is done in order to choose the one which demands less input torques ($\boldsymbol{\tau}$, $\boldsymbol{\tau}_{vss}$), similar to what it is done in [Balderas 2019] in which the total motion segment from t_0 to t_f is divided to solve the BVP. Finally, **RK4** represents the numerical integration of the expressions in (3.7)-(3.8) by using a Runge-Kutta method, and **LMUpdate** is a function representing the Levenberg-Marquardt updating law based on [Moré 1978][Roweis (Notes)]. It is thus worth mentioning that thanks to the gradient-descent technique implemented in the LM, the decision variable $\mathbf{s}$ is optimally adjusted while minimizing the boundary constraints in (3.10). Finally, it should be noted that in order to compute the Jacobians for the gradients in the LM algorithm used to solve the shooting method, the LM Matlab solver use a finite difference approximation [LeVeque 2007].

Based on the aforementioned mathematical developments, the flow of the algorithm that exploits the natural dynamics of the full actuation chain, can be thus synthesized as follows. Once the desired boundary pick-and-place conditions are given, an initial guess for $\mathbf{s}_k$ is used to evaluate the error vectors (3.10). If the pre-defined function tolerances and error thresholds are satisfied, then the algorithm stops, and numerically integrates (3.7) and (3.8) from t_k to t_f in order to compute the robot and VSS joint positions, velocities and accelerations, i.e. $\mathbf{q}_a$, $\dot{\mathbf{q}}_a$, $\ddot{\mathbf{q}}_a$, and $\mathbf{q}_s$, $\dot{\mathbf{q}}_s$, $\ddot{\mathbf{q}}_s$, respectively. Otherwise, it *shoots out* a new guess $\mathbf{s}_{k+1}$ according to an increment $\Delta\mathbf{s}_k$ computed from the gradient-descent method of the LM algorithm, until finding the one that solves the system of equations (3.10). It should be mentioned that the *Levenberg - Marquardt* (LM) algorithm is based on a combination of gradient-descent and Gauss-Newton methods (for further details the reader can refer to [Roweis (Notes)]).

In order to conclude the algorithm developments of this Subsection, so we can pass to the simulation results of these theoretical formulations, it is worth giving some final remarks. It should be noted that what the shooting algorithm minimizes is the boundary error vectors so that the robot arrives in the specified given time to the desired *place* positions, velocities and accelerations of every finite high-speed cycle. Nevertheless, since the boundaries of the states of the robot and the VSS in the iterative method, are computed from the numerical integration of the two unforced robot-plus-VSS dynamic equations, if the boundary pick-and-place error vectors converge to zero, this will ensure that the robot-plus-VSS dynamic equations will remain unforced, thus exploiting the natural dynamics for the full actuation chain, and therefore minimizing the input torques during the braking phase of the robot task. Consequently, since the input torques are related to the currents in the motor consumption model, which are associated to the preponderant losses (resistive and conduction in the generating mode), reducing the torques will lead to increase the energy efficiency in the full actuation chain.

As a final remark, it is worth emphasizing that even if the problem formulation proposed in this Section, includes decoupling the pick-and-place cycle into two interconnected trajectory segments, from t_0 to t_k, and from t_k to t_f, we ensure that by solving the BVP in the latter interval (braking mode), the input torques in the full actuation tend to zero, thus exploiting the natural dynamics, and therefore minimizing the energetic losses.

3.1.2 Application of the energy-efficient motion generator to a five-bar mechanism with VSS: for constant and variable payload

The proposed BVP approach for generating optimal pick-and-place quasi-periodic motions was validated on the five-bar mechanism presented in Chapter 2, Section 2.4. The only difference is that in this case two variable stiffness torsional springs are attached in parallel to the actuated joints $\mathbf{q} = [q_{11}, q_{21}]^T$, as shown in Fig. 3.4. The actuation for the variable stiffness joints is given by $\mathbf{q}_s = [q_{s1}, q_{s2}]^T$.

The numerical values of the geometric and dynamic parameters for the five-bar mechanism were defined according to Section 2.4. For the dynamic parameters of the variable stiffness system, the numerical values are defined as follows:

- Coulomb friction terms of the VSS active joints $f_{vss1} = 0.659$ Nm and $f_{vss2} = 0.225$ Nm;
- inertias of the couplings between the motors and springs $J_1 = J_2 = 0.0051$ kg.m^2;
- stiffness constants of the springs $k_{11} = k_{21} = 4.95$ Nm/rad;

The VSS rotor inertia terms J_1 and J_2 were defined according to the motor specifications in [Siemens], whereas the spring constants from the VSS, k_{11} and k_{21}, were defined according to the maximum allowable motor torques, i.e. the springs that resist deformation at maximum load.

The motor parameters used to examine the energetic performance, using the energetic model (2.43), with the proposed approach were defined according to Section 2.4 as well.

The validation of the algorithm was performed by using the dynamic model of the real five-bar mechanism defined in Section 2.4. On the other hand, the VSS dynamics from (2.20) is given by:

$$\boldsymbol{\tau}_{vss} = \mathbf{J}_s \ddot{\mathbf{q}}_s - \boldsymbol{\tau}_s + \begin{bmatrix} f_{vss_1} \mathrm{sign}(\dot{q}_{s1}) \\ f_{vss_2} \mathrm{sign}(\dot{q}_{s2}) \end{bmatrix} \tag{3.11}$$

where $\mathbf{J}_s = \mathrm{diag}(J_1, J_2)$, with J_1 and J_2 being the inertias of the couplings between the motors and the springs.

3.1.2.1 First set of boundary pick-and-place constraints: for constant and variable payload

In order to validate the theoretical formulations, the BVP approach is tested by defining multiple pick-and-place desired points in the workspace of the five-bar mechanism. The aim is to go multiple times to these points by finding the appropriated optimal decision variable vector $\mathbf{s}$ that solves the BVP for the system (3.5)-(3.6) with the desired boundary pick-and-place conditions defined for two different scenarios. The first set of boundary pick-and-place conditions is defined as follows:

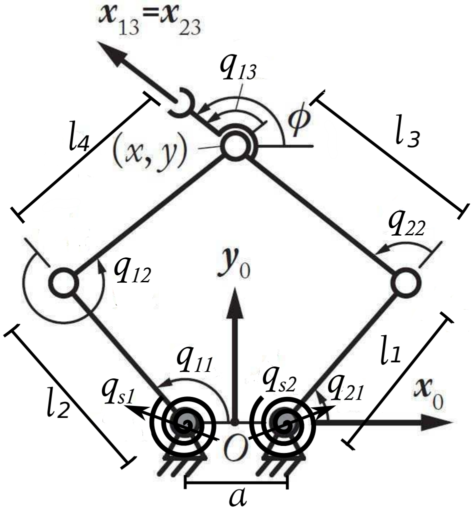

Figure 3.4: Five-bar mechanism parameterization with two actuated joints q_{11} and q_{21}, and three passive joints q_{12}, q_{22} and q_{13}. The variable stiffness torsional springs are located in parallel to the two actuated joints defined by q_{s1} and q_{s2}.

- $A = [0, 0.366], B = [0.2, 0.32], C = [-0.1, 0.4],\ D = [0, 0.42], E = [-0.16, 0.34], F = [0.1, 0.4]$.

The sequence of these conditions is defined at Fig. 3.5. For showing the effectiveness of the proposed approach, the input torques and the energy consumption of two different types of actuation are compared: (i) Nominal actuation, in which there is no spring attached at each joint, and a fifth-degree polynomial trajectory is used between each set of two successive points; (ii) actuation with VSS in parallel with each actuated link of the five-bar mechanism and with the trajectories computed from the shooting method of the BVP. Additionally, it should be noted that in order to show the effectiveness of the energy-efficient motion generator, we will consider the case of constant and variable payload, i.e. an added-mass to the end-effector in each pick-and-place segment.

For the first set of boundary conditions from (Fig. 3.5), the algorithm is tested for a constant end-effector payload (Fig. 3.6 - Fig. 3.9) and for a variable end-effector payload (Fig. 3.10 - Fig. 3.13). The results in input torques for the case of constant payload are shown in Fig. 3.6, Fig. 3.7 and Table 3.1. It can be seen that in both parallel active joints, the input efforts are drastically reduced by using VSS. The torques shown in Fig. 3.8 presents the input torques required to adjust the VSS. It is observed that most of the effort in the full actuation chain comes from the variable stiffness torques. In addition to that, based on the RMS values of the input torques in Table 3.1, it can be seen that

Table 3.1: RMS values of input torques for nominal case and for case when using VSS in parallel (constant payload).

		Nominal RMS. Torques	Using VSS in parallel RMS. Torques	
Segment	Time (s)	$\boldsymbol{\tau}_{\text{RMS}}$ (Nm)	$\boldsymbol{\tau}_{\text{RMS}}$ (Nm)	$\boldsymbol{\tau}_{vss_{\text{RMS}}}$ (Nm)
Fig. 3.5	1.6	[10.96, 8.80]	[0.47, 0.90]	[0.56, 1.88]

the reduction in the full actuation chain, i.e. robot-plus-VSS, can reach 79 % of torque reduction. In terms of energy reduction, from evaluating the energetic model (2.43), in Fig. 3.9, it can be seen that by using VSS, it is possible to reduce the energy up to 70 % in the full actuation chain (robot and VSS) with respect to the nominal case with fifth-degree polynomial trajectory. It is important to mention that the energy reduction percentage takes into account the input torques from both, the robot and the VSS. In this way, the energy consumed from the two additional motors that modify the stiffness are taken into account to analyze the complete energy reduction in the full actuation chain. It is worth mentioning that, with respect to the work in [Goya 2012] where 90 % of reduction is achieved, we do not neglect the energy required to adjust the stiffness from the VSS.

For the case with variable payload, for each segment from Fig. 3.5, there is a different added-mass at the end-effector. The masses added to the end-effector, for each segment, have the following numerical parameters: $A \rightarrow B$ ($0.2\ kg$), $B \rightarrow C$ ($0.5\ kg$), $C \rightarrow D$ ($1\ kg$), $D \rightarrow E$ (only end-effector mass), $E \rightarrow F$ ($0.1\ kg$). It can be seen that for variable payload, the robot input torques (Fig. 3.10, Fig. 3.11 and Table 3.2) are drastically reduced as well, whereas the VSS torques from Figure 3.12 provide most of the efforts in the full actuation chain. In addition to that, based on the RMS values of the input torques in Table 3.2, for variable payload, it can be seen that the reduction in the full actuation chain, i.e. robot-plus-VSS, can reach a torque reduction of 77 %. Finally, Figure 3.13 shows that the energy reduction can reach up to 68 % with respect to the nominal case.

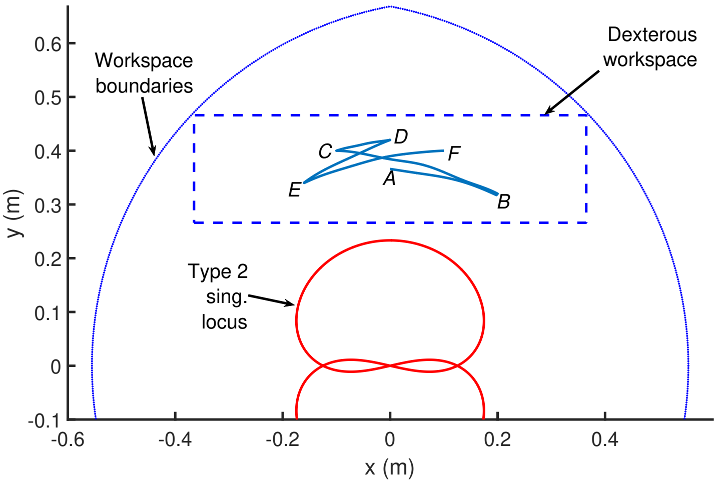

Figure 3.5: Multiple-point pick-and-place sequence in the five-bar mechanism workspace: $A \rightarrow B$ (travel time: 0.2 s), $B \rightarrow C$ (travel time: 0.4 s), $C \rightarrow D$ (travel time: 0.4 s), $D \rightarrow E$ (travel time: 0.2 s), $E \rightarrow F$ (travel time: 0.4 s). The pick-and-place points are connected through the trajectories generated from the shooting method.

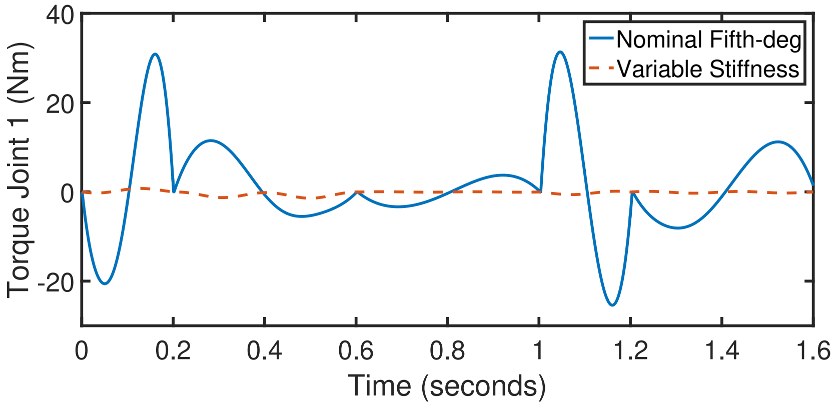

Figure 3.6: Input torques for the first joint of the parallel robot for the two cases: Nominal fifth-degree polynomial and variable stiffness with trajectories from BVP with constant payload.

Table 3.2: RMS values of input torques for nominal case and for case when using VSS in parallel (variable payload).

		Nominal RMS. Torques	Using VSS in parallel RMS. Torques	
Segment	Time (s)	τ_{RMS} (Nm)	τ_{RMS} (Nm)	$\tau_{vss_{\mathrm{RMS}}}$ (Nm)
Fig. 3.5	1.6	[11.24, 9.17]	[0.75, 0.95]	[0.56, 1.98]

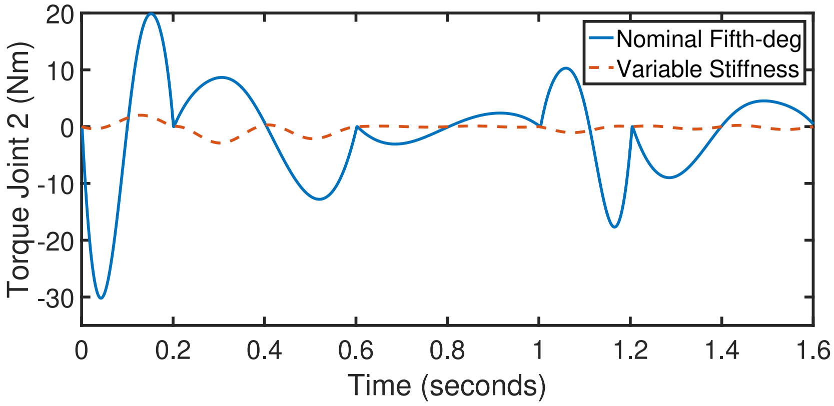

Figure 3.7: Input torques for the second joint of the parallel robot for the two cases: Nominal fifth-degree polynomial and variable stiffness with trajectories from BVP with constant payload.

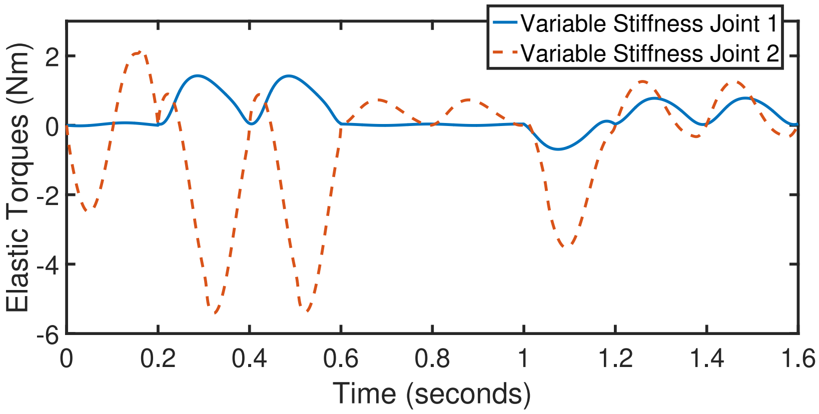

Figure 3.8: Input torques from the joints that actuate the variable stiffness joints from the VSS for the task with constant payload.

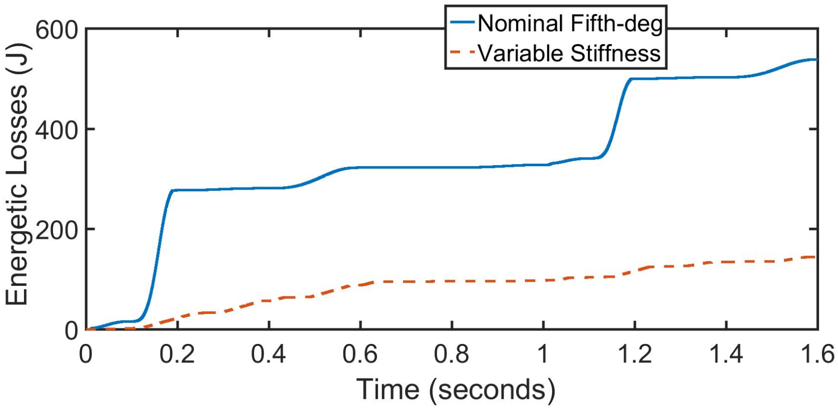

Figure 3.9: Energetic losses for the two cases compared: Nominal fifth-degree polynomial and variable stiffness with trajectories from BVP with constant payload.

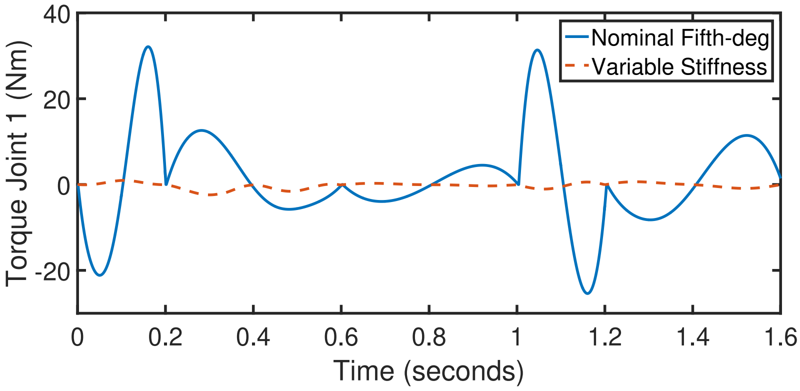

Figure 3.10: Input torques for the first joint of the parallel robot for the two cases: Nominal fifth-degree polynomial and variable stiffness with trajectories from BVP with variable payload.

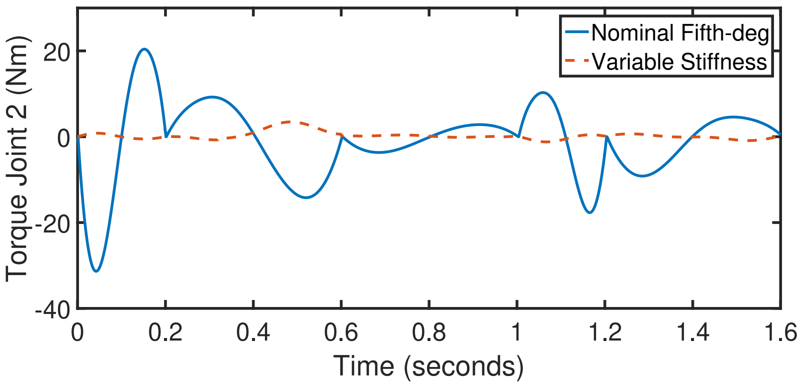

Figure 3.11: Input torques for the second joint of the parallel robot for the two cases: Nominal fifth-degree polynomial and variable stiffness with trajectories from BVP with variable payload.

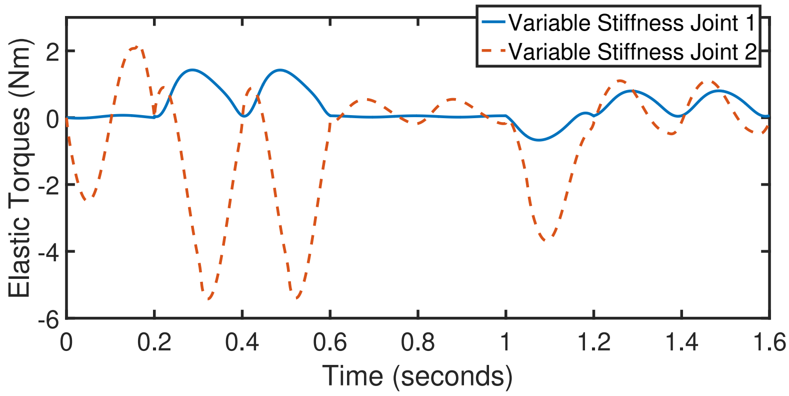

Figure 3.12: Input torques from the joints that actuate the variable stiffness joints from the VSS for the task with variable payload.

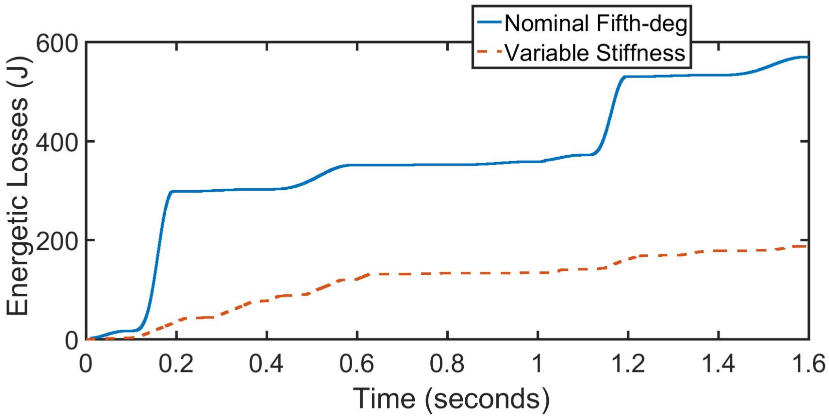

Figure 3.13: Energetic losses for the two cases compared: Nominal fifth-degree polynomial and variable stiffness with trajectories from BVP with variable payload.

3.1.2.2 Second set of boundary pick-and-place constraints: for constant and variable payload

The second set of boundary pick-and-place conditions is defined as follows:

- $A = [0, 0.366], B = [0.2, 0.45], C = [-0.1, 0.4], D = [0.1, 0.35], E = [-0.25, 0.43], F = [0, 0.45]$.

For the second set of boundary constraints for the pick-and-place task shown in Fig. 3.14, the algorithm is tested as well for a constant end-effector payload and for a variable end-effector payload. The results in input torques for the case of constant payload are shown in Table 3.3. It can be seen that in both parallel active joints, the input efforts are drastically reduced by using VSS. Additionally, it is worth noticing that most of the

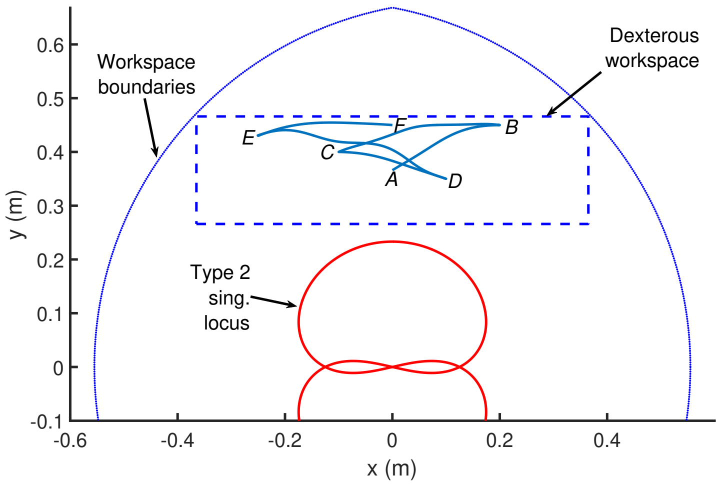

Figure 3.14: Multiple-point pick-and-place sequence in the five-bar mechanism workspace: $A \rightarrow B$ (travel time: 0.2 s), $B \rightarrow C$ (travel time: 0.4 s), $C \rightarrow D$ (travel time: 0.2 s), $D \rightarrow E$ (travel time: 0.4 s), $E \rightarrow F$ (travel time: 0.2 s). The pick-and-place points are connected through the trajectories generated from the shooting method.

efforts in the full actuation chain comes from the adjustment of the VSS. In addition to that, based on the RMS values of the input torques in Table 3.3 for both the robot and the VSS input torques, it can be seen that the reduction in the full actuation chain, i.e. robot-plus-VSS, can reach 74 % of torque reduction.

In terms of energy reduction, from evaluating the energetic model (2.43), in Fig. 3.15, it can be seen that by using VSS, it is possible to reduce the energy up to 72 % in the full actuation chain (robot and VSS) with respect to the nominal case in which a fifth-degree polynomial trajectory with no elastic element is used. It is important to recall that the percentage of energy reduction takes into account the input torques from both the robot and the VSS.

For the case with variable payload, the added-masses at the end-effector, for each segment from Fig. 3.14 are defined same as for the first set boundary constraints. It can be seen that for the case of variable payload, the robot input torques shown in Table 3.4 for the full actuation chain, are drastically reduced as well. In addition to that, it can be observed that the VSS torques computed along the given desired trajectory provide most of the efforts in the full actuation chain. Based on the RMS values of the input torques in Table 3.4, for variable payload, it can be seen that the reduction in the full actuation chain, i.e. robot-plus-VSS, can reach a torque reduction of 73 %. Finally, Figure 3.13 shows that the energy reduction can reach up to 70 % with respect to the nominal case

Table 3.3: RMS values of input torques for nominal case and for case when using VSS in parallel (constant payload).

		Nominal RMS. Torques	Using VSS in parallel RMS. Torques	
Segment	Time (s)	$\boldsymbol{\tau}_{\mathrm{RMS}}$ (Nm)	$\boldsymbol{\tau}_{\mathrm{RMS}}$ (Nm)	$\boldsymbol{\tau}_{vss_{\mathrm{RMS}}}$ (Nm)
Fig. 3.14	1.4	[14.86, 13.94]	[0.51, 1.16]	[2.93, 2.99]

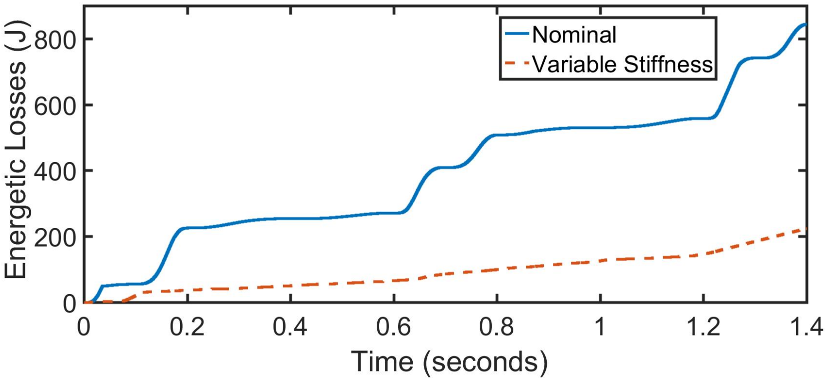

Figure 3.15: Energetic losses for the two cases compared: Nominal fifth-degree polynomial and variable stiffness with trajectories from BVP with constant payload.

Table 3.4: RMS values of input torques for nominal case and for case when using VSS in parallel (variable payload).

		Nominal RMS. Torques	Using VSS in parallel RMS. Torques	
Segment	Time (s)	$\boldsymbol{\tau}_{\mathrm{RMS}}$ (Nm)	$\boldsymbol{\tau}_{\mathrm{RMS}}$ (Nm)	$\boldsymbol{\tau}_{vss_{\mathrm{RMS}}}$ (Nm)
Fig. 3.14	1.4	[15.67, 15.18]	[1.02, 0.97]	[2.91, 3.04]

with variable payload.

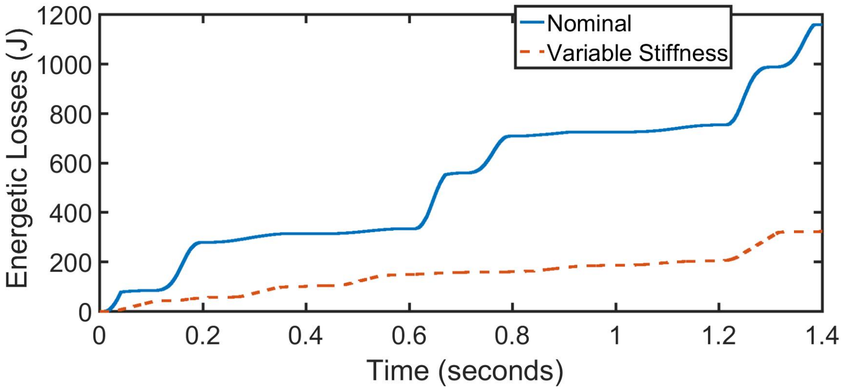

Figure 3.16: Energetic losses for the two cases compared: Nominal fifth-degree polynomial and variable stiffness with trajectories from BVP with variable payload.

3.1.3 Application of the energy-efficient motion generator to a Delta robot with VSS: for constant and variable payload

In order to show the effectiveness of the proposed approach, this Section presents the results of using VSS and the BVP formulation for exploiting quasi-periodic pick-and-place oscillations on spatial parallel robots. The case study presented in this Section is a 3-DOF Delta robot shown in Fig. 3.17. It consists of a base (1) in which three articulated links (2) provide the actuation of the robot in order to move the platform (4), and each articulated arm is connected to a pair of parallel rods (3). Furthermore, three torsional springs (5) are connected in parallel to the articulated links in order to create the variable stiffness system. The actuation of the three articulated arms is provided by $\mathbf{q} = [q_1, q_2, q_3]^T$. The vector of platform pose is given by $\mathbf{x} = [x, y, z]^T$. The actuation of the variable stiffness joints is given by $\mathbf{q}_s = [q_{s1}, q_{s2}, q_{s3}]^T$.

The numerical values of the dynamic parameters for the Delta robot were defined according to a real 3-DOF Delta robot from MG-Tech [MG-Tech], with the following values:

- platform mass (4): 0.72 kg;
- proximal links mass and inertia, respectively (2): 0.82 kg and 0.017 kg.m^2 about its center of mass, located at a distance of 0.115 m from the rotation center of the motors q_i;
- parallelogram mass and inertia, respectively (3): 0.68 kg and 0.024 kg.m^2 about its center of mass, located at the middle of the parallelogram;

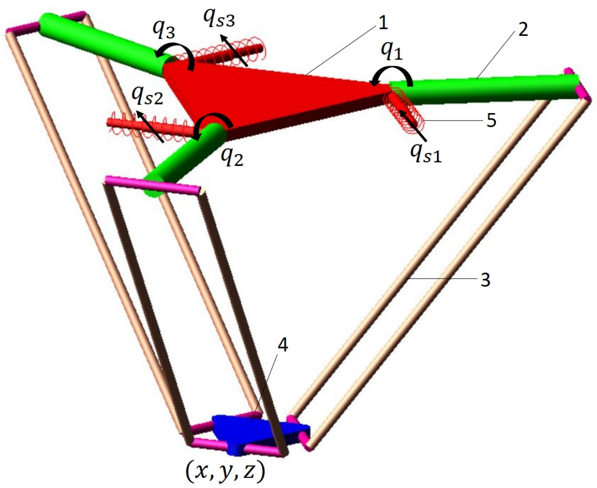

Figure 3.17: Delta robot parameterization with three actuated joints q_1, q_2 and q_3. The variable stiffness torsional springs are located in parallel to the three actuated joints defined by q_{s1}, q_{s2} and q_{s3}.

- Coulomb friction terms of the actuated joints $f_{s1} = f_{s2} = f_{s3} = 0.45$ Nm;

The dynamic parameters related to the VSS system (J_1, J_2, J_3 and k_1, k_2, k_3) were defined same as for the five-bar mechanism. The dynamic equations of the Delta robot with VSS are computed by using the Lagrange formalism shown in Section 2, and their expressions are given in Appendix B.

3.1.3.1 First set of boundary pick-and-place constraints: for constant and variable payload

In order to analyze the energetic losses on the Delta robot with the proposed BVP approach, the desired boundary pick-and-place conditions for the algorithm presented in Section 3.1.1.2, are defined for two sets of boundary constraints. The first set of boundary constraints is defined as follows:

- $G = [0, 0, -0.706]$, $H = [-0.5, -0.5, -0.5]$, $I = [-0.1, -0.2, -0.7]$, $J = [-0.3, -0.4, -0.6]$, $K = [-0.1, -0.6, -0.55]$, $L = [-0.5, -0.5, -0.6]$.

The sequence of these boundary conditions is defined according to Fig. 3.18–Fig. 3.19. For the first case, i.e. first set of boundaries, based on the RMS values of the input efforts of the Delta robot on Table 3.5 and from Fig. 3.20 to Fig. 3.22, it is possible to observe that by using VSS, a reduction of 75 % in the input torques is achieved with respect to

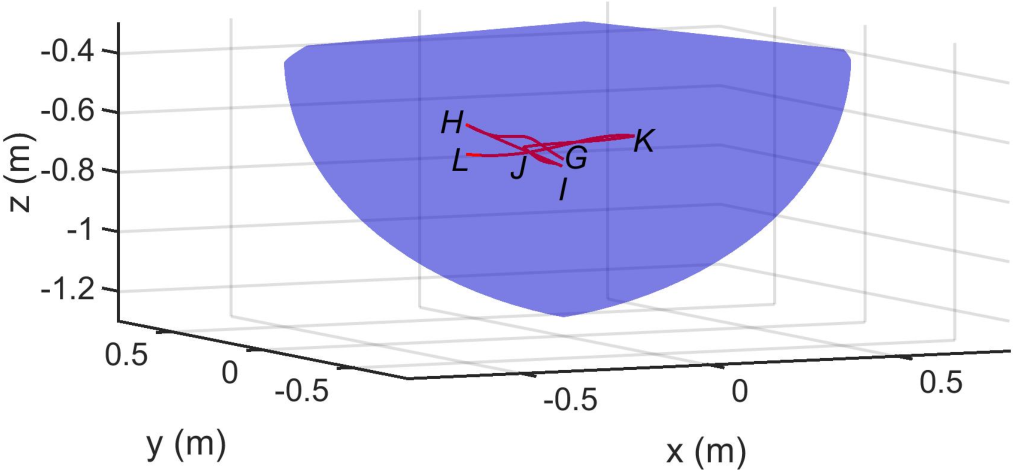

Figure 3.18: Pick-and-place sequence in the workspace of the Delta robot: $G \rightarrow H$ (travel time: 0.12 s), $H \rightarrow I$ (travel time: 0.06 s), $I \rightarrow J$ (travel time: 0.14 s), $J \rightarrow K$ (travel time: 0.08 s), $K \rightarrow L$ (travel time: 0.11 s). The pick-and-place points are connected through the trajectories generated from the shooting method.

the nominal case in which no elastic element is used. Furthermore, the reduction of input torques correspond to the full actuation chain i.e., considering the three active joints of the Delta robot plus the three variable stiffness joints. Finally, Fig. 3.23 shows the energetic losses from model (2.43) for the two different cases, nominal and VSS actuation. It can be seen that by using VSS in parallel with the BVP formulation it is possible to achieve an energy reduction of 72 % when performing high-speed spatial motions for the Delta robot.

For the case with variable payload for the Delta robot, for the first set of boundary pick-and-place conditions, i.e. Fig. 3.18–Fig. 3.19, there is an added-mass at the end-effector. The masses added to the end-effector of the Delta robot, for each segment, have the following numerical parameters: $G \rightarrow H$ (0.1 kg), $H \rightarrow I$ (0.5 kg), $I \rightarrow J$ (0.35 kg), $J \rightarrow K$ (0.4 kg), $K \rightarrow L$ (0.2 kg). It can be seen that for variable payload, the input torques from the active joints of the Delta robot, based on the input torques RMS values in Table 3.6), are drastically reduced. In addition to that, based on the RMS values of the input torques in Table 3.6, for variable payload, it can be seen that the reduction in the full actuation chain, i.e. robot-plus-VSS, can reach a torque reduction of 73 %. Finally, Figure 3.24 shows that the energy reduction can reach up to 71 % with respect to the nominal case.

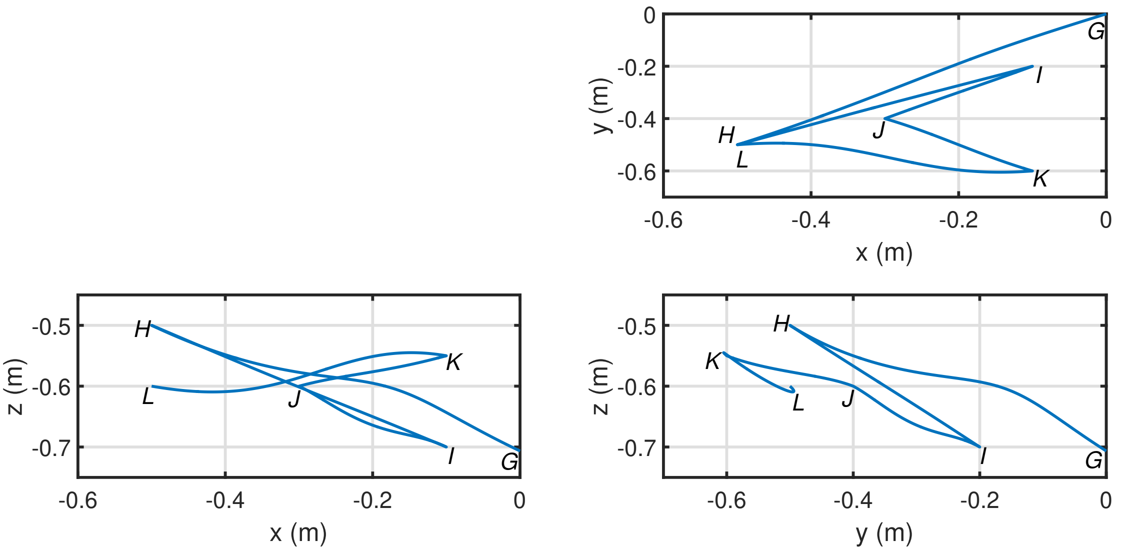

Figure 3.19: Pick-and-place sequence for the Delta robot in the three planes: $G \rightarrow H$ (travel time: 0.12 s), $H \rightarrow I$ (travel time: 0.06 s), $I \rightarrow J$ (travel time: 0.14 s), $J \rightarrow K$ (travel time: 0.08 s), $K \rightarrow L$ (travel time: 0.11 s). The pick-and-place points are connected through the trajectories generated from the shooting method.

Table 3.5: RMS values of input torques for nominal case and for case when using VSS in parallel for the Delta robot for the first set of pick-and-place conditions and for constant payload.

		Nominal RMS. Torques	Using VSS in parallel RMS. Torques	
Segment	Time (s)	$\boldsymbol{\tau}_{\text{RMS}}$ (Nm)	$\boldsymbol{\tau}_{\text{RMS}}$ (Nm)	$\boldsymbol{\tau}_{vss_{\text{RMS}}}$ (Nm)
Fig. 3.18	0.51	[5.65, 3.41, 3.85]	[0.38, 0.41, 0.53]	[0.45, 0.52, 0.59]

Table 3.6: RMS values of input torques for nominal case and for case when using VSS in parallel for the Delta robot for the first set of pick-and-place conditions and for a variable payload.

		Nominal RMS. Torques	Using VSS in parallel RMS. Torques	
Segment	Time (s)	$\boldsymbol{\tau}_{\text{RMS}}$ (Nm)	$\boldsymbol{\tau}_{\text{RMS}}$ (Nm)	$\boldsymbol{\tau}_{vss_{\text{RMS}}}$ (Nm)
Fig. 3.18	0.51	[6.48, 3.67, 4.35]	[0.56, 0.59, 0.58]	[0.65, 0.79, 0.73]

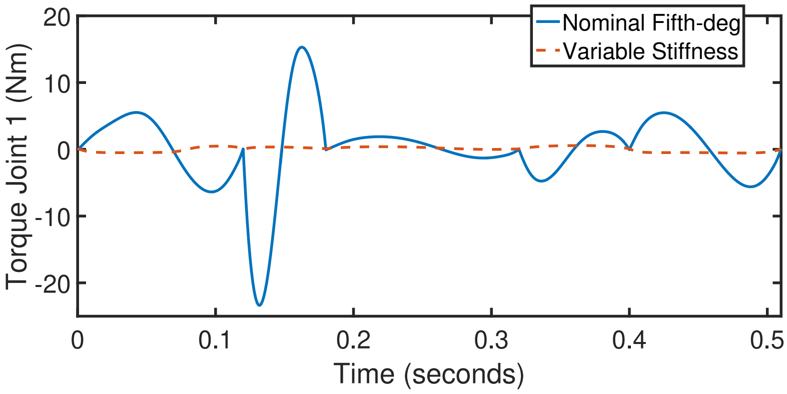

Figure 3.20: Input torques for the first joint of the Delta robot for the two cases: Nominal fifth-degree polynomial and variable stiffness with trajectories from BVP for the first set of pick-and-place conditions and for a constant payload.

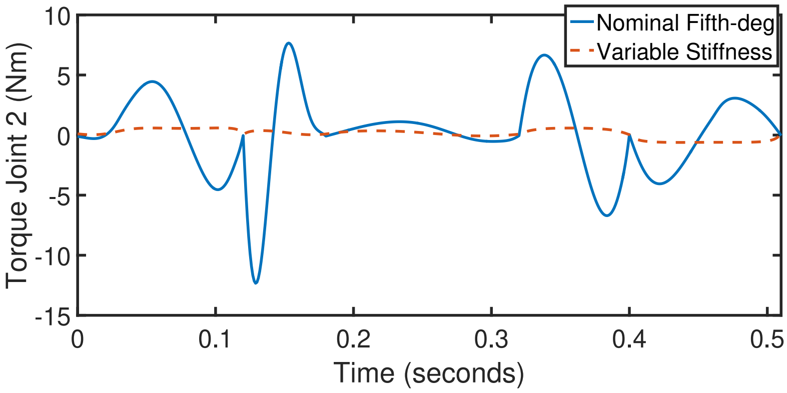

Figure 3.21: Input torques for the second joint of the Delta robot for the two cases: Nominal fifth-degree polynomial and variable stiffness with trajectories from BVP for the first set of pick-and-place conditions and for a constant payload.

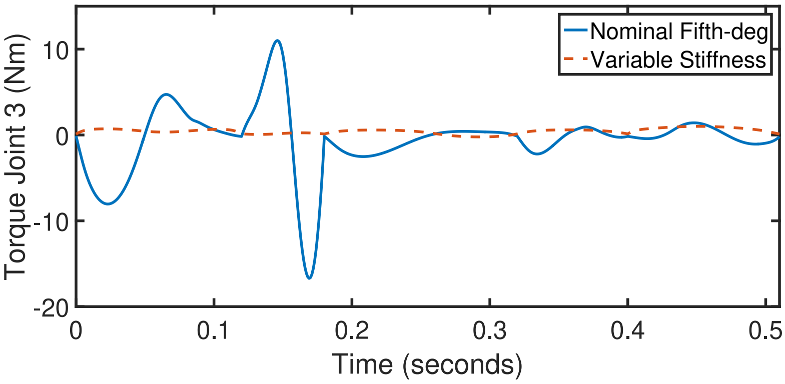

Figure 3.22: Input torques for the third joint of the Delta robot for the two cases: Nominal fifth-degree polynomial and variable stiffness with trajectories from BVP for the first set of pick-and-place conditions and for a constant payload.

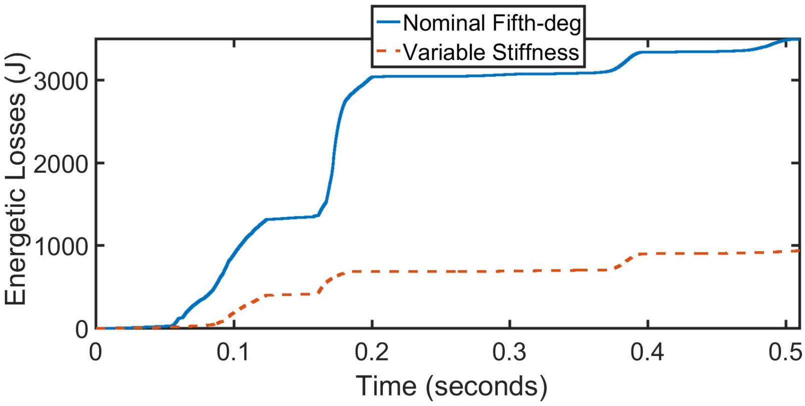

Figure 3.23: Energetic losses for the two cases compared: Nominal fifth-degree polynomial and variable stiffness with trajectories from BVP on the Delta robot for the first set of pick-and-place conditions and for a constant payload.

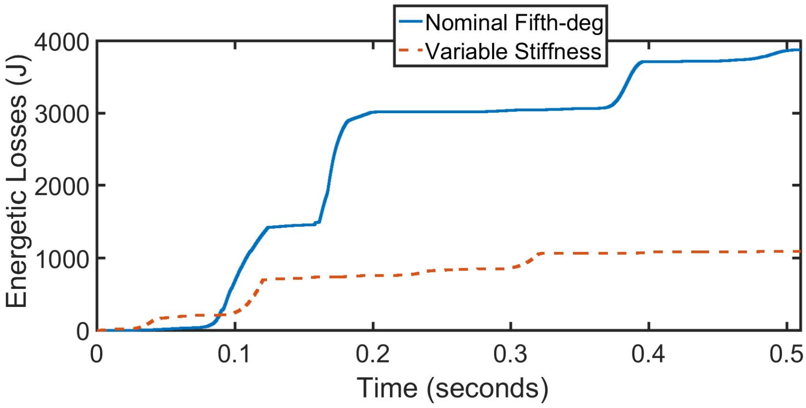

Figure 3.24: Energetic losses for the two cases compared: Nominal fifth-degree polynomial and variable stiffness with trajectories from BVP on the Delta robot for the first set of pick-and-place conditions and for a variable payload.

3.1.3.2 Second set of boundary pick-and-place constraints: for constant and variable payload

The second set of boundary constraints is defined as follows:

- $G = [0, 0, -0.706]$, $H = [0, -0.5, -0.5]$, $I = [-0.5, -0.3, -0.5]$, $J = [-0.5, -0.4, -0.7]$, $K = [-0.5, -0.1, -0.5]$, $L = [-0.1, -0.5, -0.5]$, $M = [-0.1, -0.6, -0.7]$.

For the second set of boundary conditions (Fig. 3.25–Fig. 3.26), the RMS values of the input efforts of the Delta robot for the case of constant payload are shown in Table 3.7 and from Fig. 3.27 to Fig. 3.29. It is possible to observe that by using VSS, a reduction of 78 % in the input torques of the full actuation chain is reached. Finally, Fig. 3.30 shows the energetic losses for the two different cases of actuation, nominal and with VSS. It can be seen that by using VSS in parallel with the BVP formulation it is possible to achieve an energy reduction of 71 % when performing high-speed motions for the Delta robot in the second set of conditions for the pick-and-place sequence.

For the case with variable payload for the Delta robot, for the second set of boundary pick-and-place conditions, i.e. Fig. 3.25–Fig. 3.26, there is an added-mass at the end-effector. The masses added to the end-effector of the Delta robot, for each segment, have the following numerical parameters: $G \to H$ ($0.5\ kg$), $H \to I$ ($0.8\ kg$), $I \to J$ ($0.2\ kg$), $J \to K$ ($0.9\ kg$), $K \to L$ ($0.1\ kg$), $L \to M$ ($0.5\ kg$). It can be seen that for variable payload, the input torques from the active joints of the Delta robot, based on the input torques RMS values in Table 3.8), are drastically reduced. In addition to that, based on the RMS values of the input torques in Table 3.8, for variable payload, it can be seen

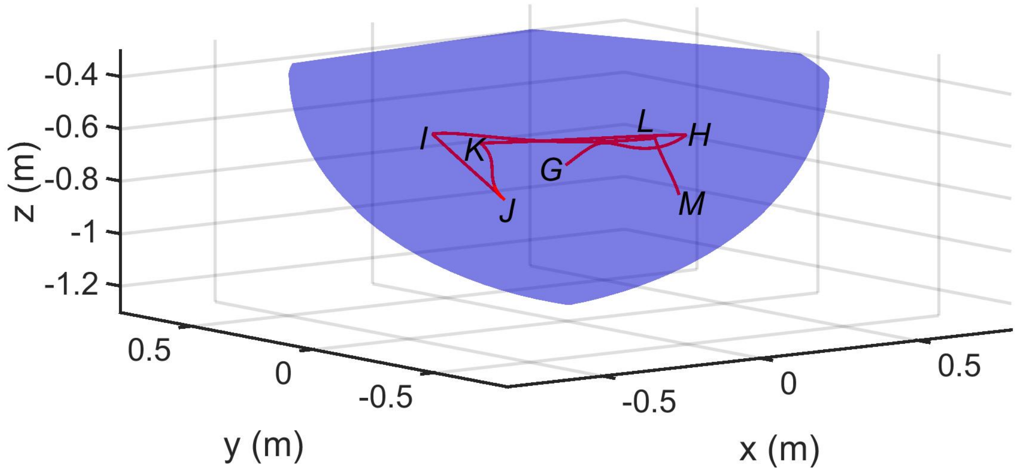

Figure 3.25: Pick-and-place sequence for the Delta robot: $G \rightarrow H$ (travel time: 0.12 s), $H \rightarrow I$ (travel time: 0.06 s), $I \rightarrow J$ (travel time: 0.1 s), $J \rightarrow K$ (travel time: 0.06 s), $K \rightarrow L$ (travel time: 0.1 s), $L \rightarrow M$ (travel time: 0.08 s). The pick-and-place points are connected through the trajectories generated from the shooting method.

Table 3.7: RMS values of input torques for nominal case and for case when using VSS in parallel for the Delta robot for the second set of pick-and-place conditions and for a constant payload.

		Nominal RMS. Torques	Using VSS in parallel RMS. Torques	
Segment	Time (s)	$\boldsymbol{\tau}_{\text{RMS}}$ (Nm)	$\boldsymbol{\tau}_{\text{RMS}}$ (Nm)	$\boldsymbol{\tau}_{vss_{\text{RMS}}}$ (Nm)
Fig. 3.25	0.52	[5.35, 6.53, 3.89]	[0.47, 0.51, 0.60]	[0.52, 0.58, 0.65]

that the reduction in the full actuation chain, i.e. robot-plus-VSS, can reach a torque reduction of 75 %. Finally, Figure 3.31 shows that the energy reduction can reach up to 69 % with respect to the nominal case.

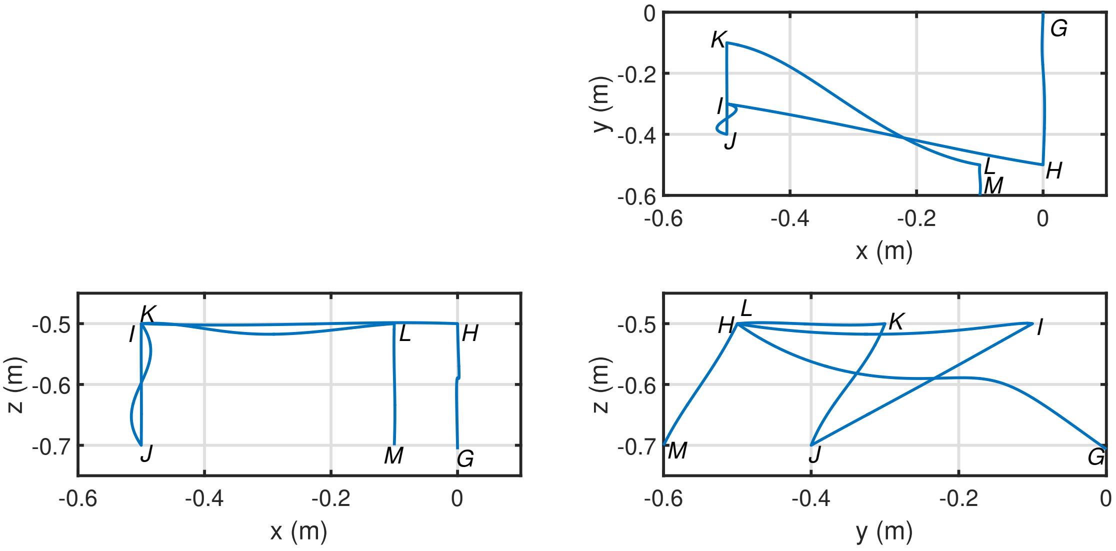

Figure 3.26: Pick-and-place sequence for the Delta robot in the three planes: $G \rightarrow H$ (travel time: 0.12 s), $H \rightarrow I$ (travel time: 0.06 s), $I \rightarrow J$ (travel time: 0.1 s), $J \rightarrow K$ (travel time: 0.06 s), $K \rightarrow L$ (travel time: 0.1 s), $L \rightarrow M$ (travel time: 0.08 s). The pick-and-place points are connected through the trajectories generated from the shooting method.

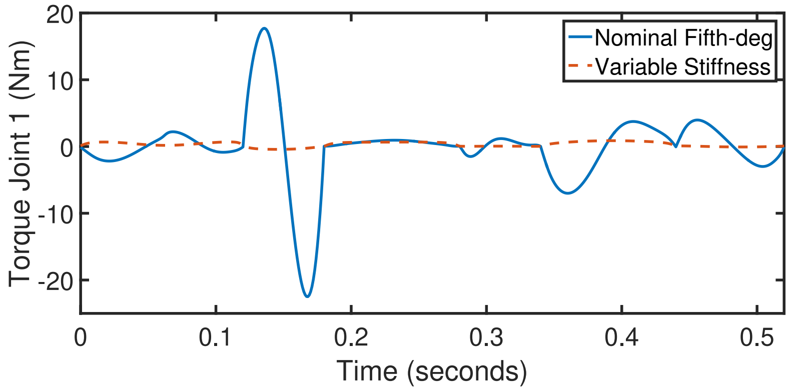

Figure 3.27: Input torques for the first joint of the Delta robot for the two cases: Nominal fifth-degree polynomial and variable stiffness with trajectories from BVP for the second set of pick-and-place conditions and for a constant payload.

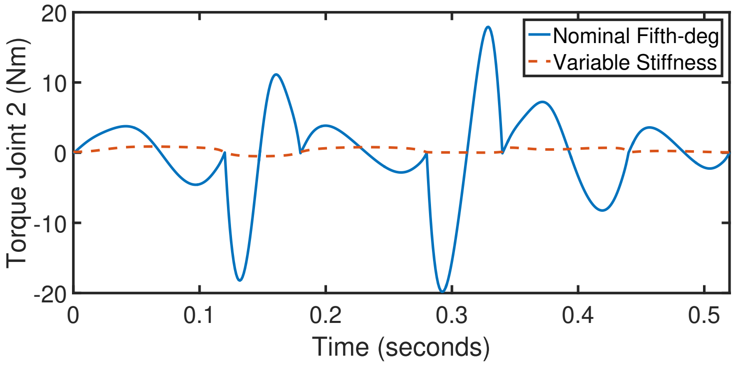

Figure 3.28: Input torques for the second joint of the Delta robot for the two cases: Nominal fifth-degree polynomial and variable stiffness with trajectories from BVP for the second set of pick-and-place conditions and for a constant payload.

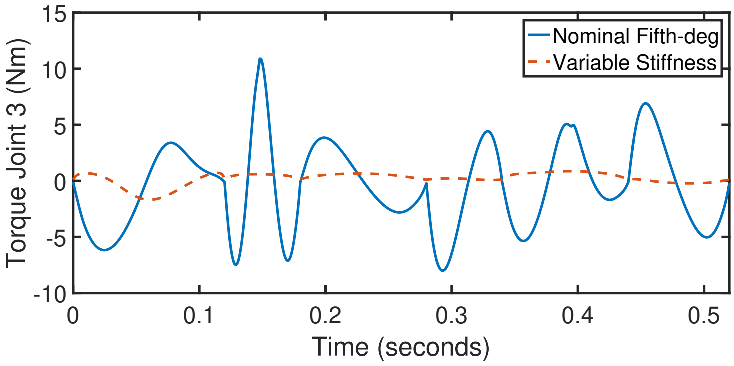

Figure 3.29: Input torques for the third joint of the Delta robot for the two cases: Nominal fifth-degree polynomial and variable stiffness with trajectories from BVP for the second set of pick-and-place conditions and for a constant payload.

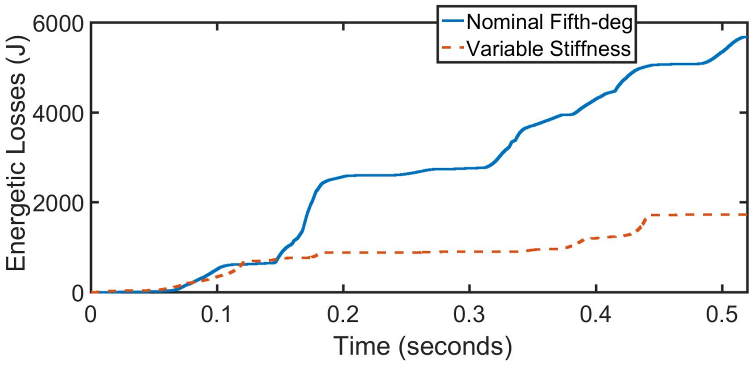

Figure 3.30: Energetic losses for the two cases compared: Nominal fifth-degree polynomial and variable stiffness with trajectories from BVP on the Delta robot for the second set of pick-and-place conditions and for a constant payload.

Table 3.8: RMS values of input torques for nominal case and for case when using VSS in parallel for the Delta robot for the second set of pick-and-place conditions and for a variable payload.

		Nominal RMS. Torques	Using VSS in parallel RMS. Torques	
Segment	Time (s)	τ_{RMS} (Nm)	τ_{RMS} (Nm)	$\tau_{vss_{\text{RMS}}}$ (Nm)
Fig. 3.25	0.52	[6.66, 7.91, 4.16]	[0.56, 0.50, 0.47]	[0.74, 0.87, 0.75]

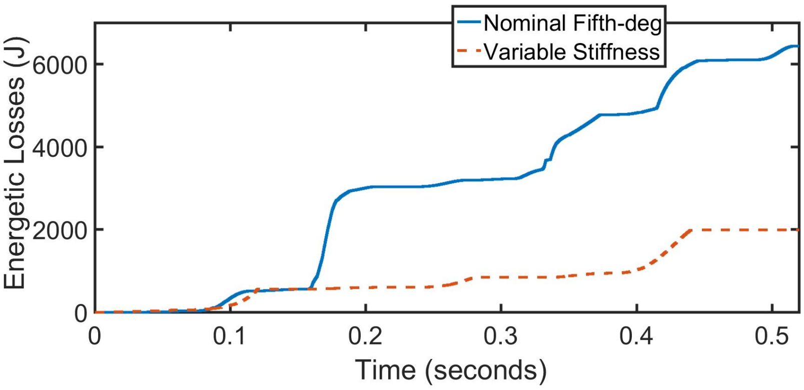

Figure 3.31: Energetic losses for the two cases compared: Nominal fifth-degree polynomial and variable stiffness with trajectories from BVP on the Delta robot for the second set of pick-and-place conditions and for a variable payload.

To summarize, this Section proposes a strategy for generating offline energy-optimal motions in order to increase the energy efficiency of high-speed pick-and-place robots by placing variable stiffness springs (VSS) in parallel to the robot active joints. The VSS in parallel configuration was combined with a boundary value problem in order to find a combined optimal motion of robot and VSS joints, since the optimal VSS stiffness is related to the force/displacement relation τ_s, controlled by $\mathbf{q}_a$ and $\mathbf{q}_s$, respectively. The goal was to match the robot free-response with the desired boundary pick-and-place conditions, defined in the extremities of a finite time interval in order to reach to the *pick* and *place* positions in a given motion time duration with minimum input torques in the full actuation chain. The main drawback of this approach is that it highly relies on the accuracy of the robot dynamic model. That is why, in the next Section a strategy that takes into account the uncertainties on the dynamic parameters will be presented.

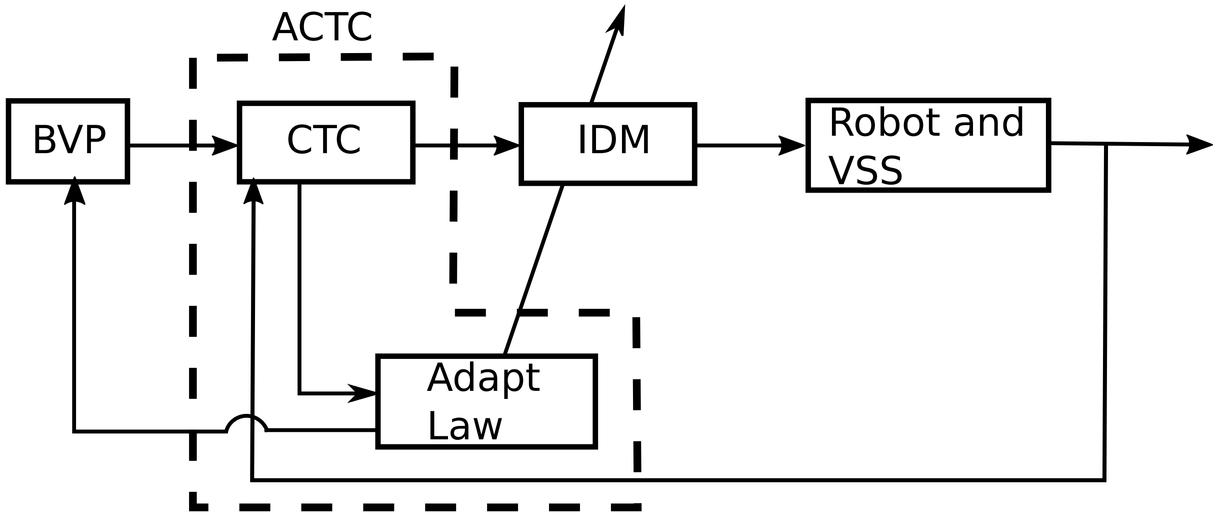

Figure 3.32: Block diagram of online solution of the BVB combined with adaptation law for dealing with dynamics uncertainties.

3.2 Performing energy-efficient pick-and-place motions in the case of unperfectly known dynamic parameters

Since the BVP formulation of previous Section 3.1 highly relies on the accuracy of the dynamic parameters in order to exploit the natural dynamics of the robot with VSS, in this Section a strategy which takes into account uncertainties on the dynamics is presented.

In order to cope with an optimal approach to exploit the natural dynamics of the robot with VSS, even if the dynamic parameters are not accurate, we propose to formulate an online boundary value problem combined with an adaptation law as shown in the block diagram of Fig. 3.32. It should be noted that here the term *online* is used in the sense of updating the optimal robot trajectory based on the current state of the robot and the estimated dynamic parameters from the adaptation law, even if it is not done in real time for the moment.

The general description of each block is as follows:

- BVP: Computes the boundary value problem at each iteration of the control system. It receives the updated parameters from the adaptation block, and the real state (position velocities and accelerations) from the robot;
- Adaptation law: Adjusts the dynamic parameters in order to update the parameters

of the inverse dynamic model, and the physical parameters for computing the BVP;

- Feedback linearization: Also known as Computed Torque Control (CTC), it ensures that the tracking error between the robot states and the desired trajectory generated through the BVP is minimum, thus ensuring accuracy.

Thus, by summarizing the functioning principle of the system in Fig. 3.32, the BVP block serves as a trajectory generator, the CTC will ensure the convergence of the tracking error as close as possible to zero, and finally the adaptation block will perform an online dynamic parameter estimation in order to match the robot-with-VSS model with its inverse model and to update the dynamic parameters of the motion generator.

3.2.1 Online solution of boundary value problem

In order to develop the formulation for solving the BVP online, we will sampled an interval of time $t \in [t_0, t_f]$ into N total number of discrete times t_m $(m = 1, ..., N)$, associated to N points along the parallel robot and VSS trajectories. The total duration of a trajectory generated from the BVP is denoted as t_f and we imposed the duration between two consecutive discrete times to be equal to $\delta = t_f/(N+1)$. According to Fig. 3.33, we thus solve the BVP as follows. Let us consider a sequence of two boundary conditions P_{A_m} and $P_{B_{t_f}}$ on the time interval $t \in [t_0, t_f]$ with $t_m = t_0 + m\delta t$ (P_B will be always fixed at t_f, i.e. $P_{B_{t_f}}$, P_A will change according to the samples $m = 1, ..., N$, and one sample m can be defined at t_0). Therefore, by considering Fig. 3.32, we thus solve the BVP for each P_{A_m} according to the method based on the shooting algorithm in Section 3.1.1.2 as shown in Algorithm 2, in which the main difference with respect to the one in Section 3.1.1.2 is that here, we pass the estimated dynamic parameters represented by $\boldsymbol{\chi}_a$ computed from the adaption law, which will be defined in the next Section. Additionally, from the pseudo-code in Algorithm 2, the function **RK4Dyn** represents the Runge-Kutta method, but now considering the dynamic parameters as variables estimated according to the adaptation law defined in the next Section.

Algorithm 2 : Online BVP applied on robot and VSS jerk equations during the time interval $[t_m, t_f]$ (See Fig. 3.33), and passing estimated dynamic parameters.

```
Input: $i \leftarrow 0, max_i \leftarrow 100$, $t_{int} \leftarrow [t_k, ..., t_f]$, $h > 0$ (integration step), $\mathbf{s}_{k_0} \leftarrow [1, 1, ..., 1]^T$, $t_k > 0$, $t_f > 0$

while $|\mathbf{E}_{q_a}| > \boldsymbol{\epsilon}_1$, $|\mathbf{E}_{\dot{q}_a}| > \boldsymbol{\epsilon}_2$, $|\mathbf{E}_{\ddot{q}_a}| > \boldsymbol{\epsilon}_3$, $|\mathbf{E}_{q_s}| > \boldsymbol{\epsilon}_4$, $|\mathbf{E}_{\dot{q}_s}| > \boldsymbol{\epsilon}_5$, $|\mathbf{E}_{\ddot{q}_s}| > \boldsymbol{\epsilon}_6$, $i \leq max_i$ do

    $[\mathbf{q}_a, \dot{\mathbf{q}}_a, \ddot{\mathbf{q}}_a, \mathbf{q}_s, \dot{\mathbf{q}}_s, \ddot{\mathbf{q}}_s]_i = \mathbf{RK4Dyn}(t_{int}, \mathbf{s}_k, h, (\dddot{\mathbf{q}}_a, \dddot{\mathbf{q}}_s), \boldsymbol{\chi}_a)$ ▷ Numerical integration Runge-Kutta 4-$th$ order of eqs. (3.7)-(3.8), and passing estimated dynamic parameters $\boldsymbol{\chi}_a$

    $[\mathbf{E}(t_f, \mathbf{s}_k)]_i = \begin{cases} \mathbf{E}_{q_a}(\mathbf{s}_k) = \mathbf{q}_a(t_f, \mathbf{s}_k, \boldsymbol{\chi}_a) - \mathbf{q}^*_{atf} \\ \mathbf{E}_{\dot{q}_a}(\mathbf{s}_k) = \dot{\mathbf{q}}_a(t_f, \mathbf{s}_k, \boldsymbol{\chi}_a) - \dot{\mathbf{q}}^*_{tf} \\ \mathbf{E}_{\ddot{q}_a}(\mathbf{s}_k) = \ddot{\mathbf{q}}_a(t_f, \mathbf{s}_k, \boldsymbol{\chi}_a) - \ddot{\mathbf{q}}^*_{atf} \\ \mathbf{E}_{q_s}(\mathbf{s}_k) = \mathbf{q}_s(t_f, \mathbf{s}_k, \boldsymbol{\chi}_a) - \mathbf{q}^*_{stf} \\ \mathbf{E}_{\dot{q}_s}(\mathbf{s}_k) = \dot{\mathbf{q}}_s(t_f, \mathbf{s}_k, \boldsymbol{\chi}_a) - \dot{\mathbf{q}}^*_{stf} \\ \mathbf{E}_{\ddot{q}_s}(\mathbf{s}_k) = \ddot{\mathbf{q}}_s(t_f, \mathbf{s}_k, \boldsymbol{\chi}_a) - \ddot{\mathbf{q}}^*_{stf} \end{cases}$ ▷ BVP errors (* means desired value)

    $[\mathbf{J}]_i = \frac{\partial \mathbf{E}(t_f, \mathbf{s}_k)}{\partial \mathbf{s}_k}$ ▷ Gradients

    $[\Delta \mathbf{s}_k]_i = \mathbf{LMUpdate}(\mathbf{s}_k, \mathbf{J})$ ▷ Levenberg-Marquardt update based on [Moré 1978]

    $[\mathbf{s}_k]_{i+1} = [\mathbf{s}_k]_i + [\Delta \mathbf{s}_k]_i$ ▷ Update of parameter vector $\mathbf{s}_k = [\mathbf{q}_a(t_k), \dot{\mathbf{q}}_a(t_k), \ddot{\mathbf{q}}_a(t_k), \mathbf{q}_s(t_k), \dot{\mathbf{q}}_s(t_k), \ddot{\mathbf{q}}_s(t_k)]^T$

end while

Output: $\mathbf{s}_k$, $\mathbf{q}_a(t_{int}, \mathbf{s}_k), \dot{\mathbf{q}}_a(t_{int}, \mathbf{s}_k), \ddot{\mathbf{q}}_a(t_{int}, \mathbf{s}_k), \mathbf{q}_s(t_{int}, \mathbf{s}_k), \dot{\mathbf{q}}_s(t_{int}, \mathbf{s}_k), \ddot{\mathbf{q}}_s(t_{int}, \mathbf{s}_k)$
```

It should be recalled that i in the aforementioned algorithm, is the integer representing the internal number of iterations for finding the solution of the BVP between P_{A_m} and $P_{B_{t_f}}$ in $[t_0, t_f]$, and m represents the number of time steps in an interval of time $[t_0, t_f]$. Furthermore, it should be noted that the decision variable vector $\mathbf{s}$ (see Section 3.1.1.2), is valued on the time instant $t_k \in [t_m, t_f]$.

Once we have defined the formulation for computing the BVP at each integration time, in the next Subsection, we describe the adaptation law used in order to update online the dynamic parameters grouped in $\boldsymbol{\chi}_a$.

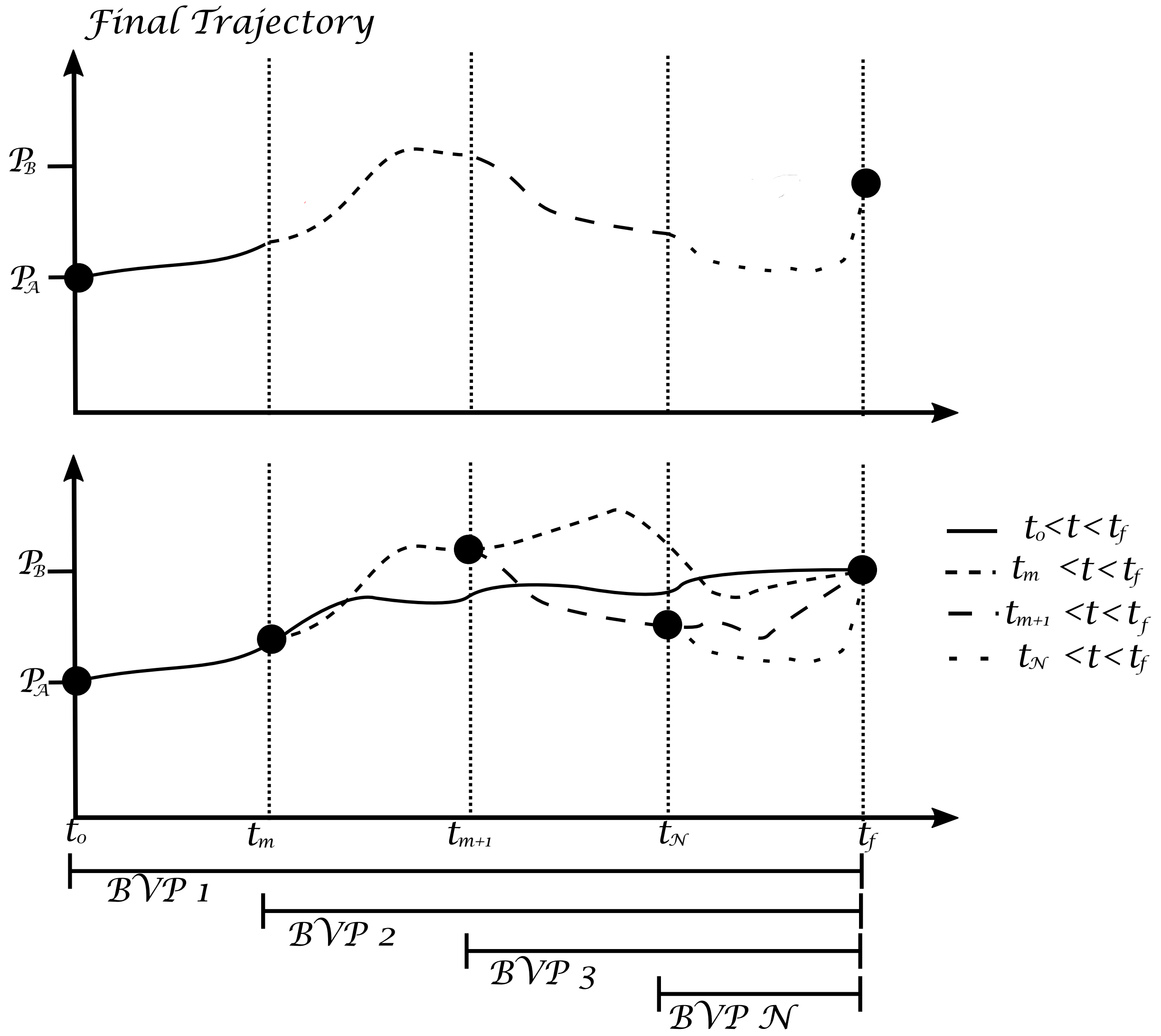
Final Trajectory
$\mathcal{P}_{\mathcal{B}}$
$\mathcal{P}_{\mathcal{A}}$
$t_o<t<t_f$
$t_m<t<t_f$
$t_{m+1}<t<t_f$
$t_{\mathcal{N}}<t<t_f$
t_o
t_m
t_{m+1}
$t_{\mathcal{N}}$
t_f
BVP 1
BVP 2
BVP 3
BVP N

Figure 3.33: BVP solved online for generating the desired optimal trajectories within the control system.

3.2.2 Adaptive feedback linearization

In adaptive control, several approaches exist [Zhang 2017][Middletone 1986][Shang 2012], however, one of the most power and easy-to-implement adaptation law is based on the adaptive computed torque control (ACTC), also known as adaptive feedback linearization [Middletone 1986][Shang 2012]. ACTC is a control technique which allows to estimate online the dynamic parameters of a physical model while the error of the trajectory tracking remain bounded. In addition to that, ACTC has been applied to identify the dynamic parameters in several applications, e.g. parallel robots in [Middletone 1986][Shang 2012], flexible robots in [Lammerts 1995]. Moreover, rigorous mathematical formulations for proving the stability of such control technique has been presented in the works from [Middletone 1986][Shang 2012].

In our application, which consists on generating energy-efficient trajectories based on the dynamic model, it is required to have a good estimation of the dynamic parameters. That is why a control technique such as ACTC seems to be a promising solution to ensure parameter estimation while having a proper trajectory tracking. Thus, in this Section, we will briefly recall the development of an ACTC law based on [Shang 2012]. In addition to that, it should be mentioned that, for our application, the adaptive strategy presented in [Shang 2012] will serve as adaptation law to update the dynamic parameters for the online estimation of the parameters $\boldsymbol{\chi}_a$ from the adaptation block in Fig. 3.32, and which will feed the online BVP. To implement the adaptive control for the robot with VSS, we will separate the dynamic parameters from the robot dynamic model (2.18) in order to obtain a linear parameterized expression with respect to those parameters as follows:

$$\mathbf{M}\ddot{\mathbf{q}}_a + \mathbf{c} + \mathbf{f}_a + \boldsymbol{\tau}_s = \mathbf{Y}_a(\mathbf{q}_a, \dot{\mathbf{q}}_a, \ddot{\mathbf{q}}_a, \mathbf{q}_s)\boldsymbol{\chi}_a \tag{3.12}$$

where $\boldsymbol{\chi}_a$, as previously mentioned, is the vector stacking all the dynamic parameters that we wish to estimate online, and $\mathbf{Y}_a(\mathbf{q}_a, \dot{\mathbf{q}}_a, \ddot{\mathbf{q}}_a, \mathbf{q}_s)$ is the so-called regression matrix [Shang 2012], whose value depends on the active robot coordinates, velocities and accelerations $\mathbf{q}_a$, $\dot{\mathbf{q}}_a$, $\ddot{\mathbf{q}}_a$, respectively, and the variable stiffness coordinates $\mathbf{q}_s$ due to the VSS placed in parallel.

It is worth mentioning that the form of the linear parameterized model (3.12) is the basis of the parameter identification algorithms for the dynamic models of robots (see [Briot 2015c][Gautier 2014]), and for which in this work will serve to synthesize the adaptive law. Additionally, as a remark, the reader should be aware that, for dynamic identification, the matrix $\mathbf{Y}_a(\mathbf{q}_a, \dot{\mathbf{q}}_a, \ddot{\mathbf{q}}_a, \mathbf{q}_s)$ may be found in the literature as observation matrix [Briot 2015c][Gautier 2014]. Furthermore, it should be pointed out that, we will recall the linear parameterized expression (3.12) later in the Chapter 4 of this manuscript when performing the dynamic identification of the experimental prototype.

In order to develop the ACTC, let us consider the tracking error of the active joints of a parallel robot with VSS:

$$\mathbf{e} = \mathbf{q}_{a_d} - \mathbf{q}_a \tag{3.13}$$

$$\dot{\mathbf{e}} = \dot{\mathbf{q}}_{a_d} - \dot{\mathbf{q}}_a \tag{3.14}$$

$$\ddot{\mathbf{e}} = \ddot{\mathbf{q}}_{a_d} - \ddot{\mathbf{q}}_a \tag{3.15}$$

where $\mathbf{q}_{a_d}$, $\dot{\mathbf{q}}_{a_d}$, and $\ddot{\mathbf{q}}_{a_d}$ represent the desired joint position, velocity and acceleration, respectively. In order to enforce the aforementioned tracking errors to tend to zero, a second order differential equation on $\mathbf{e}$ is set by:

$$\ddot{\mathbf{e}} + \mathbf{K}_d\dot{\mathbf{e}} + \mathbf{K}_p\mathbf{e} = \mathbf{0} \tag{3.16}$$

where $\mathbf{K}_p$ and $\mathbf{K}_d$ are symmetric positive definite matrices. By substituting expressions (3.13)–(3.15) into (3.16), it is possible to obtain:

$$\ddot{\mathbf{q}}_a = \ddot{\mathbf{q}}_{a_d} + \mathbf{K}_d\dot{\mathbf{e}} + \mathbf{K}_p\mathbf{e} \tag{3.17}$$

By considering this active joint acceleration term and the CTC law [Spong 1989], it is possible to enforce the input torques $\boldsymbol{\tau}$ from (2.18) as follows:

$$\boldsymbol{\tau} = \hat{\mathbf{M}}(\ddot{\mathbf{q}}_{a_d} + \mathbf{K}_d\dot{\mathbf{e}} + \mathbf{K}_p\mathbf{e}) + \hat{\mathbf{c}}(\mathbf{q}_a, \dot{\mathbf{q}}_a) + \hat{\boldsymbol{\tau}}_s + \hat{\mathbf{f}}_a \tag{3.18}$$

where $\hat{\mathbf{M}}$, $\hat{\mathbf{c}}$, $\hat{\boldsymbol{\tau}}_s$ and $\hat{\mathbf{f}}_a$ are computed from the estimated dynamic parameters. Since the estimated parameters do not match with the real robot parameters, the closed-loop system will not ensure the convergence of (3.16). Therefore, the following adaptation law is synthesized. By combining expressions (2.18) and the control law (3.18), it is possible to obtain:

$$\ddot{\mathbf{q}}_{a_d} + \hat{\mathbf{M}}^{-1}\hat{\mathbf{c}} + \hat{\mathbf{M}}^{-1}\hat{\mathbf{f}}_a + \mathbf{K}_d\dot{\mathbf{e}} + \mathbf{K}_p\mathbf{e} = \hat{\mathbf{M}}^{-1}(\mathbf{M}\ddot{\mathbf{q}}_a + \mathbf{c} + \mathbf{f}_a + \boldsymbol{\tau}_s) \tag{3.19}$$

which can be rewritten as:

$$\ddot{\mathbf{e}} + \mathbf{K}_d\dot{\mathbf{e}} + \mathbf{K}_p\mathbf{e} = \hat{\mathbf{M}}^{-1}(\mathbf{M}\ddot{\mathbf{q}}_a + \mathbf{c} + \mathbf{f}_a + \boldsymbol{\tau}_s - (\hat{\mathbf{M}}\ddot{\mathbf{q}}_a + \hat{\mathbf{c}} + \hat{\mathbf{f}}_a + \hat{\boldsymbol{\tau}}_s)) \tag{3.20}$$

Thus, by using the linear parameterized model (3.12), the error dynamics become:

$$\ddot{\mathbf{e}} + \mathbf{K}_d\dot{\mathbf{e}} + \mathbf{K}_p\mathbf{e} = \hat{\mathbf{M}}^{-1}\mathbf{Y}_a(\mathbf{q}_a, \dot{\mathbf{q}}_a, \ddot{\mathbf{q}}_a, \mathbf{q}_s)(\boldsymbol{\chi}_a - \hat{\boldsymbol{\chi}}_a) \tag{3.21}$$

where $\hat{\boldsymbol{\chi}}_a$ groups the estimated dynamic parameters, and by defining the parameter error

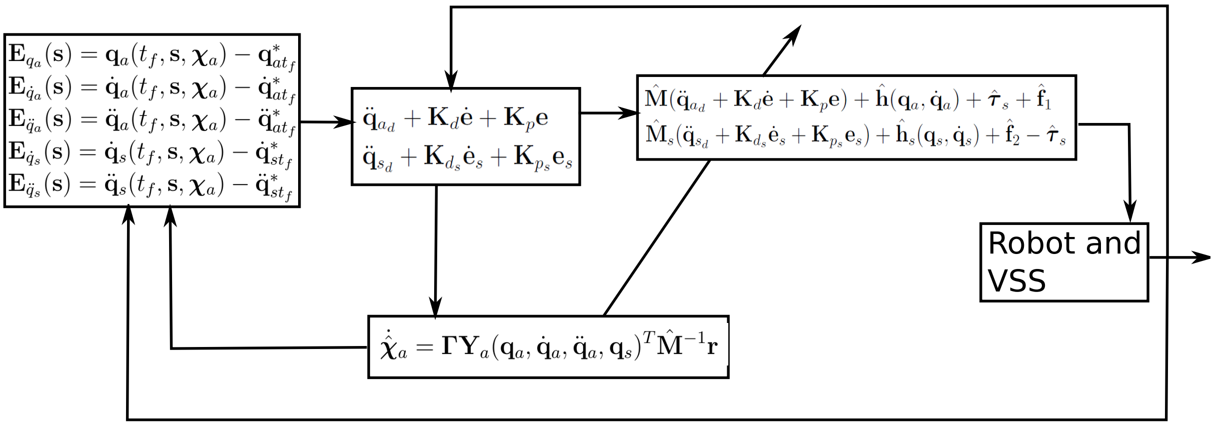
$\mathbf{E}_{q_a}(\mathrm{s}) = \mathbf{q}_a(t_f, \mathrm{s}, \boldsymbol{\chi}_a) - \mathbf{q}^*_{at_f}$
$\mathbf{E}_{\dot{q}_a}(\mathrm{s}) = \dot{\mathbf{q}}_a(t_f, \mathrm{s}, \boldsymbol{\chi}_a) - \dot{\mathbf{q}}^*_{at_f}$
$\mathbf{E}_{\ddot{q}_a}(\mathrm{s}) = \ddot{\mathbf{q}}_a(t_f, \mathrm{s}, \boldsymbol{\chi}_a) - \ddot{\mathbf{q}}^*_{at_f}$
$\mathbf{E}_{\dot{q}_s}(\mathrm{s}) = \dot{\mathbf{q}}_s(t_f, \mathrm{s}, \boldsymbol{\chi}_a) - \dot{\mathbf{q}}^*_{st_f}$
$\mathbf{E}_{\ddot{q}_s}(\mathrm{s}) = \ddot{\mathbf{q}}_s(t_f, \mathrm{s}, \boldsymbol{\chi}_a) - \ddot{\mathbf{q}}^*_{st_f}$
$\ddot{\mathbf{q}}_{a_d} + \mathbf{K}_d\dot{\mathbf{e}} + \mathbf{K}_p\mathbf{e}$
$\ddot{\mathbf{q}}_{s_d} + \mathbf{K}_{d_s}\dot{\mathbf{e}}_s + \mathbf{K}_{p_s}\mathbf{e}_s$
$\hat{\mathbf{M}}(\ddot{\mathbf{q}}_{a_d} + \mathbf{K}_d\dot{\mathbf{e}} + \mathbf{K}_p\mathbf{e}) + \hat{\mathbf{h}}(\mathbf{q}_a, \dot{\mathbf{q}}_a) + \hat{\boldsymbol{\tau}}_s + \hat{\mathbf{f}}_1$
$\hat{\mathbf{M}}_s(\ddot{\mathbf{q}}_{s_d} + \mathbf{K}_{d_s}\dot{\mathbf{e}}_s + \mathbf{K}_{p_s}\mathbf{e}_s) + \hat{\mathbf{h}}_s(\mathbf{q}_s, \dot{\mathbf{q}}_s) + \hat{\mathbf{f}}_2 - \hat{\boldsymbol{\tau}}_s$
Robot and VSS
$\dot{\hat{\boldsymbol{\chi}}}_a = \boldsymbol{\Gamma}\mathbf{Y}_a(\mathbf{q}_a, \dot{\mathbf{q}}_a, \ddot{\mathbf{q}}_a, \mathbf{q}_s)^T\hat{\mathbf{M}}^{-1}\mathbf{r}$

Figure 3.34: Online motion generator, adaptation law and feedback linearization integrated in the complete control scheme.

$\tilde{\boldsymbol{\chi}}_a = \boldsymbol{\chi}_a - \hat{\boldsymbol{\chi}}_a$, the error dynamics in (3.21), becomes:

$$\ddot{\mathbf{e}} + \mathbf{K}_d\dot{\mathbf{e}} + \mathbf{K}_p\mathbf{e} = \hat{\mathbf{M}}^{-1}\mathbf{Y}_a(\mathbf{q}_a, \dot{\mathbf{q}}_a, \ddot{\mathbf{q}}_a, \mathbf{q}_s)\tilde{\boldsymbol{\chi}}_a \tag{3.22}$$

Thus, by using the Lyapunov theory of [Shang 2012], the estimated dynamic parameters $\hat{\boldsymbol{\chi}}_a$ are obtained by imposing a first order dynamic evolution on the estimation error $\tilde{\boldsymbol{\chi}}_a$:

$$\dot{\tilde{\boldsymbol{\chi}}}_a = -\boldsymbol{\Gamma}\mathbf{Y}_a(\mathbf{q}_a, \dot{\mathbf{q}}_a, \ddot{\mathbf{q}}_a, \mathbf{q}_s)^T\hat{\mathbf{M}}^{-1}\mathbf{r} \tag{3.23}$$

where $\boldsymbol{\Gamma}$ is symmetric positive definite matrix and $\mathbf{r}$ is a function of the error signal for the joint positions and velocities in order to know at which rate to change the parameter estimation:

$$\mathbf{r} = \dot{\mathbf{e}} + \boldsymbol{\Lambda}\mathbf{e} \tag{3.24}$$

with $\boldsymbol{\Lambda}$ representing a diagonal matrix of positive entries.

Considering that the changing rate of the actual parameter vector $\boldsymbol{\chi}_a$ is very slow with respect to the changing of the estimated value $\hat{\boldsymbol{\chi}}_a$ [Shang 2012], $\dot{\boldsymbol{\chi}}_a$ can be omitted, leading to $\dot{\tilde{\boldsymbol{\chi}}}_a = 0 - \dot{\hat{\boldsymbol{\chi}}}_a$, and therefore the parameter adaptation law can be computed as:

$$\dot{\hat{\boldsymbol{\chi}}}_a = \boldsymbol{\Gamma}\mathbf{Y}_a(\mathbf{q}_a, \dot{\mathbf{q}}_a, \ddot{\mathbf{q}}_a, \mathbf{q}_s)^T\hat{\mathbf{M}}^{-1}\mathbf{r} \tag{3.25}$$

It is worth noticing that since at high-speeds the preponderant dynamic parameters are associated to the inertial effects of the parallel robot, which are grouped in matrix $\mathbf{M}$, the adaptation law is developed for the robot-plus-VSS model (2.18). Nevertheless, in similar way, it could be extended also to the dynamics of the VSS in (2.20).

Finally, from the aforementioned computations, Fig. 3.34 shows the block diagram in detailed with the expressions required in each block of the control scheme.

3.2.3 Application of the online motion generator to a five-bar mechanism with VSS

For validating the aforementioned theoretical formulations for performing online energy-efficient high-speed motions with unperfectly known dynamic parameters, the control scheme from Fig. 3.34 is tested by defining multiple pick-and-place desired points in the workspace of a five-bar mechanism as shown in Fig. 3.35. The aim is to go multiple times to these points defined as follows: $A = [0, 0.4], B = [0.15, 0.32], C = [-0.15, 0.4]$, $D = [0.2, 0.4], E = [-0.1, 0.37], F = [0.15, 0.35]$. The sequence of these conditions is defined at Fig. 3.35. Additionally, in order to analyze the influence of the dynamic parameters when computing the optimal robot trajectory thanks to the BVP, we will study the algorithm for two cases: *i*) without considering the adaptive law and with biased parameters, i.e. false parameters, and *ii*) by considering the adaptive law in the control scheme.

In order to validate that even with unperfectly known parameters it is possible to perform energy-efficient motions, we will assume that the regrouped inertial parameters zz_{11R} and zz_{21R} associated to the two robot active joints are unperfectly known, i.e. $\boldsymbol{\chi}_a = [zz_{11R}, z_{21R}]^T$ for the adaptive law. The regrouped inertial effects have been chosen to adapt due to the fact that at high-speeds these parameters are preponderant with respect to the other terms of the dynamic model. Additionally, in [Pagis 2015b] and [Koessler 2018], the sensitivity of the dynamic parameters for a five-bar mechanism has been studied, and the authors have found that the most sensitive parameters for the model are zz_{11R} and zz_{21R}, associated to the inertial effects.

3.2.3.1 Case without adaptive law and unperfectly known parameters

Firstly, here, we present the results from testing the online motion generator from Fig. 3.34 without activating the adaptation law, and with unperfectly known dynamic parameters for the motion generator and the inverse dynamic model of the robot with VSS. This is done in order to show the sensitivity of the BVP-based motion generator to the uncertainty on the inertial parameters. In order to define the unperfectly estimated dynamic

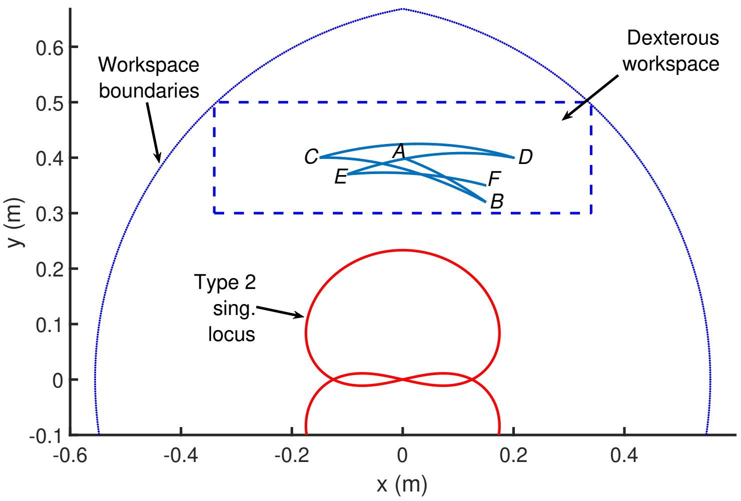

Figure 3.35: Multiple-point pick-and-place sequence in the five-bar mechanism workspace: $A \rightarrow B$ (travel time: 0.3 s), $B \rightarrow C$ (travel time: 0.4 s), $C \rightarrow D$ (travel time: 0.3 s), $D \rightarrow E$ (travel time: 0.4 s), $E \rightarrow F$ (travel time: 0.25 s).

parameters, we will bias the inertia parameters, defined in Section 2.4 for the five-bar mechanism, zz_{11R} and zz_{21R}, respectively by +0.1 kg.m^2. This leads to the following numerical values for the inertial terms: $zz_{11R} = 0.233$ kg.m^2 and $zz_{21R} = 0.222$ kg.m^2.

The input torques computed along the online motion generator without adaptation are shown in Table 3.9. Based on the RMS values for the input torques in the full actuation chain, i.e. robot-plus-VSS, and with unperfectly calibrated inertia parameters, it can be seen that the reduction in the full actuation chain, i.e. robot-plus-VSS, can reach 42 % of torque reduction. Finally, in terms of energy reduction, from evaluating the energetic model (2.43), Fig. 3.36 shows the comparison between the nominal case and the case when using VSS. It can be seen that by using VSS combined with the online motion generator and without activating the adaptation law, i.e. with unperfectly calibrated parameters for the full pick-and-place sequence, it is possible to reduce the energy up to 40 % in the full actuation chain (robot and VSS) with respect to the nominal case.

3.2.3.2 Case with adaptive law

Here, we present the results from testing the online control scheme strategy considering the adaptation of the inertial parameters. The results in input torques are shown in Table 3.10 according to the RMS values for the input torques in the full actuation chain. It can be seen that the reduction in the full actuation chain, i.e. robot-plus-VSS, can reach

Table 3.9: RMS values of input torques for nominal case and for case when using VSS in parallel without using the adaptation law.

		Nominal RMS. Torques	Using VSS in parallel RMS. Torques	
Segment	Time (s)	τ_{RMS} (Nm)	τ_{RMS} (Nm)	$\tau_{vss_{\text{RMS}}}$ (Nm)
Fig. 3.35	1.65	[6.78, 8.51]	[2.24, 2.44]	[1.44, 2.78]

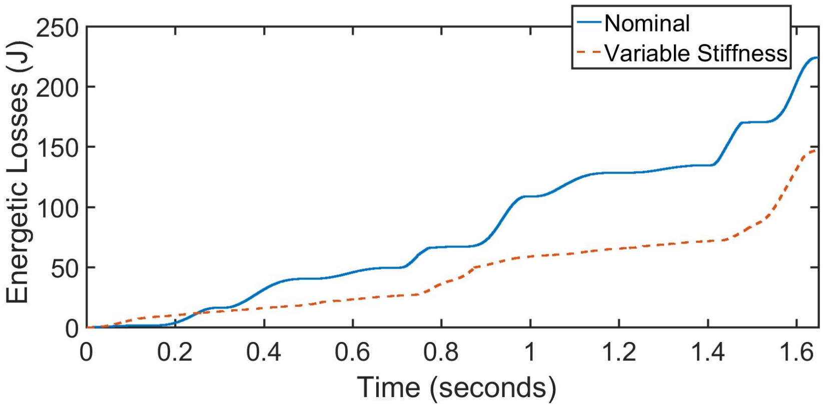

Figure 3.36: Energetic losses for the two cases compared: Nominal and by using VSS.

69 % of torque reduction. Moreover, for showing the effectiveness of the online adaptive law, the evolution for the estimation of the inertial parameters, which feed the online motion generator computed thanks to the BVP, is shown in Fig. 3.37 and Fig. 3.38 for zz_{11R} and zz_{21R}, respectively. It can be seen that, even if initially the inertia parameters are set to have more than 50 % of error with respect to the unbiased inertial parameters, i.e. $zz_{11R} = 0.133$ kg.m^2 and $zz_{21R} = 0.122$ kg.m^2 (see the five-bar parameterization of Section 2.4), the adaptation law successfully ensures the convergence of the biased inertial parameters to the real ones.

Finally, in terms of energy reduction, from evaluating the energetic model (2.43), in Fig. 3.39, it can be seen that by using VSS combined with the online motion generator and the adaptation law, it is possible to drastically reduce the energy up to 67 % in the full actuation chain (robot and VSS) with respect to the nominal case, even if the inertial parameters are unperfectly known. It should be noted that this percentage is lower than when considering perfectly known parameters, which is expected since we are estimating online, the inertial terms, which are the most preponderant physical parameters of the

Table 3.10: RMS values of input torques for nominal case and for case when using VSS in parallel by considering adaptation of the inertial parameters.

		Nominal RMS. Torques	Using VSS in parallel RMS. Torques	
Segment	Time (s)	$\boldsymbol{\tau}_{\text{RMS}}$ (Nm)	$\boldsymbol{\tau}_{\text{RMS}}$ (Nm)	$\boldsymbol{\tau}_{vss_{\text{RMS}}}$ (Nm)
Fig. 3.35	1.65	[6.76, 8.44]	[0.42, 1.13]	[1.17, 2.25]

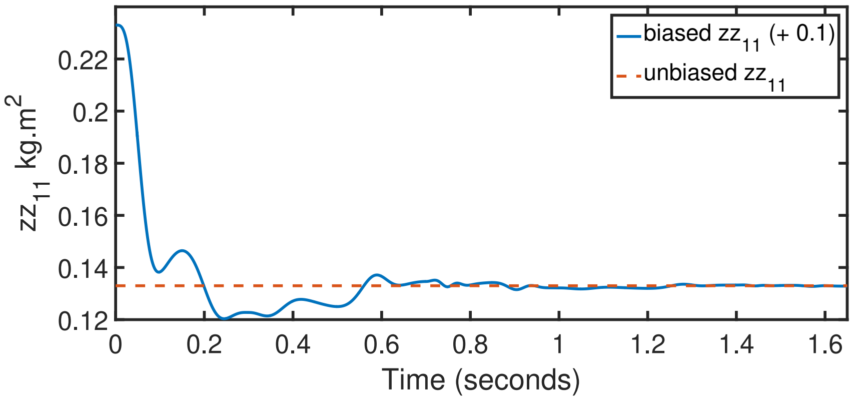

Figure 3.37: Adaptation of inertial parameter zz_{11R}.

robot dynamics at high-speeds. Nevertheless, thanks to the fast convergence of the inertial effects to their real values, the motion generator is able to ensure energy-efficient pick-and-place motions.

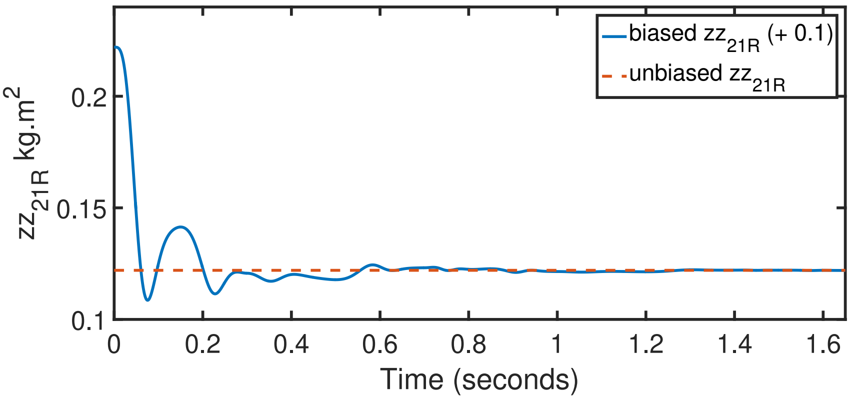

Figure 3.38: Adaptation of inertial parameter zz_{21R}.

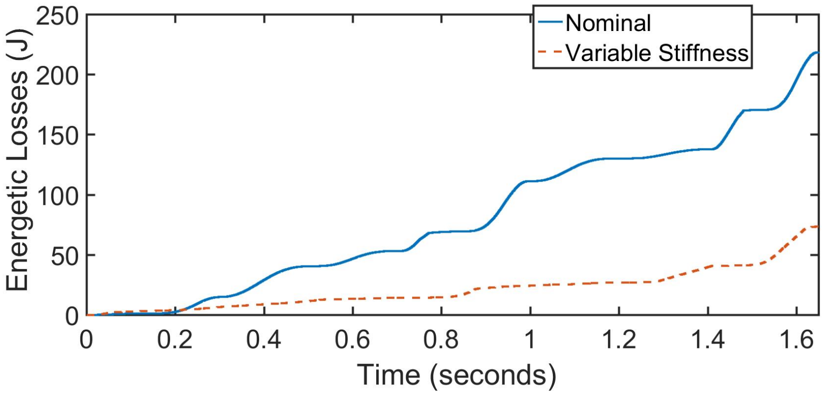

Figure 3.39: Energetic losses for the two cases compared: Nominal and by using VSS.

3.3 Summary

To summarize, this Section proposes a strategy for generating offline energy-optimal motions in order to increase the energy efficiency of high-speed pick-and-place robots by placing variable stiffness springs (VSS) in parallel to the robot active joints. The VSS in parallel configuration was combined with a a strategy that exploits the robot natural dynamics based on boundary value problem in which the algorithm seeks to find a combined optimal motion of robot and VSS joints, since the optimal VSS stiffness is related to the force/displacement relation τ_s, controlled by $\mathbf{q}_a$ and $\mathbf{q}_s$, respectively. The goal was to match the robot free-response with the desired boundary pick-and-place conditions, defined in the extremities of a finite time interval in order to reach to the *pick* and *place* positions in a given motion time duration with minimum input torques in the full actuation chain.

Different to what it has been done in previous works of the state of the art, here, we consider the energy required to adjust the equilibrium position (associated to the VSS stiffness) when analyzing the energetic losses in the full actuation chain. Additionally, the desired pick-and-place trajectories proposed in the simulation results are defined by fast quasi-periodic motions, different to the slow periodic trajectories in [Goya 2012], validating in this way our algorithm for more realistic fast pick-and-place-like tasks. Finally, it is worth noticing that different to [Goya 2012] in which they require of a nonlinear force/displacement relation to generate optimal stiffness profiles, here we do not generate stiffness profiles, but instead VSS joint trajectories, thus exploiting directly the natural dynamics from the physical models by optimizing the force/displacement relation of the VSS.

Simulations led to a considerably increase on the energy efficiency with multiple-point fast quasi-periodic trajectories on a five-bar mechanism and a Delta robot for two cases: nominal with a classical fifth-degree polynomial and by using VSS. Results show that the energy reduction for the five-bar mechanism, in the full actuation chain, i.e. robot-plus-VSS, can reach up to 70–75 % when using VSS for a constant payload, and 65–70 % for a variable payload. For the Delta robot, the results have shown that the energy efficiency can be increased to a 72–75 % when using VSS in the full actuation chain of the parallel robot for a constant payload, and 70–75 % for the case of variable payload. The main drawback of this approach is that it highly relies on the accuracy of the robot dynamic model. That is why in Section 3.2, we proposed a strategy to update online the dynamic parameters thanks to an adaption law implemented within a control scheme in which was feeding the motion generator computed with an online BVP. It should be noted that even if we have shown that it is possible to increase the energy efficiency up to a 67 % even with unperfectly known parameters on a five-bar mechanism, at this time stage, it was not possible to compute the BVP in real time due to the computational complexity of solving the optimization problem. Nevertheless, future work towards the direction of online methods for solving the BVP are included on the perspectives of this research.

Finally, it should be noted that in the simulation results from the offline motion planner presented in this Chapter we have considered perfect trajectory tracking, that is why it is necessary to validate the theoretical formulations experimentally. The next Chapter thus presents the experimental results of the developed offline energy-efficient motion generator on an industrial-sized five-bar mechanism with VSS that I designed in the scope of this thesis.

Chapter 4

Prototype and experimental validations

4.1. *Description of the prototype* p. 126
4.2. *Identification of dynamic parameters* p. 136
4.3. *Experimental results* p. 145
4.4. *Summary* p. 161

This Chapter is devoted to presenting the experimental results for increasing the energy efficiency of high-speed robots. On a first stage, the mechanical design and functioning principle of the experimental industrial-sized prototype will be explained both for the parallel robot and for the variable stiffness system of the VSS. The parallel robot architecture is based on a well-known kinematic structure: a five-bar mechanism, and for the variable stiffness system of the VSS, an actuation mechanism based on a pulley-belt-drive system combined with torsional springs is designed. In addition to that, the hardware and software for the instrumentation and communication of the experimental setup, to control the robot, are detailed.

Then, on a second stage in Section 4.2, the identification of the dynamic parameters is performed in order to implement the dynamic models for the robot and the model of the VSS for the control scheme. Finally, in Section 4.3, the obtained experimental results for the five-bar mechanism with VSS in parallel are shown. It is demonstrated that by using VSS in parallel configuration to the actuated links of the five-bar mechanism, it is possible to reduce the energy consumption for the full actuation chain when performing high-speed quasi-periodic motions, thus validating the actuation concept.

4.1 Description of the prototype

In this Section, the technical aspects of the industrial-sized prototype that I designed and commissioned in the scope of my thesis, to perform the experimental validations of the proposed approach for performing energy-efficient pick-and-place motions, will be explained. The prototype consists of two main parts: *i*) the parallel manipulator, and *ii*) the variable stiffness system. The parallel manipulator is based on a well-known kinematic architecture: a five-bar mechanism, manufactured mainly in aluminum. For the variable stiffness system of the VSS, a pulley-belt-drive transmission mechanism and torsional springs were used. Both parts of the prototype, except for the torsional springs, were manufactured in the laboratories at LS2N, and they will be explained in detail in the following Subsections.

4.1.1 CAD modeling and prototyping of robot and variable stiffness system

Here, the design process and CAD models of the full robot and VSS will be presented, firstly for the five-bar mechanism and then for the variable stiffness system. For the design of the five-bar mechanism, the two serial kinematic chains that constitute the parallel robot are of equivalent dimensions and manufactured in aluminum. According to the CAD model for prototyping the five-mechanism in Fig. 4.1, the robot is thus composed as follows:

- two motors M_1 and M_2 for the actuation of the active joints separated one from each other by a distance of 250 mm;
- two proximal links (actuated links) of dimension equal to 280 mm, and two distal links of dimension equal to 400 mm;
- the links are connected by five revolute joints from which two are active and three are passive;
- the two active joints are parameterized according to Chapter 2 by q_{a_1} and q_{a_2}, respectively;
- the rectangular workspace from Fig. 4.1 represents the operational workspace for the five-bar prototype.

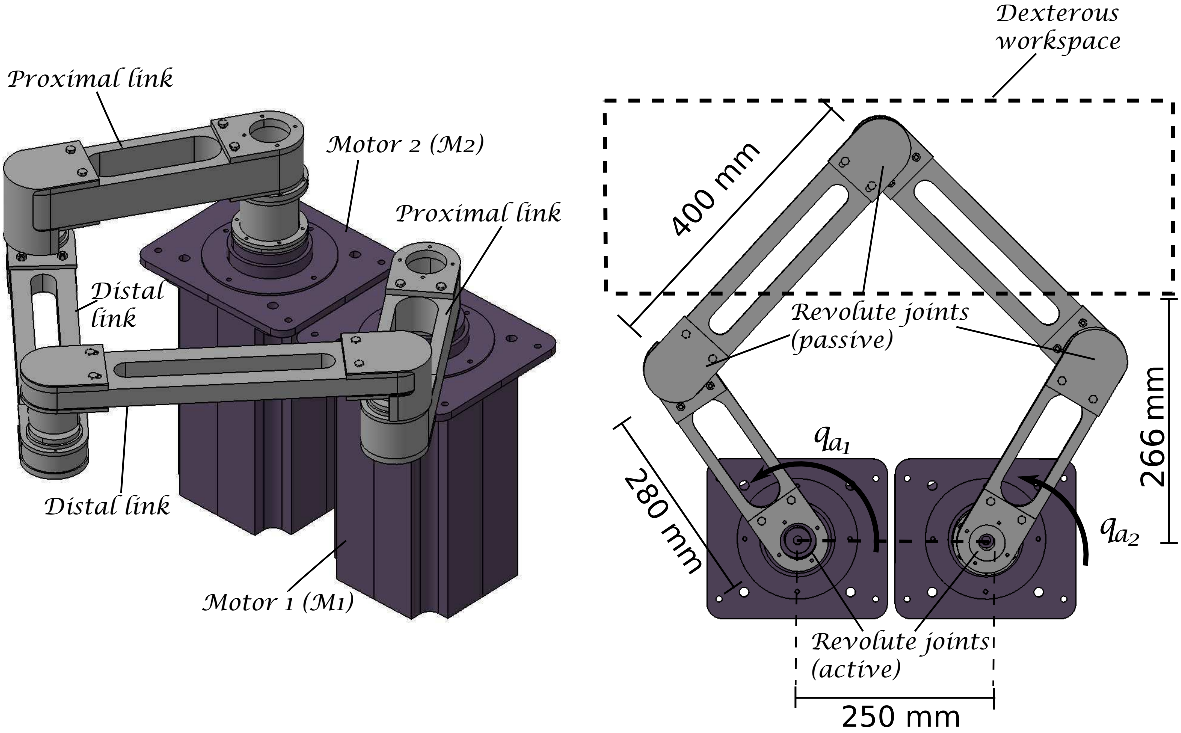

Proximal link
Motor 2 (M2)
Proximal link
Distal link
Distal link
Motor 1 (M1)
Dexterous workspace
400 mm
Revolute joints (passive)
q_{a_1}
280 mm
266 mm
q_{a_2}
Revolute joints (active)
250 mm

Figure 4.1: CAD of five-bar mechanism.

For the variable stiffness system, the design and functioning principle of the VSS are shown in Fig. 4.2 for one of the actuated links of the parallel manipulator. Based on Fig. 4.2, the link-plus-VSS system of each proximal link of the five-bar mechanism is driven by motors ① and ⑧, each of them used for actuating the VSS system (②, ③, ④, ⑤, ⑥) and the robot link ⑦, respectively. As shown in Fig. 4.2, the deformation of the spring ⑥, and therefore the VSS stiffness, can be adjusted by means of two spring anchor points (A_1 and A_2), each of them controlled by a pulley-belt-transmission system (③, ④, ⑤) on the top, associated to variable q_{s_j}, and by the active joint ⑧ of the robot link on the bottom, associated to the variable q_{a_i}. The pulley-belt-transmission system consists of a driving pulley ③, parameterized by q_{s_j}, which transmits the one-to-one ratio to the driven pulley ⑤ connected to the torsional spring ⑥ in parallel with the robot link ⑦.

To calculate the spring specifications of the VSS, in order to define the range of allowable deformations based on the efforts and geometric requirements, the design methodology presented in [Budynas 2006], which is a book of mechanical engineering design for synthesis of mechanisms, is used. According to the spring schematic in Fig. 4.3, to geometrically parameterize the spring of the VSS, it is necessary to take into account: the

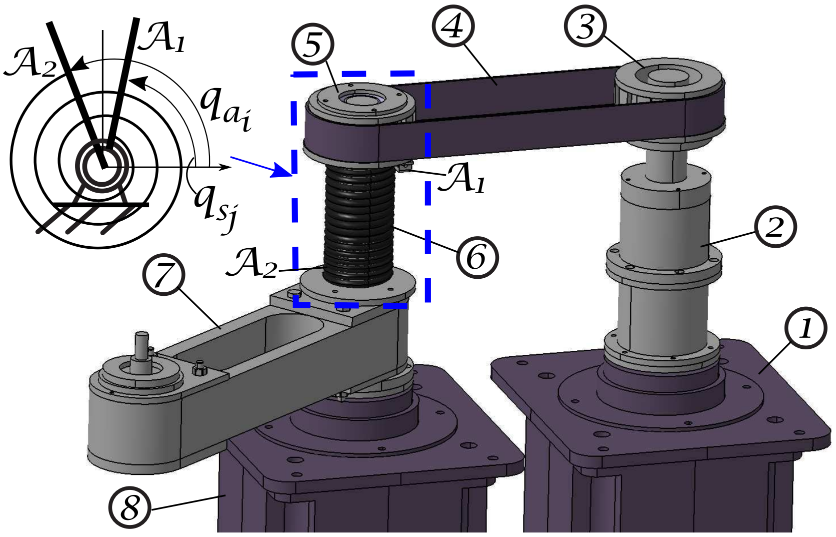
$\mathcal{A}_2$
$\mathcal{A}_1$
q_{a_i}
q_{s_j}
⑤
④
③
$\mathcal{A}_1$
②
$\mathcal{A}_2$
⑥
⑦
①
⑧

Figure 4.2: CAD of variable stiffness system.

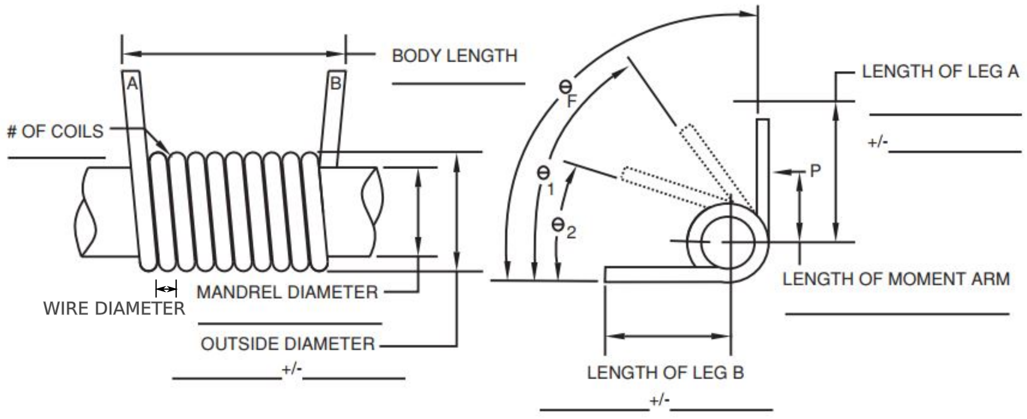
BODY LENGTH
A
B
# OF COILS
WIRE DIAMETER
MANDREL DIAMETER
OUTSIDE DIAMETER
+/-
θ_F
θ_1
θ_2
LENGTH OF LEG A
+/-
P
LENGTH OF MOMENT ARM
LENGTH OF LEG B
+/-

Figure 4.3: Spring schematic

spring wire diameter d_w, spring body turns N_b, pin/mandrel diameter D_{pin}, outside diameter D_{out}, and ending arms length L_1 and L_2. Thus, for a given initial value of these geometric parameters, it is possible to compute:

- Maximum operating torque $\tau_{s_{MAX}}$;
- Corresponding maximum deformation θ_{MAX};
- Spring inner diameter reduction at maximum load D_m;
- Mandrel/pin diametral clearance when the spring is subjected to maximum load $\varDelta$;

- Body length L;
- Minimum required spring stiffness constant k, for the VSS.

It is worth mentioning that the equations characterizing the calculation of the aforementioned specifications can be found on the spring design methodology in [Budynas 2006], and they are as well summarized in Appendix C.

Thus, considering the computations from Appendix C for designing the VSS, the resulted spring specifications for the experimental setup for the variable stiffness system of the VSS, is defined as follows: for a given mandrel diameter $D_{pin} = 32$ mm, outside diameter $D_{out} = 55$ mm, length of spring leg A and B $L_1 = L_2 = 80$ mm, number of coils $N_b = 17$, number of active coils $N_a = 17.12$, the resulted spring specifications are summarized in Table 4.1. It is important to mention that in order to define the geometrical parameters (D_{pin}, D_{out}, L_1, L_2, N_b and N_a) for the spring of the VSS, there was no particular design methodology followed. They were rather defined based on the aspects related to the real robot assembly, such as fixations, motors locations, chassis design, etc.

Table 4.1: Spring specifications

$\tau_{s_{MAX}}$ [Nm]	θ_{MAX} [deg]	D_m [mm]	$\varDelta$ [mm]	L [mm]	k [Nm/rad]
25.70	326.5	46.51	8.5	108.7	4.47

Then, once the specifications for the springs of the VSS were calculated, the torsional springs were manufactured by the provider VIT RESSORTS. Finally, the complete assembly of the VSS in parallel to the actuated links of the five-bar mechanism is shown in the CAD model of Fig. 4.4. In addition to that, the real prototype after the manufacturing process is shown in an isometric perspective in Fig. 4.5 and in a front view in Fig. 4.6.

From the aforementioned VSS design methodology, it is worth to notice that since in the scope of this thesis, the objective is to validate the proof-of-concept of the new energy-efficient actuation principle based on VSS in parallel configuration, the methodology of this Section follows from a classical engineering-based design approach. Nevertheless, the design for the variable stiffness system could be improved by following an optimal-based design approach, for instance to minimize the friction, to optimize the belt tension for a given rang of motions, etc [Carloni 2012][Visser 2011].

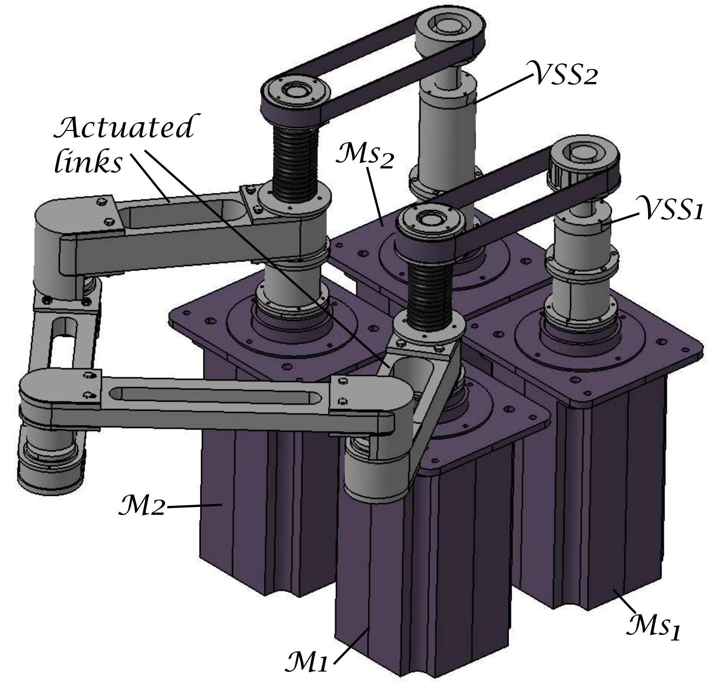
VSS2
Actuated links
Ms2
VSS1
M2
Ms1
M1

Figure 4.4: CAD of five-bar mechanism with VSS in parallel.

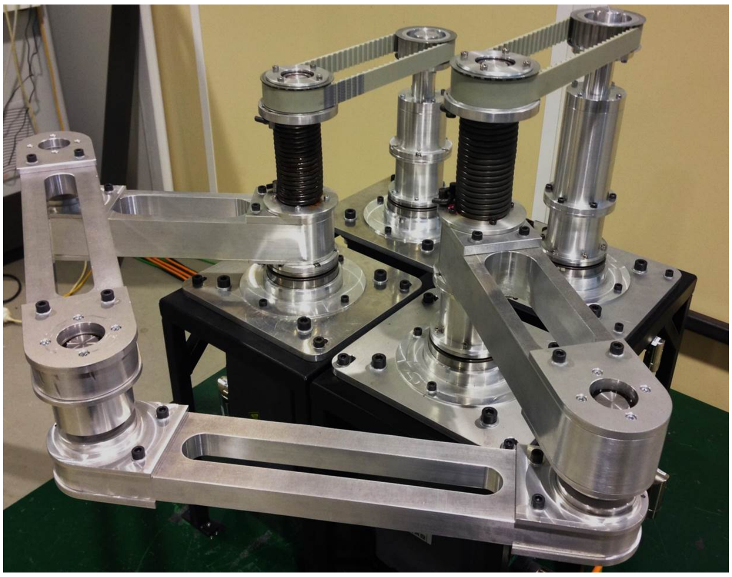

Figure 4.5: Real prototype in isometric view.

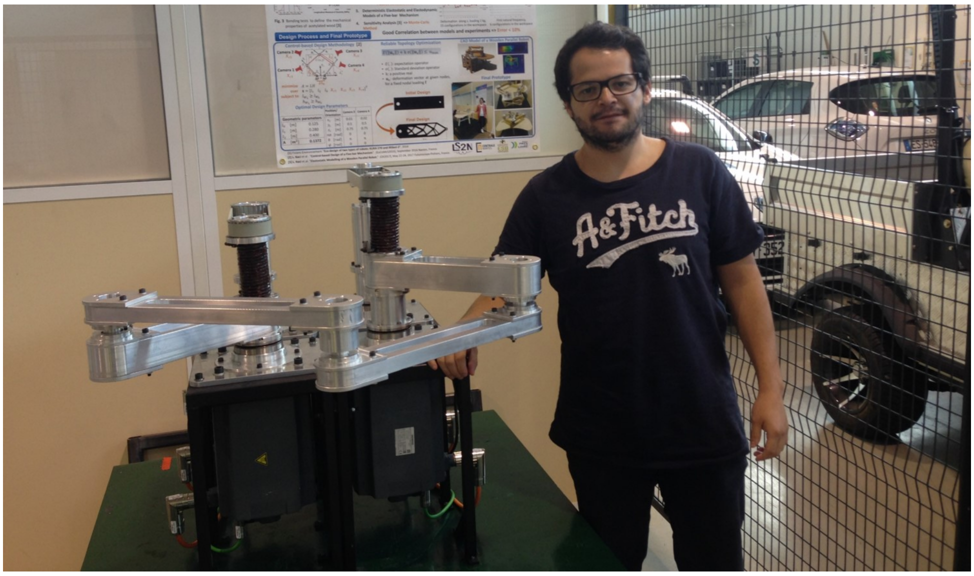

Figure 4.6: Real prototype in front view.

4.1.2 Technical description of robot revolute joints and variable stiffness joints

In this Subsection we will perform a detailed description of the joints from the full assembly in Fig. 4.4. In order to do that, we will first focus on the variable stiffness system, constituted by the motors used to adjust the stiffness of the VSS (motors M_{s_1} and M_{s_2}) and by the robot active joints (motors M_1 and M_2) due to the configuration of the VSS in parallel. On a second stage, we will describe the joints corresponding to the passive joints, i.e. the middle joints that connect the proximal and the distal links, and the end-effector joint which close the loop through the two legs from the five-bar mechanism.

We will thus firstly decompose one of the actuated links of the parallel robot into its different mechanical parts constituting the assembly as shown in the cut-plane view from Fig. 4.7. It can be seen that in order to ensure a proper transmission of the different components of the system, both for the robot active joints and the variable stiffness joints, several mechanical intermediate parts were used. Moreover, based on Fig. 4.7, it is worth noticing that since the motor shaft do not have an embedded coupling to connect directly the arm joint with the shaft, clamping rings (⑥) were designed in order to adjust and avoid the shaft to slip. Finally, in the schematics from Fig. 4.8, the components assembling the passive joints are enumerated. Based on the identification number of Fig. 4.7 and Fig. 4.8, each part of the assembly of the joints is described according to Appendix C.

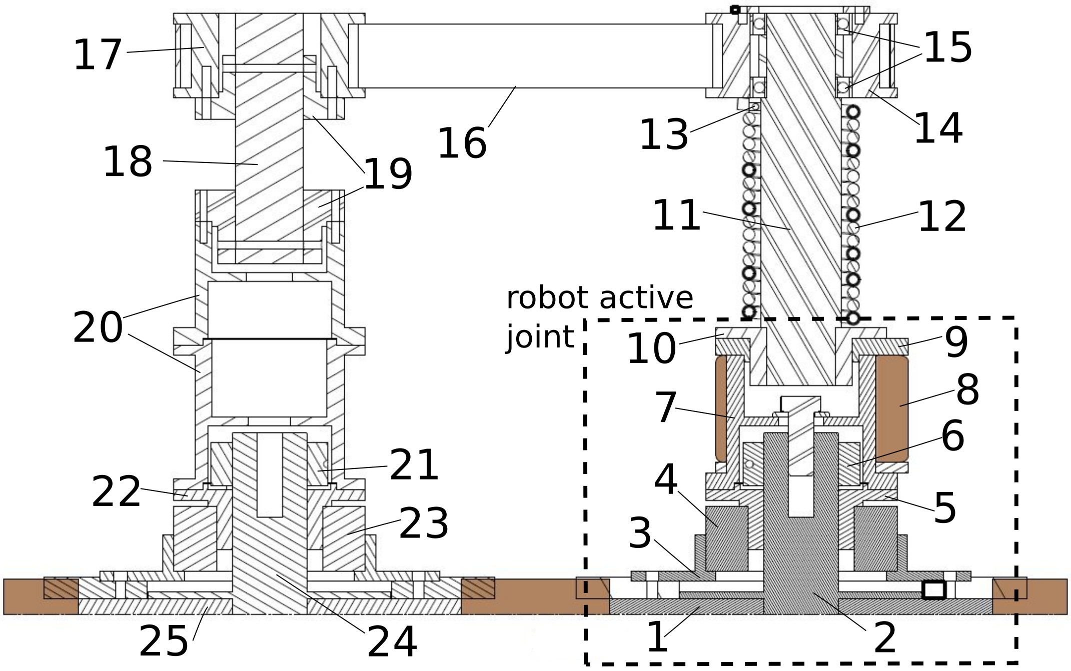
17
15
14
16
13
18
19
11
12
robot active joint
20
10
9
8
7
6
21
4
22
5
23
3
25
24
1
2

Figure 4.7: Detailed description of robot active joint and variable stiffness joint.

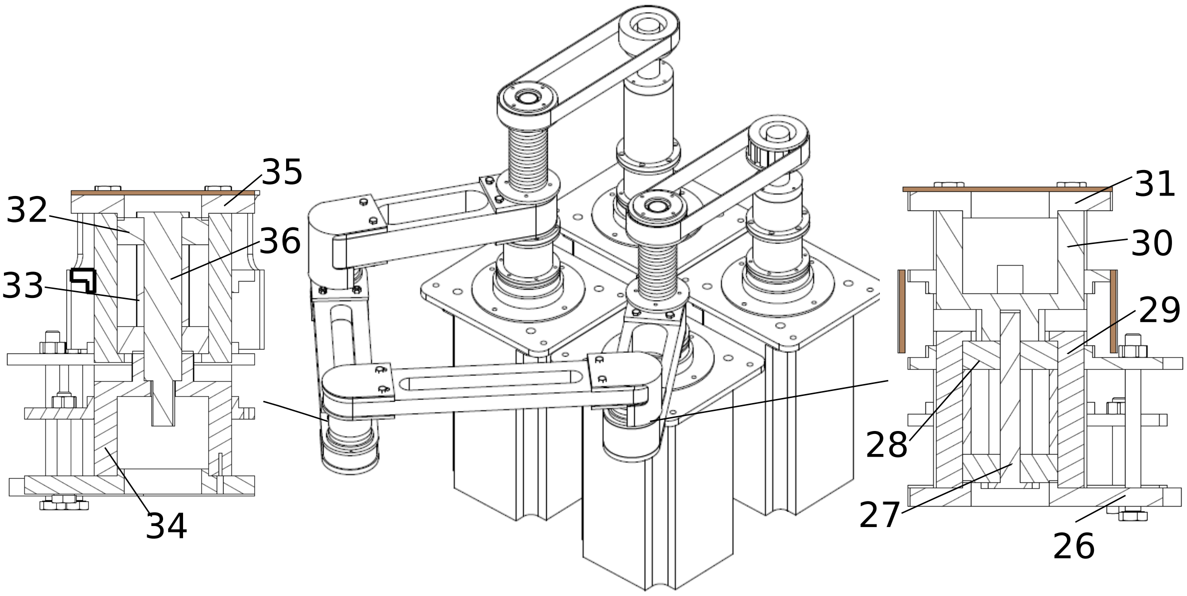
35
31
32
36
30
33
29
28
27
34
26

Figure 4.8: Detailed description of passive joints.

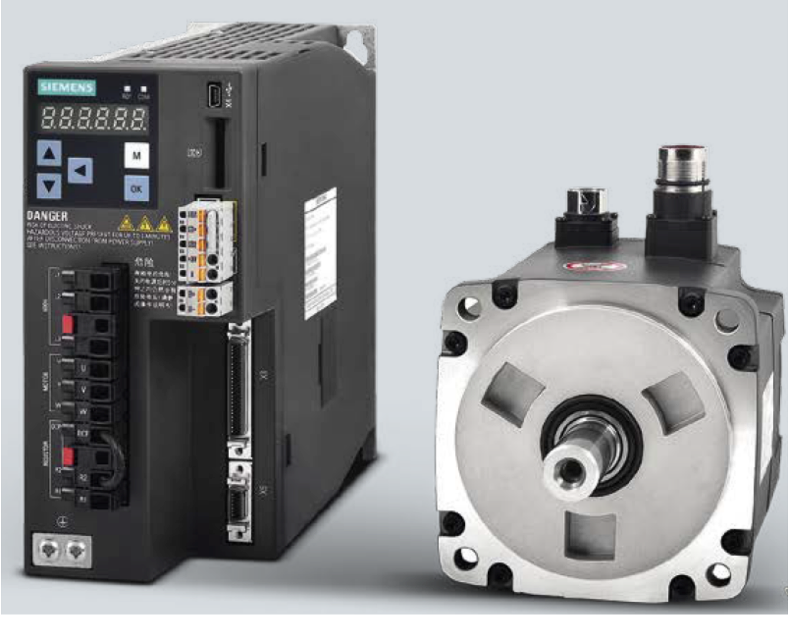

Figure 4.9: Motor drive system [Siemens].

4.1.3 Instrumentation and communication

Motor drive system

Siemens motors were used for actuating the two active joints of the five-bar mechanism (M_1 and M_2), and the two variable stiffness joints (M_{s_1} and M_{s_2}) associated to both VSS. The four motor drive systems were selected identical and their models are SIMOTICS S-1 FL6 for the motors and SINAMICS V90 for the drivers (See Fig. 4.9). The general characteristics of the motors are:

- Rated torque: 23.9 Nm;
- Rated speed: 2000 rpm;
- Incorporated absolute encoders with resolution of 16384 points/revolution;
- Holding brakes with holding torque of 30 Nm, opening time of 220 ms and closing time of 115 ms.

For further details on the specifications of the motors, the reader can refer to [Siemens]. Regarding the system integration of the motor and the driver, Fig. 4.10 shows the connection diagram in the electric and communication network. According to Fig. 4.10, the system diagram is composed of:

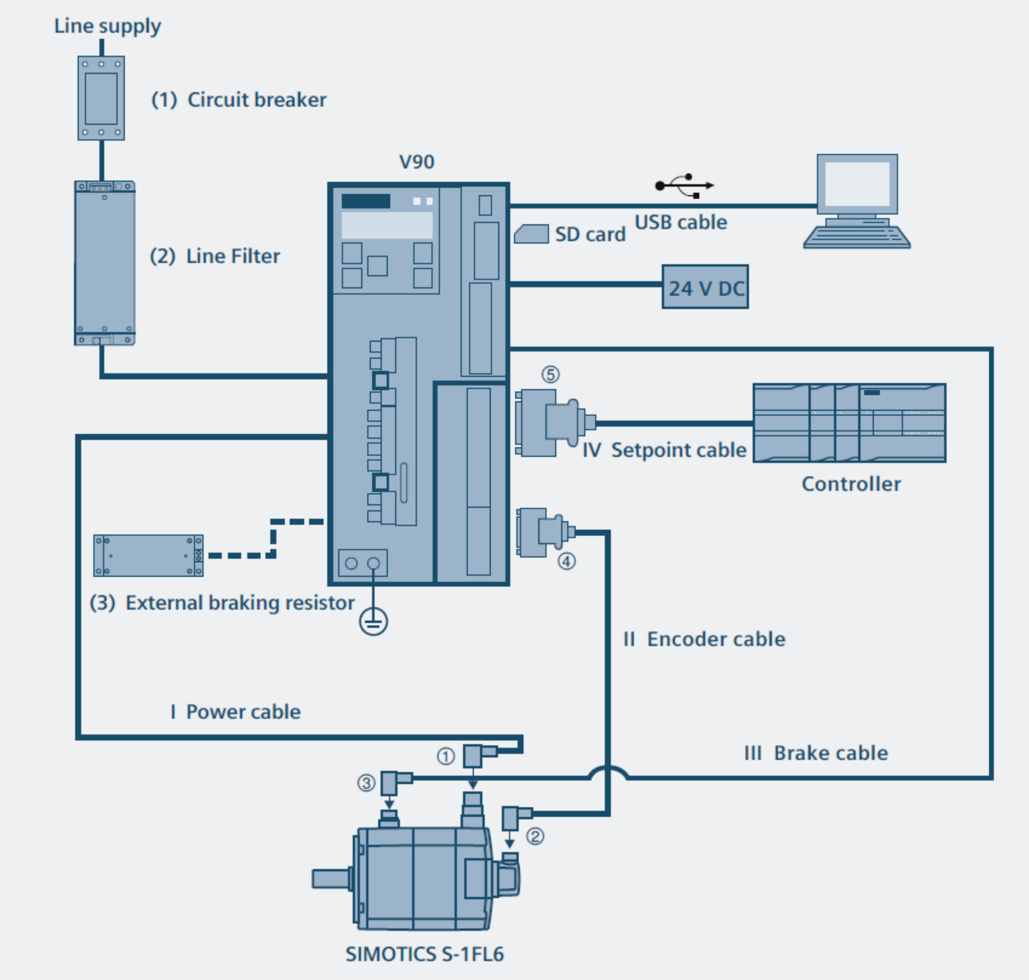
Line supply
(1) Circuit breaker
V90
(2) Line Filter
SD card
USB cable
24 V DC
⑤
IV Setpoint cable
Controller
④
(3) External braking resistor
II Encoder cable
I Power cable
①
③
III Brake cable
②
SIMOTICS S-1FL6

Figure 4.10: Motor drive system connection diagram [Siemens].

- (1) Circuit breaker: Works as an electric switch in order to protect the driver from damage caused by an overload in current or short circuit.
- (2) Line filter: Represents the rectification phase.
- (3) External braking resistor: In case the internal braking resistance R_{brake} is not sufficient for the application, an external braking resistor can be incorporated.
- I Power cable
- II Encoder cable
- III Brake cable

- IV Set-point cable
- ① Power connector
- ② Encoder connector (motor side)
- ③ Brake connector
- ④ Encoder connector (drive side)
- ⑤ Setpoint connector

The detailed electric schematics of the motor and driver from Fig. 4.10 are not given here, nevertheless, they can be found in the datasheet from [Siemens]. In addition to that, based on Chapter 2, the schematics can be generalized as in Fig. 2.11 and Fig. 2.12, respectively for the driver and the motor phases (See Chapter 2).

Control and processor card

For controlling the motors in order to perform the experiments, a dSPACE DS1103 PPC controller board, which allows to implement real-time control in combination with Matlab/Simulink was used. In addition to that, ControlDesk 5.6, which is a dSPACE experiment software, was used to design a graphical interface for measuring and monitoring data from the experiments. The general characteristics of the dSPACE controller board are:

- single-board system with real-time processor;
- CAN interface and serial interface;
- high I/O speed and accuracy;
- Phase-locked loop and universal asynchronous receiver-transmitter for accurate baud rate selection.

It is important to mention that here, the general features of the dSPACE DS1103 PPC controller board were given, nevertheless, the detail specifications of such control card can be found in [dSPACE site]. Additionally, it should be mentioned that the possibility of using Matlab/Simulink to control the dSPACE processor card is an advantageous characteristic for rapid-prototype testing.

Once the electromechanical specifications of the experimental mock-up have been defined in this Section, in what follows, the identification of the dynamic parameters of the prototype will be computed and then the experimental results from testing the algorithms developed in Chapter 3 will be presented.

4.2 Identification of dynamic parameters

4.2.1 Identification procedure based on Least Squares method

In this part, we recall the standard robot dynamic identification procedure presented in [Gautier 2014][Briot 2015c], and used for identifying the dynamic parameters of the robot and the variable stiffness system. The standard identification procedure is based on the use of the Inverse Dynamic Identification Model (IDIM), which calculates the joint forces/torques that are linear in relation to the dynamic parameters, and on the use of linear least squares techniques to calculate the parameters. In what follows, we thus recall the procedure for identification presented in [Gautier 2014][Briot 2015c], and which was applied for calculating the physical parameters of the prototype.

It is known that the complete rigid inverse dynamic model (IDM) of a parallel robot, which in this case is modified by the added force/displacement relation associated to the VSS, can be linearly written in terms of a (n_{st} x 1), and ($n_{s_{st}}$ x 1) vector of standard dynamic parameters $\boldsymbol{\chi}_{st}$ and $\boldsymbol{\chi}_{s_{st}}$, respectively for the robot and the VSS dynamics as follows:

$$\boldsymbol{\tau} = \mathbf{IDM}_{st}\boldsymbol{\chi}_{st} \tag{4.1}$$

$$\boldsymbol{\tau}_{vss} = \mathbf{IDM}_{s_{st}}\boldsymbol{\chi}_{s_{st}} \tag{4.2}$$

where $\mathbf{IDM}_{st}$ and $\mathbf{IDM}_{s_{st}}$ represent respectively the Jacobian matrices of the inverse dynamic model for the robot and the VSS, and $\boldsymbol{\chi}_{st}$, and $\boldsymbol{\chi}_{s_{st}}$ represent the vector of standard parameters given by $\boldsymbol{\chi}_{st}^T = [\boldsymbol{\chi}_{st}^{1T}, \boldsymbol{\chi}_{st}^{2T}, ..., \boldsymbol{\chi}_{st}^{nT}]$ and $\boldsymbol{\chi}_{s_{st}}^T = [\boldsymbol{\chi}_{s_{st}}^{1T}, \boldsymbol{\chi}_{s_{st}}^{2T}, ..., \boldsymbol{\chi}_{s_{st}}^{n_sT}]$ that are described in [Khalil 2004].

The identifiable parameters are the base parameters, which are the minimal number of dynamic parameters from which the dynamic model can be calculated [Gautier 1990]. They are obtained from the standard parameters, respectively $\boldsymbol{\chi}_{st}$ and $\boldsymbol{\chi}_{s_{st}}$, by eliminating those parameters which have no effect in (4.1), and (4.2) and by regrouping some of the others by means of linear relations [Hamon 2011], using simple closed-form rules

Table 4.2: Inertial dynamic parameters from CAD model.

Regrouped inertia on first robot active joint	zz_{11R}	0.1659	kg.m^2
Regrouped inertia on second robot active joint	zz_{2R}	0.1656	kg.m^2
End-effector mass	m	2.243	kg
Regrouped inertia on the first VSS axis	J_1	0.0104	kg.m^2
Regrouped inertia on the second VSS axis	J_2	0.0155	kg.m^2

[Gautier 1990], or by numerical methods based on the QR decomposition [Gautier 1991].

The minimal dynamic model can be thus written by using n_b-dimensional vector of dynamic parameters $\boldsymbol{\chi}$, and n_{bs}-dimensional vector of dynamic parameters $\boldsymbol{\chi}_s$, respectively for the robot and the VSS dynamics written as follows:

$$\boldsymbol{\tau} = \boldsymbol{\phi}(\mathbf{q}_a, \dot{\mathbf{q}}_a, \ddot{\mathbf{q}}_a, \mathbf{q}_s)\boldsymbol{\chi} \tag{4.3}$$

$$\boldsymbol{\tau}_{vss} = \boldsymbol{\phi}_s(\mathbf{q}_s, \dot{\mathbf{q}}_s, \ddot{\mathbf{q}}_s, \mathbf{q}_a)\boldsymbol{\chi}_s \tag{4.4}$$

where $\boldsymbol{\phi}$ and $\boldsymbol{\phi}_s$ are a subset of independent columns of $\mathbf{IDM}_{st}$ and $\mathbf{IDM}_{s_{st}}$, which defines the identifiable parameters $\boldsymbol{\chi}$, and $\boldsymbol{\chi}_s$, respectively related to the robot and the VSS dynamics.

Because of perturbations due to noise measurement and modeling errors, the actual torques $\hat{\boldsymbol{\tau}}$, $\hat{\boldsymbol{\tau}}_{vss}$ differ from $\boldsymbol{\tau}$, $\boldsymbol{\tau}_{vss}$ by an error $\mathbf{e}_r$ and $\mathbf{e}_{vss}$, respectively for the robot and the VSS, such that:

$$\hat{\boldsymbol{\tau}} = \boldsymbol{\tau} + \mathbf{e}_r \tag{4.5}$$

$$\hat{\boldsymbol{\tau}}_{vss} = \boldsymbol{\tau}_{vss} + \mathbf{e}_{vss} \tag{4.6}$$

Expressions (4.5) and (4.6) represent the Inverse Dynamic Identification Model (IDIM) [Briot 2015c][Gautier 2014]. In order to perform the identification of the identifiable dynamic parameters $\boldsymbol{\chi}$ and $\boldsymbol{\chi}_s$, in [Gautier 2014][Briot 2015c] an off-line strategy is considered. The main idea is to collect measured or estimated off-line data for $\boldsymbol{\tau}$, $\boldsymbol{\tau}_{vss}$, $(\mathbf{q}_a, \dot{\mathbf{q}}_a, \ddot{\mathbf{q}}_a)$, and $(\mathbf{q}_s, \dot{\mathbf{q}}_s, \ddot{\mathbf{q}}_s)$ while the robot-plus-VSS is tracking some pre-planned motions. These pre-planned trajectories are defined to be quasi-periodic with variable amplitudes and variable cycle times, and with high acceleration and deceleration ramps (respecting the motor saturation) so we can excite the robot dynamics as maximum as possible [Gautier 2014][Briot 2015c]. In addition to that, for the identification of the variable stiffness system, the trajectories for the pulley-belt transmission system were defined in such a way that the torsional springs respect the deformation limits and so that the mandrel clearance remains positive, i.e. avoiding collision between the spring coils and the mandrel when the spring is subjected to load. Furthermore, it should be mentioned that for the initialization of the dynamic parameters before the identification process, the parameters from the CAD model were used, combined with a PID controller for tracking the trajectories for identification. The initial CAD inertial physical parameters for testing the trajectories for identification are shown in Table 4.2. It should be noted in Table 4.2 that R in the inertial effects stands for regrouped parameters on the joint axes.

Once the data from the pre-planned trajectories have been collected, i.e. the data from $\boldsymbol{\tau}$, $\boldsymbol{\tau}_{vss}$, $(\mathbf{q}_a, \dot{\mathbf{q}}_a, \ddot{\mathbf{q}}_a)$, and $(\mathbf{q}_s, \dot{\mathbf{q}}_s, \ddot{\mathbf{q}}_s)$, the models in (4.5) and (4.6) are sampled at a given frequency f_m in order to get two overdetermined linear systems of (n_a x r_r), and (n_s x r_s) equations, with n_b and n_{bs} unknowns:

$$\mathbf{Y}(\hat{\boldsymbol{\tau}}) = \mathbf{W}(\hat{\mathbf{q}}_a, \hat{\dot{\mathbf{q}}}_a, \hat{\ddot{\mathbf{q}}}_a, \hat{\mathbf{q}}_s)\hat{\boldsymbol{\chi}} + \boldsymbol{\rho}_r \tag{4.7}$$

$$\mathbf{Y}_s(\hat{\boldsymbol{\tau}}_{vss}) = \mathbf{W}_s(\hat{\mathbf{q}}_s, \hat{\dot{\mathbf{q}}}_s, \hat{\ddot{\mathbf{q}}}_s, \hat{\mathbf{q}}_r)\hat{\boldsymbol{\chi}}_s + \boldsymbol{\rho}_s \tag{4.8}$$

where $\mathbf{Y}(\hat{\boldsymbol{\tau}})$, and $\mathbf{Y}_s(\hat{\boldsymbol{\tau}}_{vss})$, respectively represent the vector of input torques/forces, sampled f_m, and $\mathbf{W}(\hat{\mathbf{q}}_a, \hat{\dot{\mathbf{q}}}_a, \hat{\ddot{\mathbf{q}}}_a, \hat{\mathbf{q}}_s)$, and $\mathbf{W}_s(\hat{\mathbf{q}}_s, \hat{\dot{\mathbf{q}}}_s, \hat{\ddot{\mathbf{q}}}_s, \hat{\mathbf{q}}_r)$ represent the so-called observation matrices [Briot 2015c]. $(\hat{\mathbf{q}}_a, \hat{\dot{\mathbf{q}}}_a, \hat{\ddot{\mathbf{q}}}_a)$ and $(\hat{\mathbf{q}}_s, \hat{\dot{\mathbf{q}}}_s, \hat{\ddot{\mathbf{q}}}_s)$ represent an estimation of $(\mathbf{q}_a, \dot{\mathbf{q}}_a, \ddot{\mathbf{q}}_a)$, and $(\mathbf{q}_s, \dot{\mathbf{q}}_s, \ddot{\mathbf{q}}_s)$, respectively, obtained by band-pass filtering and sampling the measure of $\mathbf{q}_a$ and $\mathbf{q}_s$, respectively [Gautier 2014][Briot 2015c].

Then, by using the base parameters and the reference identification trajectory, well conditioned matrices $\mathbf{W}$ and $\mathbf{W}_s$ are obtained, and the least squared solutions for the dynamic parameters $\hat{\boldsymbol{\chi}}$, and $\hat{\boldsymbol{\chi}}_s$ are given by:

$$\hat{\boldsymbol{\chi}} = \mathbf{W}^{+}\mathbf{Y} \tag{4.9}$$

$$\hat{\boldsymbol{\chi}}_s = \mathbf{W}_s^{+}\mathbf{Y}_s \tag{4.10}$$

where $\mathbf{W}^{+} = (\mathbf{W}^T\mathbf{W})^{-1}\mathbf{W}^T$, and $\mathbf{W}_s^{+} = (\mathbf{W}_s^T\mathbf{W}_s)^{-1}\mathbf{W}_s^T$, being the Moore-Penrose pseudo-inverse of the matrices $\mathbf{W}$ and $\mathbf{W}_s$, respectively.

Finally, in order to statistically evaluate the accuracy of the estimation of the dynamic parameters, standard deviations can be estimated assuming that $\mathbf{W}$, and $\mathbf{W}_s$ are deterministic matrices and $\boldsymbol{\rho}_r$, and $\boldsymbol{\rho}_s$ are zero additive independent noise [Gautier 2001].

Unbiased standard deviations σ_r and σ_s, respectively can be thus express as follows:

$$\sigma_r^2 = ||\mathbf{Y} - \mathbf{W}\hat{\boldsymbol{\chi}}||^2/(r - n_b) \tag{4.11}$$

$$\sigma_s^2 = ||\mathbf{Y}_s - \mathbf{W}_s\hat{\boldsymbol{\chi}}_s||^2/(r_s - n_{bs}) \tag{4.12}$$

The covariance matrix of the estimation error is given by [Gautier 2001]:

$$\mathbf{C}_{\hat{\chi}\hat{\chi}} = E_r[(\boldsymbol{\chi} - \hat{\boldsymbol{\chi}}) - (\boldsymbol{\chi} - \hat{\boldsymbol{\chi}})^T] = \hat{\sigma}_r^2(\mathbf{W}^T\mathbf{W})^{-1} \tag{4.13}$$

$$\mathbf{C}_{\hat{\chi}_s\hat{\chi}_s} = E_s[(\boldsymbol{\chi}_s - \hat{\boldsymbol{\chi}}_s) - (\boldsymbol{\chi}_s - \hat{\boldsymbol{\chi}}_s)^T] = \hat{\sigma}_s^2(\mathbf{W}_s^T\mathbf{W}_s)^{-1} \tag{4.14}$$

where E_r and E_s are the expectation operators, and $\sigma^2_{\chi_i} = \mathbf{C}_{\hat{\chi}\hat{\chi}}(i, i)$, and $\sigma^2_{\chi_{s_j}} = \mathbf{C}_{\hat{\chi}_s\hat{\chi}_s}(j, j)$ are the ith, and jth diagonal coefficients of $\mathbf{C}_{\hat{\chi}\hat{\chi}}$ and $\mathbf{C}_{\hat{\chi}_s\hat{\chi}_s}$, respectively.

The relative standard deviation $\%\sigma_{\chi_{r_i}}$, and $\%\sigma_{\chi_{r_{sj}}}$ are given by:

$$\%\sigma_{\chi_{r_i}} = 100\sigma_{\chi_i}/|\chi_i| \tag{4.15}$$

$$\%\sigma_{\chi_{r_{sj}}} = 100\sigma_{\chi_{s_j}}/|\chi_{s_j}| \tag{4.16}$$

Once the usual identification procedure have been described in the Subsection, in what follows, we apply this methodology to identify the base parameters for the robot and the VSS, and their corresponding standard deviations. It is worth mentioning that for further details on the usual identification procedure described here, the reader can refer to [Gautier 2014][Briot 2015c].

4.2.2 Identified dynamic parameters of the robot and the variable stiffness system

In this part, the identification trajectories are tested and the dynamic model identification is carried out on the experimental prototype. According to the aforementioned procedure for identification, once the exciting trajectories were tested on the robot, the input torques and configuration variables from the four actuators were recorded and then the dynamic model for the five-bar robot and the variable stiffness system of the VSS were found.

The identification process implies the definition of a dynamic model in which typically, the physical parameters are generally related to the inertial effects, which are defined based on the geometry of the moving masses of the system, and the friction on the joints.

Regrouping the inertial parameters in one axis and considering the essential parameters is generally necessary in order to find a proper compact physical model for the identification problem [Pagis 2015b][Koessler 2018]. That is why, according to the identification of a five-bar robot performed in [Pagis 2015b][Koessler 2018], only five parameters are required to define a minimal robot dynamic model: two moments of inertia regrouped in the axes of the robot active joints, the moving platform mass, and two static friction terms (associated to the motors, and to the VSS in our case). For the variable stiffness system, we define the VSS dynamic model according to eight physical parameters: two moments of inertia grouped in the axes of the VSS active joints, two static friction terms and two viscous friction terms (associated to the motors, and the VSS system), and the two stiffness constants of the springs, associated as well to the robot dynamic model due to the parallel configuration of springs and motors. It should be noted that we do not explicitly model the belt elastodynamic effects, but the friction associated to this transmission system are taken into account. This leads to two dynamic models, respectively for the robot and for the VSS system, of the following forms:

$$\boldsymbol{\tau} = \boldsymbol{\tau}_{ta} - \mathbf{B}^T\boldsymbol{\lambda} + \boldsymbol{\tau}_s \tag{4.17}$$

$$\mathbf{w}_p = \mathbf{A}^T\boldsymbol{\lambda} \tag{4.18}$$

$$\boldsymbol{\tau}_{vss} = \mathbf{J}_s - \boldsymbol{\tau}_s \tag{4.19}$$

with

$$\boldsymbol{\tau}_{ta} = \begin{bmatrix} zz_{11R}\ddot{q}_{11} \\ zz_{21R}\ddot{q}_{21} \end{bmatrix} + \begin{bmatrix} f_{s_1}\mathrm{sign}(\dot{q}_{11}) \\ f_{s_2}\mathrm{sign}(\dot{q}_{21}) \end{bmatrix}, \qquad \mathbf{w}_p = m_R \begin{bmatrix} \ddot{x} \\ \ddot{y} \end{bmatrix} \tag{4.20}$$

$$\boldsymbol{\tau}_s = \begin{bmatrix} k_{11}(q_{11} - q_{s_1}) \\ k_{21}(q_{21} - q_{s_2}) \end{bmatrix} \tag{4.21}$$

$$\mathbf{J}_s = \begin{bmatrix} J_1\ddot{q}_{s_1} \\ J_2\ddot{q}_{s_2} \end{bmatrix} + \begin{bmatrix} f_{vss_1}\mathrm{sign}(\dot{q}_{s_1}) \\ f_{vss_2}\mathrm{sign}(\dot{q}_{s_2}) \end{bmatrix} + \begin{bmatrix} f_{v_1}(\dot{q}_{s_1}) \\ f_{v_2}(\dot{q}_{s_2}) \end{bmatrix} \tag{4.22}$$

where:

- m_R is the mass of the end-effector (point A_{13}); $m_R = 2.6370 \pm 0.08$ kg;
- zz_{11R} and zz_{21R} are the regrouped inertial effects due to rotation of the mechanism, respectively at the first active joint (A_{11}) and at the second active joints (A_{21}); zz_{11R}

$= 0.1860 \pm 8{\cdot}10^{-3}$ kg.m^2 and $zz_{21R} = 0.1805 \pm 7{\cdot}10^{-3}$ kg.m^2;

- f_{s_1} is the term of static friction (Coulomb) in the first active joint considering as well the friction effects coming from the variable stiffness system due to the parallel configuration of VSS and motors (respectively f_{s_2} for the second active joint); $f_{s_1} = 1.0778 \pm 0.1446$ Nm and $f_{s_2} = 1.2283 \pm 0.1267$ Nm;

- k_{11} and k_{21} represent the spring constants, respectively for each VSS; $k_{11} = 4.6707 \pm 0.2297$ Nm/rad and $k_{21} = 4.4789 \pm 0.1595$ Nm/rad;

- J_1 and J_2 are the grouped inertial effects due to rotational motion of the variable stiffness system, respectively for the VSS placed in parallel of each actuated link; $J_1 = 0.0223 \pm 1{\cdot}10^{-3}$ kg.m^2 and $J_2 = 0.0122 \pm 7{\cdot}10^{-4}$ kg.m^2;

- f_{vss_1} is the term of static friction (Coulomb) grouping the friction effects due to bearings, pulley-belt transmission tension and the friction due to the internal contact of the torsional spring coils (respectively f_{vss_2} for the second VSS); $f_{vss_1} = 2.1390 \pm 0.1535$ Nm and $f_{vss_2} = 2.5677 \pm 0.1726$ Nm;

- f_{v_1} is the term of viscous friction for the motor M_{s_1} of first VSS (respectively f_{v_2} for the motor M_{s_2} of the second VSS); $f_{v_1} = 0.0764 \pm 0.011$ Nms and $f_{v_2} = 0.0742 \pm 0.023$ Nms.

It is important mentioning that the static friction terms that are related to the function $\text{sign}(q_i)$ for the robot, and $\text{sign}(q_{s_j})$ for the VSS were approximated, respectively to $\tanh(aq_i)$ and $\tanh(bq_{s_j})$ in order to avoid instabilities from the controller. Additionally, these same functions being time differentiable were used for the motion generator synthesized in Chapter 3. a and b are constants experimentally tuned.

Based on the aforementioned identified dynamic parameters, it is worth noticing that the friction effects have an important contribution related to dissipative forces in the actuation chain, mostly due to the internal contact of the spring coils when the spring is under deformation, and due to the tension of the belt transmission. In addition to that, it should be mentioned that since our experimental prototype is very sensitive to variation on the friction terms due to the fact that we use a pulley-belt transmission system, it is necessary to adjust the belt after each experiment, decreasing the accuracy on the identified friction parameters. This is done in order to reduce as much as possible backlash effects or dead zones when deforming the spring of the VSS. Moreover, this means that the aforementioned dynamic parameters may vary based on how much tension there is on the belt transmission system of the VSS.

To quantify the contribution of friction effects in the full actuation chain, the following observations can be done. Based on the identification process, when testing for typical pick-and-place motions, and decoupling the different dynamic effects, it was seen that the overall percentages of friction from the calculated input torques varied from 20 to 25 % for the first VSS (associated to the proximal link 1), i.e. considering the static and viscous friction terms, and 25 to 30 % for the second VSS (associated to the proximal link 2). These percentages were compared with respect to the other dynamic effects in the full actuation chain, i.e. inertial, Coriolis and centrifugal effects.

Another important matter that should be pointed out is that in the design phase, the assumption of considering that the torsional spring used for the VSS would move freely as a revolute joint was wrong. This is due to the fact that, for some ranges of spring deformation, i.e. combined motion of robot active joints and VSS joints, the spring was not storing mechanical energy due to backlash effects, leading to have dead zones in the force/displacement relation.

Finally, in addition to the calculation of the aforementioned numerical values, from Fig. 4.11 to Fig. 4.14, the comparison between the measured and calculated input torques from identification are shown respectively for the two actuated joints of the five-bar mechanism τ_{11} and τ_{21}, and the two variable stiffness systems τ_{vss1} and τ_{vss2}. It can be seen that the errors between the measured and the calculated input torques from the robot (τ_{11} and τ_{21}), and the VSS (τ_{vss1} and τ_{vss2}) are higher in some time intervals and smaller in others. This is mainly due to the accuracy on the identification of the friction terms, which vary according to the belt tension, and contact in the internal coils of the spring, which for some motion ranges, the contact is higher, increasing the static friction.

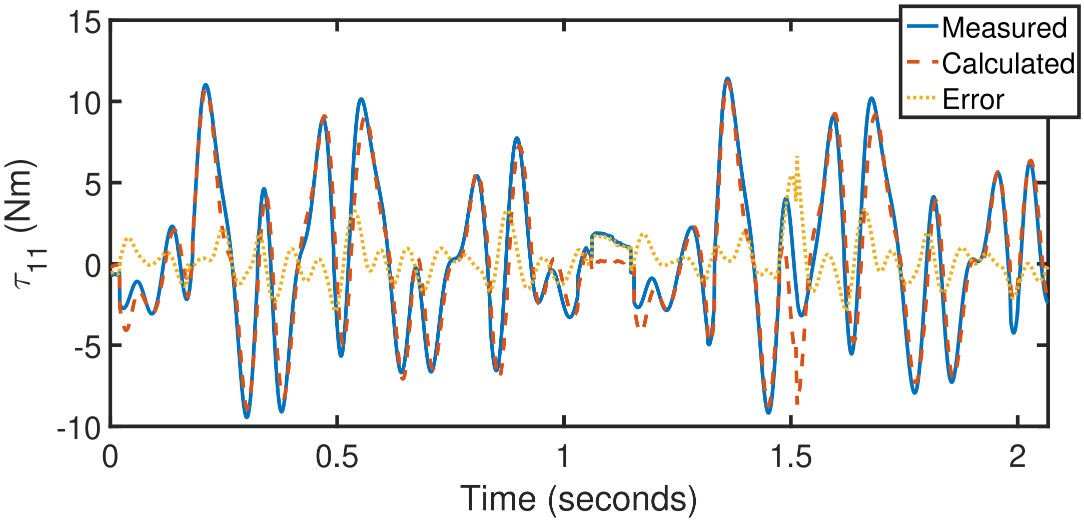

Figure 4.11: Comparison between measured and calculated input torques from robot actuated joint 1.

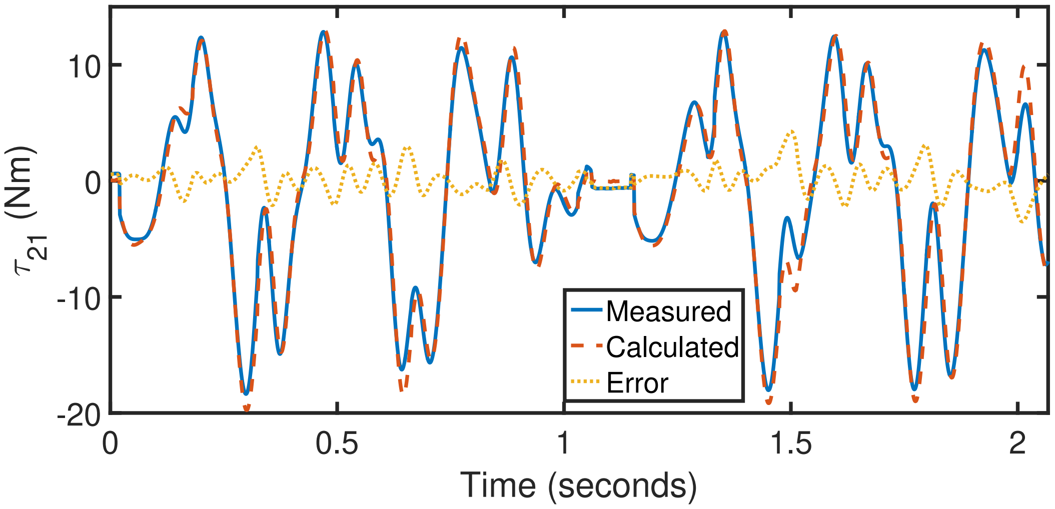

Figure 4.12: Comparison between measured and calculated input torques from robot actuated joint 2.

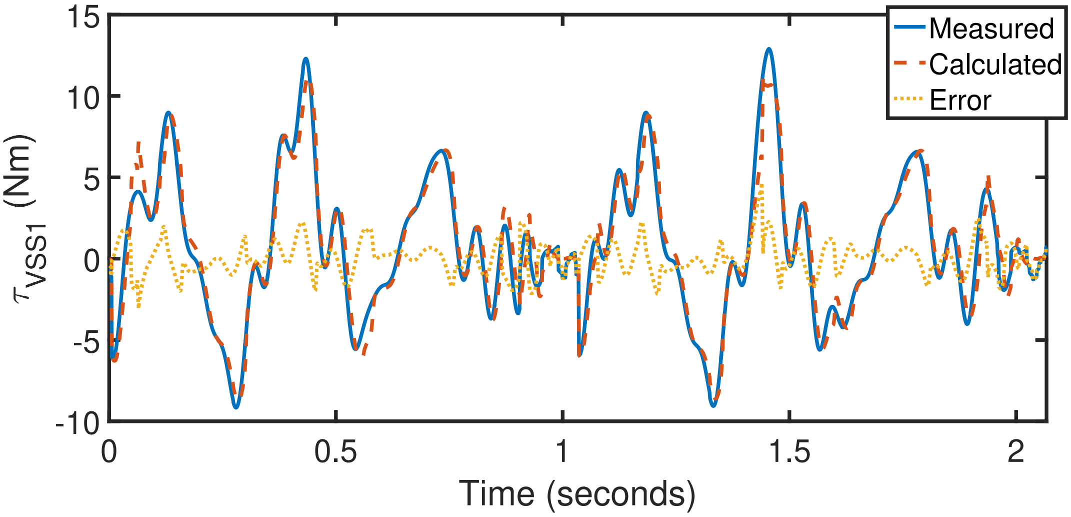

Figure 4.13: Comparison between measured and calculated input torques from variable stiffness system associated to the VSS in parallel to the first actuated link.

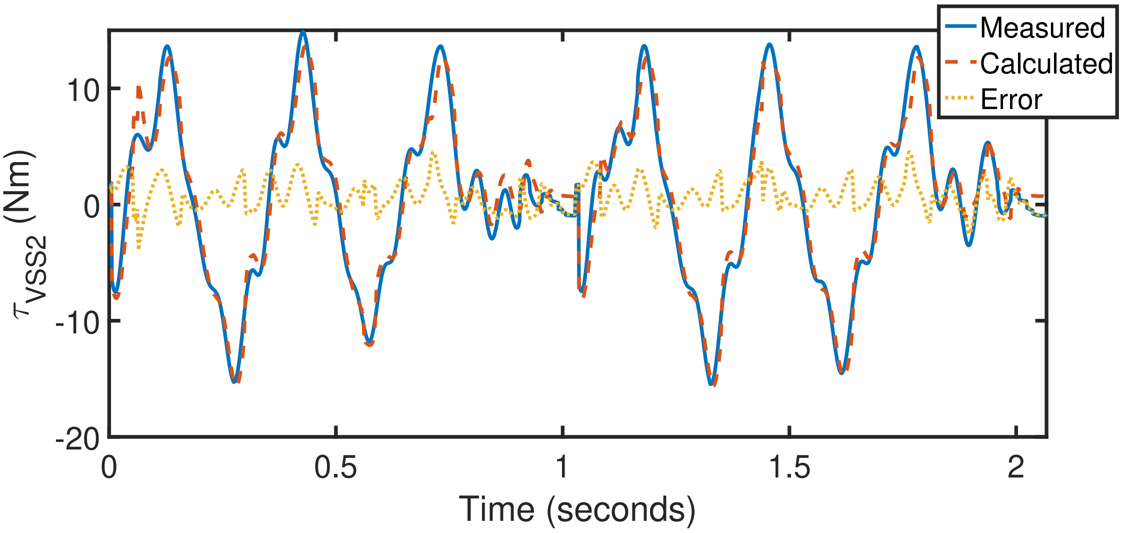

Figure 4.14: Comparison between measured and calculated input torques from variable stiffness system associated to the VSS in parallel to the second actuated link.

It should be noted that since in the experimental validation from the next Section, we will compare our approach of using VSS with a nominal type of actuation, i.e. without elastic elements, it is also important to define the numerical values for the friction terms identified in the case of nominal actuation for the five-bar mechanism. Thus by following the same aforementioned methodology of recording the input torques for the two actuators in the case of nominal actuation, the numerical values found for the friction terms are defined as follows:

- $f_{s_{1Nom}}$ is the term of static friction (Coulomb) in the first active joint without VSS (respectively $f_{s_{2Nom}}$ for the second active joint); $f_{s_{1Nom}} = 0.5255 \pm 0.11$ Nm and $f_{s_{2Nom}} = 0.6435$ Nm $\pm$ 0.17 Nm;

These numerical values for the friction effects will be used in the experimental results for computing the input torques for the case of nominal actuation for the two active joints of the five-bar mechanism. Additionally, it is worth noticing that the numerical values of the aforementioned friction terms are associated to the friction on the motors only. As it can be seen, the values of these friction terms only due to the motor represent already an important contribution to the dynamic effects for the nominal actuation.

Even if the prototype for the variable stiffness system of the VSS is not optimal for energy-efficient motions, mainly due to high friction effects, in the next Section, we will show that it is possible to experimentally reduce the energy consumption on the full actuation chain thanks to the use of VSS in parallel. It is worth adding that in the future perspectives of this work, the redesigning of the variable stiffness system is considered, for instance by designing a joint mechanism connecting directly the motor with the spring ending coils, or by redefining the motor power specifications, leading to reduce the size of the actuators, and therefore avoiding the use of a belt transmission system.

4.3 Experimental results for reducing energy consumption

4.3.1 Controller design

In this Section, the control scheme synthesized for controlling the five-bar mechanism with VSS when performing an energy-efficient motion will be presented. Since in Chapter 3, we have already developed an energy-efficient motion generator, here we require to implement a control technique which ensures an accurate trajectory tracking so that the robot-plus-VSS can move as energy-efficient as possible. For doing this we implemented a feedback linearization control technique also known as Computed Torque Control (CTC) [Spong 1989].

The CTC is an advanced controller that computes the input torques that the actuators must apply to the robot in order to track a given trajectory [Spong 1989][Pagis 2015a] [Khalil 2004]. It is based on the dynamic model. The goal of the CTC is to minimize the error either in the joint or Cartesian space. In our case we will implement it in the joint space since encoder measurements from the revolute joints motions are used to get the information regarding the states of the robot and the variable stiffness joints. In order to develop the CTC, let us consider the tracking error of the active joints of the parallel robot and the VSS:

$$\begin{aligned} \mathbf{e} &= \mathbf{q}_{a_d} - \mathbf{q}_a \\ \dot{\mathbf{e}} &= \dot{\mathbf{q}}_{a_d} - \dot{\mathbf{q}}_a \\ \ddot{\mathbf{e}} &= \ddot{\mathbf{q}}_{a_d} - \ddot{\mathbf{q}}_a \\ \mathbf{e}_s &= \mathbf{q}_{s_d} - \mathbf{q}_s \\ \dot{\mathbf{e}}_s &= \dot{\mathbf{q}}_{s_d} - \dot{\mathbf{q}}_s \\ \ddot{\mathbf{e}}_s &= \ddot{\mathbf{q}}_{s_d} - \ddot{\mathbf{q}}_s \end{aligned} \tag{4.23}$$

where $\mathbf{q}_{a_d}$, $\dot{\mathbf{q}}_{a_d}$, and $\ddot{\mathbf{q}}_{a_d}$ represent the desired robot joint position, velocity and acceleration, and $\mathbf{q}_{s_d}$, $\dot{\mathbf{q}}_{s_d}$, and $\ddot{\mathbf{q}}_{s_d}$ represent the desired variable stiffness joint position, velocity and acceleration, respectively. In order to enforce the aforementioned tracking errors to tend to zero, a second order differential equation on $\mathbf{e}$ and $\mathbf{e}_s$ is set by:

$$\begin{aligned} \ddot{\mathbf{e}} + \mathbf{K}_d\dot{\mathbf{e}} + \mathbf{K}_p\mathbf{e} &= \mathbf{0} \\ \ddot{\mathbf{e}}_s + \mathbf{K}_{s_d}\dot{\mathbf{e}}_s + \mathbf{K}_{s_p}\mathbf{e}_s &= \mathbf{0} \end{aligned} \tag{4.24}$$

where $\mathbf{K}_p$, $\mathbf{K}_d$, $\mathbf{K}_{s_p}$ and $\mathbf{K}_{s_d}$ are symmetric positive definite matrices. By substituting expressions (4.23) into (4.24), it is possible to obtain an auxiliary control input $\boldsymbol{\nu}_a$ and $\boldsymbol{\nu}_s$ corresponding to the acceleration of the robot and VSS controlled variables:

$$\boldsymbol{\nu}_a = \ddot{\mathbf{q}}_a = \ddot{\mathbf{q}}_{a_d} + \mathbf{K}_d\dot{\mathbf{e}} + \mathbf{K}_p\mathbf{e} \tag{4.25}$$

$$\boldsymbol{\nu}_s = \ddot{\mathbf{q}}_s = \ddot{\mathbf{q}}_{s_d} + \mathbf{K}_{s_d}\dot{\mathbf{e}}_s + \mathbf{K}_{s_p}\mathbf{e}_s \tag{4.26}$$

And consequently, the CTC law which computes the input efforts required for follow a prescribed given trajectory for the robot and the variable stiffness system are computed

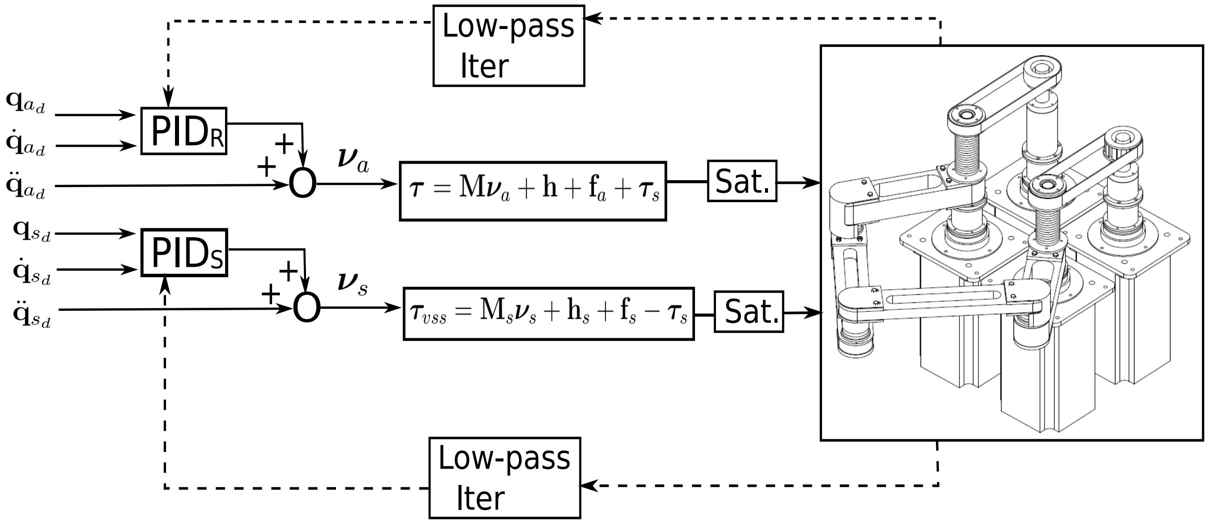
Low-pass
Iter
$\mathbf{q}_{a_d}$
$\dot{\mathbf{q}}_{a_d}$
$\ddot{\mathbf{q}}_{a_d}$
PIDR
+
+
$\boldsymbol{\nu}_a$
$\boldsymbol{\tau} = \mathrm{M}\boldsymbol{\nu}_a + \mathrm{h} + \mathrm{f}_a + \boldsymbol{\tau}_s$
Sat.
$\mathbf{q}_{s_d}$
$\dot{\mathbf{q}}_{s_d}$
$\ddot{\mathbf{q}}_{s_d}$
PIDS
+
+
$\boldsymbol{\nu}_s$
$\boldsymbol{\tau}_{vss} = \mathrm{M}_s\boldsymbol{\nu}_s + \mathrm{h}_s + \mathrm{f}_s - \boldsymbol{\tau}_s$
Sat.
Low-pass
Iter

Figure 4.15: Real-time control system for experimental validation with dSPACE controller card. Once the task finished, the data from velocities and input torques are saved from ControlDesk in order to feed the energy consumption model from Eq. (2.43).

respectively by:

$$\boldsymbol{\tau} = \mathbf{M}\boldsymbol{\nu}_a + \mathbf{c}(\mathbf{q}_a, \dot{\mathbf{q}}_a) + \mathbf{f}_a + \boldsymbol{\tau}_s \tag{4.27}$$

$$\boldsymbol{\tau}_{vss} = \mathbf{M}_s\boldsymbol{\nu}_s + \mathbf{h}_s(\mathbf{q}_s, \dot{\mathbf{q}}_s) + \mathbf{f}_s - \boldsymbol{\tau}_s \tag{4.28}$$

It is worth noticing that the decoupling property that placing the VSS in parallel to the motors brings, allows to have an independent control law for the robot and the VSS separately, which is not the case at all for the SEAs in [Haddadin 2011][Jafari 2011], in which it is possible to control either the position or the stiffness of the VSS at a time.

Finally, the synthesized control scheme for controlling the prototype in the real experimental set-up is shown in Fig. 4.15. It is worth noticing that since in our experimental mock-up (robot-plus-VSS) the friction effects are important, mostly due to the pulley-belt transmission drive and the VSS fixations (see Section 4.2), positive integral gains grouped $\mathbf{K}_I$ and $\mathbf{K}_{s_I}$, respectively for the robot and the VSS system, were added to the synthesized PD controller (from the feedback linearization). This was done in order to enhance the compensation of the friction effects, which induced chattering while tracking the desired robot and VSS trajectories. In addition to that based on Fig. 4.15, it is worth recalling that the desired robot positions, velocities and accelerations, respectively $\mathbf{q}_{a_d}$, $\dot{\mathbf{q}}_{a_d}$, and $\ddot{\mathbf{q}}_{a_d}$, and the desired VSS positions, velocities and accelerations, $\mathbf{q}_{s_d}$, $\dot{\mathbf{q}}_{s_d}$, and $\ddot{\mathbf{q}}_{s_d}$ were computed thanks to the energy-efficient motion planner from Chapter 3.

4.3.2 Synthonization of controller gains

In order to tune the gains of the aforementioned CTC-plus-integral controller, we first defined the gains of the PD controller by considering the Hurwitz polynomial characteristic [Callier 1991][Kuo 1996] as follows:

$$s^r + k_i s^{r-1} + ... + k_2 s + k_3 = 0 \tag{4.29}$$

where r represents the relative degree of the system and $k_i ... k_3$ are positive constants. Therefore, considering that the relative degree of (4.27) and (4.28) is equal to 2, the polynomial characteristic according to Hurwitz [Kuo 1996], respectively for the robot and VSS dynamics can be defined as a second order system of the following Laplace form:

$$\mathbf{s}_r^2 + \mathbf{K}_d \mathbf{s}_r + \mathbf{K}_p = 0 \tag{4.30}$$

$$\mathbf{s}_s^2 + \mathbf{K}_{s_d} \mathbf{s}_s + \mathbf{K}_{s_p} = 0 \tag{4.31}$$

from which $\mathbf{K}_p = k_p \omega_{n_r}^2 \mathbf{I}_2$, $\mathbf{K}_d = k_d 2\omega_{n_r} \mathbf{I}_2$, $\mathbf{K}_{s_p} = k_{p_s} \omega_{n_s}^2 \mathbf{I}_2$ and $\mathbf{K}_{s_d} = k_{d_s} 2\omega_{n_s} \mathbf{I}_2$ where $\mathbf{I}_2$ is a (2 x 2) identity matrix, and ω_{n_r} and ω_{n_s} represent the undamped natural frequencies associated to the robot and the VSS system, respectively. For our experimental setup, these natural frequencies were tuned empirically since the inertia matrix is joint-dependent, which complexifies to find an analytical solution. Additionally, it should be mentioned that the structure in which the motors were mounted, introduced undesired resonance for high-dynamic tasks, worsening the tuning of the natural frequencies for the gains of the controller. Finally, the values were defined $\omega_{n_r} = 12$ and $\omega_{n_s} = 20$, respectively. The constants k_p, k_d, k_{p_s}, and k_{d_s} were added to refine the tuning of ω_{n_r} and ω_{n_s} online with ControlDesk, and they were initially defined equal to $k_p = 1$, $k_d = 0.7$, $k_{p_s} = 1$, and $k_{d_s} = 0.7$.

When performing the experiments with the aforementioned PD controller with polynomial characteristic of relative degree 2, it was noted that chattering was occurring due to the high values of the friction terms. That is why integral gains, characterized by the cubic of the natural frequencies, were added to the controller, thus having a characteristic polynomial of superior order, which could compensate the friction effects. We thus defined the integral gains as follows: $\mathbf{K}_I = k_{i_r} \omega_{n_r}^3 \mathbf{I}_2$ and $\mathbf{K}_{s_I} = k_{i_s} \omega_{n_s}^3 \mathbf{I}_2$. In this way, we added one more order to compensate the chattering effects due to friction. Similar to the PD controller, additional constants multiplying the cubic of the natural frequencies were added to refine the tuning: $k_{i_r} = 1.7$, and $k_{i_s} = 5.7$.

Finally, it should be noted that the saturation block (parameterized as Sat.) from the control scheme in Fig. 4.15 was defined equal to $\boldsymbol{\tau}_{min} \leq \boldsymbol{\tau} \leq \boldsymbol{\tau}_{max}$ and $\boldsymbol{\tau}_{vss_{min}} \leq \boldsymbol{\tau}_{vss} \leq \boldsymbol{\tau}_{vss_{max}}$. The values for $\boldsymbol{\tau}_{min}$, $\boldsymbol{\tau}_{max}$, $\boldsymbol{\tau}_{vss_{min}}$, and $\boldsymbol{\tau}_{vss_{max}}$ were defined according to the motor specifications of Section 4.1 equal to 23.9 Nm. It should be noted that this motor saturation value was defined with the same value for the four motors actuating respectively the two robot active joints and the two variable stiffness joints since they have the same power specifications.

4.3.3 Results

In order to validate the theoretical formulations for performing energy-efficient motions and to validate that the controller functioning is correct, multiple-point pick-and-place sequences were defined in the dexterous workspace of the five-bar prototype. In this Subsection, we thus define two sets of desired boundary pick-and-place conditions for testing the energy-efficient motion generator developed in Chapter 3.

4.3.3.1 First set of boundary pick-and-place constraints

The first set of boundary constraints represents a trajectory symmetrically defined in the dexterous workspace of the five-bar robot (Fig. 4.16) in which each pick-and-place point is required to be joined at different travel times (quasi-periodic), and the desired positions are defined as follows:

- $A = [0, 0.4]$, $B = [0.15, 0.38]$, $C = [-0.15, 0.38]$, $D = [0.15, 0.42]$, $E = [-0.15, 0.42]$ (See Fig. 4.16).

The connecting times for the desired boundary pick-and-place constraints are defined respectively in Fig. 4.16. Additionally, it should be mentioned that all the trajectories are defined to start from the home position which was set at $\mathbf{x}_{home} = [0, 0.366]$. This position was defined thanks to the encoder index of each motor, which characterizes the absolute position reference for homing the robot.

In order to analyze the results in terms of input torque reduction and energy consumption, two different types of actuation modes were considered: *i*) nominal actuation in which the pick-and-place positions are joined thanks to a classical fifth-degree polynomial and there is no elastic element attached to the actuated links, *ii*) actuation with

VSS in parallel of each actuated link and in which the trajectories are generated thanks to the BVP formalized in Chapter 3. In addition to that, since in Section 4.3 was shown that the friction terms have important physical values, which is not beneficial for energy-efficient motions, we will analyze the results with and without friction effects. This to define roughly up to which percentage we would reduce in absence of friction effects.

For the first set of boundary constraints, the results in terms of input torques are shown in Fig. 4.17–Fig. 4.18, and their RMS values from the full actuation chain are grouped in Table 4.3 for the case when considering the friction effects due to the VSS. In Table 4.4 on the other hand, the input torques from the full actuation chain are grouped without considering the effects due to the friction from the variable stiffness system. Additionally to the RMS values of the input torques in Table 4.3 and Table 4.4, the percentages of gain in terms of input torques reduction are shown separately for the first active joint and the second joint, respectively. This to visualize the contribution of efforts from each actuation chain (actuated link-plus-VSS). It is worth noticing that as it was pointed out in Section 4.3, the contribution from friction effects due to the second VSS (in parallel to the second actuated link) is higher than for the first VSS, which lead to a lower reduction. Nevertheless, based on Table 4.3, it can be seen that the reduction on the full actuation chain from the quasi-periodic desired motion of Fig. 4.16 when considering the friction effects from our prototype, can reach up to 50 %. On the other hand, if we neglect the friction effects from the variable stiffness system, according to the RMS values from the efforts in the full actuation in Table 4.4, it is possible to achieve a reduction of 63 %. It is worth noticing that even in the identification process we have pointed out that the efforts due to friction, mainly due to the VSS, contribute in 30 % to the actuation torques, it is possible to prove that experimentally the efforts in the full actuation chain can be reduced by using VSS. Additionally, it is worth to point out that during the experiments, we noted that by releasing the belt tension that transmits the effort for deforming the VSS (without having *sag effect* on the belt), it was possible to reduce the friction effects, thus contributing to improve the overall dynamic performance of the robot while performing the motions.

In addition to the aforementioned results in terms of input torques reduction, in Table 4.5 and Table 4.6, we present the distribution of the robot torques and VSS torques by summing them up and comparing them with respect to the nominal actuation. Analyzing the summation of the torques in the full actuation chain when using VSS is of great importance due to the fact that our actuation principle seeks to distribute the efforts required

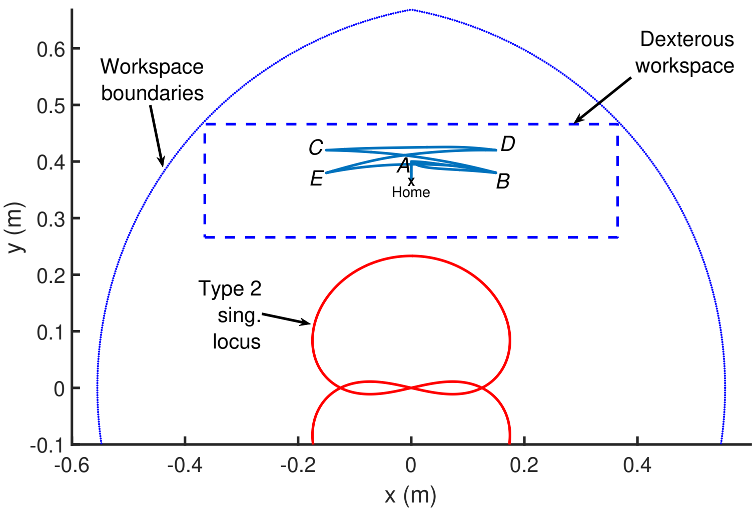

Figure 4.16: Multiple-point pick-and-place sequence in the five-bar mechanism workspace: $A \rightarrow B$ (travel time: 0.32 s), $B \rightarrow C$ (travel time: 0.31 s), $C \rightarrow D$ (travel time: 0.30 s), $D \rightarrow E$ (travel time: 0.31 s), $E \rightarrow B$ (travel time: 0.34 s), $B \rightarrow A$ (travel time: 0.31 s).

to move the links of the robot at high-speeds. Thus, by analyzing its combined contribution, we can demonstrate that by optimally exploiting the combined motion of active joints and VSS joints, which are associated to $\boldsymbol{\tau}_s$, it is possible to properly distribute the efforts to actuate the robot links. The results in terms of torque distribution are shown in Table 4.5 and Table 4.6, respectively for the case when the friction is considered and when it is not. It can be seen that based on the RMS values of the addition of robot and VSS torques, the input torque reduction can reach up to 58 % when considering the friction effects, and 69 % without considering friction.

Finally, for the first set of boundary pick-and-place conditions, the results in terms of energetic losses from the two types of actuation (nominal and by using VSS) are shown in Fig. 4.19 and Fig. 4.20, respectively for the case when considering friction and when separating the friction effects. It can be seen that the energetic losses from the full actuation chain when considering the friction losses in Fig. 4.19 can be drastically reduced by a 53 %. For the case in which we separate the contribution due to friction losses in Fig. 4.20, the energetic losses can be drastically reduced by a 60 %. It is worth to emphasize that these percentages are far from the 90 % of energy reduction presented in [Goya 2012]. Nevertheless, contrary to [Goya 2012], we do not neglect the energy required to adjust the VSS, which based on this study has an important contribution for the full actuation chain. It should be also noted that based on Fig.4.21, in addition to ensure an

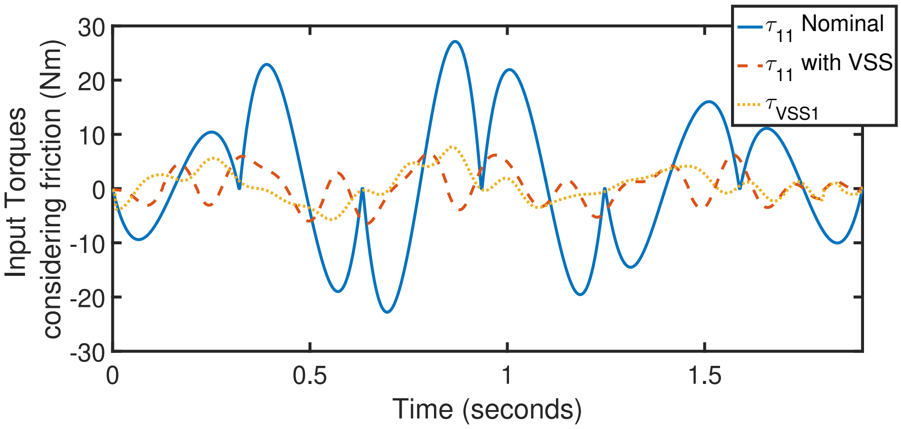

Figure 4.17: Input torques grouping the first actuation chain considering a nominal case and the case when using VSS for the first set of boundary pick-and-place constraints.

energy-efficient motion from the robot, also the tracking error from the CTC performed along the desired pick-and-place motion remains bounded on the order of 10^{-3} rad, thus ensuring the accuracy.

To conclude the explanation and interpretation of the results obtained for this first symmetric trajectory, it is worth mentioning that in order to generate the optimal trajectories for the experimental prototype, i.e. considering the dynamic parameters of our real robot, we did not consider the friction effects in the BVP optimization (also for the next experiment). This is due to the fact that the friction effects, having important physical values multiplied by almost non-differentiable functions (tanh from the Coulumb friction), complexified the convergence of the BVP, and made it converge towards a local minima. Nevertheless, as it was previously shown, in the results presented in this Section we considered the friction effects when analyzing the energy reduction in the full actuation chain. In addition to that, it should be mentioned that the difference between the 70 % of energy savings that we achieved in simulations with respect to the 60 % obtained in experiments are mainly due to the fact that as it can be seen on the dynamic parameters of the prototype, the physical values of real prototype are higher than the ones in simulation. As a future work, an initial optimization of the robot architecture, including the stiffness of the spring of the VSS, in the design phase could be proposed to keep the physical parameters bounded. Nevertheless, even if there are some differences from the simulation and experimental results, the actuation principle for high speeds was validated experimentally. Let us now test an asymmetric desired pick-and-place task.

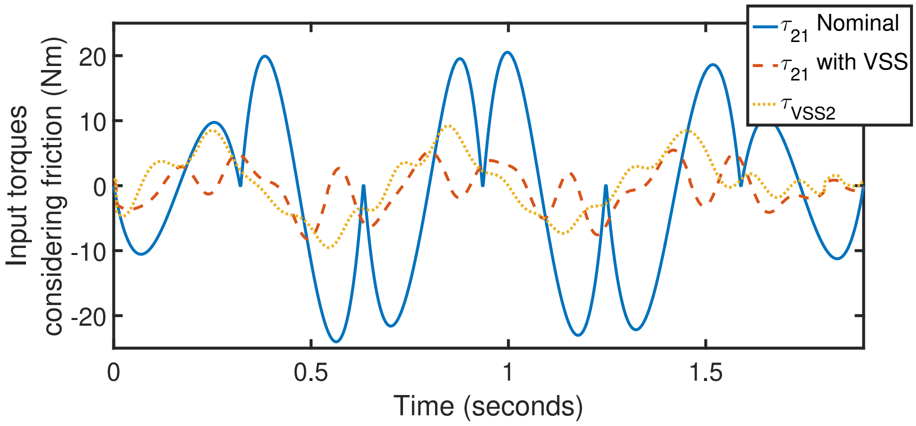

Figure 4.18: Input torques grouping the second actuation chain considering a nominal case and the case when using VSS for the first set of boundary pick-and-place constraints.

Table 4.3: RMS values of input torques for nominal case and for case when using VSS in parallel for the first set of boundary pick-and-place conditions considering the friction effects.

		Nominal RMS. Torques	Using VSS in parallel RMS. Torques		Gain each joint	Overall gain
Segment	Time (s)	$\boldsymbol{\tau}_{\mathrm{RMS}}$ (Nm)	$\boldsymbol{\tau}_{\mathrm{RMS}}$ (Nm)	$\boldsymbol{\tau}_{vss_{\mathrm{RMS}}}$ (Nm)	%	%
Fig. 4.16	1.89	[12.84, 13.62]	[3.12, 3.18]	[2.70, 4.28]	[54.79, 45.21]	50

Table 4.4: RMS values of input torques for nominal case and for case when using VSS in parallel for the first set of boundary pick-and-place conditions without considering the friction effects.

		Nominal RMS. Torques	Using VSS in parallel RMS. Torques		Gain each joint	Overall gain
Segment	Time (s)	$\boldsymbol{\tau}_{\mathrm{RMS}}$ (Nm)	$\boldsymbol{\tau}_{\mathrm{RMS}}$ (Nm)	$\boldsymbol{\tau}_{vss_{\mathrm{RMS}}}$ (Nm)	%	%
Fig. 4.16	1.89	[12.84, 13.62]	[2.23, 2.27]	[1.98, 3.14]	[67.21, 60.27]	63.74

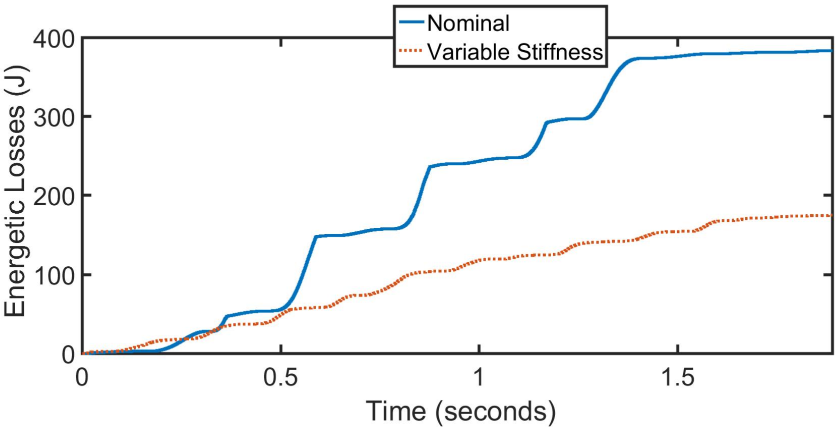

Figure 4.19: Comparison of energetic losses for two types of actuation: nominal and case when using VSS and considering the friction effects due to the VSS for the first set of boundary pick-and-place constraints.

Table 4.5: RMS values of input torques for nominal case and for case when using VSS in parallel for the first set of boundary pick-and-place conditions considering the friction effects and by analyzing the distribution of torques for the actuation with VSS.

		Nominal RMS. Torques	Using VSS in parallel RMS. Sum of Torques	Gain each joint	Overall gain
Segment	Time (s)	$\boldsymbol{\tau}_{\text{RMS}}$ (Nm)	$\lvert\boldsymbol{\tau}+\boldsymbol{\tau}_{vss}\rvert_{\text{RMS}}$ (Nm)	%	%
Fig. 4.16	1.89	[12.84, 13.62]	[4.64, 6.40]	[63.86, 53.01]	58.43

Table 4.6: RMS values of input torques for nominal case and for case when using VSS in parallel for the first set of boundary pick-and-place conditions without considering the friction effects and by analyzing the distribution of torques for the actuation with VSS.

		Nominal RMS. Torques	Using VSS in parallel RMS. Sum of Torques	Gain each joint	Overall gain
Segment	Time (s)	$\boldsymbol{\tau}_{\text{RMS}}$ (Nm)	$\lvert\boldsymbol{\tau}+\boldsymbol{\tau}_{vss}\rvert_{\text{RMS}}$ (Nm)	%	%
Fig. 4.16	1.89	[12.84, 13.62]	[3.35, 4.64]	[73.90, 65.93]	69.91

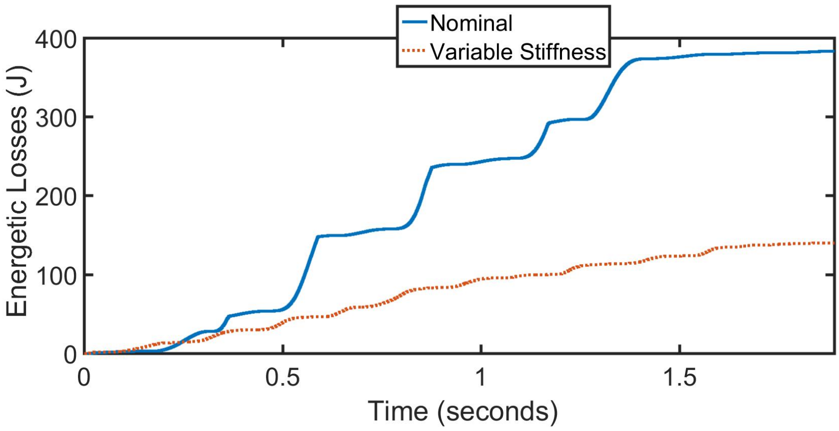

Figure 4.20: Comparison of energetic losses for two types of actuation: nominal and case when using VSS and without considering the friction effects due to the VSS for the first set of boundary pick-and-place constraints.

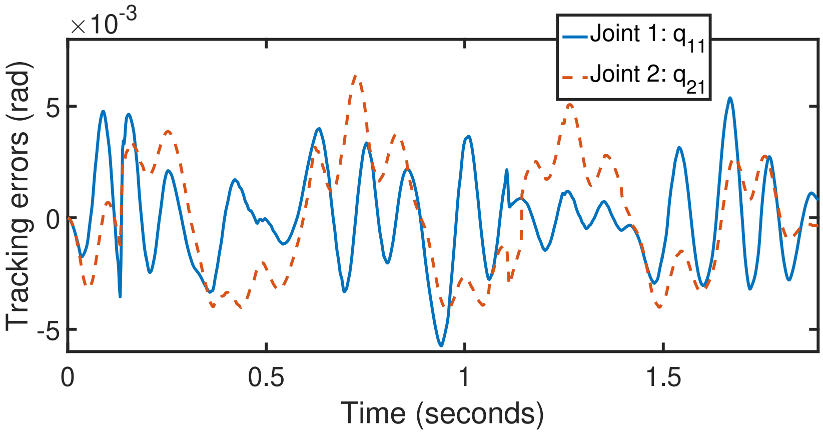

Figure 4.21: Tracking errors along the trajectory generated for the first set of boundary pick-and-place conditions in order to show that thanks to the direct power connection between the motors and the proximal links of the five-bar robot we can ensure accuracy at high-speeds.

4.3.3.2 Second set of boundary pick-and-place constraints

For the second set of boundary constraints, the required pick-and-place task to be performed follows from an asymmetric shape as it can be seen in Fig. 4.22. The desired positions of boundary constraints defines an asymmetric trajectory in the five-bar workspace as shown in Fig. 4.22, as well with variable travel times. This to demonstrate the effectiveness of the algorithm to perform high-speed tasks in different parts of the dexterous workspace. The pick-and-place desired positions must be joined at variable times defined in Fig. 4.22, which leads as well to a quasi-periodic task:

- $A = [0, 0.4]$, $B = [0.2, 0.32]$, $C = [-0.1, 0.4]$, $D = [0.15, 0.42]$, $E = [-0.15, 0.32]$ (See Fig. 4.22).

Before starting to describe the results for this trajectory, it should mentioned that since the motor limits of our prototype are set to 23.9 Nm, we could not test this trajectory on the real robot for the nominal case, since the input torques were exceeding the motor saturations. That is why the results presented for the nominal type of actuation for this trajectory were computed in simulation. However, for the actuation case when using VSS this was not a problem. Thus, the input torques and energy consumption from the case of using VSS presented in this part correspond to the real prototype. Let us show the obtained results.

The results from the input efforts are presented in Fig. 4.23–Fig. 4.24, and their RMS values from the full actuation chain are shown in Table 4.7 for the case when considering the friction effects due to the VSS. In Table 4.8 on the contrary, the input torques from the full actuation chain are grouped without considering the effects due to the friction from the variable stiffness system. Based on Table 4.7, it can be seen that the reduction on the full actuation chain from the quasi-periodic desired motion of Fig. 4.22 when considering the friction effects from our prototype, can reach up to 43 %. On the other hand, if we do not consider the friction effects from the variable stiffness system, according to the RMS values from the efforts in the full actuation in Table 4.8, it is possible to achieve a reduction of 59 %. It is important to point out that the overall percentage of input torques reduction from Table 4.7 is low due to the fact that as it can be seen, the gained percentage on the second joint reach only 33 % of reduction with respect to the nominal one. This is mainly due to the fact that as it was shown in Section 4.2, in the prototype for the second VSS the friction effects are more important than in the first VSS. This results on an increase of the controller gains in order to try to compensate these effects, leading on increasing the input torques in the closed-loop system in order to ensure a good tracking of the desired trajectories.

In addition to the aforementioned results in terms of input torques reduction, for this set of boundary constraints will also consider the distribution of torques for the actuation chain with VSS. Thus, in Table 4.9 and Table 4.10, the sum of robot plus VSS input torques are compared with respect to the nominal type of actuation. The results show that thanks to the distribution of efforts in the energy-efficient actuation, based on Table 4.9 and Table 4.10, respectively with and without friction, it can be seen that the input torque reduction can reach up to 52 % and 65 %, respectively.

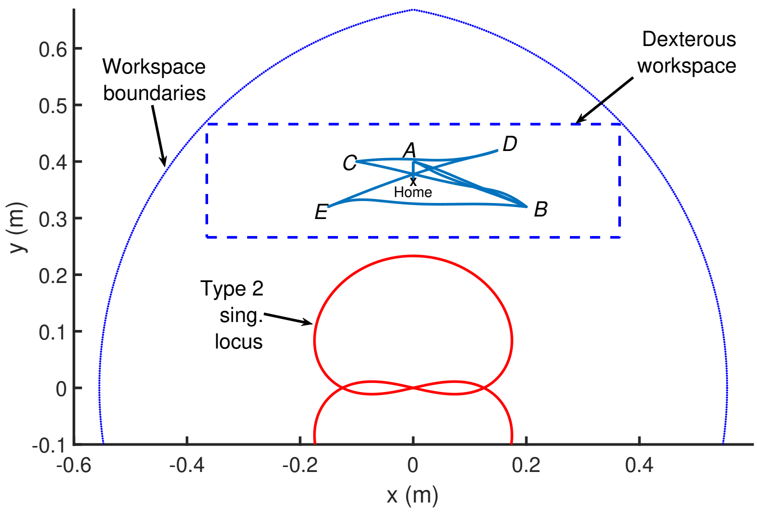

Figure 4.22: Multiple-point pick-and-place sequence in the five-bar mechanism workspace: $A \rightarrow B$ (travel time: 0.33 s), $B \rightarrow C$ (travel time: 0.32 s), $C \rightarrow D$ (travel time: 0.32 s), $D \rightarrow E$ (travel time: 0.31 s), $E \rightarrow B$ (travel time: 0.33 s), $B \rightarrow A$ (travel time: 0.31 s).

Finally, for the second set of boundary pick-and-place conditions, the results in terms of the reduction of the energetic losses from the two types of actuation (nominal and by using VSS) are shown in Fig. 4.25 and Fig. 4.26, respectively for the case when considering friction and when decoupling the friction. It can be seen that the energetic losses from the full actuation chain when considering the friction losses in Fig. 4.25 can be drastically reduced by a 54 %. For the case in which we separate the contribution due to friction losses in Fig. 4.26, the energetic losses can be drastically reduced by a 65 %. It is worth noticing that for this experiment, the distribution of efforts characterized by $|\boldsymbol{\tau}+\boldsymbol{\tau}_{vss}|_{\mathrm{RMS}}$ plays an important role for the reduction of the energetic losses. This can be seen by comparing the reduction percentages separately from the input efforts of the robot and from the VSS in Tables 4.7 and 4.8, in which the separated reduction percentages are lower than the reduced energy consumption. Nevertheless, if we analyze the reduction percentages of input efforts from Tables 4.9 and 4.10, these percentages are more or or less of the same order as the energy gained from Fig. 4.25 and Fig. 4.26, respectively. This can be explained by analyzing the energetic model (2.43) in which the summation of energy losses from the motors in the full actuation chain is taken into account. Therefore at each integration time of the power losses model it is important to consider the value for the input torques respectively from adding the input efforts from the robot and the VSS, thus considering the distribution of input torques. It should be also noted that based on

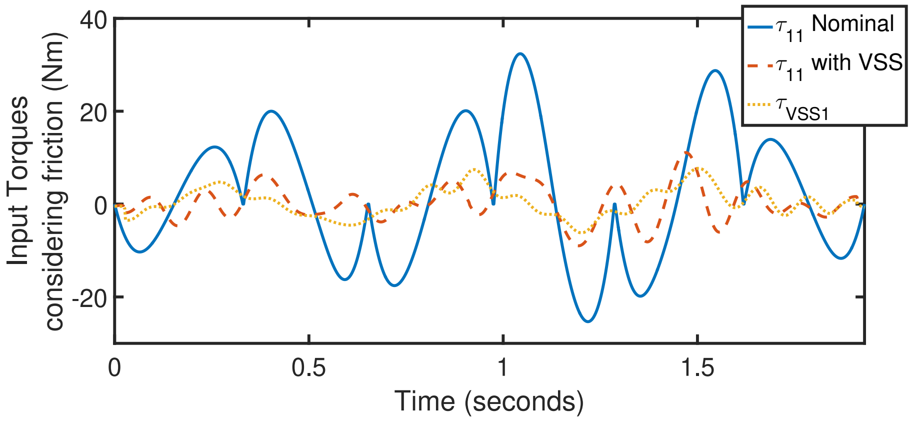

Figure 4.23: Input torques grouping the first actuation chain considering a nominal case and the case when using VSS for the second set of boundary pick-and-place constraints.

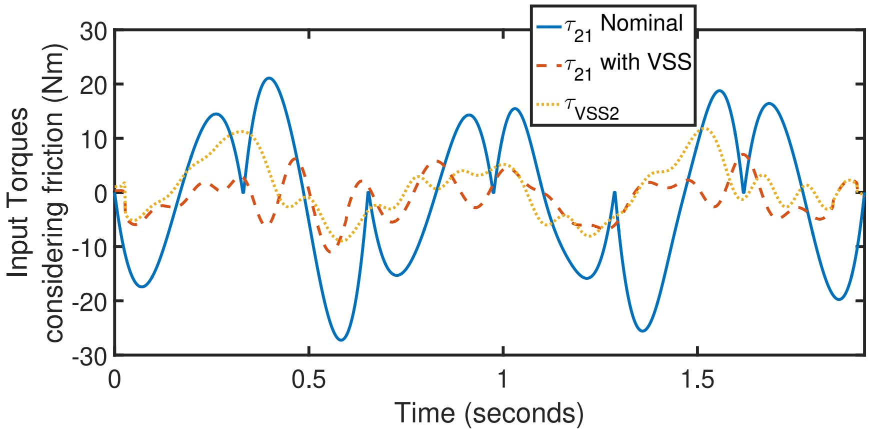

Figure 4.24: Input torques grouping the second actuation chain considering a nominal case and the case when using VSS for the second set of boundary pick-and-place constraints.

Fig.4.27, in addition to ensure an energy-efficient motion from the robot, also the tracking error from the CTC performed along the desired pick-and-place motion remains bounded, thus ensuring the accuracy.

Table 4.7: RMS values of input torques for nominal case and for case when using VSS in parallel for the second set of boundary pick-and-place conditions considering the friction effects.

		Nominal RMS. Torques	Using VSS in parallel RMS. Torques		Gain each joint	Overall gain
Segment	Time (s)	$\boldsymbol{\tau}_{\text{RMS}}$ (Nm)	$\boldsymbol{\tau}_{\text{RMS}}$ (Nm)	$\boldsymbol{\tau}_{vss_{\text{RMS}}}$ (Nm)	%	%
Fig. 4.22	1.92	[14.38, 13.17]	[3.70, 3.82]	[3.00, 4.92]	[53.40, 33.62]	43.51

Table 4.8: RMS values of input torques for nominal case and for case when using VSS in parallel for the second set of boundary pick-and-place conditions without considering the friction effects.

		Nominal RMS. Torques	Using VSS in parallel RMS. Torques		Gain each joint	Overall gain
Segment	Time (s)	$\boldsymbol{\tau}_{\text{RMS}}$ (Nm)	$\boldsymbol{\tau}_{\text{RMS}}$ (Nm)	$\boldsymbol{\tau}_{vss_{\text{RMS}}}$ (Nm)	%	%
Fig. 4.22	1.92	[14.38, 13.17]	[2.64, 2.72]	[2.20, 3.60]	[66.34, 52.01]	59.17

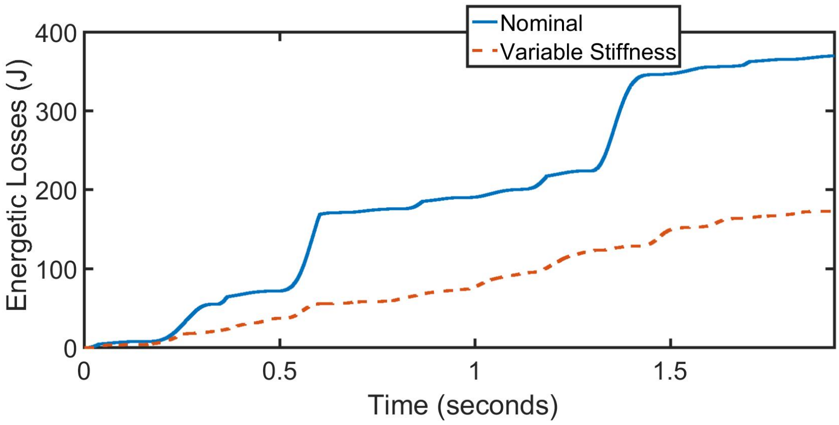

Figure 4.25: Comparison of energetic losses for two types of actuation: nominal and case when using VSS and considering the friction effects due to the VSS for the second set of boundary pick-and-place constraints.

Table 4.9: RMS values of input torques for nominal case and for case when using VSS in parallel for the second set of boundary pick-and-place conditions considering the friction effects and by analyzing the distribution of torques for the actuation with VSS.

		Nominal RMS. Torques	Using VSS in parallel RMS. Sum of Torques	Gain each joint	Overall gain
Segment	Time (s)	$\boldsymbol{\tau}_{\text{RMS}}$ (Nm)	$\lvert\boldsymbol{\tau}+\boldsymbol{\tau}_{vss}\rvert_{\text{RMS}}$ (Nm)	%	%
Fig. 4.22	1.92	[14.38, 13.17]	[5.56, 7.40]	[61.32, 43.76]	52.54

Table 4.10: RMS values of input torques for nominal case and for case when using VSS in parallel for the second set of boundary pick-and-place conditions without considering the friction effects and by analyzing the distribution of torques for the actuation with VSS.

		Nominal RMS. Torques	Using VSS in parallel RMS. Sum of Torques	Gain each joint	Overall gain
Segment	Time (s)	$\boldsymbol{\tau}_{\text{RMS}}$ (Nm)	$\lvert\boldsymbol{\tau}+\boldsymbol{\tau}_{vss}\rvert_{\text{RMS}}$ (Nm)	%	%
Fig. 4.22	1.92	[14.38, 13.17]	[4.02, 5.37]	[72.05, 59.19]	65.62

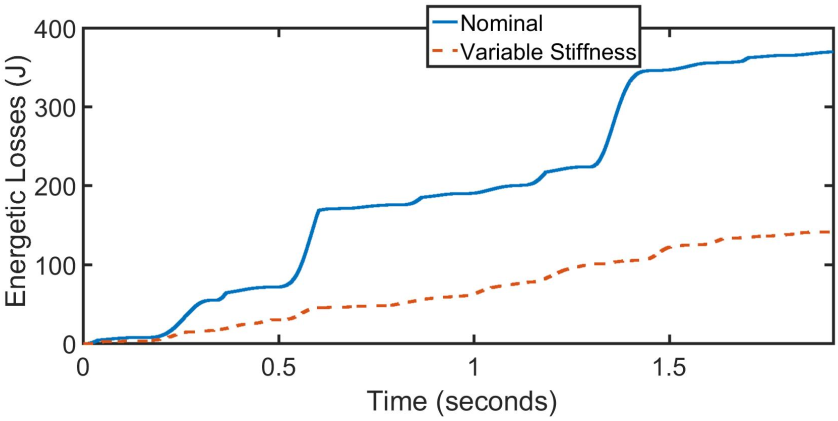

Figure 4.26: Comparison of energetic losses for two types of actuation: nominal and case when using VSS and without considering the friction effects due to the VSS for the second set of boundary pick-and-place constraints.

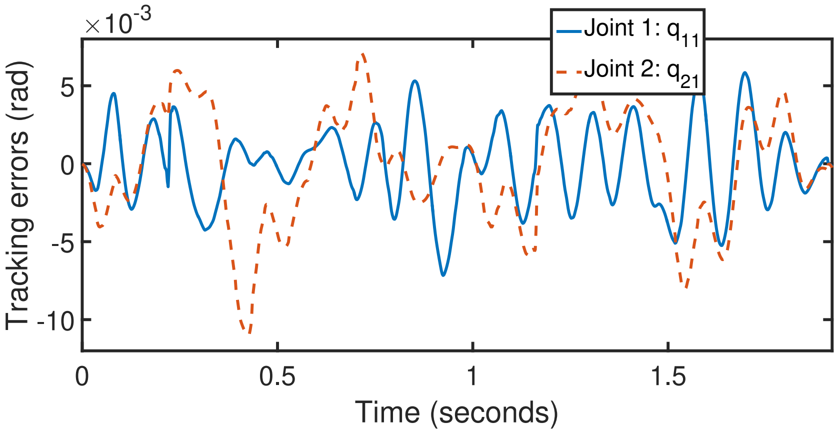

Figure 4.27: Tracking errors along the trajectory generated for the second set of boundary pick-and-place conditions in order to show that thanks to the direct power connection between the motors and the proximal links of the five-bar robot we can ensure accuracy at high-speeds.

As final remarks of this Chapter, it is worth mentioning that even if the friction effects are preponderant in the full actuation chain, it has been shown that experimentally through the addition of the VSS in parallel it is possible to drastically reduce the energy consumption in the full actuation chain with respect to a nominal type of actuation. This is due to a proper distribution of efforts between the robot active joints and the VSS joints. Additionally, since we exploit the natural dynamics through a forced oscillator, i.e. motors to control the force/displacement relation $\boldsymbol{\tau}_s$ (related to the optimal stiffness), the energy-efficient actuation chain only has to compensate, in addition to the inertial effects associated to the resonance modes that could not be set along the displacement, the effects of friction forces. Different to what it would occur with an unforced oscillator, in which after a certain number of oscillations, the system would brake due to these dissipative forces.

4.4 Summary

In this Chapter, the experimental results obtained in this thesis were presented. In the first Section of this Chapter, the industrial-sized prototype used for experimental validation was described. Additionally, the mechanical design and functioning principle of our variable stiffness system was explained in detail, from the process of designing until prototyping the final real mock-up. A detail explanation of the active and passive joints of the parallel robot was given, including schematics of assembly both for the robot joints and variable stiffness joints. Then, the instrumentation and communication network including hardware and software components to control the prototype was explained.

In the second Section, the identification of the physical parameters for the prototype was performed in order to build the dynamic model used for the experimental validations. It was shown that the physical values of the friction terms represent an important contribution in the actuation chain due to the transmission system developed for the variable stiffness system, mainly due to the pulley-belt drive and the internal contact on the spring coils. This allowed as well to identify the limitations of our prototype when performing energy-efficient motions. That is why when analyzing the results in terms of energy efficiency from our proposed actuation chain, we considered the energetic losses with and without the friction forces.

Finally, in the last Section, we validated the theoretical formulations by considering quasi-periodic multiple-point sequences of desired pick-and-place points. In order to have a comparison index for validating that our actuation principle was optimal for increasing energy efficiency, two types of actuation were compared: *i*) nominal actuation, in which we removed physically the pulley-belt transmission drive of the VSS, so we only have the five-bar mechanism, and *ii*) by using VSS in parallel to the actuated links of the five-bar robot. The results of experiments on the real prototype showed that by considering the friction effects, the gain in energy consumption varied between 50 to 55 %, and without considering the friction effects we can achieve between 60 to 65 % of energy reduction. Furthermore, the tracking errors show that thanks to the direct power connection between the motors and the actuated links of the five-bar robot, it is possible with a classical CTC ensure the accuracy, in addition to the gain on energy efficiency. It is worth noticing that the percentages of energy reduction vary depending on the assembly of the variable stiffness system, and also on the amplitude of the deformation under which the spring is subjected. This is due to the fact that there are some deformation directions for which the torsional spring is less prone to have internal contact of its coils. Additionally, it is worth noticing that the assumption of considering that the torsional spring of the VSS would be moving only as a revolute joint, i.e. in a rotational way, was wrong. This is due to the fact that for some given combination of robot and VSS motions, backlash effects occurred, leading to affect the optimal potential energy required to exploit the natural dynamics for a given task due to dead zones on the required force/displacement relation. Nevertheless, even if the variable stiffness prototype had some mechanical constraints, the proof-of-concept for the actuation principle proposed in this thesis for performing energy-efficient motions was validated for high-speed quasi-periodic tasks. Future works on this subject may be on the direction of optimal design for the VSS system. Additionally, it should be noted that at this step, there was not enough time to test the algorithm for online motion generation with dynamic parameters adaptation experimentally. Nevertheless, it is included in the future works of this subject.

Chapter 5

Exploiting natural dynamics: other application cases

5.1. *Definition of application cases* p. 166

5.2. *Reducing the energy consumption of an omnidirectional spherical rolling robot* p. 167

5.3. *Increasing the feasible static-wrench workspace of robots* p. 186

5.4. *Summary* p. 197

This Chapter is dedicated to demonstrate that the concept of exploiting natural dynamics can be applied to any robot in which a continuous exchange from potential to kinetic energy may occur. In previous Chapters it has been shown that by using VSS, it has been possible to exploit the natural quasi-oscillations of pick-and-place robots through the smart exchange between kinetic and VSS spring potential energy in order to put the system near resonance, thus considerably decreasing the energy consumption. In similar way, in this Chapter we will present an extension of this concept based on exploiting the natural dynamics of robots, but for two different applications: i) the reduction of energy consumption of mobile robots by using VSS in parallel, as it was done for parallel robots, and ii) for increasing the feasible static-wrench workspace of robots by exploiting the exchange from gravity potential energy to kinetic energy in order to join disconnected aspects of the static-wrench workspace. For doing this, in the first part of this Chapter we will formulate an optimization problem for reducing the energy consumption of an omnidirectional rolling robot with VSS in parallel. In the second part of this Chapter, a strategy for exploiting the gravity potential energy will be presented in order to increase the feasible static-wrench workspace of robots, i.e. to exploit the robot natural oscillations in dynamics, so that the robot can carry payloads out of its feasible static-wrench workspace. This strategy will be validated on a 2-DOF serial robot.

5.1 Definition of application cases

Over the last decades, several researchers and companies have kept special attention on the idea of creating robots whose dynamic performance in terms of reducing the required moving efforts and minimizing the energy expenditure could be drastically improved. In order to contribute to solve these problems, in previous Chapters we have focused on developing strategies for reducing the energy consumption of high-speed pick-and-place robots by exploiting the robot natural dynamics in such a way that the desired quasi-oscillations match with the robot free-response. That is why, following the same motivation, in this Chapter we propose to apply the same concept of exploiting the natural dynamics, for robots in other types of applications in which they are not necessarily required to perform high-speed tasks and in which a continuous exchange from potential to kinetic energy may be smartly controlled.

In order to define the cases of application in which the concept of natural dynamics will be extended, we have chosen two types of systems: i) a mobile robot with VSS in parallel, similar to what it was done for parallel robots in Chapters 2–4, and ii) a robot carrying a payload for which the reachable workspace is typically reduced due to the maximal value that each actuator can deliver, resulting on a division of its static-wrench workspace into several disconnected aspects.

The choice of the aforementioned application cases has been done due to the impact in their respective fields of applications. In mobile robots one of the main problems is the lack of energetic autonomy for instance to perform exploration tasks [Mei 2002][Sun 2005] [Liu 2014] or for mobile robots in factories [Canfield 2018]. That is why by using VSS in parallel, once the actuation concept has been proven in previous Chapters, we seek to reduce the energy consumption while performing a desired mobile robot motion to go from one position to another. For the case of robots carrying a payload, we will seek to smartly exploit the exchange from gravity potential energy to kinetic energy (similar to what we did with the VSS potential energy previously) in order to connect two desired payload positions, which are placed in two disconnected aspects of its static-wrench workspace divided due to the actuator limits.

This Chapter is thus divided as follows: Section 5.2 presents the formulation of an optimal motion planner for reducing the energy consumption for an omnidirectional rolling robot with VSS in parallel to the motors. Section 5.3 shows the algorithm formulation for performing optimal trajectories that connect two aspects of the static-wrench workspace of robots, divided due to the maximal actuator torques. Finally in Section 5.4, some conclusions and perspectives to other application cases in which the concept of exploiting natural dynamics could be applied, are discussed.

5.2 Reducing the energy consumption of an omnidirectional spherical rolling robot

Before starting this part, I would like to mention that the results presented in this Section 5.2 were obtained as part of two supervised Master projects from Matthieu FURET in M2, and Ashwin BOSE and Sooraj ANILKUMAR in M1.

In mobile robots, the energetic performance is a key issue due to the limited amount of energy to perform exploration tasks. The classical approach to increase the energetic autonomy of a mobile robot is by adding more batteries and electrical components. Even if this allows increasing the working time of the robot, the heavy mobile robot architecture affects the efficiency due to an increase on the required input forces, and thus on the power demanding.

In order to avoid these drawbacks and to increase the energy efficiency, this Section proposes to apply the actuation concept presented in Chapter 3 based on variable stiffness springs (VSS) in parallel configuration with the motors to minimize the energy consumption. The VSS will be used to carry out the reduction of the energy consumption and their parallel configuration with the motors ensures the accuracy of the robot motion while performing a given path. The idea is similar to a pick-and-place robot, to smartly tune the stiffness of the VSS so that the exchange of energies between kinetic and the VSS potential energy is optimized and the robot is put in near a resonance mode, thus considerably minimizing the energy consumed during tasks of the mobile robot.

In order to define the mobile robot which will be used as case study in this Section, we will choose a robot that may be useful in real applications like exploration tasks, such as humanitarian demining, surveillance tasks, etc. [Marques 2012]. For such types of exploration applications, several types of robots can be used, e.g. wheeled robots, tracked robots, rolling robots, etc. [Zhuang 2014]. For the studies presented in this Section we will use a spherical rolling robot [Tomik 2012][Mojabi 2002]. Among several advantages of using a spherical mobile robot with respect to wheeled, or tracked mobile robots, we can list:

- All the moving elements of the robot, from which the motion is produced, such as mobile masses, are kept inside the spherical shape of the mobile robot. This provide protection to the mechanical components from environmental effects;
- Thanks to the fact that all moving elements are inside the spherical shape of the robot, there are not extremities that could get blocked with obstacles;
- Rolling robots can potentially move in any direction (omnidirectional), allowing to turn easily in case an obstacle is encountered.

It should be noted as well that in this study, we will consider spherical rolling robots that move based on the principle of moving the center of gravity thanks to the motion of mobile masses inside the sphere. Thus, in order to validate all the theoretical formulations that will be developed in this Section, simulations on a spherical rolling robot, which can perform omnidirectional motions thanks to the movement of reciprocating masses, will show the reduction of the energy consumption.

5.2.1 Description of spherical rolling robot with mobile masses

The type of rolling robot studied in this Section belongs to the category of *reciprocating mass driven* [Tomik 2012][Mojabi 2002]. This category of spherical robots generates a desired motion by shifting their center of mass or *barycenter*. When the barycenter is shifted from the vertical neutral axis, the robot rolls towards the new barycenter to stabilize itself. The robot can smoothly traverse its environment with proper timing and control methodologies. The main limitation to this design is its constraint on the maximum output torque.

The *reciprocating mass driven* type rolling robots have a low torque requirement as the majority of its mass is located in its core, which is connected to the spherical shell using multiple shafts. The drive mechanism consists of weights, designed to traverse about these shafts, thereby shifting the center of mass of the robot and causing the robot to roll. This design was applied in robots like *Spherobot* [Tomik 2012] and *August* [Mojabi 2002] (see Fig. 5.1). This type of robots can move in any direction, irrespective of the orientation of the robot (within the torque limits). However, they usually operate in a low rate as the internal masses move slowly. The control of this type of robot is also challenging as one has to keep in track of the orientation as well as distance of all masses from the center at all times.

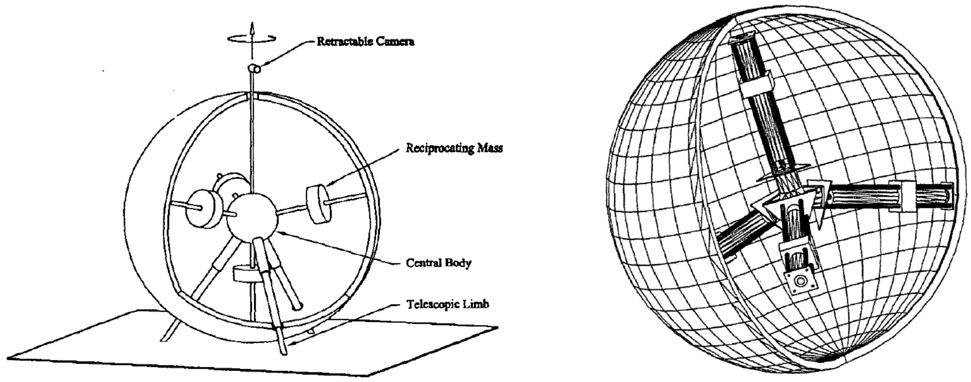

(a) Spherobot [Tomik 2012] **(b)** August [Mojabi 2002]

Figure 5.1: Reciprocating mass driven rolling robots

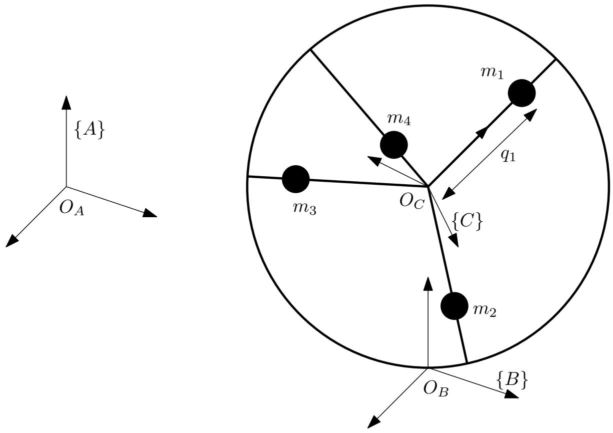

Figure 5.2: Schematic of the rolling robot without elastic elements: In this type of actuation, q_i can be controlled to propel the robot.

In this Section, we perform a detailed study on a reciprocating mass based rolling robot. We will analyzed the energy consumption for two cases: (i) a nominal robot with no elastic elements, and (ii) a robot with VSS in parallel.

5.2.2 Modeling of spherical rolling robot with mobile masses

Let us consider the spherical robot from Fig. 5.2. It consists of a spherical shell, a tetrahedral frame centered at the center of the shell, and masses that can move along each link of the frame (See Fig. 5.2). The position of the *barycenter* of the robot can be controlled by moving the reciprocating masses. This causes an imbalanced moment that propels the robot.

We define three coordinate systems as shown in Fig. 5.2. $\{A\}$ is a global coordinate system with its origin at O_A, and z-axis along the vertical. The coordinate system $\{B\}$ has its origin, O_B, located at the point of contact of the shell with the ground. Its axes are aligned along those of $\{A\}$. The origin of $\{C\}$ is located at the center of the sphere. Its z-axis is aligned with the axis of reciprocation of Mass 1. The axis of motion of Mass 2 lies on the x-z plane of $\{C\}$.

The kinematic and dynamic equations of the systems were developed in `Mathematica` (symbolic computation software). The derivation of those equations are explained in detail in the following Sections.

5.2.2.1 Geometric Model

The robot is assumed to have a pure rolling motion with respect to the ground. We need seven variables to fully represent the robot in $\{B\}$ (four for the displacement of masses and 3 for the orientation of the $\{C\}$ w.r.t $\{B\}$). The state vector of the robot is thus defined by:

$$\mathbf{q} = [q_1, q_2, q_3, q_4, \alpha, \beta, \gamma]^\top \tag{5.1}$$

where, q_i $(i = 1, \ldots, 4)$ is the displacement of i^{th} mass from the center, α, β, γ are the roll-pitch-yaw angles. The position of the center of the shell:

$$^{B}\mathbf{p}_{O_c} = [0, 0, R]^\top \tag{5.2}$$

where R is the radius of the spherical shell.

The unit vectors along the tetrahedral spokes are defined as:

$$\begin{aligned}
^{C}\hat{\mathbf{p}}_1 &= [0, 0, 1]^\top \\
^{C}\hat{\mathbf{p}}_2 &= \mathbf{R}_Y(\phi)\ ^{C}\hat{\mathbf{p}}_1 \\
^{C}\hat{\mathbf{p}}_3 &= \mathbf{R}_Z(2\pi/3)\ ^{C}\hat{\mathbf{p}}_2 \\
^{C}\hat{\mathbf{p}}_4 &= \mathbf{R}_Z(2\pi/3)\ ^{C}\hat{\mathbf{p}}_3
\end{aligned} \tag{5.3}$$

where, $\mathbf{R}_Y$ and $\mathbf{R}_Z$ represent rotations about Y and Z axes respectively and ϕ ($\approx 109.47°$) is the *tetrahedral angle*.

The position vectors of the masses in $\{C\}$ are defined as:

$$ {}^{C}\mathbf{p}_i = q_i\ {}^{C}\hat{\mathbf{p}}_i; \qquad i = 1, \ldots, 4 \tag{5.4} $$

where, q_i is the displacement of mass i from the center of the sphere.

The positions of these masses in $\{B\}$ are defined as:

$$ \begin{aligned} {}^{B}\mathbf{p}_i &=^{B} \mathbf{p}_{O_c} +^{B} \mathbf{R}_C(\alpha, \beta, \gamma)\ {}^{C}\mathbf{p}_i \\ &=^{B} \mathbf{p}_{O_c} + q_i^{B}\hat{\mathbf{p}}_i; \qquad i = 1, \ldots, 4 \end{aligned} \tag{5.5} $$

where, ${}^{B}\mathbf{R}_C(\alpha, \beta, \gamma)$ is the rotation matrix using Z-Y-X Euler angle convention, and ${}^{B}\hat{\mathbf{p}}_i$ is ${}^{C}\hat{\mathbf{p}}_i$ represented in $\{B\}$. ${}^{B}\mathbf{p}_i$ was found to be a function of q_i, α, β and γ.

5.2.2.2 First Order Kinematic Model

The angular velocity of the spherical shell about $\{B\}$,

$$ \boldsymbol{\omega} = [\omega_x, \omega_y, \omega_z]^{\top} \tag{5.6} $$

The velocity of the masses in $\{B\}$:

$$ \begin{aligned} {}^{B}\mathbf{v}_i &= \boldsymbol{\omega} \times^{B} \mathbf{r} + \mathbf{v}_{rel} \\ &= \boldsymbol{\omega} \times^{B} \mathbf{r}_i + \dot{q}_i\ {}^{B}\hat{\mathbf{p}}_i \qquad i = 1, \ldots, 4 \end{aligned} \tag{5.7} $$

where, ${}^{B}\mathbf{r}_i$ is the position vector of Mass i, $\mathbf{v}_{rel}$ is ${}^{C}\mathbf{v}_i$ expressed in $\{B\}$, $\dot{q}_i$ is the translational velocity of Mass i along its axis. ${}^{B}\mathbf{v}_i$ is a function of $q_i, \dot{q}_i, \alpha, \beta, \gamma$, and $\boldsymbol{\omega}$.

5.2.2.3 Second Order Kinematic Model

Similarly, the angular accelerations of the spherical shell about $\{B\}$,

$$ \dot{\boldsymbol{\omega}} = [\dot{\omega}_x, \dot{\omega}_y, \dot{\omega}_z]^{\top} \tag{5.8} $$

The accelerations of the masses:

$$\begin{aligned} {}^{B}\mathbf{a}_i &= \dot{\boldsymbol{\omega}} \times^{B} \mathbf{r} + \boldsymbol{\omega} \times (\boldsymbol{\omega} \times q_i^{B}\hat{\mathbf{p}}_i) + 2(\boldsymbol{\omega} \times \mathbf{v}_{rel}) + \mathbf{a}_{rel} \\ &= \dot{\boldsymbol{\omega}} \times^{B} \mathbf{r} + \boldsymbol{\omega} \times (\boldsymbol{\omega} \times q_i^{B}\hat{\mathbf{p}}_i) + 2(\boldsymbol{\omega} \times \dot{q}_i \; {}^{B}\hat{\mathbf{p}}_i) + \ddot{q}_i \; {}^{B}\hat{\mathbf{p}}_i \qquad i = 1, \ldots, 4 \end{aligned} \tag{5.9}$$

where, $\mathbf{a}_{rel}$ is ${}^{C}\mathbf{a}_i$ expressed in $\{B\}$, $\ddot{q}_i$ is the acceleration of Mass i along its axis. ${}^{B}\mathbf{a}_i$ is a function of $q_i, \dot{q}_i, \ddot{q}_i, \alpha, \beta, \gamma, \boldsymbol{\omega}$ and $\dot{\boldsymbol{\omega}}$.

For the static case, the accelerations of the masses can be approximated as:

$${}^{B}\mathbf{a}_i \approx \ddot{q}_i \; {}^{B}\hat{\mathbf{p}}_i \tag{5.10}$$

This approximation is reasonable as we operate at slow speeds, thus having slow dynamics.

5.2.2.4 Dynamic Model

In this Section, we study the effect of different forces, namely the actuator forces and gravity on the robot. For this, we first define the various mass parameters of the robot. The reciprocating bodies are assumed to be point masses with mass m and zero moment of inertia. The spherical shell has a mass M and radius R.

Its moment of inertia about its center (the thickness of the shell is assumed to be negligible compared to its radius) is $\frac{2}{3}MR^2$. Using parallel axis theorem, we find the moment of inertia of the shell about the origin of $\{B\}$ as:

$$I_{shell} = \begin{bmatrix} \frac{5}{3}MR^2 & 0 & 0 \\ 0 & \frac{5}{3}MR^2 & 0 \\ 0 & 0 & \frac{2}{3}MR^2 \end{bmatrix} \tag{5.11}$$

At any instant, the inertial and gravitational forces acting on the masses, along the direction of the spoke, are balanced by the actuators. Therefore, the force applied by the actuators can be found as:

$$\begin{aligned} F_i &=^{B} \hat{\mathbf{q}}_i.(\mathbf{F}_{inertia,i} + \mathbf{F}_{gravity,i}) \\ &= m^{B}\hat{\mathbf{q}}_i.(-\mathbf{g} +^{B} \mathbf{a}_i) \end{aligned} \tag{5.12}$$

where, $\mathbf{g} = [0, 0, -g]^{\top}$ is the gravity vector.

The force balance about O_B would give us the reaction forces at B. We omit that computation since it is not relevant for our application. We now compute the moment balance about O_B. The total gravity moment:

$$\mathbf{M}_{gravity} = \sum_{i=1}^{4} \mathbf{M}_{gravity,i} = \sum_{i=1}^{4} m({}^{B}\mathbf{p}_i \times \mathbf{g}) \tag{5.13}$$

Similarly, the inertia moment due to the masses,

$$\mathbf{M}_{inertia,masses} = -m \sum_{i=1}^{4} {}^{B}\mathbf{p}_i \times \mathbf{a}_i \tag{5.14}$$

The inertia moment due to the shell,

$$\mathbf{M}_{inertia,shell} = \mathbf{I}_{shell}\ \dot{\boldsymbol{\omega}} + (\boldsymbol{\omega} \times (\mathbf{I}_{shell}\ \boldsymbol{\omega})) \tag{5.15}$$

The total inertia moment:

$$\mathbf{M}_{inertia} = \mathbf{M}_{inertia,shell} + \mathbf{M}_{inertia,masses} \tag{5.16}$$

Inertia balance about O_B gives us:

$$\mathbf{M}_{inertia} + \mathbf{M}_{gravity} = 0 \tag{5.17}$$

Equation (5.17) gives us the relationship between the rolling motion of the robot and the translation motion of the reciprocating masses.

For the static case, this equation can be approximated as:

$$I_{shell}\dot{\boldsymbol{\omega}} = -\sum_{i=1}^{4} m({}^{B}\mathbf{p}_i \times \mathbf{g}) + m \sum_{i=1}^{4} {}^{B}\mathbf{p}_i \times (\ddot{q}_i\ {}^{B}\hat{\mathbf{p}}_i) \tag{5.18}$$

5.2.3 Modeling of variable stiffness springs in parallel configuration with the mobile masses

5.2.3.1 Rolling Robot with VSS in Parallel

In this Section, we add a variable stiffness spring to the system. The schematic is shown in Fig. 5.3. In this system the variable stiffness joint from the VSS in parallel, q_{s_i} is adjustable.

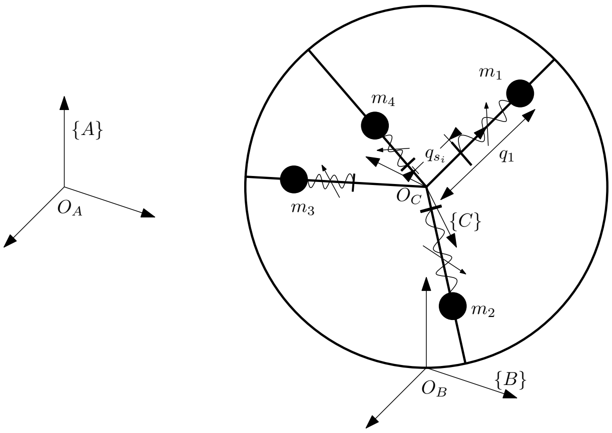

Figure 5.3: Schematic of the rolling robot with VSS: In this case, we can control the position of the mass, q_i, and spring base, q_{s_i}, located in the i^{th} link.

This lead to a state vector of the robot of dimension eleven and parameterized by:

$$\mathbf{q} = [q_1, q_2, q_3, q_4, q_{s1}, q_{s2}, q_{s3}, q_{s4}, \alpha, \beta, \gamma]^\top \tag{5.19}$$

where, q_i and q_{s_i} are the position of the masses and spring bases of i^{th} link respectively and α, β, and γ the roll, pitch and yaw angles. Finally the actuator force at i^{th} actuator is defined by:

$$\begin{aligned} F_i &= \hat{\mathbf{q}}_i.(\mathbf{F}_{inertia,i} + \mathbf{F}_{gravity,i})\mathbf{F}_{spring,i} \\ &= m\hat{\mathbf{q}}_i.(-\mathbf{g} +^B \mathbf{a}_i) + k(q_i - q_{s_i} - l_s) \end{aligned} \tag{5.20}$$

And the dynamics associated to the variable stiffness system is given by the relation:

$$F_{s_i} = m_s\ddot{q}_i + h_s(q_s, \dot{q}_s) + k(q_{s_i} + l_s - q_i) \tag{5.21}$$

where m_s is the mass associated to the coupling system of the spring and motor.

5.2.4 Energy-efficient motion generation and control

In this Section, we address the problem of motion planning both for the positions of the masses and for the spring bases used to adjust the VSS. It should be noted that by investigating the aforementioned mathematical formulations (modeling of the dynamics of the mobile robot with VSS), it is not obvious how to set a problem formulation to exploit the natural dynamics of the system. This is due to fact that firstly it is necessary to define a strategy which permits to propel the center of mass of the sphere according to the change of positions of the masses (very few works have addressed this problem, e.g. see [Tomik 2012][Mojabi 2002]). And on a second stage we encounter the challenge of defining an adequate motion planner for the spring bases of the VSS in such a way that for a given sphere motion, we minimize the energy consumption of the full actuation chain.

Thus, in order to overcome the aforementioned issues, and to move the center of the rolling robot from an initial position to a final position, we will firstly present an algorithm for steering the spherical rolling robot by continuously changing the location of its center of mass through the motion of masses positions. And on a second stage, an energy-based optimal trajectory planner will be formulated. In such optimization problem, the variable stiffness joints will be used as decision variables for the optimization formulation, and an energetic criterion will be minimized.

5.2.4.1 Motion generation for spherical rolling robot

Steering Algorithm

In this part, we propose an algorithm for steering the robot by continuously modifying the locations of the moving masses. The position of the center of mass of the robot in local frame is described as:

$$^{B}\mathbf{p}_{COM} = \frac{1}{4}\sum_{i=1}^{4} {}^{B}\mathbf{p}_i \tag{5.22}$$

where $^{B}\mathbf{p}_i$ is defined in equation (5.5).

The moment generated due to the weight of the masses about $\{B\}$ are given by the relation:

$$\begin{bmatrix} M_x \\ M_y \\ M_z \end{bmatrix} = 4m^{B}\mathbf{p}_{COM} \times \begin{bmatrix} 0 \\ 0 \\ g \end{bmatrix} \tag{5.23}$$

where mg is the weight of the masses and × is the cross product. It should be noted that, $M_z = 0$. This means that the robot cannot generate a spin about the vertical axis. By controlling q_i, we can control $^{B}\mathbf{p}_{COM}$ and thus generate desired M_x and M_y. Since

${}^{B}x_{COM}$ and ${}^{B}y_{COM}$ are the only terms that effect the moments, we just have to control them. However, we have the freedom to control the positions of four masses. We thus use the extra degrees of freedom to ensure that the masses stay as close as possible to the initial position. The following equations were solved to find the positions of the masses:

$$\begin{aligned} {}^{B}\mathbf{p}_{COM} &= \frac{1}{4}\sum_{i=1}^{4} {}^{B}\mathbf{p}_{i} \qquad (5.24) \\ \sum_{i=1}^{4} q_i &= 4q_{init} \end{aligned}$$

where q_{init} is the home position of the masses. Furthermore, it should be noted that since ${}^{B}x_{COM}$, ${}^{B}y_{COM}$ and ${}^{B}z_{COM}$, grouped in ${}^{B}\mathbf{p}_{COM}$, are functions of ${}^{B}\mathbf{p}_{i}$ in (5.22), and therefore functions of q_i, α, β and γ in (5.5), we can find an analytic expression representing the reciprocating masses positions q_1, q_2, q_3 and q_4 as a function of a given set of desired sphere positions ${}^{B}x_{COM} = x_{desired}$ and ${}^{B}y_{COM} = y_{desired}$ (${}^{B}z_{COM} = R$). This will permit us to control the masses in order to enforce a desired behavior of the center of the mass of the sphere and therefore to generate the desired moment M_x and M_y to steer the sphere.

In order to find these expressions, we used the *symbolic* toolbox from Matlab in order to solve the expressions grouped in (5.24), for q_1, q_2, q_3 and q_4, respectively since ${}^{B}\mathbf{p}_{COM}$ can be expressed as function of the mobile masses positions in (5.22). The resulted analytic expressions for representing the positions of the masses were found as:

$$\begin{aligned} q_1 =& q_{init} + 3x\sin(\alpha)\sin(\gamma) + 3\cos(\alpha)(x\sin(\beta)\cos(\gamma) - y\sin(\gamma)) \qquad (5.25) \\ &+ 3y\sin(\alpha)\sin(\beta)\cos(\gamma) \\ q_2 =& q_{init} - x\sin(\alpha)\sin(\gamma) + \cos(\alpha)\left(-x\sin(\beta)\cos(\gamma) + 2\sqrt{2}x\cos(\beta) + y\sin(\gamma)\right) \\ &- y\sin(\alpha)\sin(\beta)\cos(\gamma) + 2\sqrt{2}y\sin(\alpha)\cos(\beta) \\ q_3 =& q_{init} - x\sin(\alpha)\sin(\gamma) - \sqrt{6}x\sin(\alpha)\cos(\gamma) \\ &+ \cos(\alpha)\left(-\sqrt{2}x\cos(\beta) + \sin(\gamma)\left(\sqrt{6}x\sin(\beta) + y\right) + \cos(\gamma)\left(\sqrt{6}y - x\sin(\beta)\right)\right) \\ &+ \sqrt{6}y\sin(\alpha)\sin(\beta)\sin(\gamma) - y\sin(\alpha)\sin(\beta)\cos(\gamma) - \sqrt{2}y\sin(\alpha)\cos(\beta) \\ q_4 =& q_{init} - x\sin(\alpha)\sin(\gamma) + \sqrt{6}x\sin(\alpha)\cos(\gamma) \\ &- \cos(\alpha)\left(\sqrt{6}x\sin(\beta)\sin(\gamma) + x\sin(\beta)\cos(\gamma) + \sqrt{2}x\cos(\beta) - y\sin(\gamma) + \sqrt{6}y\cos(\gamma)\right) \\ &- \sqrt{6}y\sin(\alpha)\sin(\beta)\sin(\gamma) - y\sin(\alpha)\sin(\beta)\cos(\gamma) - \sqrt{2}y\sin(\alpha)\cos(\beta) \end{aligned}$$

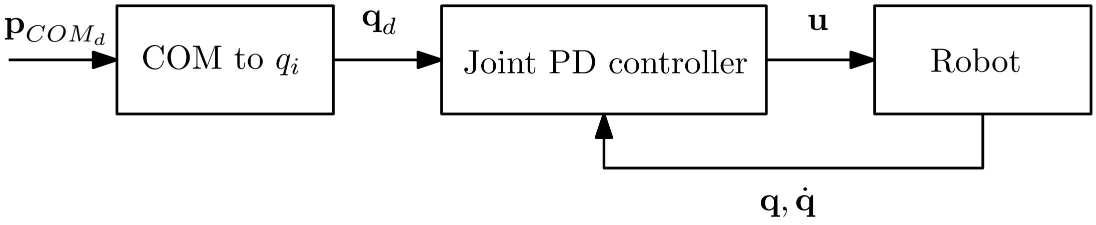

Figure 5.4: Joint control scheme

Now, based on these previous computations, we can move the robot by shifting its center of mass. The control scheme to do this is shown in Figure. 5.4. Here, $\mathbf{p}_{COM_d}$ is the desired position of the center of mass, $\mathbf{q}_d$ is the desired displacement for the moving mass in order to attain this center of mass (calculated using equation. (5.25)), $\mathbf{u}$ the control signal, and $\mathbf{q}$ and $\dot{\mathbf{q}}$ the state vector and its derivative respectively.

Position Control of Masses

For ensuring the proper position tracking of the masses motion, in order to generate the adequate moments for moving the robot, a classical PD controller to control the position of the masses is used:

$$\ddot{q}_i = -k_p e_{q_i} - k_d \dot{e}_{q_i} \tag{5.26}$$

where k_p and k_d are positive constants of proportional and derivative gains. e_{q_i} and $\dot{e}_{q_i}$ represent the tracking error in position and velocity. This control law is implemented in the block of *Joint PD controller* from Figure. 5.4.

5.2.4.2 Variable stiffness joint trajectories from VSS placed in parallel

In order to develop the motion planner from the variable stiffness joints of the spring bases of the VSS placed in parallel to the motors of the mobile masses, one could think of implementing the same BVP strategy presented in Chapter 3 for exploiting the natural dynamics of high-speed robots. Nevertheless, for the case of the spherical rolling robot with VSS, such strategy from Chapter 3 is not applicable. This is due to the fact that different to the case of a pick-and-place task in which there is no restriction on how to go from an initial position to a final position, here, it is necessary for the rolling robot to respect the moment generation motion law from the steering algorithm, which is define in the full time interval of the robot motion. This to ensure that the center of mass of the rolling robot is properly propelled by the four reciprocating masses.

In previous Chapters, we have already proven that in order to exploit as best as possible the exchange from VSS potential energy to kinetic energy, to reduce the input torques in the full actuation chain, i.e. considering the efforts required to adjust the VSS, it is necessary to optimally move the robot and VSS joints simultaneously (associated to the VSS force/displacement relation). However, for this case the mobile masses that produce the sphere motion are restricted to a prescribed trajectory to ensure a proper steering towards the desired final positions of the sphere (See expression (5.25)). That is why, in order to approximate as best as possible a VSS trajectory, which can exploit the robot natural dynamics (considering the inertia, Coriolis and centrifugal effects), and having the restriction of the robot motion defined in the full time span, we use a finite Fourier Series approach [Taheri 2014]. The advantage of using an expansion of Fourier series for building the variable stiffness joint motion planner is that the coefficients in the sum of sines and cosines functions of the Fourier series can be later used as decision variables for minimizing the energy consumption in the full actuation chain.

We will thus build the variable stiffness motion planner as follows. In order to exploit the dynamic equations from the robot and the VSS in expressions (5.20) and (5.21), so that we can minimize the actuator forces and therefore the energy consumption of the full actuation chain, we propose a motion profile for the spring bases of the VSS based on an expansion of Fourier series as follows:

$$\begin{aligned} q_{s_i}(t) = a_{0_i} + a_{1_i}\cos(\omega t) + b_{1_i}\sin(\omega t) + a_{2_i}\cos(2\omega t) \\ b_{2_i}\sin(2\omega t) + a_{3_i}\cos(3\omega t) + b_{3_i}\sin(3\omega t) \end{aligned} \tag{5.27}$$

where a_{0_i}, a_{1_i}, b_{1_i}, a_{2_i}, b_{2_i}, a_{3_i} and b_{3_i} are the coefficients of the Fourier series and ω represents the angular velocity. All these parameters characterizing the variable stiffness motion planner will be set as decision variables of the optimization problem. It should be noted that in order to define the number of coefficients in (5.27), considering that the periodic functions in the Fourier series can be written as an infinite sum [Taheri 2014], we use a heuristic approach of experimentally testing different number of coefficients in the VSS planner, until obtaining the best number of coefficients based on the energy consumed for the full actuation chain.

5.2.4.3 Optimization problem formulation: cost function and decision variables

The optimization problem aims to minimize the energy consumed by the spherical rolling robot with VSS, considering the full actuation chain, and taking into account physical constraints of the robot and the motors. The cost function of the optimization problem corresponds to the power consumption of the motors that actuate the reciprocating masses and the variable stiffness joints since the spherical robot must be as energy efficient as possible. The cost function for the optimizing process is thus defined as follows:

$$J = \int_0^{t_f} \sum_{i=1}^{4} (|P_{r_i}| + |P_{VSS_i}|)\, dt \tag{5.28}$$

where P_{r_k} and P_{VSS_k} represents the power consumed from the eight motors in the full actuation chain, mobile robot and VSS respectively, and defined as follows:

$$P_{r_i} = F_i \dot{q}_i \tag{5.29}$$

$$P_{VSS_i} = F_{s_i} \dot{q}_{s_i} \tag{5.30}$$

It is worth noticing that in this case we decided to minimize a criterion based on the output energy from the motors required to actuate the masses and not on the energetic losses. Even if this implies that the losses are not minimized in the power flow from input to output power, the acceleration and deceleration phases will be less preponderant since we will operate at slow speeds, leading to less resistive losses in the motor drive system (not the case for high-speed robots). Although resistive losses would be present, a generic capacitor could be placed in parallel to have regenerative phase, which in this case may be feasible since the amplitude of the currents related to the input forces will be low due to the nature of the application.

Based on the description of the trajectory planner in the previous Sections, the decision variable vector of the optimization problem, denoted as $\mathbf{x_{DecVar}}$, contains all aforementioned parameters from the Fourier series a_{0_i}, a_{1_i}, b_{1_i}, a_{2_i}, b_{2_i}, a_{3_i}, b_{3_i} and ω.

The optimal trajectory aims thus at finding the decision variable vector $\mathbf{x_{DecVar}}$ that minimizes the power consumption of th eight motors while respecting physical constraints, such as motor and joint limits.

The optimization problem was solved by means of MATLAB *fmincon* function and it is formulated as follows:

$$\begin{aligned} &\text{minimize} && J \\ &\text{over} && \mathbf{x_{DecVar}} \\ &\text{subject to} && |\tau_{e_k}| \leq \tau_{e_{max}} \\ & && |q_{s_i}| \leq q_{s_{max}} \end{aligned} \tag{5.31}$$

where τ_{e_k} is the electromagnetic torque of the kth motor $(k = 1, ..., (n + n_s))$, and $q_{s_{max}}$ represents the limit on the spring base motion considering the limitations on the allowable spring deformation.

Once the full trajectory definition both for the sphere and the variable stiffness joints have been parameterized, and the optimization has been set, in the following Section the simulation results are presented.

5.2.5 Simulation results

In order to validate the aforementioned energy-based optimization formulation, numerical validations are made thanks to a co-simulation between Matlab/Simulink and ADAMS. The proposed approach for increasing the energy efficiency was validated by comparing two actuation cases: i) nominal actuation in which no elastic elements are attached in parallel to the motors of the reciprocating masses and ii) the actuation in which the spherical rolling robot has VSS in parallel to the motors..

5.2.5.1 SolidWorks model

Since the CAD modeling capability of ADAMS is limited, we first developed the CAD model of the robot in `SolidWorks`. The components of the CAD model are shown in Fig. 5.5, and are listed as follows:

- Spherical shell
- Tetrahedral frame
- Reciprocating masses
- Spring base

The nominal rolling robot was modeled as shown in Figure. 5.5a and the robot with VSS in parallel is shown in Figure. 5.5b. The outer radius of the spherical shell R, was chosen to be 290 mm.

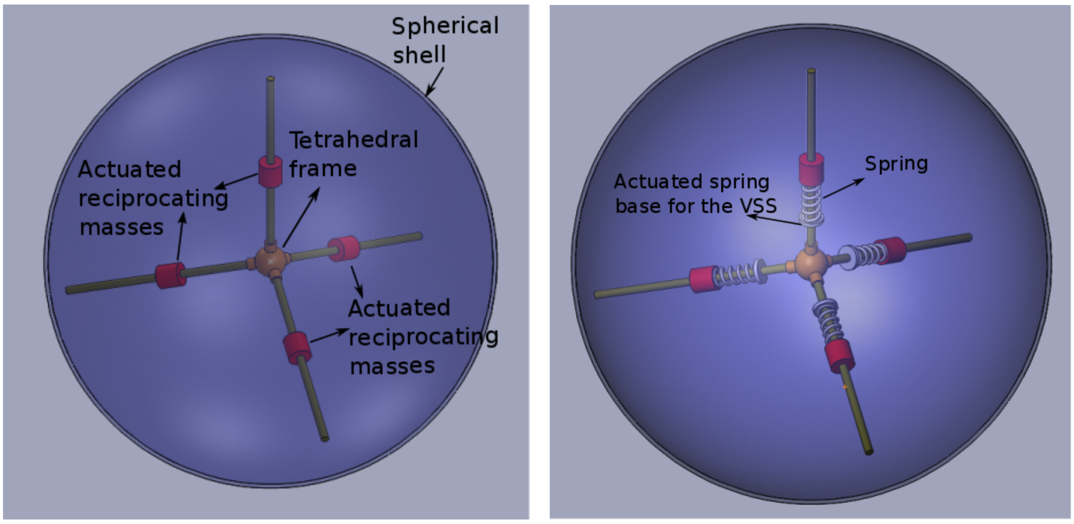
Spherical shell
Tetrahedral frame
Actuated reciprocating masses
Actuated reciprocating masses
Actuated spring base for the VSS
Spring

(a) Rolling robot without elastic elements **(b)** Rolling robot with spring/VSS

Figure 5.5: CAD models of the rolling robots

5.2.5.2 ADAMS Model

Once the CAD models were developed in `SolidWorks`, they were then imported as a *parasolid* file (.x_t) to ADAMS. We used *parasolid* format as it models geometric features with exact curvature. This model preserves the curvature of the spherical shell as it does not convert it to an edged surface. This leads to an accurate modeling of the system, the simulations were observed to be highly noisy when other formats were chosen. The models of the nominal spherical rolling robot and the robot with VSS are shown in Fig. 5.6.

5.2.5.3 Model Properties and Parameters

On importing the CAD model, ADAMS creates separate bodies for the four masses, four spokes, core, sphere, base and spring base (in the case of model with VSS). We update the mass properties of the bodies as given in Table. 5.1. The other relevant parameters are given in Table. 5.2.

To get a satisfactory representation of the ADAMS model of the rolling robot it is important to set the contact forces between the sphere and the base accurately. That is why in Table 5.3 relevant information regarding the contact model configuration set in ADAMS for the simulation experiments, is provided.

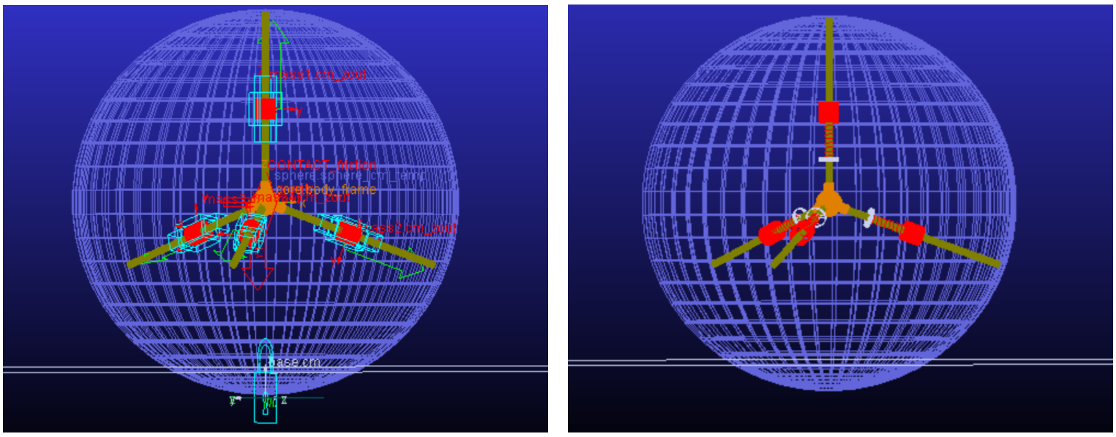

(a) Rolling robot without elastic elements **(b)** Rolling robot with spring/VSS

Figure 5.6: `ADAMS` models of the rolling robots

Table 5.1: Mass properties: `ADAMS` model

Body	**Mass**(kg)	**Inertia**$(kg.mm^2)$
Masses	1	1.0×10^{-09}
Spokes	0	-
Core	0	-
Sphere	5	2.8033×10^{05}
Spring Base	0.1	1.0×10^{-09}

5.2.5.4 Simulations

In order to test the aforementioned motion planners, generated from the steering algorithm and the optimization problem formulation for minimizing the energy consumed from the mobile robot with VSS the following scenario is defined. We will consider the case in which the robot must follow a straight line and complete a full rotation, i.e. $2\pi R$. Furthermore, a fifth-degree polynomial trajectory for the sphere is parameterized in order to ensure that the robot starts and ends the task with null velocities and accelerations.

The results in terms of the motion generated for the reciprocated masses from expression (5.25) are shown in Fig. 5.7. The trajectories generated from the Fourier series that parameterized the spring bases of the VSS, and whose coefficients where computed from the optimization formulation, are shown in Fig. 5.8. Additionally, in Fig. 5.9–Fig. 5.10, the input forces from the two analyzed actuation cases, are shown. It is worth noticing that even if the forces for the case of using VSS are not drastically reduced with respect to the nominal actuation, in overall what the energetic criteria seeks to minimize is the

Table 5.2: Relevant parameters: `ADAMS` model

Parameters	**Values**
Initial position of masses	140 mm
Initial position of spring base	70 mm
Free length of the spring	70 mm
Spring stiffness	$7.5 \times 10^{-03} N.mm^{-1}$

Table 5.3: `ADAMS` Contact Model Parameters

Parameter	Option set
Normal Force	Impact
Stiffness	1.0×10^{08}
Force Exponent	2.2
Damping	1.0×10^{04}
Penetration Depth	1.0×10^{-04}
Frictional Force	Coulomb
Static Coefficient	0.3
Dynamic Coefficient	0.1
Sticition Trans. Vel	0.1
Friction Trans. Vel	1.0

energy consumed, i.e. the product between actuating forces and velocities. That is why, the results regarding the energy consumed from the nominal case and from the case of using VSS in parallel are shown in Fig. 5.11. It can be seen that the reduction on the energy consumed can reach up to 40 %. It should be mentioned that even if for a high-speed robot an energy reduction of 70 % can be achieved according to Chapter 3, here we do not optimize the motion of the reciprocating masses as well, which was the case for the active joints of the high-speed robots since the optimal stiffness should be function not only of the VSS variables q_{s_i}, but also on the configuration of the robot q_i.

For a visualization of the results, a video of the co-simulation of the spherical rolling robot with VSS can be found in `https://bit.ly/2XXLJGv`

To summarize, in this Section we have applied the concept of exploiting natural dynamics for a mobile robot in which the VSS were arranged in parallel to the reciprocating masses seeking to optimize the exchange of VSS potential energy to kinetic energy, and thus minimizing the energy consumed. In the next Section, we will demonstrate this concept now by using the gravity potential energy through a robot carrying a payload. This will be done with the goal of increasing its static-wrench workspace in dynamics.

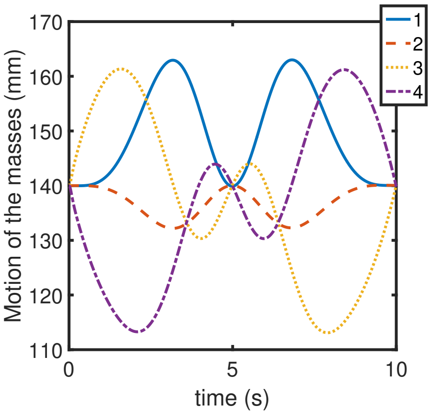

Figure 5.7: Trajectories from the four reciprocating masses in order to move the center of mass of the sphere.

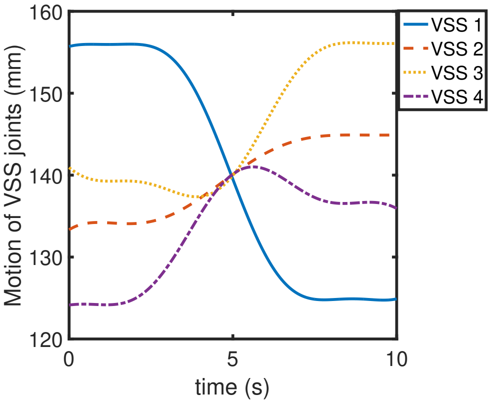

Figure 5.8: Trajectories computed from the optimal motion planner for the spring bases of the VSS.

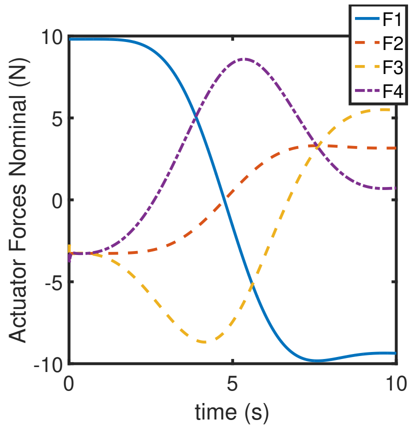

Figure 5.9: Forces computed along the masses trajectories without springs.

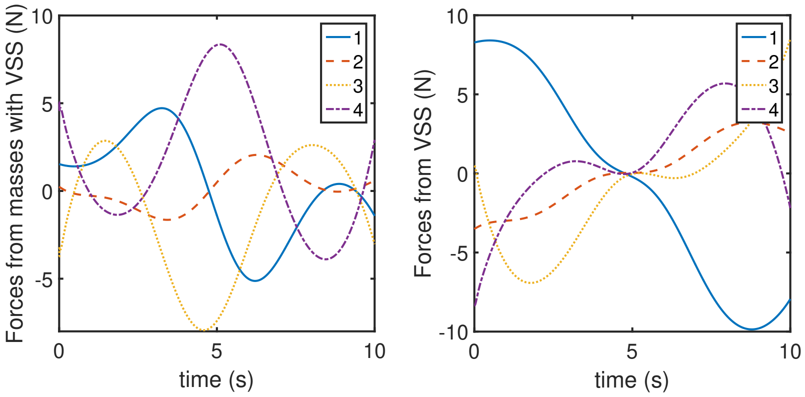

Figure 5.10: On the left the forces computed along the masses trajectories are shown when VSS are place in parallel. On the right the forces from adjusting the VSS springs bases are shown.

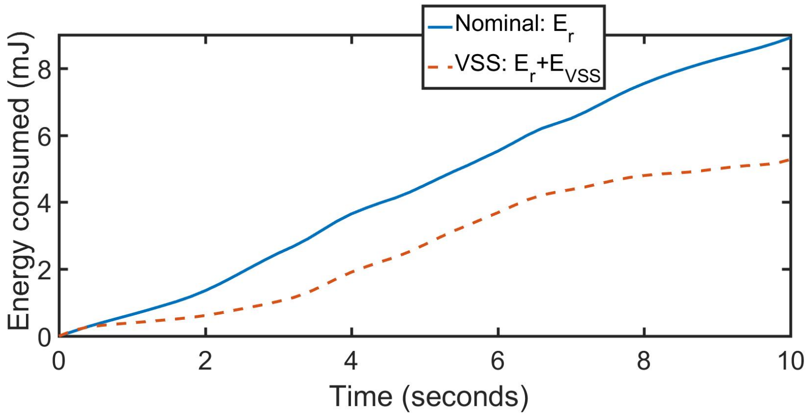

Figure 5.11: Energy consumed from the two types of actuation.

5.3 Increasing the feasible static-wrench workspace of robots

As mentioned in Section 5.1, in order to improve the dynamic performance of a robot in such a way that the input efforts or the energy consumption are minimized, exploiting the robot natural dynamics have shown to be a promising strategy. That is why in this Section, we will apply this concept for robots which are required to carry a payload that in statics may be out of the feasible wrench workspace due to actuator limits. To overcome reachability issues, we will thus propose a strategy to exploit the exchange from gravity potential energy to kinetic energy in dynamics, for a robot that in statics cannot reach a given desired configuration of its end-effector with payload due to reachability limitations and actuator limits. Therefore, if we ensure that the robot has an optimal exchange from potential to kinetic energy, we will guarantee that for large amplitude payload oscillations, the input torques will remain bounded leading to increase the feasible static-wrench workspace.

The reachable workspace of a robot carrying a payload is usually limited by the maximal value of the torque that each actuator can deliver. This results in limiting the zones for the robot to operate with the payload due to a possible division of its static-wrench workspace into several disconnected aspects.

In order to increase the reachable workspace areas, this Section proposes to exploit the natural oscillations in dynamics, so that the robot can carry a payload which is out of its feasible static-wrench workspace, i.e. to perform motions between two disconnected aspects, while constraining the torques of the actuators. This is done thanks to the solution of a BVP, which seeks to smartly exchange the gravity potential energy and the kinetic energy in order to connect two desired payload positions, which are placed in two disconnected aspects. Simulations of the suggested approach on a 2-degree-of-freedom robot are performed and show the efficiency of the proposed approach.

It is well-known that in several industrial robotic processes, robot manipulators are required to have as large as possible workspace. Nevertheless, when for some specific tasks, the robots are required to carry heavy payload objects, the workspace can be limited by the actuator maximum torques. The remaining workspace, limited by the torque limits, is called feasible static-wrench workspace, and it is generally defined by the set of all feasible end-effector poses for which the platform with payload can be reached statically, i.e. taking into account only the gravity effects [Gouttefarde 2007][Duan 2014][Hiller 2005].

As a consequence, if the maximal values of the actuator torques are not sufficiently high for a given payload, the reachable robot workspace will be reduced. This will restrict the zones where the robot can place the payload, and it may lead to disconnect the robot workspace into several aspects.

Most of the techniques developed for increasing static-wrench workspace feasibility have been applied for cable-driven parallel robots (CDPRs), in which the cables have been used as passive elements to find dynamic trajectories that seek to match the free response of the system with the desired payload motions [Jiang 2018][Gosselin 2012][Mottola 2019] [Jiang 2016]. The main idea is to replace the CDPR motor-cable arrangements with linear springs, from which an undamped mass-spring system is approximated. Then, the natural frequencies from such passive mechanical system are computed, and periodic trajectories are derived. Moreover, the natural frequencies of the virtual spring-based passive system are used for exploiting the dynamics of the system in order to find natural free-motion trajectories, thus increasing the feasible static-wrench workspace. Even if such techniques have shown their effectiveness when working with CDPRs, it is not the same case for rigid-link robots, in which no elastic element can be considered unless a spring is added in parallel to the active joints, as it was done in Chapter 3. In that Chapter, torsional VSS springs were placed in parallel to the actuators, and they were used as energy storage in order to exploit the natural oscillations of pick-and-place robots in order to put the system near resonance, thus considerably decreasing the input torques.

Contrary to what we proposed in Chapter 3, in which the spring potential energy is used to exploit the natural dynamics of the system, in this Section we propose to keep the robot unmodified, i.e. without any additional elastic element, and instead, to exploit the natural dynamics by using the payload potential energy. This will allow to increase the robot feasible static-wrench workspace thanks to a smart control of the natural oscillations in order to perform large amplitude motions between two disconnected aspects of the static-wrench workspace, similarly to the phenomenon occurring on an oscillating pendulum, in which all the energy is stored as potential energy when the payload is at the highest position of its swing, and it is then transferred continuously to kinetic energy.

5.3.1 Exploiting natural oscillations for enlarging feasible static-wrench workspace

In this Subsection, we propose a strategy to smartly exploit the exchange between the gravity potential energy and the kinetic energy of a robot with payload, so that it can be put in near its free response, thus decreasing the input torques. In order to do so, we will propose the formulation of a BVP, which will allow us to compute the necessary optimal velocity, associated to the kinetic energy required to cross from one disconnected aspect to another with minimum effort. Then, similarly to an oscillating pendulum, thanks to the formulation of an optimization problem, we will exploit the natural oscillations of the robot with payload to achieve the optimal velocity that match the system to its free response, obtained from the solution of the BVP.

5.3.1.1 Shooting method applied on robot manipulators with heavy payloads

To develop the BVP for the robot, we will denote $\dot{\mathbf{q}}_A$, as the optimal velocity at point A in one disconnected aspect of the static-wrench workspace, that will allow to connect the aspects in point B (See Fig. 5.12a).

In order to exploit the natural dynamics of the robot with payload to join two different aspects of the robot disconnected static wrench-workspace, in this Section we propose to formulate a BVP, which can be solved with the *shooting method*, similar to the one formulated in Chapter 3. The BVP formulation seeks to find the optimal velocity grouped in $\dot{\mathbf{q}}_A$, or slope (see Section 3.1.1.1), and associated to the optimal kinetic energy required to connect two aspects, that solve (2.17) for $\boldsymbol{\tau} = 0$, while ensuring to meet the desired boundary positions defined in two disconnected aspects (A and B in Fig. 5.12a), i.e.:

$$\ddot{\mathbf{q}}_a = -\mathbf{M}^{-1}(\mathbf{c}(\mathbf{q}_a, \dot{\mathbf{q}}_a) + \mathbf{f}_a) \tag{5.32}$$

with the boundary conditions defined as the desired positions in two disconnected aspects of the feasible static-wrench workspace by $\mathbf{q}_a(t_0) = \mathbf{q}_A^*$, $\mathbf{q}_a(t_f) = \mathbf{q}_B^*$ with the formulation of the following position error vector:

$$\mathbf{E}_q(\dot{\mathbf{q}}_A) = \mathbf{q}_a(t_f, \dot{\mathbf{q}}_A) - \mathbf{q}_B^* \tag{5.33}$$

where t_f is the final time, and $\dot{\mathbf{q}}_a$ and $\mathbf{q}_a$ are obtained from numerical single and double integration of $\ddot{\mathbf{q}}_a$, respectively. The *shooting method* is applied to iteratively find the proper joint velocities, grouped in $\dot{\mathbf{q}}_A$, such that expression (5.33) converge to zero as follows:

```
while $\mathbf{E}_q > \boldsymbol{\epsilon}_n$, $k \leq max_k$ do
    $\mathbf{E}_q(\dot{\mathbf{q}}_A) = \mathbf{q}_a(t_f, \dot{\mathbf{q}}_A) - \mathbf{q}_B^*$
    $\dot{\mathbf{q}}_{A_k} : \mathbf{E}_q(\dot{\mathbf{q}}_{A_k}) = 0$
    $\dot{\mathbf{q}}_{A_k} = \dot{\mathbf{q}}_{A_k} + \Delta\dot{\mathbf{q}}_{A_k}$
end
```

where $\dot{\mathbf{q}}_{A_k} = \dot{\mathbf{q}}_{A_{k+1}}$ representing the optimal set of joint velocities, max_k is the maximum number of iterations, and $\boldsymbol{\epsilon}_n$ is the error threshold.

Since we will consider that all motions of the robot will start from the equilibrium position of the system, i.e. lowest end-effector location, at $\mathbf{q}_{a_0} = [-\pi, 0]^T$, in the following Subsection, we develop a strategy to optimally go from the equilibrium configuration velocity of the robot, to the optimal aspect-connecting velocity $\dot{\mathbf{q}}_A$.

5.3.1.2 Initial oscillations for achieving optimal aspect-connecting velocity

In the aforementioned formulation, we have presented a strategy based on a BVP to compute the optimal velocity $\dot{\mathbf{q}}_A$, associated to the kinetic energy required to join two disconnected aspects. Nevertheless, since we have chosen to start the motion from the equilibrium configuration of the robot ($\dot{\mathbf{q}}_{a_0} = \mathbf{0}$), i.e. null initial stored potential energy U_0 to attain $\dot{\mathbf{q}}_A$, it is thus necessary to find a strategy to reach $\dot{\mathbf{q}}_A$ from rest state. One could think of planning a classical motion based on a fifth-degree polynomial which can fix the position, velocity and acceleration at the trajectory extremities, thus allowing to fix $\dot{\mathbf{q}}_A$. Nevertheless, since we seek to constrain the torques to operate within a range of motor limits, it is thus necessary to develop an optimal motion planner that integrates the effects of the dynamics to reach $\dot{\mathbf{q}}_A$. That is why, contrary to the aforementioned BVP formulation, which allows us to compute the kinetic energy required to connect boundary positions in different aspects, in this part we seek to propose an optimal strategy to attain that aspect-connecting velocity $\dot{\mathbf{q}}_A$. Similar to an oscillating pendulum, this can be done by exploiting the oscillations of the robot with payload in order to store the optimal payload potential energy to reach $\dot{\mathbf{q}}_A$. Thus, we propose to find such exciting initial oscillatory motions that accelerates the robot to reach $\dot{\mathbf{q}}_A$, while minimizing the input torques, by defining the following optimization formulation:

$$\begin{aligned} &\text{minimize} \quad && J = \int_0^{t_{f'}} \sum_{i=1}^{n} \tau_i^2 \, dt \\ &\text{over} && \mathbf{x_{DecVar}} \\ &\text{subject to} && |\tau_i| \leq \tau_{max}, t_{min} \leq t \leq t_{max}, |q_i| \leq q_{max} \end{aligned} \tag{5.34}$$

where the decision variable vector $\mathbf{x_{DecVar}}$ contains the following parameters: q_{i_k}, v_{i_k}, a_{i_k} and t_{i_k}. Similar to the strategy based on the via-point motion planner of [Balderas 2018], each of these parameters represents the amplitude, velocity, acceleration and time of oscillation for the exciting trajectories parameterized by using fifth-degree order polynomials, respectively (See from Fig. 5.14 to Fig. 5.20, exciting oscillations). k is an integer representing the number of required oscillations (via points) for attaining $\dot{\mathbf{q}}_A$. Finally, $t_{f'}$ represents the final time of the optimization, and τ_i represents the torque of the actuated joints grouped in $\mathbf{q}_a$.

It is worth noticing that we use the cost function J that computes the squared of the input efforts $\boldsymbol{\tau}$ of the system. Nevertheless, any other criterion characterizing the reduction of the input torques could be used. One could think also of including the link lengths, ℓ_{AB} and ℓ_{BC}, in the decision variable vector for the BVP and the optimization formulation in order to optimize the robot performance. Nevertheless, our approach focused on exploiting the robot dynamics for performing large oscillations while constraining the input efforts, with a fix set of geometric parameters.

5.3.2 Case study: 2-DOF serial robot

In this Section, numerical validations are made thanks to a co-simulation between Matlab and ADAMS in order to show the effectiveness of our approach. The proposed strategy for enlarging the feasible static-wrench workspace was validated on a 2-DOF serial robot with payload, as shown in Fig. 5.12b. The active joint coordinates of the robot are parameterized by $\mathbf{q}_a = [q_1, q_2]^T$. The vector of payload pose is denoted as $\mathbf{x} = [x, y]^T$. The link lengths ℓ_{AB} and ℓ_{BC} are identical, and the center of mass of each link is located at a distance ℓ_{AS_1} and ℓ_{BS_2} from the rotation center of the motors q_1 and q_2, respectively. Moreover, the gravity field is directed along $\mathbf{y}_0$ and is equal to $\mathbf{g} = [0, -g, 0]^T$, $g > 0$, being equal to 9.81 m/s^2. Each link mass is parameterized by m_1 and m_2, and the payload mass is denoted by m. Finally, the inertia of each link is given by zz_1 and zz_2, and it is

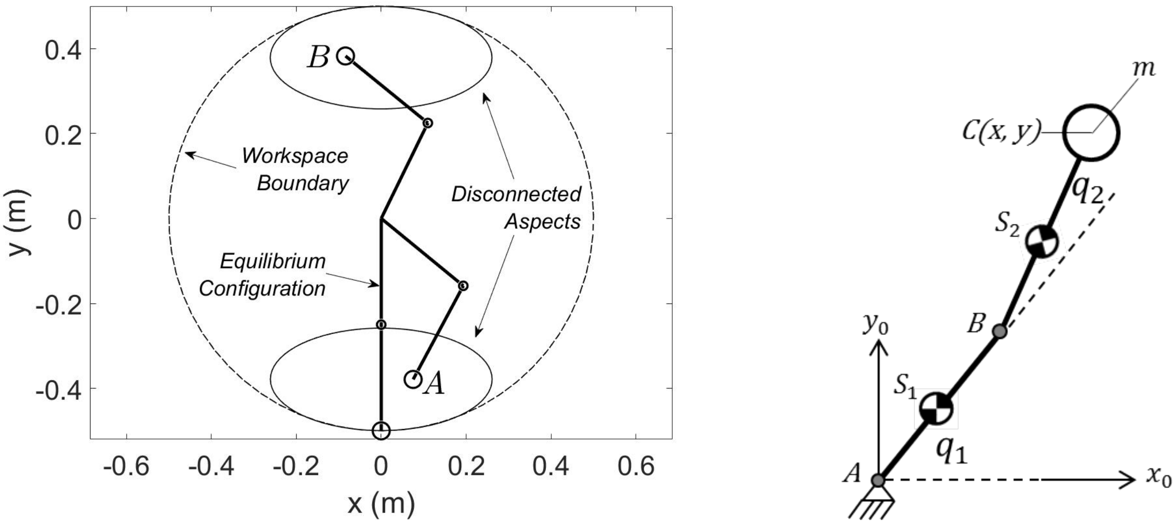

(a) Division of static-wrench workspace in different aspects

(b) Parameterization of 2R serial robot

Figure 5.12: On the left, the graphical interpretation of the disconnection between aspects due to actuation limits on a 2R serial robot workspace. A and B represent the boundary conditions which seek to be joined thanks to the BVP. On the right, the kinematic structure of the 2-DOF robot with payload is shown.

measured about its center of mass S_1 and S_2, respectively.

The dynamic and geometric parameters for the simulations, were defined by the following numerical values: inertia of the two links $zz_1 = zz_2 = 0.133$ kg/m^2, mass of each link $m_1 = m_2 = 0.1$ kg, Coulomb friction terms $f_{s1} = f_{s2} = 0.3$ Nm, link lengths $\ell_{AB} = \ell_{BC} = 0.25$ m and the distance to center of mass for each link $\ell_{AS_1} = \ell_{BS_2} = 0.125$ m. The dynamic equations for the 2-DOF serial robot are not given here, but by following the Lagrange formalism shown in Chapter 2 they are computed in Appendix D.

The algorithm proposed in Section 5.3.1 was tested by defining two desired points in disconnected aspects of the static-wrench workspace, as it is shown in the interpretation from Fig. 5.12a. The aim is to connect both separated aspects of the static-wrench workspace by solving the corresponding BVP. Moreover, in order to show the effectiveness of the proposed approach, four cases corresponding to different payloads, maximal actuator torques and desired boundary positions (m, τ_{max}, A, B, respectively) have been studied: Case 1: $m = 0.5$ kg, $\tau_{max} = 1$ Nm, $A = [0, -0.43]$, $B = [0.05, 0.4]$; Case 2: $m = 1$ kg, $\tau_{max} = 2$ Nm, $A = [0.15, -0.4]$, $B = [0, 0.4]$; Case 3: $m = 1.25$ kg, $\tau_{max} = 2.25$ Nm, $A = [0, -0.45]$, $B = [0, 0.45]$; Case 4: $m = 1.5$ kg, $\tau_{max} = 3$ Nm, $A = [0, -0.45]$,

Table 5.4: Maximum values of input torques and optimal values for $\dot{\mathbf{q}}_A$ from the solution of the BVP.

	Max. Torques Shooting method for BVP	Max. Torques Exciting trajectories	Optimal Velocity BVP
	$\lvert\boldsymbol{\tau}\rvert_{\max}$ (Nm)	$\lvert\boldsymbol{\tau}\rvert_{\max}$ (Nm)	$\dot{\mathbf{q}}_A$ (rad/s)
Case 1	[0.007, 0.001]	[0.597, 0.604]	[-7.257, 4.494]
Case 2	[0.007, 0.007]	[1.153, 2]	[-10.052, 10.179]
Case 3	[0.011, 0.013]	[2.062, 2.105]	[-10.916, 10.625]
Case 4	[0.032, 0.022]	[2.993, 2.999]	[-11.802, 12.649]

$B = [0.1, 0.4]$.

The results in input torques for the four cases, for both BVP and exciting trajectories, are shown Table 5.4. In addition to that, the optimal values $\dot{\mathbf{q}}_A$ from the BVP, for the different boundary conditions from the four cases, are shown as well in Table 5.4. It can be seen that, based on the maximum value of the input torques, the efforts from the trajectory based on the *shooting method* are minimum, while the input efforts from the exciting trajectories are within the maximal motor torque values, thus constraining the actuator torques. In addition to that, from Fig. 5.13 to Fig. 5.19, the input torques computed along the motion from the four studied cases are presented. This to show the effectiveness of the approach to constrain the input efforts within a range of maximal actuator values that allows to join two disconnected aspects from the static-wrench workspace. Additionally, from Fig. 5.14 to Fig. 5.20 the optimal motions from the *shooting method* and from the exciting trajectories are shown in the workspace of the 2-DOF serial robot for the four cases. It can be seen that thanks to the solution of the BVP, two points in different aspects of the divided static-wrench workspace can be joined while constraining the torques of the actuators. Furthermore, as it is shown in Table 5.4 and from Fig. 5.13 to Fig. 5.19, the input torques computed from the BVP are closed to zero, which means a correct optimal dynamics exploitation since we were seeking to solve (2.17) for $\boldsymbol{\tau} = 0$. Finally, it is worth mentioning that the full motions (Exciting-plus-BVP trajectory) from the four studied cases start from the equilibrium position of the system, i.e. $\mathbf{q}_{a_0} = [-\pi, 0]^T$.

For a visualization of the results, a video of the co-simulations of the 2-DOF serial robot connecting two different aspects, can be found in `https://bit.ly/2QuLQdb`

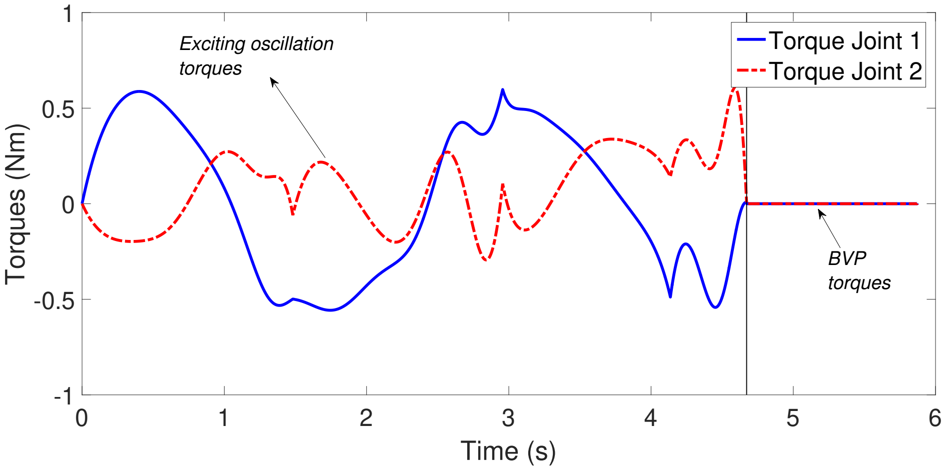

Figure 5.13: Torques computed from the exciting-plus-BVP trajectory for the case 1.

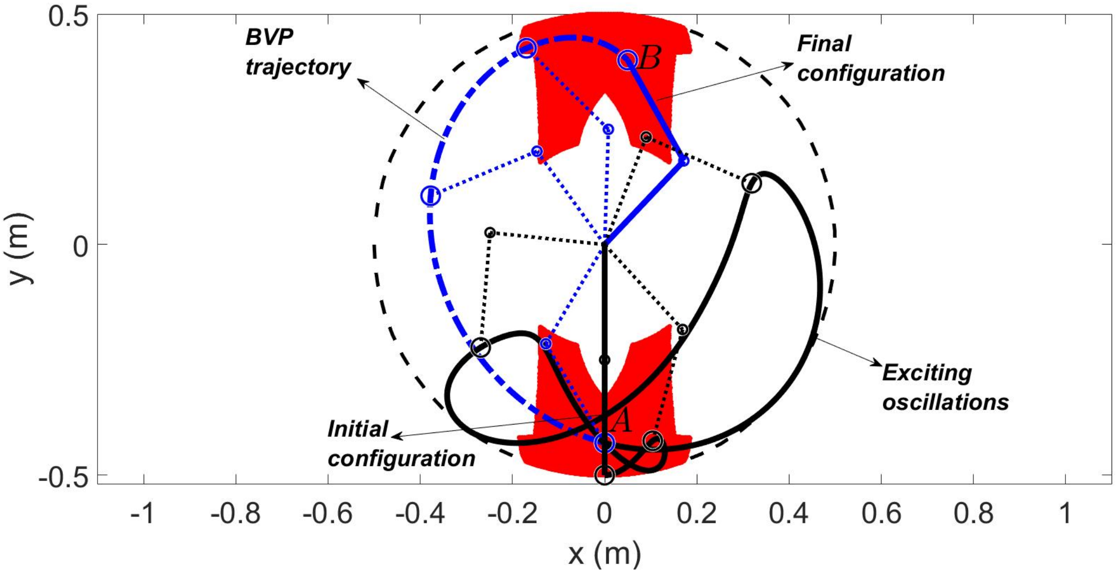

Figure 5.14: Optimal trajectory for connecting two points by solving the BVP from boundaries of case 1. A and B represent the boundary conditions of case 1 and they are joined thanks to the solution of the BVP.

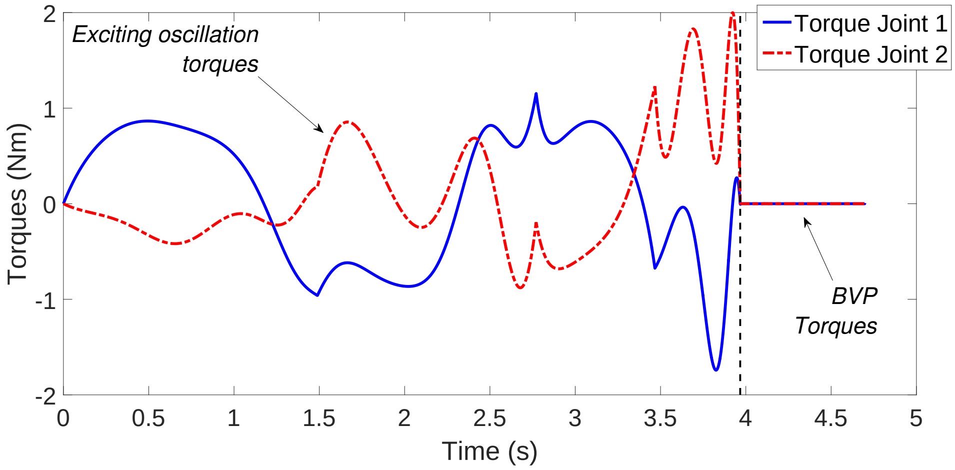

Figure 5.15: Torques computed from the exciting-plus-BVP trajectory for the case 2.

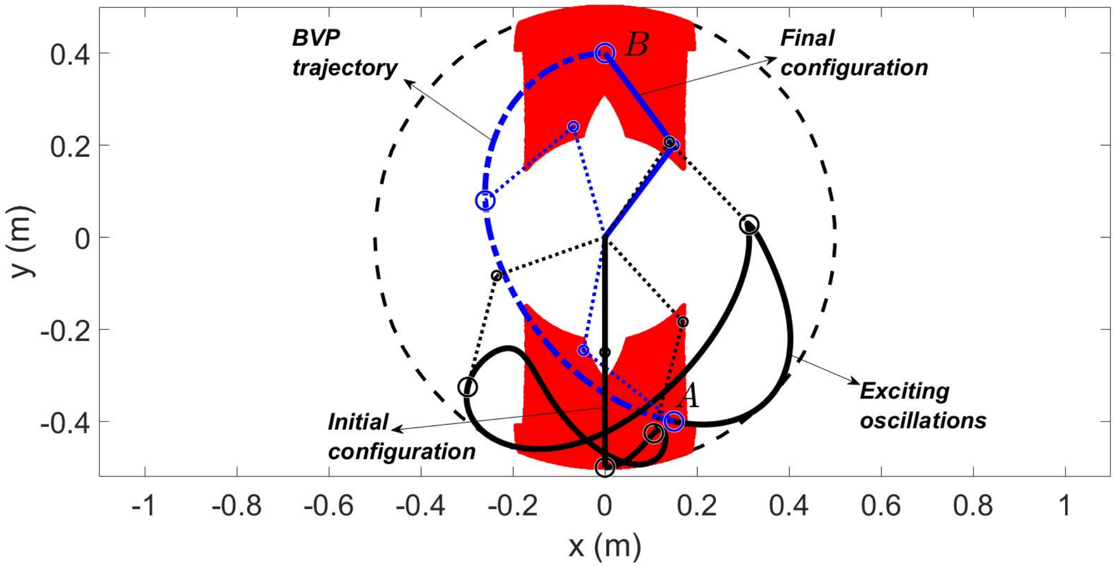

Figure 5.16: Optimal trajectory for connecting two points by solving the BVP from boundaries of case 2. A and B represent the boundary conditions of case 2 and they are joined thanks to the solution of the BVP.

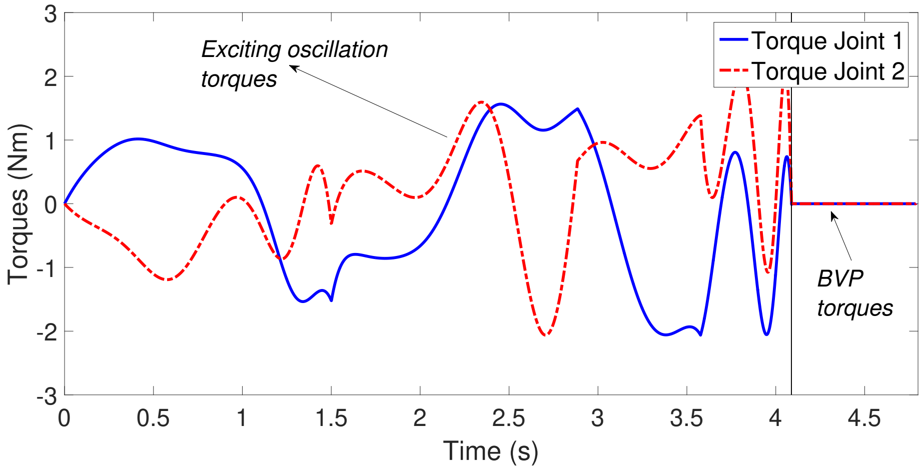

Figure 5.17: Torques computed from the exciting-plus-BVP trajectory for the case 3.

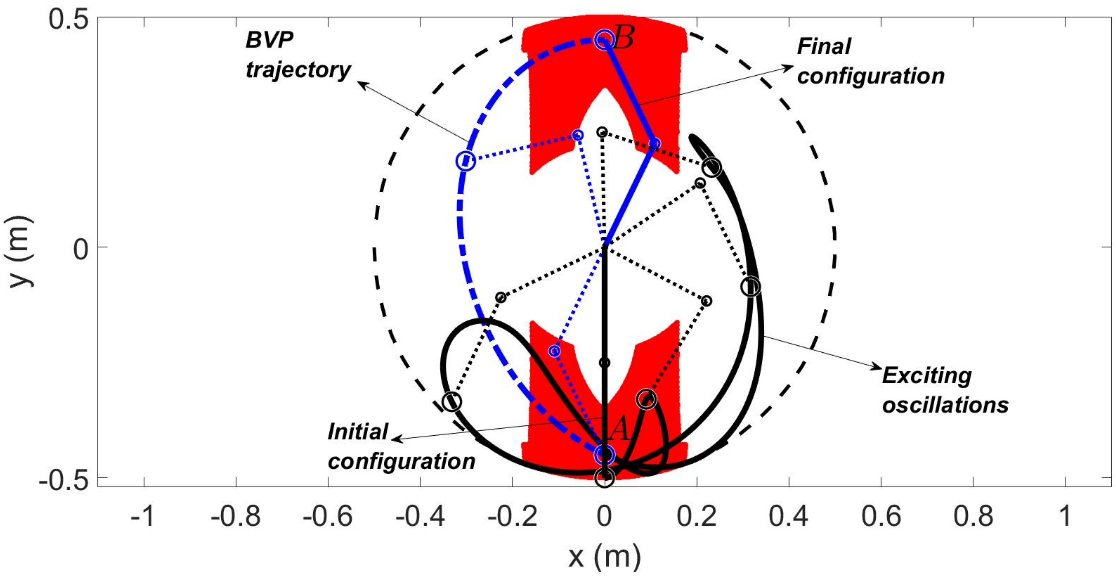

Figure 5.18: Optimal trajectory for connecting two points by solving the BVP from boundaries of case 3. A and B represent the boundary conditions of case 3 and they are joined thanks to the solution of the BVP.

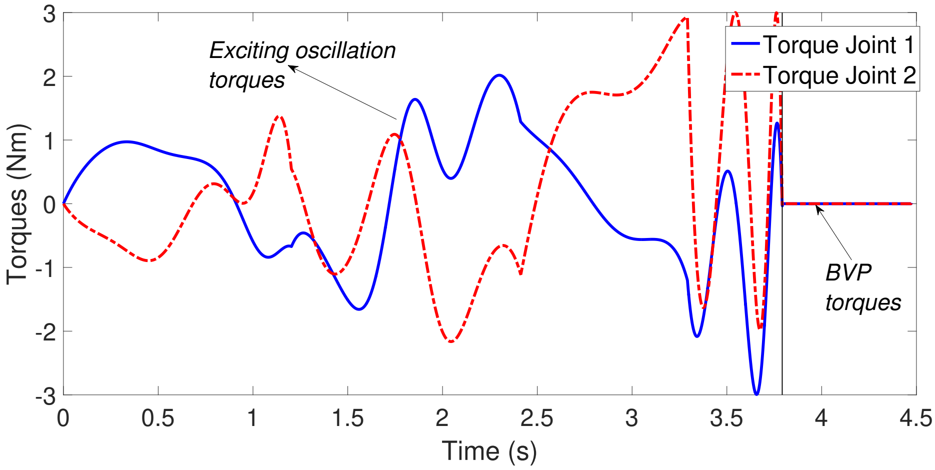

Figure 5.19: Torques computed from the exciting-plus-BVP trajectory for the case 4.

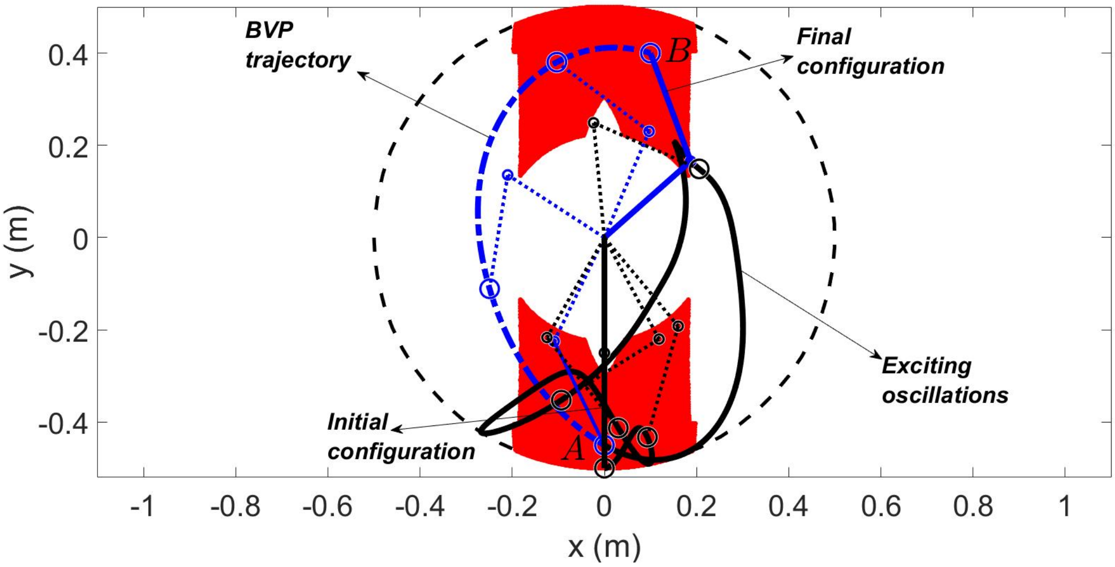

Figure 5.20: Optimal trajectory for connecting two points by solving the BVP from boundaries of case 4. A and B represent the boundary conditions of case 4 and they are joined thanks to the solution of the BVP.

5.4 Summary

This Chapter has been devoted to present an extension of exploiting natural dynamics to other application cases. This to demonstrate the potential of exploiting the natural free-response not only for applications in which high-speed is involved as it was shown for pick-and-place robots in Chapter 3, but also to other type of systems, in this case for a mobile robot with VSSs to reduce the energy consumption and for a serial robot for carrying payloads out of its feasible static-wrench workspace.

In Section 5.2, the concept of using the VSS to optimize the exchange from VSS potential energy to kinetic energy was applied for an omnidirectional robot in order to minimize its energy consumption while performing a given path. It was shown that by using VSS combined with an optimisation formulation, it was possible to reduce the energy consumption by a 40 %.

Finally in Section 5.3, it was presented a strategy for increasing the feasible static-wrench workspace for robots by exploiting the robot dynamics through the solution of a BVP which seeks to smartly control the free-response of the system to perform motions that connect two different aspects of the static-wrench workspace. This has allowed to considerably increase the reachability to disconnected areas of the workspace of a 2-DOF serial robot with different payloads and for multiple desired boundary positions. Simulations led to a successful connection of two different aspects of the feasible static-wrench workspace for different actuator torque limits and different payload weights.

Conclusions and perspectives for future works

Summary and contribution of the thesis

This thesis has addressed mainly the reduction of the energy consumption of high-speed pick-and-place robots. Nevertheless, along the manuscript, it has been shown as well some other potential applications in which the concept of natural dynamics may lead to great reductions of energy consumption for other types of robots.

The first Chapter of our manuscript was devoted to detail the historical evolution of high-speed robots, mainly used in highly dynamic tasks, such as industrial pick-and-place operations. Additionally, it was shown that in the recent years, the design trends to operate at high-speeds have changed to the development of robots that in addition to operate fast, they can move as energy-efficient as possible. The most promising techniques for improving the energy efficiency were shown to be those based on the use of elastic elements, such as linear or torsional springs. This is due to the possibility of adding a mechanical energy storage to the robot, thus distributing the efforts to move the robots, between the active joints motors and the potential energy stored in the springs. Some examples of this compliant actuation concept are the series elastic actuators (SEAs), variable stiffness actuators (VSAs), constant stiffness springs in parallel, and more recently variable stiffness springs in parallel (VSS). Nonetheless, among the main drawbacks and open research questions of these compliant actuators for improving the energy efficiency of industrial robots, we can list:

- uncontrolled robot deflections appear at high-speeds when using SEAs or VSAs due to the serial connection of springs and motors, which worsen the accuracy of the robot end-effector;
- limited level of adaptation when using constant stiffness springs in parallel due to the fact that the level of compliance to adapt for different operational tasks is restricted by the constant of the spring;

- even if the use of VSAs or VSS have shown to compensate the issues in terms of adaptability, the energy required to adjust the stiffness of these actuators has been never consider in the energetic analysis, thus underestimating the energy consumed by the actuators used to adjust the stiffness;

- the use of VSS in parallel to the motors for robot manipulators have been only used for slow tasks with cycle times of 5 s. Additionally, a non-linear force/displacement relation has been required to control the VSS, since they have always generated stiffness profiles. This complexifies the controller, since it is required to measure the stiffness, and moreover, working at the stiffness level, instead of at the level of the physical models with dynamic equations lead to lower percentages of energy reduction, since the natural dynamics are not exploited.

In order to overcome the aforementioned issues, in Chapter 2 we have proposed to introduce the actuation concept of VSS in parallel to the motors, for high-speed robots. It should be noted that this concept has been only used at slow speeds, and without considering the energy required to adjust the stiffness of the VSS. That is why in Chapter 2, we have presented the dynamic model of robots with VSS in parallel to the actuated links, considering as well the dynamics associated to the variable stiffness system of the VSS, which has never been done before. Additionally, in order to consider the energy consumption of the full actuation chain, i.e. robot and VSS systems, a full model of energetic losses have been proposed. In this model the losses associated to all phases of the electromechanical motor-drive systems that actuate the robot active joints and the variable stiffness joints have been taken into account. Based on an analysis for typical high-speed quasi-periodic motions showed that the most preponderant losses when performing such tasks are the ones associated to the electric currents, i.e. resistive and conduction losses.

That is why, considering that the electric currents, related to the input torques are the most preponderant terms in the energy consumption, in Chapter 3, we developed a strategy to exploit the robot natural dynamics, thus reducing the input torques and therefore the energetic losses. This strategy was based on a motion generator computed from a boundary values problem (BVP), in which the objective was to exploit the combined motion of the robot active joints and VSS joints. This was done due to the fact that the force/displacement relation of the VSS associated to the VSS optimal stiffness, being controlled simultaneously by the robot and the variable stiffness joints, couples the dynamics associated to the robot and the VSS. Thus, by exploiting it, we could minimize the robot and VSS input torques simultaneously, and thus the full actuation chain energy consumption for fast quasi-periodic motions. Simulations of the suggested approach on a five-bar mechanism and on a Delta robot showed the drastic reduction of energy consumption.

In Chapter 4, the experimental proof of actuation concept based on VSS was validated in an industrial-sized robot, that I designed and commissioned in the scope this thesis. The experimental results showed that, independently of the drawbacks on the design of the variable stiffness system for the VSS, the robot could perform fast energy-efficient pseudo-periodic motions, thus exploiting the natural dynamics of the robot. The experimental results showed a considerable increase on the energy efficiency of the robot full actuation chain while performing pick-and-place-like motions with energy savings of 50–55 % considering the friction effects, and 60–65 % without considering the friction effects.

Finally, in Chapter 5, we presented an extension of the concept of exploiting the robot natural dynamics by studying robots operating in other applications, and in which a continuous exchange from potential to kinetic energy could be exploited. Two applications were addressed: *i*) for reducing the energy consumption of a spherical rolling robot by using VSS in parallel, and *ii*) for increasing the feasible static-wrench workspace of robots carrying a payload for which the reachable workspace is usually limited due to the maximal value of the torque that each actuator of the robot joints can deliver. Simulation results showed an increase on the energy efficiency of the spherical rolling robot, and in the case of increasing the static-wrench workspace, the results showed that thanks to a smart exchange from gravity potential energy to kinetic energy, we could joined desired payload positions placed in disconnected aspects of the static-wrench workspace.

We would like to mention that these works have been presented in several articles, listed in Appendix E.

Direction for future works

This thesis has established a proof of concept for reducing the energy efficiency for high-speed robots by using the actuation principle based on VSS in parallel to the motors. Nonetheless, the designed experimental prototype, within the time limits of this study, did not allow to have a complete notion of the achievable energy reduction mainly due to a non-optimized design of the variable stiffness system.

That is why, concerning a future research and developments of VSS for increasing energy efficiency, for a first research axis, it could be interesting to explore techniques to optimize the design of the variable stiffness springs. As it was shown in the developed prototype of this thesis, since the objective was to validate the proof-of-concept of an actuation principle for high-speeds, the methodology for designing the VSS followed from a technological-based approach. Nevertheless, it would be interesting to explore optimal design approaches of compliant actuators such as in [Carloni 2012][Visser 2011]. In those works, the authors propose guidelines for designing energy-efficient VSAs (with springs in series) based on the power flow undergoing through the actuation chain for different operational situations. The main idea of this mentioned approach is to model the energy flow using port-based mathematical tools, such as bond graphs [Carloni 2012][Visser 2011], and to obtain an energetic-design metric for VSAs, which could be optimized to minimize the energy consumption in the actuation chain. Even is those techniques have been applied to VSAs in which the springs are set in series, it could be interesting to explore a power flow approach for designing VSS in parallel. That is why several points could be considered as constraints for optimally designing the VSS with springs in parallel: to find a proper architecture for allowing large motion range, to deal with the compactness issues, with the design simplicity, and to define what type of spring material (metals, polymers, bio-sourced materials such as latex, etc. [Kawamura 2002]).

It should be noted that the design optimization approach does not necessarily may be restricted to the design of the VSS, but also it could be interesting to optimize the structure of the high-speed robot. That is why, a second axis of research could be oriented to the design optimization of the robot structure. Recently, topological optimization techniques have been introduced to robots in order improve the inherent robot limitations from their physical performance [Briot 2018]. Typically, the most common robot performances that have been improved with these techniques are related to increase the robot accuracy, improve the deformation behavior, and to minimize the vibrations. Nevertheless, it could be interesting to perform topology optimization for designing robots operating at high-speeds with a performance criteria based on the minimization of the energy consumption for typical high-speed pick-and-place trajectories. In order to do that the work presented in [Briot 2018], which performs topological optimization for optimally redistributing the material (and thus the mass of the movable bodies) of the links of a five-bar mechanism with a link elasticity criteria, could be the starting point.

A third axis of research could be oriented to explore strategies, such as numerical optimal control [Geisert 2016], in order to implement the boundary value problem proposed in this thesis for minimizing the energy consumption, within an online optimizer. This would permit to compute the optimal trajectory at each integration time, allowing to include parametric uncertainties in the control system, and thus avoiding to perform a previous calibration of the dynamic parameters. The main challenge of developing an online approach based on numerical optimal control, is that the cycle times on a high-speed pick-and-place task as it was shown in this study, are very fast up to the order of 0.23 s. This time constraint for an online optimizer could be difficult to deal with, considering that in the objective criterion, in addition to minimize the boundary pick-and-place constraints, should be able as well to reduce the input torques of the full actuation for a system whose dynamics are quite fast. It should be noted that optimal control techniques allow to use dynamic models like the ones developed for the robot and the VSS in Chapter 2. Nevertheless, the computational load can restrict the online applicability considering that the cycle times between two consecutive pick-and-place positions are too short. Even if optimal control approaches have achieved a strong level of applicability for real-time control trajectory generation, they consider only system states in the proximity of the current robot state, thus determining local optimal trajectories. This could potentially affect the percentages of energy reduction that we could achieve, leading to partially minimize the energy consumption of the full actuation chain. Nevertheless, it is a technique worth to explore, whose relevant works that could be used as starting points towards this research can be found in [Ghazaei 2015][Geisert 2016].

Finally, it could be interesting to apply the concept of variable stiffness springs to robots in other applications in which not necessarily they are required to operate at high speeds. For instance, in the past few years, more and more researches oriented to designing exoskeletons have been performed for rehabilitation applications [Liu 2018][Rehmat 2018]. In such systems it is required to produce highly repetitive, and precisely controllable motions, and with a high degree of adaptability. Additionally, compactness on the on the powered actuation of such systems is desirable. That is why, by using VSS in parallel to the powered actuation system, or even optimal constant stiffness springs, it could be possible to distribute the required efforts for the powered actuated exoskeleton, thus reducing the size of the actuators, and thus leading to a compact design.

Appendix A

Dynamic model of the five-bar mechanism

The inverse dynamic model of the five-bar robot in its decoupled form, i.e. decoupling the acceleration terms from the inertia matrices, can be written as follows:

$$\boldsymbol{\tau} = \begin{bmatrix} zz_{11R} & 0 \\ 0 & zz_{21R} \end{bmatrix} \begin{bmatrix} \ddot{q}_{11} \\ \ddot{q}_{21} \end{bmatrix} + m_R \mathbf{J}_{inv}^{-T} \begin{bmatrix} \ddot{x} \\ \ddot{y} \end{bmatrix} + \begin{bmatrix} f_{s_1}\text{sign}(\dot{q}_{11}) \\ f_{s_2}\text{sign}(\dot{q}_{21}) \end{bmatrix} \tag{A.1}$$

where $\mathbf{J}_{inv} = -\mathbf{B}^{-1}\mathbf{A}$, defined in [Briot 2016] for a five-bar mechanism of equivalent legs, represents the inverse Jacobian matrix. By using the second-order kinematic constraint relations, obtained by differentiating (2.11) with respect to time and given by:

$$\mathbf{A}\ddot{\mathbf{x}} + \mathbf{B}\ddot{\mathbf{q}}_a = \mathbf{b} \Rightarrow \ddot{\mathbf{x}} = -\mathbf{A}^{-1}\mathbf{B}\ddot{\mathbf{q}}_a + \mathbf{b}^{'} = \mathbf{J}_{inv}^{-1}\ddot{\mathbf{q}}_a + \mathbf{b}^{'} \tag{A.2}$$

where $\mathbf{b} = -\dot{\mathbf{A}}\dot{\mathbf{x}} - \dot{\mathbf{B}}\dot{\mathbf{q}}_a$, and $\mathbf{b}^{'} = \mathbf{A}^{-1}\mathbf{b}$, and introducing them into (A.1), we get the general dynamic model form:

$$\boldsymbol{\tau} = \mathbf{M}\ddot{\mathbf{q}}_a + \mathbf{c} + \mathbf{f}_a \tag{A.3}$$

where

- $\mathbf{M} = \begin{bmatrix} zz_{11R} & 0 \\ 0 & zz_{21R} \end{bmatrix} + \mathbf{J}_{inv}^{-T} m_R \mathbf{I}_2 \mathbf{J}_{inv}^{-1}$
- $\mathbf{c} = \mathbf{J}_{inv}^{-T} m_R \mathbf{I}_2 \mathbf{b}^{'}$
- $\mathbf{f}_a = \begin{bmatrix} f_{s_1}\text{sign}(\dot{q}_{11}) \\ f_{s_2}\text{sign}(\dot{q}_{21}) \end{bmatrix}$

The terms zz_{11R}, zz_{21R}, m_R, f_{s_1} and f_{s_2} represent the essential parameters, i.e. the parameters that are well-identified because they represent the large majority of the robot dynamic effects [Briot 2015c][Gautier 2014].

It should be noted that the form of the dynamic model presented in this Appendix is valid for the five-bar mechanism used for the simulation results in Chapter 2 and Chapter 3, and in the experimental prototype from Chapter 4. The only difference is that the essential dynamic parameters from simulation and experimentation are not the same.

APPENDIX B

Dynamic model of the 3-DOF Delta robot

The expressions of the inverse dynamic model of the 3-DOF Delta robot used as a case study in Chapter 3, separately for each input torque are equal to:

$$\begin{aligned}\tau_1 = zz_b\ddot{q}_1 + m_p(j_{11}\ddot{x} + j_{21}\ddot{y} + j_{31}\ddot{z}) + m_{pg}j_{31}\\ -m_b\cos(q_1) - m_{pal}(\sin(q_1)(\cos(q_1)\ddot{x} + \sin(q_1)\ddot{y} + \cos(q_1)\ddot{z}\\ -m_{pal}(j_{11}t_{41} + j_{21}t_{42} + j_{31}t_{43})\\ f_{s_1}\text{sign}(\dot{q}_1) + I_a\ddot{q}_1\end{aligned} \tag{B.1}$$

$$\begin{aligned}\tau_2 = zz_b\ddot{q}_2 + m_p(j_{12}\ddot{x} + j_{22}\ddot{y} + j_{32}\ddot{z}) + m_{pg}j_{32}\\ -m_b\cos(q_2) - m_{pal}(\sin(q_2)(\cos(q_2)\ddot{x} + \sin(q_2)\ddot{y} + \cos(q_2)\ddot{z}\\ -m_{pal}(j_{12}t_{41} + j_{22}t_{42} + j_{32}t_{43})\\ f_{s_2}\text{sign}(\dot{q}_2) + I_a\ddot{q}_2\end{aligned} \tag{B.2}$$

$$\begin{aligned}\tau_3 = zz_b\ddot{q}_3 + m_p(j_{13}\ddot{x} + j_{23}\ddot{y} + j_{33}\ddot{z}) + m_{pg}j_{33}\\ -m_b\cos(q_3) - m_{pal}(\sin(q_3)(\cos(q_3)\ddot{x} + \sin(q_3)\ddot{y} + \cos(q_3)\ddot{z}\\ -m_{pal}(j_{13}t_{41} + j_{23}t_{42} + j_{33}t_{43})\\ f_{s_3}\text{sign}(\dot{q}_3) + I_a\ddot{q}_3\end{aligned} \tag{B.3}$$

where j_{1i}, j_{2i} and j_{3i} $(i = 1, ...3)$ represent the terms from the Jacobian of the robot, and

$$\begin{aligned}t_{41} = (\cos(q_1)(\ddot{q}_1\sin(q_1) + \dot{q}_1^2\cos(q_1))\\ +\cos(q_2)(\ddot{q}_2\sin(q_2) + \dot{q}_2^2\cos(q_2))\\ +\cos(q_3)(\ddot{q}_3\sin(q_3) + \dot{q}_3^2\cos(q_3)))\end{aligned} \tag{B.4}$$

$$
\begin{aligned}
t_{42} = {} & (\sin(q_1)(\ddot{q}_1\sin(q_1) + \dot{q}_1^2\cos(q_1)) \\
& +\sin(q_2)(\ddot{q}_2\sin(q_2) + \dot{q}_2^2\cos(q_2)) \\
& +\sin(q_3)(\ddot{q}_3\sin(q_3) + \dot{q}_3^2\cos(q_3)))
\end{aligned}
\tag{B.5}
$$

$$
\begin{aligned}
t_{43} = {} & (\ddot{q}_1\cos(q_1) + \dot{q}_1^2\sin(q_1)) \\
& +(\ddot{q}_2\cos(q_2) + \dot{q}_2^2\sin(q_2)) \\
& (\ddot{q}_3\cos(q_3) + \dot{q}_3^2\sin(q_3))
\end{aligned}
\tag{B.6}
$$

The terms $zz_b, m_p, m_{pg}, m_b, m_{pal}, f_{s_i}$ and I_a regrouped the essential dynamic parameters associated to the inertial, mass and friction effects, respectively from the proximal links, the parallelograms, and the rotor from the motors.

Appendix C

Equations and joints specifications of the variable stiffness system

---

Following the methodology to design a torsional spring in [Budynas 2006], the expressions associated to the specifications for the VSS design in Chapter 4, are defined as follows:

- Tensil strength:

$$S_{ut} = \frac{A_{mat}}{d_w^m} \tag{C.1}$$

  where A_{mat} is a constant associated to the type of material.

- Static Strength:

$$S_y = 0.78 S_{ut} \tag{C.2}$$

- Spring mean diameter:

$$D = D_{out} - d_w \tag{C.3}$$

- Spring index:

$$C = \frac{D}{d_w} \tag{C.4}$$

- Bending stress correction factor:

$$K_i = \frac{4C^2 - C - 1}{4C(C-1)} \tag{C.5}$$

- Maximum operating torque $\tau_{s_{MAX}}$:

$$\tau_{s_{MAX}} = \frac{\pi d_w^3 S_y}{32 K_i} \tag{C.6}$$

  where S_y represents the static strength, and K_i is the bending stress correction factor;

- Maximum deformation of the spring in number of turns:

$$\theta_{MAX_{turns}} = \Big(\frac{10.8\tau_{s_{MAX}} D N_b}{d_w^4 E}\Big) \tag{C.7}$$

- Corresponding maximum deformation θ_{MAX}:

$$\theta_{MAX} = \Big(\frac{10.8\tau_{s_{MAX}} D N_b}{d_w^4 E}\Big)360 \tag{C.8}$$

  where E represents the elastic modulus, and D is the spring mean diameter $D = D_{out} - d_w$;

- Spring inner diameter reduction at maximum load D_m:

$$D_m = \frac{N_b D}{N_b + \theta_{MAX_{turns}}} \tag{C.9}$$

  where $\theta_{MAX_{turns}}$ is the maximum deformation in turns, i.e. $\theta_{MAX}/360$;

- Mandrel/pin diametral clearance when the spring is subjected to maximum load $\varDelta$:

$$\varDelta = D_m - d_w - D_{pin} \tag{C.10}$$

- Number of active turns considering the legs from the upper and lower endings of the torsional spring:

$$N_a = N_b + \frac{L_1 + L_2}{3\pi D} \tag{C.11}$$

- Total body length:

$$L = d_w(N_a + 1) \tag{C.12}$$

- Minimum required spring constant for each VSS:

$$k = \frac{d_w^4 E}{10.8 D N_a} = \frac{\tau_{s_{MAX}}}{\theta_{MAX_{turns}}} \tag{C.13}$$

Table C.1: Components of the joints from the variable stiffness system and the five-bar active joints.

①	Motor from active joint of the robot
②	Shaft from the motor of the robot active joint
③	Coupling for the motor bearing
④	Double row angular contact ball bearing
⑤	Shaft aligner
⑥	Clamping ring
⑦	Aligner
⑧	Arm corresponding to proximal link
⑨	Coupling arm-motor
⑩	Support for pin/mandrel of VSS
⑪	Pin/mandrel of VSS
⑫	Torsional spring
⑬	Fixation of spring leg
⑭	Driven pulley
⑮	Bearing for decoupling motion from arm and VSS
⑯	Timing belt of the pulley-belt-transmission system
⑰	Driving pulley
⑱	Transmitting shaft
⑲	Couplings
⑳	Couplings
㉑	Clamping ring
㉒	Shaft aligner
㉓	Double row angular contact ball bearing
㉔	Shaft from the motor of the variable stiffness joint
㉕	Motor from variable stiffness joint
㉖	Arm support
㉗	Joint shaft
㉘	Bearing
㉙	Bearing bushing
㉚	Shaft bushing
㉛	Support

㉜	Double row angular contact ball bearing
㉝	Spacer for separating the bearings
㉞	Shaft bushing
㉟	Support

APPENDIX D

Dynamic model of the 2R serial robot with payload

The dynamic model of the 2-DOF serial robot is computed by using the Lagrange formalism and can be written under the form presented in [Briot 2015b], as follows:

$$\boldsymbol{\tau} = \mathbf{M}\ddot{\mathbf{q}} + \mathbf{c}(\mathbf{q}_a, \dot{\mathbf{q}}_a) + \mathbf{g}_r(\mathbf{q}) + \mathbf{f}_a \tag{D.1}$$

where $\mathbf{M}$ is a definite positive matrix of inertia:

$$\mathbf{M} = \begin{bmatrix} M_{11} & M_{12} \\ M_{21} & M_{22} \end{bmatrix} \tag{D.2}$$

with

- $M_{11} = m_1 l_{AB}^2 + zz_1 + m_2(l_{AB}^2 + l_{BS_2}^2 + 2l_{AB}l_{BS_2}\text{cos}(q_2)) + zz_2 + m(l_{AB}^2 + l_{BC}^2 + 2l_{AB}l_{BC}\text{cos}(q_2))$
- $M_{12} = m_2(l_{BS_2}^2 + l_{AB}l_{BS_2}\text{cos}(q_2)) + zz_2 + m(l_{BC}^2 + l_{AB}l_{BC}\text{cos}(q_2))$
- $M_{21} = M_{12}$
- $M_{22} = m_2 l_{BS_2}^2 + zz2 + ml_{BC}^2$

$\mathbf{h}(\mathbf{q}, \dot{\mathbf{q}})$ is a vector of Coriolis and centrifgural effects:

$$\mathbf{h}(\mathbf{q}, \dot{\mathbf{q}}) = \begin{bmatrix} -l_{AB}\dot{q}_2\text{sin}(q_2)(2\dot{q}_1 + \dot{q}_2)(ml_{BC} + m_2 l_{BS_2}) \\ m_2 l_{AB} l_{BS_2}\text{sin}(q_2)\dot{q}_1^2 + ml_{AB}l_{BC}\text{sin}(q_2)\dot{q}_1^2 \end{bmatrix} \tag{D.3}$$

$\mathbf{g}_r(\mathbf{q})$ is the vector grouping the gravitational effects including the payload:

$$\mathbf{g}_r(\mathbf{q}) = \begin{bmatrix} g_{r_1} \\ g_{r_2} \end{bmatrix} \tag{D.4}$$

with

- $g_{r_1} = m_1 g l_{AS_1}\cos(q_1) + m_2 g(l_{AB}\cos q_1 + l_{BS_2}\cos(q_1+q_2)) + mg(l_{AB}\cos(q_1) + l_{BC}\cos(q_1 + q_2)$
- $g_{r_2} = g\cos(q_1 + q_2)(m_2 l_{BS_2} + m l_{BC})$

and $\mathbf{f}_a$ groups the friction terms in the active joints:

$$\mathbf{f}_a = \begin{bmatrix} f_{s_1}\text{sign}(\dot{q}_1) \\ f_{s_2}\text{sign}(\dot{q}_2) \end{bmatrix} \tag{D.5}$$

From the aforementioned mathematical computations for calculating the inverse dynamic model, the numerical values of the dynamic and geometric parameters zz_1, zz_2, m_1, m_2, m, f_{s1}, f_{s2}, ℓ_{AB}, ℓ_{BC}, ℓ_{AS_1}, and ℓ_{BS_2} are defined respectively in Section 5.3.2 of Chapter 5.

Appendix E

List of publications of presented works

Publications in international congress

- R. Balderas Hill, S. Briot, A. Chriette and P. Martinet. *Minimizing the Energy Consumption of a Delta Robot by Exploiting the Natural Dynamics.* Submitted to 23rd CISM IFToMM Symposium on Robot Design, Dynamics and Control (RoManSy 2020). September 20-24, 2020 Sapporo, Japan. (**Submitted**)
- R. Balderas Hill, S. Briot, A. Chriette and P. Martinet. *Exploiting Natural Dynamics in order to Increase the Feasible Static-Wrench Workspace of Robots.* Proceedings of the 15th IFToMM World Congress, June 30–July 4, 2019, Krakow, Poland.
- R. Balderas Hill, S. Briot, A. Chriette and P. Martinet. *Increasing energy efficiency of high-speed parallel robots by using variable stiffness springs and optimal motion generation.* Proceedings of the ASME 2018 International Design Engineering Technical Conferences & Computers and Information in Engineering Conference IDETC/CIE 2018, August 26–29, 2018, Quebec, Canada.
- R. Balderas Hill, S. Briot, A. Chriette and P. Martinet. *Minimizing Input Torques of a High-Speed Five-Bar Mechanism by using Variable Stiffness Springs* Proceedings of the 22nd CISM IFToMM Symposium on Robot Design, Dynamics and Control (RoManSy 2018). June 25–28, Rennes, France, 2018.
- R. Balderas Hill, D. Six, A. Chriette, S. Briot, and P. Martinet. *Crossing Type 2 Singularities of Parallel Robots without Pre-planned Trajectory with a Virtual-constraint-based Controller.* Proceedings of 2017 IEEE International Conference on Robotics and Automation (ICRA 2017). May 29–June 3, Marina Bay Sands Convention Centre, Singapour, 2017.

Poster presentations

- R. Balderas Hill, S. Briot, A. Chriette and P. Martinet. *Design of High-Speed Robots with Drastically Reduced Energy Consumption.* Journé des Jeunes Chercheurs en Robotique Edition 2017 (JJCR 2017), Bayonne, France.

Other publications

- R. Balderas Hill. *Minimizing the input torques of a high-speed five-bar robot by using variable stiffness springs.* Journé des doctorants Edition 2018 (JDOC 2018), Doctoral school MathSTIC, Nantes, France.

References

[Adept] Adept Robotics. https://automation.omron.com/en/us/products/category/robotics

[Agrawal 2004] S. K. Agrawal, A. Fattah, 2004. Reactionless Space and Ground Robots: Novel Designs and Concept Studies. In Mech. Mach. Theory, Vol. 34, pp. 437–452.

[Albus 1992] Albus, J., Bostelman, R., and Dagalakis, N., 1992. The NIST SPIDER, A robot crane. In Journal of Research of the National Institute of Standards and Technology, 97(3), p. 373.

[Angeles 2006] Angeles, J., Caro, S., Khan, W. and Morozov, A. Kinetostatic design of an innovative Schönflies motion generator. Journal of Mechanical Engineering Science Vol. 220, pp. 935-943 (2006).

[Arakelian 2000] V. Arakelian, M. Dahan, M. Smith, 2000. A historical review of the evolution of the theory on balancing of mechanisms. In: Proceedings HMM2000. International Symposium on History of Machines and Mechanisms. Casino, pp 291–300. Springer, Berlin, Heidelberg, New York (2000).

[Arakelian 2015] V. Arakelian, and S. Briot, 2015. Balancing of Linkages and Robot Manipulators: Advanced Methods and Illustrative Examples. Springer, 2015. ISBN: 9783319124896.

[AREUS 2013] Automation and Robotics for EUropean Sustainabile manufacturing (AREUS) (2013–2016). European Commission. https://cordis.europa.eu/project/rcn/108857/factsheet/en.

[Asada 1983] H. Asada, T. Kanade, 1983. Design of Direct-Drive Mechanical Arms. In Journal of Vibration, Acoustics, Stress, and Reliability, Vol. 105, pp. 312-316.

[Ascher 1987] U. M. Ascher, R. M. M. Mattheij and R. D. Russel. Numerical Solution of Boundary Value Problems for Ordinary Differential Equations. Society for Industrial and Applied Mathematics, 1987. ISBN 978-0898713541.

[Bai 2016] G. Wu, S. Bai, and P. Hjørnet. Architecture optimization of a parallel Schonflies-motion robot for pick-and-place applications in a predefined workspace. In Mech. Mach. Theory, 106:148–165, 2016.

[Balderas 2017] R. Balderas Hill, D. Six, A. Chriette, S. Briot, and P. Martinet. Crossing Type 2 Singularities of Parallel Robots without Pre-planned Trajectory with a Virtual-constraint-based Controller. Proceedings of 2017 IEEE International Conference on Robotics and Automation (ICRA 2017). May 29 - June 3, Marina Bay Sands Convention Centre, Singapore, 2017.

[Balderas 2018] R. Balderas Hill, S. Briot, A. Chriette, and P. Martinet, 2018. Increasing energy efficiency of high-speed parallel robots by using variable stiffness springs and optimal motion generation. Proceedings of the ASME 2018 IDETC/CIE 2018, pp. V05BT07A011 10 pages, August 26-29, 2018, Quebec City, Canada.

[Balderas 2019] R. Balderas Hill, S. Briot, A. Chriette and P. Martinet, 2019. Exploiting Natural Dynamics in order to Increase the Feasible Static-Wrench Workspace of Robots. Proceedings of the 15th IFToMM World Congress, June 30–July 4, 2019, Krakow, Poland.

[Barreto 2016] J.P. Barreto, F.J.-F. Schöler and B. Corves: The concept of natural motion for pick and place operations. In: New advances in mechanisms, mechanical transmissions and robotics. Springer, pp. 89-98.

[Baradat 2008] C. Baradat, V. Arakelian, S. Briot and S. Guégan: Design and Prototyping of a New Balancing Mechanism for Spatial Parallel Manipulators. ASME, Journal of Mechanical Design, 2008, 130 (7), 072305, 13 pp.

[Birnie 1974] J. V. Birnie, 1974. Practical Implications of Programmable Manipulators. In Industrial Robot: An International Journal, Vol. 1 Issue: 3, pp.122-128.

[Bonev 2001] I. Bonev, 2001. Delta Parallel Robot - the Story of Success. https://www.parallemic.org/Reviews/Review002.html.

[Briot 2015a] S. Briot and V. Arakelian: A New Energy-free Gravity-compensation Adaptive System for Balancing of 4-DOF Robot Manipulators with Variable Payloads. In Proc. of the 14th International Federation for the Promotion of Mechanism and Machine Science World Congress (2015 IFToMM World Congress), October 2015, Taipei, Taiwan.

[Briot 2015b] S. Briot and W. Khalil: Dynamics of Parallel Robots: From Rigid Bodies to Flexible Elements. Springer, 2015. ISBN 9783319197883.

[Briot 2015c] S. Briot, M. Gautier, 2015. Global Identification of Joint Drive Gains and Dynamic Parameters of Parallel Robots. In Multibody System Dynamics, vol. 33, no. 1, 2015.

[Briot 2016] S. Briot, G. Pagis, N. Bouton and P. Martinet, 2016. Degeneracy Conditions of the Dynamic Model of Parallel Robots. In Multibody System Dynamics, vol. 37, no. 4, pp. 371–412, 2016.

[Briot 2018] S. Briot, and A. Goldsztejn, 2018. Topology Optimization of Industrial Robots: Application to a Five-bar Mechanism. In Mechanism and Machine Theory, 2018, Vol. 120, pp. 30-56.

[Brooks 1999] Brooks, R., Breazeal, C., Marjanovic, M., Scassellati, B., Williamson, M. The Cog project: Building a humanoid robot. In Springer-Verlag Lecture Notes in Computer Science Volume, 1999.

[Brossog 2015] Brossog, M., Bornschlegl, M., Franke, J., 2015. Reducing the energy consumption of industrial robots in manufacturing systems. International Journal of Advanced Manufacturing Technology, Vol. 78 Issue 5-8, pp. 1315-1328.

[Budynas 2006] R. G. Budynas and J. K Nisbett. Shigley's Mechanical Engineering Design, 8th ed. McGraw-Hill Science/Engineering/Math, 2006.

[Callier 1991] F. M. Callier and C. A. Desoer, Linear Systems Theory, Springer-verlag, 1991.

[Canfield 2018] S. L. Canfield, T. W. Hill, S. G. Zuccaro. Prediction and experimental validation of power consumption of Skid-Steer mobile robots in manufacturing environments. Journal of Intelligent Robot. Syst. 2018, pp. 1-15.

[Carabin 2017] G. Carabin, E. Wehrle, and R. Vidoni. A review on energy-saving optimization methods for robotic and automatic systems. In Robotics, vol. 6, no. 39, 2017.

[Carloni 2012] R. Carloni, L.C. Visser, S. Stramigioli. Variable stiffness actuators: a port-based power-flow analysis. IEEE Transactions on Robotics 28(1) (2012), pp. 1-11.

[Ceccarelli 2001] M. Ceccarelli, 2001. A Historical Perspective of Robotics Toward the Future. International Journal of Robotics and Mechatronics, Vol.13, No.3, pp. 299-313, 2001.

[Ceccarelli 2004] M. Ceccarelli, 2004. Fundamentals of Mechanics of Robotic Manipulation, Springer Netherlands, ISBN 978-1-4020-2110-7.

[Chapman 1991] Chapman, S. J., 1991. Electric Machinery Fundamentals, Fifth Edition, McGraw-Hill Education, International Edition. ISBN: 978-0-073-52954-7.

[Clavel 1990] R. Clavel, 1990. Device for movement and displacing of an element in space. US Patent No. 4,976,582, December 11.

[Company 2011] O. Company, F. Pierrot, S. Krut, C. Baradat, and V. Nabat, 2011. PAR2: a spatial mechanism for fast planar two-degree-of-freedom pick-and-place applications. In Meccanica 46:239–248.

[DEMAT 2010] Final Report Summary - DEMAT (A multi-technological approach for Dematerialising the production systems within a view of productive, reliable and eco-efficient machining processes), (2010–2013). https://cordis.europa.eu/project/rcn/94795/reporting/en

[Devol 1954] G. Devol, 1954. Programmable Article Transfer. https://patents.google.com/patent/US2988237.

[dSPACE site] dSPACE. URL: https://www.dspace.com/

[Duan 2014] QJ. Duan and X. Duan: Workspace classification and quantification calculations of cable-driven parallel robots. In Adv. Mech. Eng. Volume 2014, Article ID 358727, 9 pages.

[Ebert-Uphoff 2000] Ebert-Uphoff, I., Gosselin, C. M., and Laliberté, T., 2000. Static Balancing of Spatial Parallel Mechanisms: Revisited. In ASME J. Mech. Des., Vol. 122, pp. 43-51.

[Fasse 1994] E.D Fasse, N. Hogan, S. R. Gomez, N. R. Mehta. A novel variable mechanical impedance electromechanical actuator, Dynamic Systems and Control 55(1) (1994), pp. 311-318.

[Gasparetto 2016] A. Gasparetto, 2016. Robots in History: Legends and Prototypes from Ancient Times to the Industrial Revolution. In Explorations in the History of Machines and Mechanisms. History of Mechanism and Machine Science, vol. 32, pp. 39-49. Berlin/Heidelberg: Springer.

[Gasparetto 2019] A. Gasparetto, L. Scalera, 2019. A Brief History of Industrial Robotics in the 20th Century. In Advances in Historical Studies. Vol. 08, No. 01, 12 pages.

[Gautier 1990] M. Gautier, and W. Khalil, 1990. Direct Calculation of Minimum Set of Inertial Parameters of Serial Robots. In IEEE Transaction Robotics Automation, vol 6, no. 3, pp. 368–373.

[Gautier 1991] M. Gautier, 1991. Numerical Calculation of the Base Inertial Parameters. In J. Rob. Syst., vol. 8, no. 4, pp. 485–506.

[Gautier 2001] M. Gautier, P. Poignet, 2001. Extended Kalman Filtering and Weighted Least Squares Dynamic Identification of Robot. In Control. Eng. Pract., vol. 9, pp. 1361–1372.

[Gautier 2014] M. Gautier, S. Briot, 2014. Global Identification of Joint Drive Gains and Dynamic Parameters of Parallel Robots. In ASME Journal of Dynamic Systems, Measurement and Control, vol. 136, no. 5, 2014.

[Gavin 2013] H. P. Gavin. The Levenberg-Marquardt method for nonlinear least squares curve-fitting problems. Dept. Civil Environ. Eng., Duke Univ., Durham, NC, USA, Oct. 2013.

[Geisert 2016] M. Geisert, and N. Mansard, 2016. Trajectory Generation for Quadrotor based Systems using Numerical Optimal Control. In Proc. of International Conference on Robotics and Automation, ICRA 2016, Stockholm, Sweden. pp. 2958–2964.

[Germain 2013] Germain, C., Caro, S., Briot, S., Wenger, P., Singularity-free Design of the Translational Parallel Manipulator IRSBot-2. Mechanism and Machine Theory, 2013, Vol. 64, pp. 262-285.

[Ghazaei 2015] M. Ghazaei, B. Olofsson, A. Robertsson, R. Johansson, 2015. Real-Time Trajectory Generation using Model Predictive Control. In Proc. of 2015 IEEE Conference on Automation Science and Engineering (CASE), 2015, pp. 942-948.

[Gleesona 2016] D. Gleesona, S. Bjorkenstama, R. Bohlina, J. S. Carlsona, B. Lennartsonb, 2016. Towards Energy Optimization using Trajectory Smoothing and Automatic Code Generation for Robotic Assembly. In Proc. 6th CIRP Conference on Assembly Technologies and Systems, pp. 341-346.

[Gomes 2016] A. Gomes, L. Junior, R. Milanezi de Andrade and A. B. Filho, 2016. Series Elastic Actuator: Design, Analysis and Comparison. In Recent Advances in Robotic Systems, IntechOpen. ISBN: 978-953-51-2571-6.

[Gosselin 1990] C. Gosselin, and J. Angeles. 1990. Singularity analysis of closed-loop kinematic chains. IEEE Trans. on Rob. and Aut., 6(3), pp. 281-290.

[Gosselin 2012] C. Gosselin, P. Ren, and S. Foucault: Dynamic trajectory planning of a two-dof cable-suspended parallel robot. In Proc. IEEE International Conference on Robotics and Automation, St. Paul, MN, USA, May 14–18, 2012, pp. 1476-1481.

[Gouttefarde 2007] M. Gouttefarde, J.-P. Merlet, and D. Daney: Wrench-feasible workspace of parallel cable-driven mechanisms. In Proc. IEEE International Conference on Robotics and Automation, Rome, Italy, 2007, pp. 1492-1497

[Goya 2012] Goya, H., Matsusaka, K., Uemura, M., Nishioka, Y., and Kawamura S., 2012. Realization of high-energy efficient pick-and-place tasks of scara robots by resonance. In IEEE/RSJ International conference on Intelligent Robots and Systems, IROS 2012, pp. 2730-2735, Vilamoura, Algarve (Portugal).

[Haddadin 2011] S. Haddadin, K. Krieger, M. Kunze, and A.Albu-Schaeffer, 2011. Exploiting potential energy storage for cyclic manipulation: An analysis for elastic dribbling with an anthropomorphic robot. In Proc. of IEEE IROS 2011, pp. 1789-1796.

[Hamon 2011] P. Hamon, M. Gautier, and P. Garrec, 2011. New Dry Friction Mdel with Load and Velocity-Dependence and Dynamic Identification of Multi-DOF Robots. In Proc. of the IEEE International Conference on Robotics and Automation (ICRA 2011), Shanghai, China, pp. 1077–1084.

[Haq 2011] A. Haq, Y. Aoustin, C. Chevallereau, 2011. Compliant Joints Increase the Energy Efficiency of Bipedal Robot. In Proc. of the 14th International Conference on Climbing and Walking Robots and the Support Technologies for Mobile Machines (CLAWAR2011), Sep 2011, Paris, France.

[Haq 2012] A. Haq, Y. Aoustin, C. Chevallereau, 2012. Effects of Knee Locking and Passive Joint Stiffness on Energy Consumption of a Seven-Link Planar Biped. In Proc. of the 2012 IEEE International Conference on Robotics and Automation, Saint Paul, MN, USA, 14-18 May 2012.

[Herder 2001] J. L. Herder, 2001. Energy-Free Systems: Theory, Conception and Design of Statically Balanced Mechanisms. PhD thesis, Delft University of Technology.

[Herder 2002] Herder, J. L., 2002. Some Considerations Regarding Statically Balanced Parallel Mechanisms. In Proceedings of the Workshop on Fundamental Issues and Future Research Directions for Parallel Mechanisms and Manipulators, Quebec City, QB, Canada, Oct. 3 and 4.

[Hiller 2005] M. Hiller, S. Fang, S. Mielczarek, R. Verhoeven, and D. Franitza: Design, analysis and realization of tendon-based parallel manipulators. In Mech. Mach. Theory, vol. 40, no. 4, pp. 429-445, April 2005.

[IFR] IFR International Federation of Robots. Robot History. https://ifr.org/robot-history.

[Jafari 2011] A. Jafari, N.G.Tsagarakis, and D.G.Caldwell, 2011. Exploiting Natural Dynamics for Energy Minimization using an Actuator with Adjustable Stiffness (AwAS). In Proc. of IEEE International Conference on Robotics and Automation Conference, (ICRA 2011), Shanghai, pp. 4632-4637.

[Jiang 2016] X. Jiang, C.Gosselin: Dynamic point-to-point trajectory planning of a three-DOF cable-suspended parallel robot. IEEE Transactions on Robotics 32(6), 1550-1557 (2016).

[Jiang 2018] X. Jiang, E. Barnett, C. Gosselin: Periodic Trajectory Planning Beyond the Static Workspace for 6-DOF Cable-Suspended Parallel Robots. IEEE Transactions on Robotics, 2018, vol. 34, no. 4, pp. 1128-1140.

[Kaci 2018] Kaci, L., Briot, S., Boudaud, C., and Martinet, P., 2018. Design of a Wooden Five-bar Mechanism. Proceedings of the 22nd CISM-IFToMM Symposium on Robot Design, Dynamics, and Control (ROMANSY 2018), pp. 331-339, June 25-28, 2018, Rennes, France.

[Kawamura 2000] Kawamura, S., Kino, H., and Won, C., 2000. High-speed manipulation by using parallel wire-driven robots. Robotica, 18(1), p. S0263574799002477.

[Kawamura 2002] Kawamura, S., Yamamoto, T., Ishida, D., Ogata, T., Nakayama, Y., Tabata, O., Sugiyama, S. 2002. Development of passive elements with variable mechanical impedance for wearable robots. In IEEE International Conference on Robotics and Automation, ICRA 2002, vol. 1, 2002, pp.248–253.

[Kawasaki robotics] Pick-and-Place Robots. Kawasaki Delta robot. https://robotics.kawasaki.com/en1/products/robots/pick-place/

[Khalil 2004] Khalil, W., Dombre, E. (2004). Modeling, identification and control of robots, Vol. 56. Hermes, ISBN: 190399666X; 978-1903996669.

[Kim 2017] Y. J. Kim, 2017. Anthropomorphic Low-Inertia High-Stiffness Manipulator for High-Speed Safe Interaction. In IEEE Transactions on Robotics, vol. 33, No. 6, pp. 1358-1374, December 2017.

[Koessler 2018] A. Koessler, N. Bouton, S. Briot, B.C. Bouzgarrou and Y. Mezouar. Linear Adaptive Computed Torque Control for Singularity Crossing of Parallel Robots. Proceedings of the 22nd CISM-IFToMM Symposium on Robot Design, Dynamics, and Control (ROMANSY 2018), pp. 222-229, June 25-28, 2018, Rennes, France.

[Koetsier 2019] T. Koetsier, 2019. Towards the Global Intelligent Machine. In The Ascent of GIM, the Global Intelligent Machine. History of Mechanism and Machine Science, vol 36, pp. 293-317. Berlin/Heidelberg: Springer.

[Kong 2010] Kong, K., Bae. J., Tomizuka, M., 2010. A compact rotary series elastic actuator for knee joint assistive system. in Proc. IEEE Int. Conf. Robot. Autom., May 2010, pp. 2940-2945.

[Krupp 2000] Krupp, B., 2000. Design and control of a planar robot to study quadrupedal locomotion. Master's thesis, Massachusetts Institute of Technology, 2000.

[Kuo 1996] B. C. Kuo, Automatic Control Systems, Prentice-Hall Int. 1996.

[Lagoda 2010] Lagoda, C., Schouten, A., Stienen, A., Hekman, E., and van der Kooij, H., 2010. Design of an electric series elastic actuated joint for robotic gait rehabilitation training. In Proc. IEEE 3rd RAS and EMBS Int. Conf. Biomed. Robot. Biomechatron., Sep. 2010, pp. 21-26.

[Lammerts 1995] I. M. M. Lammerts, F. E. Veldpaus, M. J. G. Van de Molengraft and J. J. Kok. Adaptive Computed Reference Computed Torque Control of Flexible Robots. In Journal of Dynamic Systems, Measurement, and Control, vol. 117, no. 1, pp. 31-36, 1995.

[Leblond 1998] M. Leblond, and C. M. Gosselin, 1998. Static Balancing of Spatial and Planar Parallel Manipulators with Prismatic Actuators. In Proc. of the DETC 1998, Atlanta, GA, pp. 1–12.

[Lessard 2007] S. Lessard, P. Bigras, I.A. Bonev, S. Briot and V. Arakelian, "Optimum Static Balancing of a Parallel Robot for Medical 3D-Ultrasound Imaging," Proceedings of the 12th IFToMM World Congress, 18-21 juin, 2007, Besançon, France.

[LeVeque 2007] R. LeVeque. Finite Difference Methods for Ordinary and Partial Differential Equations: Steady-State and Time-dependent Problems (Classics in Applied Mathematics). ISBN: 978-0898716290.

[Liu 2014] S. Liu and D. Sun. Minimizing energy consumption of wheeled mobile robots via optimal motion planning. IEEE/ASME Trans. Mechatronics, 2014: 19(2): 401-411.

[Liu 2018] Y. Lui, S. Guo, H. Hirata, H. Ishihara, and T. Tamiya, 2018. Development of a powered variable-stiffness exoskeleton device for elbow rehabilitation. In Biomedical Microdevices, vol. 20, no. 3, 2018.

[Makino 1980] H. Makino, N. Furuya, 1980. Selective Compliance Assembly Robot Arm. In Proceedings of 1st International Conference on Assembly Automation (ICAA), Brighton, March 25-27, pp. 77-86.

[Malone 2011] B. Malone, 2011 . George Devol: A Life Devoted to Invention, and Robots. IEEE Spectrum Magazine, September 26th, 2011. Available at: https://spectrum.ieee.org/automaton/robotics/industrialrobots/george-devol-a-life-devoted-to-invention-and-robots.

[Marques 2012] L. Marques, a. T. D. Almeida, M. Armada, R. Fernández, H. Montes, P. González, and Y. Baudoin, 2012. State of the Art Review on Mobile Robots and Manipulators for Humanitarian Demining. In IARP WS Humanit. Demining, pp. 2-8, 2012.

[McGeer 1990] T. McGeer, 1990. Passive dynamic walking. International Journal of Robotics Research, 9(2):62-82, 1990.

[Mei 2002] Y. Mei, Y-H. Lu, et al. Energy-Efficient motion planning for mobile robots. In Proc. Australian Conference Robotics and Automation. Auckland, New Zealand, 2002, pp. 117-121.

[Meike 2011] D. Meike and L. Ribickis (2011). Recuperated energy savings potential and approaches in industrial robotics. In Proc. of the IEEE 15th Int. Conf. on Automation Science and Engineering, pp. 299-303, 2011.

[Merlet 2006] J-P. Merlet: Parallel Robots. Springer, 2006. ISBN 9781402041334.

[MG-Tech] MG-Tech. URL https://www.mg-tech.fr/

[Middletone 1986] R. H. Middletone, G. C. Goodwin, 1986. Adaptive computed torque control for rigid link manipulators. In Proc. 25th IEEE Conference on Decision and Control, 1986, Athens, Greece.

[Millman 1986] Millman, J., 1986. Microelectronics: Digital and Analog Circuits and Systems. McGraw-Hill Inc., US. ISBN: 978-0-070-42330-5.

[Mitsubishi] Industrial Robots-MELFA. Mitsubishi Electric. https://us.mitsubishielectric.com/fa/en/products/industrial-robots-melfa.

[Mo 2017] J. Mo, Z. Shao, L. Guan, F. Xie and X. Tang. Dynamic performance analysis of the X4 high-speed pick-and-place parallel robot. In Robotics and Computer-Integrated Manufacturing, pp. 48–57.

[Moré 1978] J.J. Moré, 1978. The Levenberg-Marquardt algorithm: Implementation and theory. In: Watson G.A. (eds) Numerical Analysis. Lecture Notes in Mathematics, vol 630. Springer, Berlin, Heidelberg.

[Mojabi 2002] P. Mojabi, et. al. Introducing August: a novel strategy for an omnidirectional spherical rolling robot. In Proc. IEEE International Conference on Robotics and Automation 2002, pp. 3595-3600, 2002.

[Mottola 2019] G. Mottola, C. Gosselin and M. Carricato: Dynamically feasible motions of a class of purely-translational cable-suspended parallel robots. In Mech. Mach. Theory, vol. 132, pp. 193-206, 2019.

[Nabat 2005] Nabat, V., Rodrigues, O., Company, O., Krut, S., Pierrot, F. Par4: very high speed parallel robot for pick-and-place. In Proceedings of the IEEE/RSJ International Conference on Intelligent Robots and Systems, IROS 2005, pp. 1202-1207, Alberta, Canada, August 2-6 2005.

[Nabat 2007] V. Nabat. Robots parallèles à nacelle articulée, du concept à la solution industrielle pour le pick-and-place. fr, thèse de doct., 2007.

[Neuberger 2009] J. Neuberger, 2009. Sobolev Gradients and Differential Equations. Spring ASIN: B01K0S5RRM.

[Newman 1986] Newman, W. S., and Hogan, N., 1986. The Optimal Control of Balanced Manipulators. In Proceedings of the Winter Annual Meeting of the ASME, Anaheim, CA..

[Pagis 2015a] Pagis, G., Bouton N., Briot S., Martinet P.: Enlarging parallel robot workspace through type-2 singularity crossing. in Control Engineering Practice, Vol. 39, pp. 1-11, June 2015.

[Pagis 2015b] Georges Pagis. Augmentation de la taille de l'espace de travail opérationnel des robots paralléles en traversant les singularités de Type 2 : génération de trajectoires optimales et commande avancée". PhD thesis. Ecole Centrale de Nantes, 2015 (in French).

[Penta Robotics 2004] Penta Robotics, 2014. Introducing Veloce. Penta Robotics, Vreeland, The Netherlands, http://pentarobotics.com/.

[Pellicciari 2013] M. Pellicciari, G. Berselli, F. Leali, and A. Vergnano, 2013. A method for reducing the energy consumption of pick-and-place industrial robots. In Mechatronics, vol 23, pp. 326-334.

[Pellicciari 2015] M. Pellicciari, A. Avotins, K. Bengtsson, G. Berselli, N. Bey, B. Lennartson, D. Meike (2015). AREUS - Innovative Hardware and Software for Sustainable Industrial Robotics. In 2015 IEEE International Conference on Automation Science and Engineering (CASE), Aug 24-28, 2015. Gothenburg, Sweden, pp. 1325-1332.

[Pierrot 1999] F. Pierrot and O. Company. H4 : a new family of 4-DOF parallel robots. In 1999 IEEE/ASME International Conference on Advanced Intelligent Mechatronics, Atlanta, GA, USA : IEEE, 1999, pp. 508–513, isbn : 978-0-7803-5038-0.

[Pierrot 2001] F. Pierrot, F. Marquet, O. Company and T. Gil. H4 parallel robot: modeling, design and preliminary experiments. In Proceedings 2001 ICRA. IEEE International Conference on Robotics and Automation, Seoul, South Korea: IEEE, 2001, pp. 3256–3261.

[Pierrot 2009] F. Pierrot, V. Nabat, O. Company, S. Krut and P. Poignet. Optimal Design of a 4-DOF Parallel Manipulator: From Academia to Industry. In IEEE Transactions on Robotics, vol. 25, no 2, pp. 213–224.

[Pillay 1989] Pillay, P., Krishnan R., 1989. Modeling, simulation, and analysis of permanent-magnet motor drives. Part II. The brushless DC motor drive. IEEE Transactions Industry Applications, Vol. 25, pp. 274-279.

[Pott 2010] Pott, A., Meyer, C., and Verl, A., 2010. Large-scale assembly of solar power plants with parallel cable robots. Isr/Robotik 2010, pp. 999–1004.

[Pratt 1995a] Pratt, G. and Williamson, M., 1995. Series elastic actuators. In Proc. IEEE/RSJ Int. Conf. Intell. Robot. Syst. Human Robot Interact. Cooper. Robot., Aug. 1995, vol. 1, pp. 399-406.

[Pratt 1995b] Jerry E.Pratt. Virtual model control of a biped walking robot.Master's thesis, Massachusetts Institute of Technology, August 1995.

[Pratt 1998] Pratt J., and Pratt, G., 1998. Intuitive control of a planar bipedal walking robot. In Proc. IEEE Int. Conf. Robot. Autom., May 1998, vol. 3, pp. 2014-2021.

[Pratt 2002] Pratt, J., Krupp B., and Morse C., 2002. Series elastic actuators for high fidelity force control. Industrial Robot: An International Journal, vol. 29, no 3, p. 234-241, 2002.

[Rehmat 2018] N. Rehmat, J. Zuo, W. Meng, Q. Liu, S. Q. Xie, and H. Liang, 2018. Upper rehabilitation using robotic exoskeleton systems: a systematic review. In International Journal of Intelligent Robotics and Applications, vol. 2, no. 3, pp. 283–295, 2018.

[Riazi 2016] S. Riazi, K. Bengtsson, R. Bischoff, A. Aurnhammer, O. Wigstrom, and B. Lennartson, 2016. Energy and Peak-power Optimization of Existing Time-optimal Robot Trajectories. In Proc. of 2016 IEEE International Conferences on Automation Science and Engineering (CASE 2016). TX, USA, August 21-24, 2016, pp. 321-327.

[RobEcolo 2015] Project RobEcolo (2015–2019). URL http://robecolo.irccyn.ec-nantes.fr/

[Roberts 1972] S. M. Roberts and J. S. Shipman. Two-Point Boundary Value Problems: Shooting Methods. New York: Elsevier, 1972. ISBN 978-0444001023.

[Robinson 1999] Robinson, D., Pratt, J., Paluska, D., Pratt, G., 1999. Series Elastic Actuator development for a biomimetic walking robot. In IEEE/ASME AIM99, 1999.

[Roweis (Notes)] S. Roweis. Levenberg-Marquardt Optimization. Computer Science Department at New York University.

[Scheinman 1973] V. Scheinman, 1973. Design of a Computer Controlled Manipulator. PhD Thesis, Stanford, CA: Stanford University.

[Schiavi 2008] R. Schiavi, G. Grioli, S. Sen, A. Bicchi. VSA-II: A novel prototype of variable stiffness actuator for safe and performing robots interacting with humans. In Proceedings of the IEEE International Conference on Robotics and Automation, pp. 2171-2176, 2008.

[Schiehlen 2005] W. Schiehlen, and N. Guse: Control of Limit Cycle Oscillations, In Proc. of the IUTAM Symposium on Chaotic Dynamics and Control of Systems and Processes in Mechanics, pp. 429-439, 2005.

[Shang 2012] W. W. Shang, S.Chong and Y. Ge, 2012. Adaptive computed torque control for a parallel manipulator with redundant actuation. In Robotica, vol. 30, no. 3, pp. 457-466, May 2012.

[Siciliano 2008] B. Siciliano, O. Khatib, 2008. Springer Handbook of Robotics. ISBN 978-3-540-30301-5.

[Siemens] Siemens, The performance-optimized and easy-to-use servo drive system, SINAMICS V90 datasheet.

[Spong 1989] Spong, M. W., Vidyasagar, M., Robot dynamics and control, John Wiley and Sons, New York, 1989.

[Sun 2005] Z. Sun and JH Reif. On finding energy-minimizing paths on terrains. IEEE Transactions on Robotics 2005, 21 (1): pp. 102-114.

[Taheri 2014] E. Taheri. Master thesis: Rapid space trajectory generation using a Fourier Series Shape-Based Approach. Michigan Technological University, 2014.

[Tomik 2012] F. Tomik, S. Nudehi, L. Flynn and R. Mukherjee. Design, fabrication and control of spherobot: A spherical rolling robot. Journal of Intelligent and Robotic Systems, 67(2), pp. 117-131, 2012.

[Tonietti 2005] G. Tonietti, R. Schiavi, A. Bicchi. Design and control of a variable stiffness actuator for safe and fast physical human/robot interaction. In Proceedings of the IEEE International Conference on Robotics and Automation, pp. 526-531, 2005.

[Uemura 2009] M. Uemura, and S. Kawamura, 2009. Resonance-based Motion Control Method for Multi-Joint Robot through Combining Stiffness Adaptation and Iterative Learning Control. In Proc. of 2009 IEEE International Conference on Robotics and Automation, Kobe International Conference Center Kobe, Japan, May 12-17, 2009, pp. 1543-1548.

[Vanderborght 2008] B. Vanderborght, B. Verrelst, R. Van Ham, M. Van Damme, P. Beyl, D. Lefeber. Development of a compliance controller to reduce energy consumption for bipedal robots. Autonom. Robots, vol. 24, no. 4, pp. 419-434, May 2008.

[VIACTORS 2009] Variable Impedance ACTuation systems embodying advanced interaction behaviORS (VIACTORS). A project supported by the European Commission under the 7th Framework Programme. https://www.viactors.org/

[Visser 2010] L.C. Visser, R. Carloni, S. Stramigioli, 2010. Variable Stiffness Actuators: a Port-based Analysis and a Comparison of Energy Efficiency. In Proc. 2010 IEEE International Conference on Robotics and Automation, Anchorage Convention District, May 3-8, 2010, Anchorage, Alaska, USA, pp. 3279-3284.

[Visser 2011] L.C. Visser, R. Carloni, S. Stramigioli. Energy efficient variable stiffness actuators. IEEE Transactions on Robotics 27(5) (2011), pp. 865-875.

[Wang 1993] F. Y. Wang and J. L. Russell, 1993. Minimum-weight robot arm for a specified fundamental frequency. In Robotics and Automation, vol. 3, pp. 490-495, 1993.

[Westerlund 2000] L. Westerlund, 2000. The Extended Arm of Man: A History of Industrial Robot. ISBN: 978-9177364672.

[Williamson 1999] M. M. Williamson. PhD thesis: Robot Arm Control Exploiting Natural Dynamics, 1999. MIT.

[Zhang 2017] D. Zhang, B. Wei. A review on model reference adaptive control of robotic manipulators. In Annual Reviews in Control, vol. 43, pp. 188-198, February 2017.

[Zhuang 2014] H. Zhuang, H. Gao, Z. Deng, L. Ding, and Z. Liu, 2014. A review of heavy-duty legged robots. Sci. China Technol. Sci., vol. 57, no. 2, pp. 298-314, 2014.

UNIVERSITE
BRETAGNE
LOIRE / MATHSTIC

CENTRALE
NANTES

Titre : Conception des robots rapides à consommation énergétique drastiquement réduite

Mots clés : robots rapides de prise et dépose, ressort à raideur variable, exploiter la dynamique naturelle, échange entre énergie potentielle et énergie cinétique, réduction de la consommation d'énergie.

Résumé : Il est bien connu qu'un des plus importants défis de la robotique industrielle est d'augmenter l'efficacité énergétique des robots manipulateurs. Dans les applications industrielles, telles que les opérations de prise et dépose à grande vitesse, la précision est généralement le critère le plus important pour mesurer les performances du robot. Cependant, les méthodes de conception des robots rapides ont évolué vers la conception des robots, pas seulement précis, mais également performants sur le plan énergétique.

Cette thèse propose un principe d'actionnement pour réduire la consommation d'énergie des robots à grande vitesse en plaçant des ressorts à raideur variable en parallèle des actionneurs d'un robot rapide. L'idée est de régler la raideur de ces ressorts à l'aide d'autres actionneurs afin de mettre le robot à proximité de modes de résonance lors de son déplacement (les trajectoires de prise et dépose étant pseudo-oscillantes). En ajoutant un ressort à raideur variable en parallèle des liaisons actionnées par le robot, deux performances sont obtenues: i) la connexion directe entre les liaisons du moteur et du robot, garantissant ainsi la précision à grande vitesse, et ii) le contrôle de l'énergie potentielle stockée à libérer par cycle du mouvement de prise et dépose, exploitant ainsi la dynamique naturelle du robot à hautes vitesses et réduisant la consommation d'énergie.

Les résultats expérimentaux de l'approche suggérée sur un prototype de taille industrielle montrent la réduction drastique de la consommation d’énergie pour des mouvements rapides pseudo-oscillants.

Title : Design of high-speed robots with drastically reduced energy consumption

Keywords : high-speed pick-and-place robots, variable stiffness springs, exploiting the natural dynamics, exchange from potential to kinetic energy, reduction of the energy consumption.

Abstract : It is well-known that one of the most representative future challenges in industrial robotics, is to increase the energy efficiency of robot manipulators. In industrial applications, such as high-speed pick-and-place operations, the accuracy is typically the most important criteria to measure the robot performance. Nevertheless, the design trends to operate at high speeds are shifting to the design of robots, which are not only accurate, but also they can perform in an energy-efficient way.

This thesis proposes an actuation principle for reducing the energy consumption of high-speed robots by placing variable stiffness springs (VSS) in parallel to the motors that actuate the links of a high-speed robot. The main idea is to smartly tune online the force/displacement relation of the VSS, associated to the VSS stiffness, so that the robot is put in near a resonance mode, thus considerably decreasing the energy consumption during fast pseudo-periodic pick-and-place motions. By adding a spring with controllable stiffness in parallel to the robot actuated links, two performances are achieved: i) direct power connection between the motor and the robot links, thus ensuring accuracy at high-speeds; ii) control of the stored potential energy to be released per cycle of the pick-and-place motion, thus exploiting the robot natural dynamics at high-speeds, and therefore reducing the energy consumption.

The experimental results of the suggested approach on an industrial-sized prototype show the drastic reduction of energy consumption for fast quasi-periodic pick-and-place-like motions.